Tesis Doctoral

TIME-FREQUENCY ANALYSIS FOR THE DYNAMIC QUANTIFICATION OF THE INTERACTIONS BETWEEN SIGNALS RELATED TO THE CARDIOVASCULAR SYSTEM

Autor

Orini, Michele

Director/es

Bailón Lesma, Raquel
Mainardi, Luca
Laguna Lasaosa, Pablo

INSTITUTO DE INVESTIGACION EN INGENIERIA DE ARAGON
2012

Time-frequency analysis for the dynamic quantification of the interactions between signals related to the cardiovascular system

PhD dissertation

Author: Michele Orini[1,2]

Director: Raquel Bailón[1]
Co-directors: Luca Mainardi[2], Pablo Laguna[1]

[1] Grupo de tecnologías de las comunicaciones, Universidad de Zaragoza
Instituto de Investigacíion en Ingeniería de Aragón, I3A, Spain

[2] Dipartimento di ingenieria biomedica, Politecnico di Milano, Italy

December 6, 2011

Abstract

In this dissertation, some advanced methodologies for the study of non-stationary signals in the joint time-frequency (TF) domain are presented, with the purpose of characterizing the dynamic interactions between cardiovascular signals. This study is motivated by the necessity of improving the understanding of the autonomic control of the cardiovascular system, whose impairment is related with many pathologies. The dissertation is articulated in three parts: An introduction in which relevant physiological and methodological aspects are described; a methodological part; and a part in which the proposed methodologies are applied to physiological studies.

In the introduction, the control of sympathetic and parasympathetic nervous systems on the cardiovascular regulation as well as the interactions between cardiovascular parameters and respiration are described. In particular, the physiological mechanisms that are still unclear or that are currently matter of debate are highlighted. To better contextualize the work proposed in the dissertation, a description of the most recent time-varying techniques of analysis is also given.

The second part is composed of four chapters, §2–§5, which face the following issues: simulation of non-stationary signals, spectral analysis, coherence analysis and phase analysis in the TF domain.
In chapter §2, a method to generate non-stationary stochastic processes which mimic the dynamics of cardiovascular signals is described. These processes are characterized by a predetermined and controlled TF structure: the design parameters that are used as input of the model are either the instantaneous frequency and power or the instantaneous frequency and spectral amplitude of each spectral component, and the output is the stochastic process associated to them. The accuracy and robustness of the method are evaluated in simulation studies which aim at simulating heart rate variability during exercise stress test and listening to different music excerpts.
In chapter §3, the TF distributions belonging to the Cohen's class are introduced. In particular, the smoothed pseudo Wigner-Ville distribution (SPWVD) is described. Owing to the possibility of performing an independent smoothing in time and frequency, the SPWVD is considered one of the best options to analyze non-stationary signals. A method to quantify the TF resolution of these distributions is proposed and it is used throughout the entire dissertation. A simulation study based on signals generated by means of the method presented in §2 is carried out to evaluate the accuracy of the SPWVD in conditions characterized by different degree of non-stationarity. Finally, a method that performs a parametric decomposition of the SPWVD is described. The advantage of this method, which will be used in a physiological study in §6, is that it allows separating relevant signal components from noise, thus offering the possibility of reducing the interference terms that usually appear in the distributions of the Cohen's class.
Chapter §4 is about the estimation of time-frequency coherence between non-stationary signals. Time-frequency coherence has the advantage of allowing the simultaneous localization of temporal intervals and spectral bands in which two signals are locally correlated, thus providing robust and accurate tracking of local correlation changes.

Coherence estimates depend on the TF resolution of the distribution used in the estimation. To give a correct interpretation of the results, two methods based on surrogate data are proposed to assess whether the coherence estimates are statistically significant. Two algorithms to automatically determine signal-dependent kernels which allow estimating TF coherence by SPWVD are proposed. In a comparative study which involve both simulated and physiological recorded data, the SPWVD is shown to localize with higher accuracy than other distributions, such as the multitaper spectrogram (MTSP) and the continuous wavelet transform, the TF regions in which signals are locally correlated. Finally, an example of application of TF coherence analysis on cardiovascular signals, such as heart period variability, systolic arterial pressure variability and respiration, is given.

Chapter §5 is about the estimation of phase differences between cardiovascular signals in the TF domain. Time-frequency phase difference analysis allows a fast tracking of the variation of the degree of synchronization between the spectral components of two signals. Moreover, phase difference information can be used to establish, to a certain degree, causal relationships between non-stationary spectral components. The use of the SPWVD to estimate TF phase differences is particularly suited because TF phase difference estimates are reliable only around well localized time-varying spectral band in which spectral components are locally correlated. The proposed methodology is evaluated in different simulation studies based on both computer generated and recorded physiological data.

In the second part of the dissertation, composed of chapters §6–§8, three physiological studies are described.

In chapter §6, the effect that musical excerpts characterized by different emotional valence has on HRV and respiration is studied. The characterization of the influence of music on cardiovascular parameters has both physiological and clinical relevance, since the use of music for therapeutic purposes is a matter of increasing interest. In this study, it is shown that the emotional valence of music specifically affects the respiratory frequency and the respiratory oscillations in HRV. It is shown that the transition from a musical stimulus to another provokes variations characterized by a first rapid response, which lasts about 10-20 seconds, and a seconds slower phase, which last more than one minute. The cardio-respiratory interactions are also studied. It is shown that musical excerpts characterized by different emotional valence do not provoke different pattern of response in the coherence and phase differences between HRV and respiration.

In chapter §7 the degree of similarity between the TF structure of HRV and the pulse rate variability (PRV) obtained from the photoplethysmography (PPG) signal, during tilt table test, is studied. The aim of the study is to assess whether PRV can be used as a surrogate for HRV during non-stationary conditions. The use of PRV to indirectly estimate HRV is interesting since the device used to estimate the PPG signal is not cumbersome, is cheap, and widely used in the clinical environment. Time-frequency and TF coherence analysis suggest that PRV can be used as alternative measurement of the HRV, at least during tilt table test. The study also reveals that some differences between HRV and PRV also exist, especially in the oscillations related with respiration. However, in the analyzed signals, these differences, which are due to variations in

the pulse transit time, are not sufficient to modify the conclusions of the physiological study.

In chapter §8, the cross TF analysis presented in chapters §4–§5 is applied to the study of the dynamic interactions between RRV and systolic arterial pressure variability (SAPV). The study of these interactions is interesting because they are still partially unclear, and due to the clinical relevance of baroreflex sensitivity, which has both diagnostic and prognostic value. This study shows that during tilt table test, postural changes provoke a fast decrease in the baroreflex sensitivity and phase changes between RRV and SAPV. In another data base, the indices obtained by TF analysis allows discriminating between healthy subjects and subjects with autonomic dysfunctions.

Resumen y conclusiones de la tesis

En esta tesis doctoral se presentan algunas metodologías avanzadas para el estudio de señales no estacionarias en el dominio conjunto tiempo-frecuencia (TF), con el objetivo de caracterizar las interacciones dinámicas entre señales de origen cardiovascular. El estudio está motivado por la necesidad de profundizar en la comprensión del control autonómico del sistema cardiovascular, cuya disfunción está relacionada con numerosas patologías. La tesis se articula en tres partes: una introducción a los aspectos fisiológicos y metodológicos mas relevantes y estado del arte, una parte en la cual se describen las metodologías propuestas y una parte en la que éstas metodologías se aplican a estudios fisiológicos.

En la introducción se describen tanto el control que las dos ramas del sistema nervioso autónomo, el sistema simpático y parasimpático, ejercen sobre ritmo cardíaco, presión arterial y circulación periférica, como las relaciones entre estas variables y la respiración. En particular, se destacan los aspectos fisiológicos que todavía no se han clarificado o cuya explicación no ha encontrado consenso general en la comunidad científica. Además, se hace una breve descripción de las técnicas de análisis tiempovariante mas recientes para contextualizar el trabajo propuesto en la tesis.

La segunda parte se compone de cuatro capítulos, §2–§5, en los cuales se proponen soluciones a los siguientes problemas : simulación de señales no estacionarias, análisis espectral, análisis de coherencia y de fase, todo ello en el dominio TF.

En el capítulo §2 se describe una metodología para generar señales no estacionarias estocásticas que simulen las dinámicas de señales de origen cardiovascular. Estas señales se caracterizan por tener una estructura TF predeterminada y controlada, en el sentido que el modelo de generación de datos recibe en ingreso los valores de frecuencia y potencia instantaneas, o de frecuencia y amplitud del espectro instantaneas, de cada componente espectral y devuelve el proceso estocástico asociado a ellos. La estabilidad y fiabilidad del modelo de generación de datos se estudia en dos condiciones que simulan la variabilidad del ritmo cardíaco (HRV) en prueba de esfuerzo y durante la escucha de estímulos musicales.

En le capítulo §3 se introducen las distribuciones TF de la clase de Cohen, y en particular la pseudo distribución de Wigner-Ville suavizada (SPWVD). La posibilidad de realizar de manera independiente el suavizado temporal y frecuencial confiere a la SPWVD una muy buena resolución TF, por lo que se considera una de las mejores opciones para realizar el análisis no estacionario de la señal. Se propone un método para cuantificar la resolución TF que caracteriza estas distribuciones, y que se usará a lo largo de toda la tesis. Además se realiza un estudio de simulación, basado en señales estocásticas generadas a partir del modelo presentado en el capítulo §2, para evaluar su precisión en condiciones caracterizadas por distintos grados de no estacionariedad. Por último, se describe una metodología que realiza una descomposición paramétrica de las distribuciones de la clase de Cohen. La ventaja de esta metodología, que se usará en el estudio fisiológico descrito en capítulo §6, está en que permite separar ruido y componentes relevantes de la señal, permitiendo así eliminar los términos de interferencia que suelen aparecer en las distribuciones de la clase de Cohen.

El capítulo §4 trata de metodologías para la estimación de la coherencia TF en señales no estacionarias. Estas metodologías tienen la ventaja de permitir la localización de intervalos de tiempo a la vez que de bandas espectrales en las cuales las señales están correladas, permitiendo un seguimiento fiel y robusto de las variaciones del grado de correlación local. El grado de coherencia entre dos señales depende de la resolución TF de la distribución usada para su estimación. Para permitir una correcta interpretación de los resultados, se proponen dos métodos en los que se determina si el grado de coherencia estimado es estadísticamente significativo o si se debe a otras razones, como a fluctuaciones aleatorias, ruido o a los parámetros del estimador empleado. En este marco, se propone usar la SPWVD para la estimación de la coherencia. Se proponen dos algoritmos para determinar de forma automática y adaptada a las señales el kernel necesario para obtener estimaciones robustas de coherencia. En un estudio de comparación, la precisión, sensibilidad y especificidad, con la cual la SPWVD localiza en el plano TF zonas en las cuales las señales están correladas y zonas en la que no están correladas resulta superior a la precisión de otras técnicas basadas en espectrogramas multi-ventanas (MTSP) y transformadas wavelet. Por último, se muestra un ejemplo de aplicación de análisis de coherencia de señales cardiovasculares, que incluye el estudio conjunto de la variabilidad del periodo cardíaco (RRV), del intervalo del pulso (PIV) y la respiración.

El capítulo §5 trata el análisis de las diferencias de fase entre señales cardiovasculares en el plano TF. El análisis de fase tiempo-variante permite determinar las variaciones del grado de sincronización entre componentes espectrales contenidas en distintas señales del sistema. Además, las estimaciones de las diferencias de fase se pueden usar para establecer, aunque con un cierto grado de incertidumbre, relaciones causales entre componentes espectrales. El uso de la SPWVD para la estimación de la diferencia de fase entre señales no estacionarias resulta particularmente apropiado debido a que ésta solo tienen sentido entorno a una estrecha banda frecuencial tiempo-variante en la cual las señales estén significativamente correladas. La metodología propuesta se evalúa en variados estudios de simulación basados tanto en señales simuladas como en señales fisiológicas.

En la segunda parte de la tesis, capítulos §6–§8, se describen tres estudios fisiológicos basados en el análisis no estacionario de la señal.

En el capítulo §6, se estudia el efecto de estímulos musicales, caracterizados por tener distinta valencia emocional, sobre las dinámicas de la HRV y de la respiración. La caracterización de la influencia de la música sobre ritmos cardiovasculares tiene, además de interés fisiológico, relevancia clínica en cuanto el uso de la música con propósitos terapéuticos ha crecido en los últimos años. Este estudio demuestra que la valencia emocional de la música afecta de manera especifica a la frecuencia respiratoria y a las componentes del ritmo cardíacos relacionadas con el respiro. Además se demuestra que la transición de un estimulo a otro provoca variaciones caracterizadas por una primera fase rápida, de unos 10-20 segundos de duración, y una fase lenta del orden de los minutos. Además del contenido espectral de estas señales, se estudian las interacciones cardio-respiratorias. Sin embargo, se observa que estímulos musicales con distinta valencia emocional no provocan distintas respuesta en el grado de coherencia y en la diferencia de fase entre HRV y señal respiratoria.

En el capítulo §7 se estudia el grado de similitud entre las estructuras TF de la señal HRV y la señal de variabilidad del pulso (PRV) obtenida a partir de la señal fotopletismográfica de pulso (PPG) en prueba de tilt. El objetivo del estudio es comprobar si la PRV puede usarse como medida indirecta de la HRV. El uso de la señal PPG para la estimación de la HRV es de interés en cuanto la PPG es una medida muy empleada en entorno clínico, y cuya adquisición necesita de una instrumentación barata y cómoda. Tanto el análisis de la estructura TF de la HRV y PRV, como el análisis de coherencia entre éstas, sugieren que la PRV puede ser empleada como medida alternativa a la HRV. A pesar del elevado grado de similitud entre estas señales, por lo menos en prueba de tilt, en el estudio se destacan algunas diferencias existentes entre las dos señales, en particular en la componente relacionada con la respiración. Sin embargo, en la base de datos analizada, estas diferencias, que se deben a la variabilidad del tiempo que el pulso emplea para llegar al punto de medida de la PPG, no son suficientes para modificar las conclusiones del estudio fisiológico.

En el capítulo §8, el análisis TF cruzado presentado en los capítulos §4–§5 se aplica al estudio conjunto de la RRV y de la variabilidad de la presión sistolica (SAPV). El estudio de las interacciones dinámicas entre presión arterial y periodo cardiaco es de interés fisiológico, en cuanto algunos aspectos de estas interacciones no están claros, y tienen relevancia clínica, debido a que indices de sensibilidad barorefleja cardíaca tienen valor diagnóstico y pronóstico. En prueba de tilt, el estudio muestra que el estrés ortostático debido al cambio postural provoca una rápida disminución de la sensibilidad barorefleja y un cambio en la diferencia de fase entre RRV y SAPV. En otra base de datos, los indices extraídos del análisis TF permiten discriminar entre sujetos sanos y sujetos con disfunción del control autonómico del sistema cardiovascular.

Riassunto e conclusioni della tesi

In questa tesi di dottorato si propongono alcune metodologie avanzate per l'analisi di segnali non stazionari nel dominio congiunto tempo-frequenza (TF), con l'obbiettivo di caratterizzare le interazioni dinamiche tra segnali di origine cardiovascolare. Lo studio è motivato dalla necessità di approfondire la comprensione del controllo che il sistema nervoso autonomo esercita sul sistema cardiovascolare, le cui disfunzioni possono manifestarsi in gravi patologie. La tesi si articola in tre parti: una prima parte di stato dell'arte ed introduzione riguardante gli aspetti fisiologici e metodologici più rilevanti e recenti; una seconda parte nella quale si descrivono le metodologie proposte; una terza parte nella quale le metodologie proposte si applicano a studi fisiologici.

Nell'introduzione si descrivono sia il controllo che il sistema nervoso simpatico e parasimpatico esercita sul ritmo cardiaco, sulla pressione arteriosa e sulla circolazione periferica, sia le interazioni di queste con l'attività respiratoria. Vengono messi in rilievo quei meccanismi che a tutt'oggi non risultano del tutto chiari o la cui spiegazione non ha ancora trovato consenso generale tra la comunità scientifica. Inoltre, per poter meglio contestualizzare le metodologie proposte, vengono brevemente descritte le tecniche di analisi tempo-variante più recenti.

La seconda parte della tesi consta di quattro capitoli, §2-§5, nei quali vengono proposte alcune soluzioni ai seguenti problemi: simulazione di segnali non stazionari, analisi spettrale, di coerenza e di fase nel dominio TF.

Nel capitolo §2 viene proposta una metodologia per generare processi stocastici non-stazionari che simulino le dinamiche tipiche di segnali di origine cardiovascolare. Questi segnali sono caratterizzati da una struttura TF predeterminata e controllata, nel senso che il modello di generazione dei dati riceve in ingresso i valori di frequenza e potenza istantanei, oppure di frequenza ed ampiezza spettrale istantanei, di ogni componente spettrale e da in uscita il processo stocastico associato ad essi. La stabilità e l'accuratezza del modello di generazione dei dati viene studiato in condizioni che simulano la variabilità del ritmo cardiaco (HRV) in prova di sforzo e durante l'ascolto di stimoli musicali.

Nel capitolo §3 si introducono le distribuzioni TF della classe di Cohen, ed in particolare si descrive la smoothed pseudo Wigner-Ville distribution (SPWVD). La possibilità di realizzare in maniera indipendente il filtro della Wigner-Ville distribution in tempo ed in frequenza rende la SPVWD una delle migliori opzioni per lo studio dei segnali non stazionari. Per quantificare la risoluzione TF di ciascuna di queste distribuzioni viene proposto un metodo, che si userà in tutto il lavoro di tesi. Inoltre, per valutare l'accuratezza della SPWVD in condizioni caratterizzate da diversi gradi di non stazionarietà, si realizza uno studio di simulazione nel quale vengono utilizzati segnali stocastici generati a partire dal modello presentato nel capitolo §2. Questo studio di simulazione mostra che la SPWVD è accurata e robusta. In fine, viene descritta una metodologia che realizza una scomposizione parametrica delle distribuzioni della classe di Cohen. Il vantaggio di questa metodologia, che verrà usata nello studio fisiologico descritto nel capitolo §6, risiede nel fatto che essa permette di separare le componenti rilevanti del segnale dal rumore, permettendo così

di eliminare i termini di interferenza che appaiono nelle distribuzioni della classe di Cohen.

Nel capitolo §4 viene affrontato il problema della stima della coerenza TF tra segnali non stazionari. Le metodologie TF hanno il vantaggio di permettere di localizzare simultaneamente intervalli temporali e bande spettrali nei quali due segnali sono correlati, permettendo così di stimare in maniera accurata e robusta l'andamento temporale del grado di correlazione locale tra essi. Si mostra come il livello di coerenza dipenda anche dalla risoluzione TF della distribuzione utilizzata per la stima. Per poter permettere una corretta interpretazione dei risultati, vengono proposte due metodologie attraverso le quali è possibile determinare, per ogni punto del piano TF, se il livello di coerenza sia statisticamente significativo. In questo capitolo viene proposto l'uso della SPWVD per la stima della coerenza TF. Vengono proposte due metodologie per poter determinare in maniera automatica, a partir da due segnali qualsiasi, i kernels necessari per ottenere stime di coerenza TF robuste senza allo stesso tempo compromettere la risoluzione TF. In uno studio comparativo l'accuratezza con la quale la SPWVD localizza nel piano TF regioni nelle quali due segnali sono localmente correlati risulta essere maggiore dell'accuratezza di altre tecniche di analisi TF, come quelle basate sul multitaper spectrogram o sulla trasformata wavelet. In fine si mostra un esempio di applicazione che include lo studio congiunto della variabilità del periodo cardiaco, dell'intervallo del pulso e del respiro.

Nel capitolo §5 si affronta il problema dell'analisi delle differenze di fase tra segnali di origine cardiovascolare nel dominio TF. L'analisi di fase tempo-variante permette di determinare le variazioni del grado di sincronizzazione delle componenti spettrali di due segnali. Inoltre, la stima delle differenze di fase permette di stabilire, seppure con un certo grado di incertezza, relazioni causali tra due componenti spettrali. L'uso della SPWVD per la stima delle differenze di fase tra segnali non stazionari è particolarmente appropriata in quanto essa ha senso solo se realizzata in strette bande spettrali tempo-varianti nelle quali le componenti spettrali analizzate siano localmente correlate. Attraverso specifici studi di simulazione che includono sia segnali simulati che segnali fisiologici, si dimostra che la metodologia proposta è accurata e robusta.

Nella seconda parte della tesi, capitoli §6-§8, vengono descritti tre studi fisiologici basati sull'analisi non-stazionaria dei segnali.

Nel capitolo §6 si studia l'effetto che stimoli musicali, caratterizzati da diversa valenza emozionale, hanno sulle dinamiche della HRV e del respiro. La caratterizzazione dell'influenza che la musica esercita sulle oscillazioni dei segnali cardiovascolari ha sia rilevanza fisiologica sia clinica, in quanto l'uso della musica per scopi terapeutici è aumentato negli ultimi anni. Questo studio dimostra che la valenza emozionale della musica influisce in maniera significativa sulla frequenza respiratoria e sulle componenti del ritmo cardiaco relazionate col respiro. Inoltre si mostra che la transizione da uno stimolo musicale ad un altro provoca variazioni caratterizzate da una prima fase rapida, della durata di circa 10-20 secondi, e da una fase più lenta, della durata nell'ordine dei minuti. Oltre all'analisi della struttura TF di questi segnali, in questo capitolo vengono studiate le interazioni cardiorespiratorie. Da questo studio emerge che stimoli musicali caratterizzati da diversa valenza emozionale non provocano diverse risposte nel grado di coerenza e differenza di fase tra HRV e respiro.

Nel capitolo §7 si studia il grado di somiglianza tra la struttura TF della HRV e della variabilità del pulso (PRV) ottenuta a partire dal segnale fotopletismografico (PPG) durante prova di tilt. L'obbiettivo dello studio è valutare se la PRV può essere usata come misura indiretta della HRV. L'uso del segnale PPG per la stima dell'HRV è di interesse in quanto il PPG è un segnale molto utilizzato in ambito clinico, e la cui acquisizione necessita di dispositivi economici e comodi per il paziente. Sia l'analisi della struttura TF della HRV e della PRV, sia l'analisi di coerenza tra queste, suggeriscono che la HRV può essere usata come misura alternativa della HRV. Nonostante la somiglianza che caratterizza questi due segnali, per lo meno in prova di tilt, nello studio vengono anche evidenziate alcune differenze, visibili soprattutto nella componente relazionata con il respiro. Nella base di dati analizzata, queste differenze, che sono principalmente dovute al tempo impiegato dal pulso pressorio per raggiungere il punto di misura del PPG, non sono sufficienti a modificare le conclusioni dello studio fisiologico.

Nel capitolo §8, l'analisi presentata nei capitoli §4-§5 viene applicata allo studio congiunto della RRV e della variabilità della pressione sistolica (SAPV). Lo studio delle interazioni dinamiche tra pressione arteriosa e periodo cardiaco è di interesse fisiologico, in quanto può aiutare a chiarire alcuni aspetti delle interazioni cardiovascolari a tutt'oggi poco chiari, ed ha rilevanza clinica, in quanto indici della sensibilità del baroriflesso hanno valore diagnostico e prognostico. In prova di tilt, questo studio mostra che lo stress ortostatico dovuto al cambio posturale provoca una rapida diminuzione della sensibilità del baroriflesso ed un cambio nella differenza di fase tra RRV e SAPV. In un'altra base di dati, gli indici estratti dall'analisi TF permettono di discriminare tra soggetti sani e soggetti con disfunzioni del sistema nervoso autonomo.

Contents

III Conclusions 185

IV Appendix 197

List of Figures

Chapter 1

Introduction

Contents

This work has been realized within a joint PhD program in biomedical engineering at both the University of Zaragoza, Spain, and the Politecnico di Milano, Italy. Part of the work has also been done at the Universitat Politecnica de Catalunya, Barcelona, Spain and at the Ecole Normale Supérieure de Lyon, France, where I studied during four and five months, respectively.

1.1 Motivations

In western countries, cardiovascular diseases represent one of the major cause of death. In order to detect and care cardiovascular dysfunctions, it is first necessary to understand how the cardiovascular system works. Indeed, "increasing our understanding of integrative cardiovascular physiology [...] will help us to elucidate how the system works, when it works, and what may go wrong when it does not" [59]. Since the late Seventies, mathematics and engineering has been used in the study of the cardiovascular system. The work presented in this dissertation goes along with this line.

The overall aim of this study is to present some advanced methodologies for the characterization of cardiovascular dynamics. In particular, two words, which will be extensively used throughout the dissertation, deserve attentions: *characterization* and *dynamics*. By speaking of dynamics of the system, we refer to those mechanisms which make the system able to continuously adapt to changing conditions. Given that the system is subject to continuous (never ending and never stopping) perturbations, it has an intrinsically non-stationary behavior. These changes are described through the quantification of few relevant indices, derived by processing signals that can be non-invasively acquired in usual clinical practice, such as electrocardiogram, continuous arterial pressure, photopletismographic signal, respiratory signals etc. These indices and their temporal evolution characterize the system. Among the different types of methodologies that can be, or have been, used to analyze biomedical signals, we focused on time-frequency analysis. This choice is motivated by the need of measuring at the same time the spectral content of cardiovascular signals, whose spectral components have a specific physiological meaning, and its temporal evolution. Special attention is put into the characterization of heart rate variability as well as into the dynamic interactions of heart rate variability with respiration and arterial pressure.

To give a picture of the amount of studies concerning these topic, we counted the number of papers on "heart rate variability" and "baroreflex" that have been published in the PubMed data-base[1] from the Seventies up to now. The results are shown in Fig. 1.1, both in absolute unites, as number of papers (see panel (a)), and normalized on the total number of papers that have been published in a given range of time (see panel (b)). We observe that, although these topics were already studied in the Seventies, the number of publications on them is still growing. Analogous results can be find in [215]. Furthermore, if we refine the search and we select from the previous results only those that also contain the word "time-frequency", we see that in the last five years, only 34 over 3132 papers published on heart rate variability, and 3 over 1603 papers on the baroreflex, included time-frequency analysis (refer to the right-side y-label of

---

[1]http://www.ncbi.nlm.nih.gov/pubmed
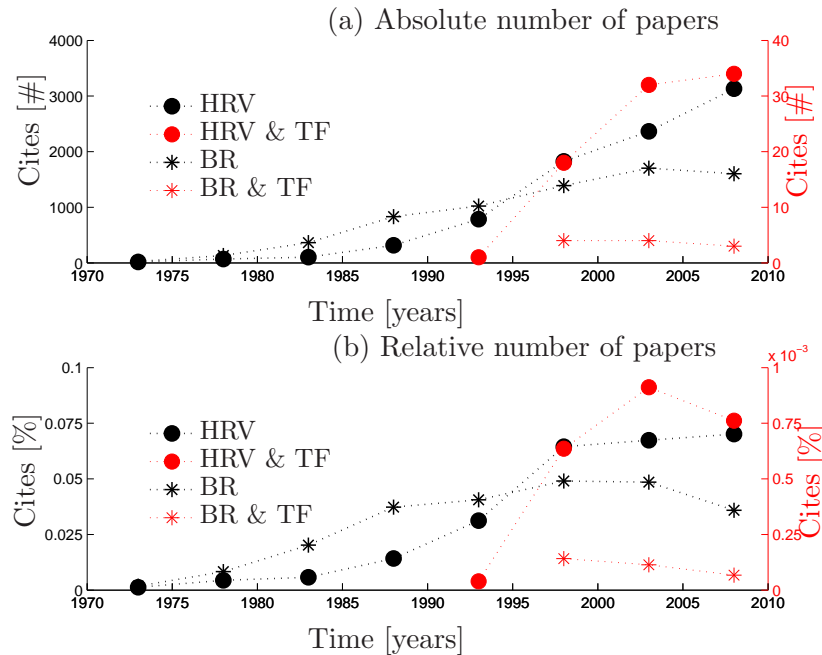
Figure 1.1: Number of publications in the PubMed data-base. Results are given as the number of papers published every five years from 1970 to 2010, both in absolute unites, as in (a), and normalized on the total number of papers published in the same interval of time, as in (b). Black markers (left–side y–ticks) correspond to the search "heart rate variability" (HRV) and "baroreflex" (BR), while red markers (right–side y–ticks) correspond to "heart rate variability & time-frequency" (HRV+TF) and "baroreflex & time-frequency" (BR+TF).

the Fig. 1.1). Time-frequency analysis, which was applied to the study of these topics for the very first time in the late Nineties, is still little used in the characterization of the cardiovascular dynamics.

Our hope is that the work presented in this dissertation could help to make this kind of non-stationary signal processing a common tool for the analysis of biomedical signals, with the aim of improving the understanding of the cardiovascular control.

1.2 Physiological aspects

The methodologies presented in the first part of this dissertation are used to characterize changes and dynamic interactions between heart period, blood pressure and respiration. In the following, a short description of important mechanisms involved in cardiovascular control is given. Focus is put on short-term regulation that controls cardiac cycle. Simultaneous changes that occur during cardiac cycle are shown in Fig. 1.2. An important characteristic of cardiac cycle, highlighted in this graphic, is that changes in arterial pressure, cardiac output, heart period, etc., are simultaneous and dynamically related.

Before describing relevant mechanisms of the neural control of the cardiovascular system, it is important to mention some important parameters involved in hemodynamics.
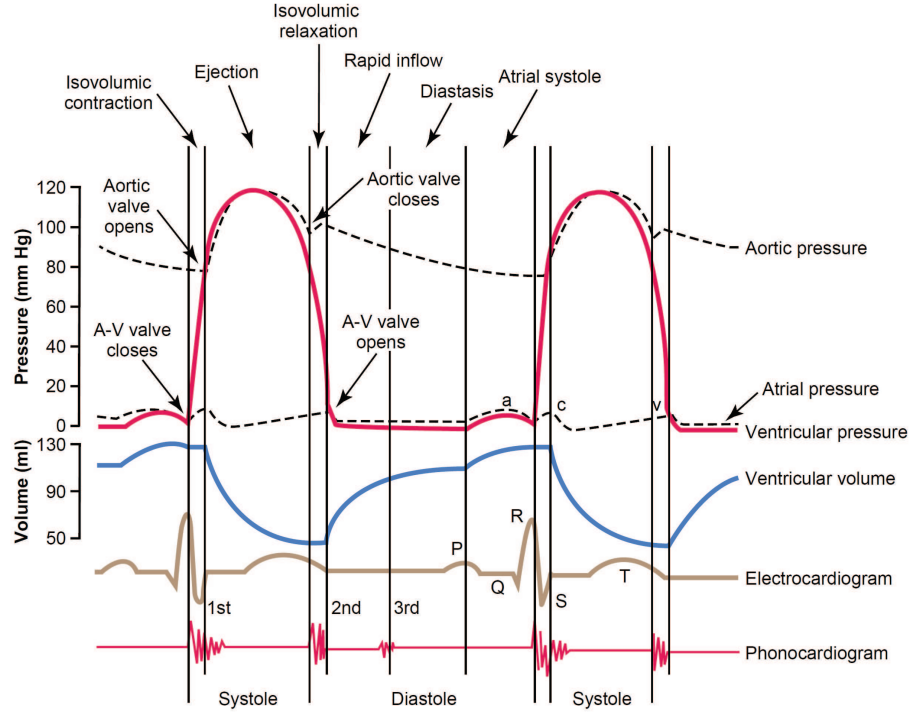
Figure 1.2: Events of the cardiac cycle for left ventricular function, showing changes in left atrial pressure, left ventricular pressure, aortic pressure, ventricular volume, the electrocardiogram, and the phonocardiogram (From [114])

Table 1.1 shows the normal range of blood volumes, cardiac output, blood pressure and heart rate in adults. Knowledge of these values is relevant because hemodynamics and the neural control of the cardiovascular system are continuously, dynamically and mutually related.

As a brief introduction, it is helpful to review the relationships between mean arterial pressure (MAP), cardiac output (CO), total peripheral resistance (TPR), heart rate (HR), and stroke volume (SV) [120], whose normal ranges are shown in Table 1.1:

$$MAP = CO \times TPR = (HR \times SV) \times TPR \tag{1.1}$$

1.2.1 Neural control of the cardiovascular system

The autonomic nervous system plays a primarily role in the maintaining of homeostasis, through the regulation of arterial pressure. All the variables considered in the graphic of Fig. 1.2, which depicts the cardiac cycle, are controlled by the nervous system.

The efferent autonomic signals are transmitted to the various organs of the body through two major subdivisions called the sympathetic nervous system and the parasympathetic nervous system [115]. In Table 1.2 and 1.3, some anatomical and physiological characteristics of these systems are reported. In particular, in Table 1.2,

Table 1.1: Important variables of the cardiovascular system

Measure	Typical value	Normal range
End-diastolic volume (EDV)	120 ml	65–240 ml
End-systolic volume (ESV)	50 ml	16–143 ml
Stroke volume (SV)	70 ml	55–100 ml
Ejection fraction (Ef)	58%	55–70%
Cardiac output (CO)	4.9 L/min	4.0–8.0 L/min
Systolic pressure		90–119 mmHg
Diastolic pressure		60–79 mmHg
Heart rate (HR)	70 bpm	60–100 bpm

the transmitters of the different nerves are shown. The sympathetic and parasympathetic nerve fibers secrete mainly one or the other of two synaptic transmitter substances, acetylcholine or norepinephrine. Those fibers that secrete acetylcholine are said to be cholinergic. Those that secrete norepinephrine are said to be adrenergic, a term derived from adrenalin, which is an alternate name for epinephrine.

Table 1.3 lists the effects on different visceral functions of the body caused by stimulating either the parasympathetic nerves or the sympathetic nerves. From this table, it can be seen that sympathetic stimulation causes excitatory effects in some organs but inhibitory effects in others. Likewise, parasympathetic stimulation causes excitation in some but inhibition in others. Also, when sympathetic stimulation excites a particular organ, parasympathetic stimulation sometimes inhibits it, demonstrating that the two systems occasionally act reciprocally to each other. However, most organs are dominantly controlled by one or the other of the two systems.

In contrast with skeletal nervous system, low frequency of stimulation is required for full activation of autonomic effectors. In general, only one nerve impulse every few seconds suffices to maintain normal sympathetic or parasympathetic effect. Moreover, the sympathetic and parasympathetic systems are continuously active, and the mean basal rates of activity are known, respectively, as sympathetic tone and parasympathetic tone [115]. While the tonic influences of a system are usually associated with an average modulation, variations over the tone are usually called phasic stimulations. The activity of the autonomic nerves that regulate cardiovascular function is determined by a network of neurons located in the medulla oblongata that receive inputs from (i) other central structures including the hypothalamus, cerebral cortex, and medullary chemoreceptors; and (ii) peripheral reflexes arising from baroreceptor, chemoreceptor, mechanoreceptor, thermoreceptor, and nociceptor afferents located in the blood vessels, heart, lungs, skeletal muscles, skin, and viscera [241].

With respect to the expression shown in expression (1.1), the major point to make is that the sympathetic nervous system can rapidly increase MAP by constricting arterioles, or by increasing heart rate or stroke volume. While predominant effect of activation of the parasympathetic nervous system is a rapid decrease of heart rate, which will influence cardiac output [120].

Table 1.2: Transmitters substances in the autonomic nervous system

Nerves	Type	Transmitter
Sympathetic preganglionic	cholinergic	acetylcholine
Sympathetic postganglionic	adrenergic	norepinephrine
Parasympathetic preganglionic	cholinergic	acetylcholine
Parasympathetic postganglionic	cholinergic	acetylcholine

Table 1.3: Effect of sympathetic and parasympathetic activation

Organ	Sympathetic stimulation	Parasympathetic stimulation
Heart	Increased rate	Slowed rate
Heart	Increased force of contraction	Decreased force of contraction
Coronaries	Constricted (α), dilated (β_2)	Dilated
Vessel	Constricted	No effect
Arterioles	Constricted	No effect
Adrenal medullae	Release of (nor)epinephrine	No effect
Arterial pressure	Short-term increase	Short-term decrease

(a) Sympathetic nervous system (b) Parasympathetic nervous system
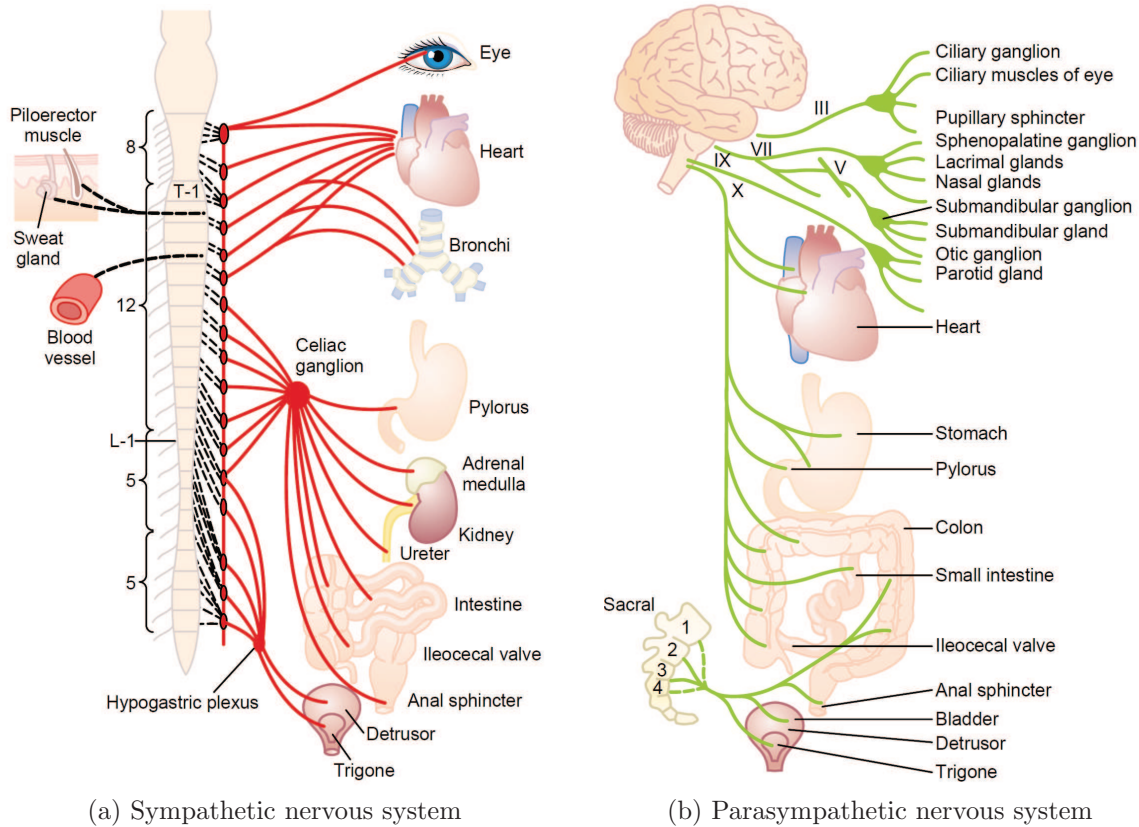
Figure 1.3: Sympathetic and parasympathetic system (From [115])

The sympathetic nervous system

Figure 1.3a shows the general organization of the peripheral portions of the sympathetic nervous system. It is shown that sympathetic nervous system innervates the heart, blood vessels, kidneys and adrenal medulla, and consequently it has a predominant role in cardiovascular regulation.

Each sympathetic pathway from the cord to the stimulated tissue is composed of two neurons, a short preganglionic neuron and a long postganglionic neuron. Such an arrangement allows sympathetic discharge to cause diffuse responses involving multiple regional effectors [241]. All preganglionic sympathetic neurons are cholinergic, while most of the postganglionic sympathetic neurons are adrenergic (see Table 1.2). Ordinarily, the norepinephrine secreted directly into a tissue remains active for only a few seconds, demonstrating that its reuptake and diffusion away from the tissue are rapid. Epinephrine and norepinephrine are almost always released by the adrenal medullae at the same time that the different organs are stimulated directly by generalized sympathetic activation. Therefore, the organs are actually stimulated in two ways: directly by the sympathetic nerves and indirectly by the adrenal medullary hormones. The two means of stimulation support each other, and either can, in most instances, substitute for the other. When secreted into the blood by the adrenal medullae, both norepinephrine and epinephrine remain very active for 10 to 30 seconds; but their activity declines to extinction over 1 to several minutes [115].

Before a transmitter substance secreted at an autonomic nerve ending can stimulate an effector organ, it must first bind with specific receptors on the effector cells. There are two major types of adrenergic receptors, alpha receptors and beta receptors. Norepinephrine and epinephrine have slightly different effects in exciting the alpha and beta receptors. Norepinephrine excites mainly alpha receptors but excites the beta receptors to a lesser extent as well. Conversely, epinephrine excites both types of receptors approximately equally. Therefore, the relative effects of norepinephrine and epinephrine on different effector organs are determined by the types of receptors in the organs.

Sympathetic nerves are continuously active so all innervated blood vessels remain under some degree of continuous constriction. Direct observation of the sympathetic nerve activity shows that (i) discharges occur in a synchronized fashion, with many of the nerves in the bundle being active at approximately the same time, and (ii) that discharges generally occur with each cardiac cycle in a highly rhythmical fashion. Postganglionic sympathetic nerves are composed of hundreds to thousands of unmyelinated fibers that fire action potentials at almost the same time (synchronization) to give discharges of summed spikes. Two features seem to characterize sympathetic discharges: their firing frequency and amplitude. Some researches have made the hypothesis of a differential control over the amplitude and frequency of sympathetic activity [173]. This hypothesis suggests that the network of cells involving the rostral ventrolateral medulla (at brainstem) provide the basal level of nerve recruitment and determine the firing frequency based on the intrinsic rhythmicity and phasic input from arterial baroreceptors, but that inputs from cell groups with direct projections to the spinal cord provide an extra level of gain/recruitment of fibers [173].

Assessment of the sympathetic nerve activity: Because it is difficult to directly record sympathetic outflow in humans, plasma concentrations of norepinephrine are often used as a surrogate measure of postganglionic sympathetic nerve activity. Caution is warranted, however, as blood levels will be affected by changes not only in the release of noreprinephrine but also in its reuptake and metabolism (clearance from the blood). Furthermore, plasma norepinephrine provides limited insight into regional differences in sympathetic nerve activity as it reflects the contribution of norepinephrine spillover from all potential sources [241].

Radiotracer technology has been used extensively for studying norepinephrine kinetics in humans and has now become a gold standard for assessing SNA in humans [173]. Norepinephrine in the plasma reflects the transmitter released by sympathetic nerves that has spilled over into the circulation. Norepinephrine spillover rate gives the rate at which norepinephrine released enters plasma and provides information about the activity of sympathetic nerves in regions that are not accessible by percutaneous microneurography, such as the heart and kidney [59]. While this technique offers good estimations of regional SNA, limitations are related to its low repeatability, to the fact that it does not allows for continuous recording and to the evidence of non linear relationship between actual sympathetic activity and the norepinephrine spillover [173]. Researchers have also attempted to use a measurement of heart rate variability [1, 210, 172] (see also §1.2.3) as an index of sympathetic tone. However, there are serious limitations to this technique. Specifically, while the low frequency variability in heart rate is influenced by the sympathetic nervous system, there were also many examples where known increases in SNA were not associated with changes in low frequency variability [173, 79].

In humans, sympathetic activity is most often measured at the peroneal nerve, and the most common measurement is muscle sympathetic neural activity, often called MSNA. The technique involves the percutaneous insertion of a high-impedance tungsten microelectrode (the tip of which is only a few microns in diameter). Most sympathetic neural recordings involve multiunit recordings, but single-neuron recordings are also possible. The level of muscle sympathetic neural activity did not correlate to the resting heart rate or blood pressure (within normal range) but was found to relate to cardiac output and thus total peripheral resistance in males [173]. Muscle sympathetic neural activity is characterized by a striking inter-individual variability in resting humans, but it is very reproducible in a given person [59]. Recently, it has been suggested to be a good index of whole-body "net" sympathetic vasoconstrictor tone in healthy young men [59].

Effect of the sympathetic nervous activity: As also shown in Table 1.3, the sympathetic nerves have a dominant role in cardiovascular control due to their effects to increase cardiac rate and contractility, cause constriction of arteries and veins, cause release of adrenal catecholamines, and activate the reninangiotensin-aldosterone system [241].

- **Effects on the heart:**
  Cardiac sympathetic innervation of the heart includes innervation of the sinoatrial node, which allows sympathetic nerves to increase heart rate by increasing

the slope of diastolic depolarization during the spontaneous sinoatrial node action potential [59]. Sympathetic nerves also innervate the myocardium; increases in sympathetic activity increase myocardial contractility and, therefore, increase stroke volume. Thus, the sympathetic nervous system has both chronotropy and inotropy effects on the heart [241]. Given the ability to modulate both cardiac rate and stroke volume, the autonomic nerves provide an important remote mechanism to rapidly adjust cardiac output to meet short-term changes in the body's needs. In humans, there is a good deal of tonic vagal discharge and a moderate amount of tonic sympathetic discharge. The interplay of these tonic activities results in a resting heart rate that is $\approx 30\%$ lower than the intrinsic heart rate of 90–100 beats/min and a cardiac output that is $\approx 30\%$ higher than in the absence of sympathetic discharge [173]. Additional sympathetic discharge can increase heart rate and stroke volume and increase cardiac output. Conversely, withdrawal of tonic vagal or sympathetic discharge has opposing effects to increase or decrease cardiac output, respectively [173].

- **Effects on blood vessels:** Sympathetic innervation of the peripheral vasculature causes vasoconstriction primarily through the action of norepinephrine at postsynaptic α-adrenergic receptors [59].

  Vascular capacitance, mainly driven by venous capacitance, is strongly influenced by sympathetic nervous activity. It is often overlooked that the venous circulation receives considerable sympathetic innervation, and with 70% of the blood volume can play a significant role in the acute cardiovascular responses to sympathetic activation. Venoconstriction in the splanchnic circulation results in a significant shift of blood towards the heart, increasing diastolic filling, and thus increasing cardiac output. Blood that is forced out of the veins returns to the heart, increasing end-diastolic volume and, via the Frank-Starling mechanism, increasing stroke volume and cardiac output. As 20% of blood volume is located in the veins of the splanchnic circulation, translocation of blood from this venous reservoir due to sympathetic venoconstriction is a particularly effective way to quickly redistribute blood from the venous side to the arterial side of the circulation. Recently, it has been suggested that increases in venomotor tone driven by sympathetic activity may be important mediators in cardiovascular disease development [173].

- **Effects on blood pressure:** Sympathetic stimulation increases both propulsion by the heart and resistance to flow, which usually causes a marked acute increase in arterial pressure [115]. To understand how sympathetic activity can control blood pressure, it is important to remind relationships reported in (1.1), which show that blood pressure = cardiac output × total peripheral resistance. Flow varies directly (and resistance inversely) with the fourth power of the vessel radius. As a result, even small changes in vessel caliber can have relatively large effects on vascular resistance and blood flow. Sympathetic neural control of arteriolar resistance therefore offers a powerful mechanism to regulate regional blood flows to individual organs and tissues. As the arterioles are the major contributors to total peripheral resistance, sympathetic control plays a principal role in the regulation of systemic blood pressure [241].

Sympathetic control of blood vessels is mediated by the baroreflex, which is one of the most important mechanisms for the short-term maintaining of the blood pressure (see §1.2.2).

Pathophysiology: What distinguishes the sympathetic nervous system is the emerging evidence that overactivity is strongly associated with a variety of cardio-vascular diseases [173]. Whether this increased sympathetic activity acts as a driver of the disease progression or whether it is merely a follower is currently matter of debate. In the following, we revised some of the conditions that are known to be associated to chronic sympathoexitation [59, 173].

- **Hypertension:** The study of the mechanisms underlying hypertension is clinically relevant because hypertension is a causative factor in the development of heart failure, renal failure, and stroke. The causes of sympathoexcitation in association with hypertension are unclear but may involve increases in chemoreflex sensitivity to hypoxia or hypercapnia [59]. However, it is important to consider that in the vast majority of cardiovascular diseases, there is a disproportionate increase in renal sympathetic activity compared with sympathetic activity to the muscle [173]. Chronic changes in blood pressure may be related with sympathetic action on the kidney.
- **Heart failure:** Among patients with heart failure, muscular sympathetic activity is strikingly increased. In terms of the occurrence of sympathetic bursts, a healthy person may experience 30 to 50 bursts per 100 heart beats, whereas patients with heart failure can experience as many as 90 to 100 bursts per 100 heart beats. This extreme sympathoexcitation has been shown to be a predictor of mortality for patients with heart failure [59, 151]. Rapid increases in cardiac sympathetic activity are associated with ventricular arrhythmias, coronary occlusion, and damage to myocytes associated with the resulting high norepinephrine levels. Moreover, the degree of sympatho-activation appears to be a good indicator of long-term prognosis [173]. The fundamental processes underlying the sympathetic activation in heart failure remain uncertain.
- **Obesity:** Muscle sympathetic neural activity is increased markedly among obese patients and decreases with weight loss induced by exercise and diet [59]. Obesity is often related with hypertension, with up to 70% of newly diagnosed hypertensive cases are attributable to obesity [173]. Obese hypertensive subjects present high level of norepinephrine spillover from the kidneys. The mechanism(s) by which weight gain elicits sympathetic neural activation remains unclear [173].
- **Sleep apnea:** Sleep-related breathing disorders play an important pathophysiological role in cardiovascular disease, and sympathetic activation is thought to be a key mechanism linking sleep apnea to cardiovascular disease. For instance, in patients with obstructive sleep apnea, muscular sympathetic activity is increased, even during the awake state without apnea [59]. Over time, periodic nocturnal sympathetic activation related to apnea appears to evolve into a rise in the mean daytime level of sympathetic activity.
- **Mental stress:** Large-scale studies link hypertension development with chronic mental stress in the workplace. Blood pressure has been shown to be elevated

soon after migration, presumably due to stress [173]. The role of the sympathetic nervous system in these events need further studies.

The parasympathetic nervous system

The anatomical organization of the parasympathetic nervous system is shown in Fig. 1.3b. About 75% of all parasympathetic nerve fibers are in the vagus nerves (cranial nerve X), passing to the entire thoracic and abdominal regions of the body. The vagus nerves supply parasympathetic nerves to the heart, lungs, esophagus, stomach, entire small intestine, proximal half of the colon, liver, gallbladder, pancreas, kidneys, and upper portions of the ureters [115].

Parasympathetic division consists of long preganglionic fibers that synapse on short postganglionic fibers arising from ganglia located close to the effector targets. Therefore, parasympathetic discharge causes fairly localized responses [241].

Either all or almost all of the postganglionic neurons of the parasympathetic system are cholinergic. Thus, as shown in Table 1.2, all or virtually all the terminal nerve endings of the parasympathetic system secrete acetylcholine. Acetylcholine activates mainly two types of receptors, called muscarinic and nicotinic receptors.

Effect of the parasympathetic nervous system:

- **Effects on the heart:**
  Tonic parasympathetic activation predominates over sympathetic tone at rest [200]. Parasympathetic stimulation on the heart causes mainly opposite effects than sympathetic stimulation: decreased heart rate and strength of contraction. Heart rate reduction is mediated by inhibition of the sympathetic nervous system and by direct hyperpolarization of sinus nodal cells. The membrane hyperpolarization decreases the spontaneous firing rate of the sinoatrial node and slows conduction in the atrioventricular node, thereby slowing the intrinsic heart rate [200].
- **Effects on blood vessels:**
  Parasympathetic stimulation has almost no effects on most blood vessels except to dilate vessels in certain restricted areas, such as in the blush area of the face [115].
- **Effects on arterial pressure:**
  Parasympathetic stimulation can provoke a decrease in arterial pressure, because it decreases pumping by the heart but has virtually no effect on vascular peripheral resistance [115]. Very strong vagal parasympathetic stimulation can almost stop or occasionally actually stop the heart entirely for a few seconds and cause temporary loss of all or most arterial pressure.

Clinical implications: While elevated sympathetic activity is associated with an adverse prognosis, a high level of parasympathetic activation confers cardio-protection by several potential mechanisms [200]. Epidemiological data indicate that the resting heart rate, a measure of vagus nerve function, predicts mortality. The higher the vagus

nerve activity is, the slower the heart rate is, the greater the increase in the parasympathetic component of heart rate variability is, and the better the outcome is [200]. Moreover, parasympathetic activation and its physiological effects are attenuated in heart failure. And either direct or indirect vagus nerve stimulation could have direct beneficial effects on remodeling and clinical outcomes.

1.2.2 Baroreflex

The baroreflex is a negative feedback system that buffers short-term fluctuations in arterial pressure [120] by modifying the cardiovascular variables which, as shown in (1.1), determine arterial pressure. Under a variety of environmental and physiological circumstances, arterial blood pressure is regulated around a narrow range and arterial baroreflexes are critically important for the beat-to-beat regulation of blood pressure [120]. The importance of the baroreflex has been demonstrated in several experimental data in which it has been observed that, in many animal species, arterial baroreceptor denervation results in an increase of the variability of blood pressure [151].
The arterial baroreflex senses changes in blood pressure via baroreceptors, which are sensory afferent nerve endings mainly located in the carotid sinus and the aortic arch. The baroreceptors respond to stretching of the vessel wall. In general, increases in this stretching as the result of a short-term increase in blood pressure lead to an increase in afferent input into central autonomic nuclei (notably the nucleus tractus solitarius). This increase in afferent input results in a reflex decrease in sympathetic neural outflow (sympathetic baroreflex), which in turn decreases vasoconstrictor tone, myocardial contractility (to decrease stroke volume), and heart rate. These sympathetic influences work in conjunction with parasympathetic influences on the sinoatrial node to decrease heart rate (vagal cardiac baroreflex). During a short-term decrease in blood pressure, the opposite occurs, and the autonomic nervous system acts to increase vasoconstriction, increase stroke volume, and increase heart rate [59].

Baroreflex control of sympathetic and parasympathetic outflow: Figure 1.4 summarizes arterial baroreflex control of sympathetic and parasympathetic outflow [120]. At normal arterial pressures (middle graphic in Fig. 1.4) there is activity from all neural components of the arterial baroreflex: both afferent and efferent limbs. Both resistance and capacitance vessels are partially constricted. With regard to determinants of heart rate, the sinoatrial and atrioventricular nodes receive sympathetic and parasympathetic innervation, and both efferent outflows are active at rest. Baseline heart rate is determined by the balance between these two opposing influences and the relative contribution of the sympathetic and parasympathetic nervous systems varies among species. In conscious humans, basal parasympathetic nerve activity to the heart is the major determinant of baseline heart rate, whereas basal sympathetic nerve activity has small or negligible effects. In addition, variation in resting heart rate among individuals is caused mainly by differences in basal parasympathetic tone. There are significant differences in the time delay of the response mediated by parasympathetic and sympathetic efferents. Following a rapid rise in arterial pressure, parasympathetic activation produces an immediate reaction (between 200 and 600 ms) [151]. On the

contrary, the reaction to cardiac and vasomotor sympathetic activation occurs with a 2-3 seconds delay and reaches maximal effect more slowly. An even more sluggish response has been observed in the baroreflex control of venous return. Therefore, the ability of the baroreflex to control heart rate on a beat-to-beat basis is exerted through vagal but not sympathetic activity [151]. However, even for fast maneuvers, like standing up from the supine position, the ability to increase heart rate quickly is not of primary importance. Heart-transplant patients provide dramatic proof of this contention since they can only change their heart rate by way of circulating hormones, like norepinephrine, which takes at least a minute to have effect on heart rate after standing up. Still, these individuals can stand up without any problem [139]. However, when the sympathetic innervation to the vasculature is lost, as it may occur in autonomic failure, then the patient can no longer stand up since blood pressure starts to drop immediately and, after some 5 s, consciousness is lost due to cerebral hypoxia [139]. Therefore, the sympathetic efferent part of the baroreflex is of much more importance, since it induces vasoconstriction in response to a drop in blood pressure [139, 140]. Thus, for the control of blood pressure sympathetic outflow to the heart and vasculature is far more important than what the vagus nerve does to heart rate [140].

Although baroreflex has been widely studied, many aspects of the cardiovascular control are still unclear. For instance, in a recent debate [81, 141, 136], the involvement of the baroreflex in the respiratory sinus arrhythmia (oscillations in heart period synchronous with respiration, described in §1.2.4) has been discussed. Some authors [141], advocated that baroreflex should be considered as the main responsible for respiratory sinus arrhythmia. Following this hypothesis, the first explanation of respiratory sinus arrhythmia is that it is due to respiratory induced blood pressure oscillations that are translated into heart rate oscillations by the baroreflex. Others suggested that respiratory sinus arrhythmia has a central origin [80, 81, 136] and is not baroreflex mediated [240]. This debate clearly shows that cardiovascular control, including baroreflex, is far from being completely understood and that much work is still needed.

In a recent study, orthostatic hypotension was observed in patients with pure autonomic failure despite the increase in leg vascular resistance [111]. The results shown in [111] demonstrate that leg vasoconstriction during orthostatic challenges in patients with pure autonomic failure is not abolished. This indicates that the sympathetic nervous system is not the sole or pivotal mechanism inducing leg vasoconstriction during orthostatic challenges. Additional vasoconstrictor mechanisms may compensate for the loss in sympathetic nervous system control.

Baroreceptors: In the normal operating range of arterial pressure, around 100 mmHg, even a slight change in pressure causes a strong change in the baroreflex signal to readjust arterial pressure back toward normal. The baroreceptors respond extremely rapidly to changes in arterial pressure; in fact, the rate of impulse firing increases in the fraction of a second during each systole and decreases again during diastole. Furthermore, the baroreceptors respond much more to a rapidly changing pressure than to a stationary pressure. That is, if the mean arterial pressure is 150 mmHg but at that moment is rising rapidly, the rate of impulse transmission may
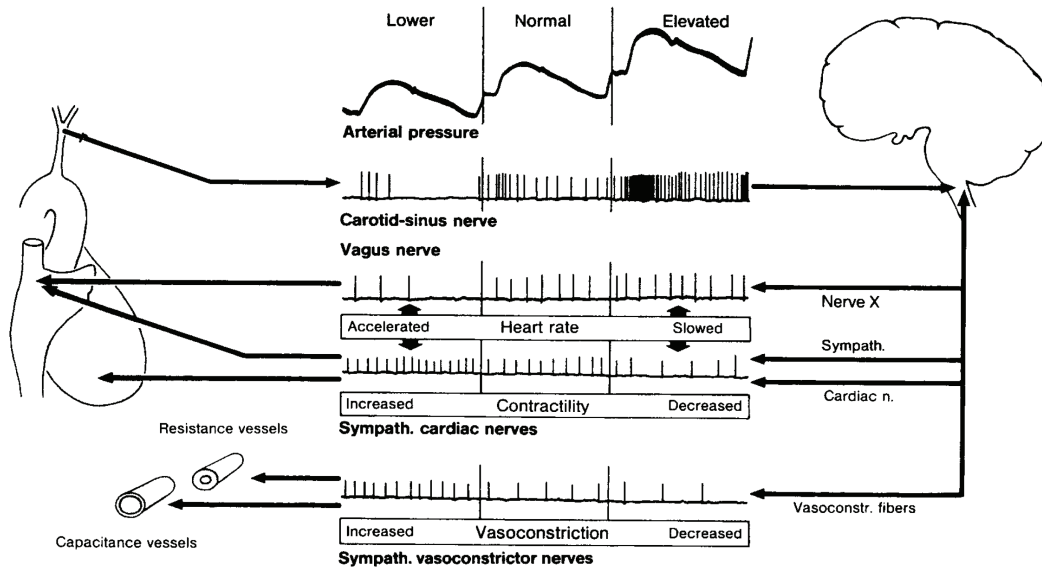
Figure 1.4: Baroreceptor reflex responses to changes in arterial pressure. When arterial pressure is elevated, afferent firing increases in carotid sinus nerve, which results in decreased sympathetic nerve activity to heart and blood vessels and increased parasympathetic nerve activity to heart, responses that will decrease arterial pressure. When arterial pressure is lowered, the opposite responses occur. Also note the relationship of phasic aortic blood pressure to firing of a single baroreceptor afferent nerve fiber at different levels of mean arterial pressure (From [120]).

be as much as twice that when the pressure is stationary at 150 mmHg [114]. The arterial baroreflex also responds to the normal small variations in blood pressure that are continually induced by the respiratory cycle and by changes in posture in healthy, resting humans.

Although the arterial baroreceptors provide powerful moment-to-moment control of arterial pressure, their importance in long-term blood pressure regulation has been controversial [114]. Some physiologists consider the baroreflex relatively unimportant in chronic regulation of arterial pressure because baroreceptors tend to reset in 1 to 2 days to the pressure level to which they are exposed; the control level. This resetting of the baroreceptors may attenuate their potency as a control system for correcting disturbances that tend to change arterial pressure for longer than a few days at a time. Experimental studies, however, have suggested that the baroreceptors do not completely reset and may therefore contribute to long-term blood pressure regulation, especially by influencing sympathetic nerve activity of the kidneys [114]. Recently, it has been suggested that arterial baroreceptors play a role in long-term regulation of arterial pressure under conditions of increased dietary salt intake [173].

Measurement of baroreflex sensitivity: Traditionally, baroreflex sensitivity (BRS) is measured as the induced heart period lengthening (in ms) divided by the causative change in previous systolic pressures (in mmHg) [139, 155]. Effectively, the baroreflex appears to trade (unwanted) blood pressure variability for physiological

heart rate variability. When the sympathetic baroreflex is less sensitive, the response of the sympathetic nerves to a given change in arterial pressure will be less pronounced and may be less able to return the pressure to baseline levels [59].

Originally, a pharmacological tool was used to quickly increase or decrease blood pressure, i.e. an intravenous bolus injection of phenylephrine or nitroprusside, which increases and decreases blood pressure, respectevely. While vasoconstrictor drugs, as phenylephrine, allows one to mainly explore the vagal component of the baroreceptor control of heart rate, the excitation of the sinus node that accompanies a reduction in arterial pressure caused by the administration of vasodilators, as nitroglycerin, is partly mediated through sympathetic mechanisms. Therefore vasodilators have been used to obtain information on the sympathetic limb of heart rate control [151].

The lack of selectivity in the response has been claimed as one of the major limitations of the use of vasoactive drugs. Indeed, the pressure stimulus causes a simultaneous activation of multiple reflexogenic areas, particularly cardiopulmonary receptors, which may interfere with or even counteract the arterial baroreceptor reflex. Moreover, vasoactive drugs may directly affect the transduction properties of baroreceptors, the central nervous system part of the reflex arc and the response of the sinus node [151]. Later, it was shown that this intervention could be replaced by the measurement of spontaneous blood pressure variations and the ensuing heart period variations [215, 225]. Specifically, the variations around the "Eigen frequency" of the baroreflex at 0.1 Hz are useful, while the variations around respiratory frequency are controversial [81, 136, 141, 142], for this purpose. Resonances in low frequency are induced mainly by the latencies in the sympathetic efferent arm of the baroreflex, excited by spontaneous variations in blood pressure. This explanation for the genesis of so-called low-frequency blood pressure oscillations received its theoretical basis by the modeling work of De Boer et al. [75, 139].

Two basic approaches have been established for spontaneous BRS quantification: one based on time domain and the other on frequency domain measurements. In time-domain, the sequence method [214] is based on the identification of three or more consecutive beats in which progressive increases/decreases in systolic blood pressure are followed by progressive lengthening/shortening in RR interval. The sensitivity of the reflex is obtained by computing the slope of the regression line relating changes in systolic pressure to changes in RR interval [151]. Evaluation of BRS by spectral methods is based on the concept that each spontaneous oscillation in blood pressure elicits an oscillation at the same frequency in RR interval by the effect of arterial baroreflex activity [151]. There are some differences in the computational algorithms of spectral indexes of BRS [155], which can be divided in autoregressive spectral methods [212, 168] and transfer function based methods [225].

However, BRS gives only a measure of part of the baroreflex, and not even the most important component. It describes the ability of the baroreflex to change heart period (or heart rate) in response to a change in blood pressure [139], while it gives no information about the changes in the blood vessels operated by sympathetic nerves. Given that the changes in heart period are principally related to the vagal efferent activity to the heart, the BRS is sometime called vagal BRS or cardiac BRS [77]. For a more detailed description of methods used for the assessment of spontaneous baroreflex sen-

sitivity based in spectral analysis, please refer to §8.1.

An index of baroreflex control of sympathetic outflow (sympathetic BRS) is provided by the relationship between muscular sympathetic nervous activity and diastolic blood pressure during the drug boluses [77]. Diastolic blood pressure is used because muscular sympathetic nervous activity correlates more closely with diastolic blood pressure than with systolic pressure. In a recent study [77], it was shown that that, within individuals, there does not appear to be any direct correlation between the sensitivities of the cardiac and sympathetic efferent arms of the baroreflex mechanism, i.e. between cardiac and sympathetic BRS. This result emphasizes the distinct pathways associated with cardiac and sympathetic baroreflex control and the need to use caution when drawing conclusions about the baroreflex as a whole if only one or the other arm of the reflex is studied [77]. However, these observations do not reduce the clinical relevance of cardiac baroreflex [151].

Clinical relevance: A quantitative description of baroreflex gain, that is, BRS, may provide a useful index of neural regulation at the sinus atrial node. This information has clinical and prognostic value in a variety of cardiovascular diseases, including myocardial infarction and heart failure [151]. The knowledge that BRS may be altered in patients with cardiovascular disease is not new [82]. Cardiovascular diseases are often accompanied by an impairment of baroreflex mechanisms, with a reduction of inhibitory activity and an imbalance in the physiological sympathetic-vagal outflow to the heart, thus resulting in a chronic adrenergic activation [151].

Age and blood pressure have been demonstrated to be the most important correlates of BRS. Although the exact mechanism is not known, loss of arterial distensibility is generally regarded to be the main mechanism responsible for reduction of BRS in older subjects [151]. The clinical relevance of spontaneous BRS analysis [215] is shown by its ability to detect early impairment of autonomic function [96] and to provide information of prognostic value, as in patients after stroke [226] or myocardial infarction [149], or in the diagnosis of brain death [69]. In particular, the study described in [149] enrolled almost 1300 patients under 80 years and showed that impaired vagal reflexes, expressed by a depressed BRS (< 3 ms/mmHg), was a significant predictor of total cardiac mortality, independently of well-established risk factors such as depressed left ventricular function and the number of ectopic beats/hour [151].

Patients with low heart-rate variability or BRS have a reduced capability to antagonise sympathetic activation through vagal mechanisms [149]. However, a low BRS added predictive value to that of low heart-rate variability [149].

A number of papers have supported the pathophysiological and clinical relevance of spontaneous BRS estimates. Indeed, the information yielded by laboratory and spontaneous methods appears to be complementary, when exploring the complexity inherent in baroreflex cardiovascular modulation [213].

1.2.3 Heart rate variability

Heart rate is not constant, but varies over very short periods, even from beat to beat [138]. These variations do not follow strictly regular patterns, but repeating phenom-

ena may be observed. Best known is the respiratory sinus arrhythmia (see §1.2.4): quickening of the heartbeat at inspiration, slowing at expiration [138]. This is entirely vagally mediated. But this is not the only rhythm that can be discerned. Slow variations, with repetition periods of approximately 10 seconds, not related to respiration, are present most of the time [135]. These may be very prominent in the upright posture [138, 71]. Even slower rhythms can be observed over the course of the day if sufficient time is allowed for recording, with the slowest one being the circadian pattern-speeding heart rate up during the waking day and slowing it down during sleep.

In 1981, Akselrod et al. introduced power spectral analysis of these heart rate fluctuations to quantitatively evaluate beat-to-beat cardiovascular control [2, 1]. From the Eighties, heart rate variability analysis has received great attention from physiologists, clinicians and bioengineers, because it was considered as a useful tool to assess sympathetic and parasympathetic outflows [210, 171, 188]. Frequency-domain analyses contributed to the understanding of the autonomic background of RR interval fluctuations in the heart rate record [1]. However, as discussed in the following paragraph, the usefulness of HRV indices to evaluate nerve traffic is controversial [79, 172, 138, 215, 170].

The clinical importance of HRV became apparent in the late 1980s when it was confirmed that HRV was a strong and independent predictor of mortality following an acute myocardial infarction [1].

Nowadays, heart rate variability analysis is considered as a non invasive methodology of substantial utility to evaluate autonomic control mechanisms and to identify patients with an increased cardiac mortality [157]. It is accepted that it does not carry quantitative measures of autonomic outflow [215, 170]. However, when associated to other components of cardiovascular variability (blood pressure variability, respiration, baroreflex etc.), heart rate variability provides important information about the autonomic control of circulation, in normal and diseased conditions [215, 170].

Indices of HRV: Many indices have been proposed to quantify HRV properties. Most of them were included in the Task Force of 1996 [1], and are reported in the Table 1.4. They can divided in two groups:

- Time-domain indices:
  These indices, reported in the upper part of Table 1.4, are the most simple. In spite of their simplicity, a number of reports have confirmed, also in prospective studies, their prognostic value as predictors of arrhythmic and total cardiac mortality not only after myocardial infarction but also in patients with heart failure [157, 1, 150]. In a continuous electrocardiographic (ECG) record, each QRS complex is detected, and the so-called normal-to-normal (NN) intervals (that is all intervals between adjacent QRS complexes resulting from sinus node depolarizations), are determined and mathematically processed [1, 223]. Time-domain indices can be divided in two subgroups: statistical indices, mainly obtained form mean and standard deviations of heart period, and geometric indices, mainly obtained from the probability density function of the NN.
- Frequency domain indices:
  Interest for frequency domain parameters derives from the possibility of iden-

tifying periodic oscillations in HRV and to correlate these oscillation patterns to neural discharge. In fact, vagal and sympathetic cardiac controls operate on heart rate in different frequency bands [215]. Low frequency (LF; 0.04–0.15 Hz) fluctuations in HR are affected by electrical stimulation of both vagal and sympathetic cardiac nerves in animals. Similarly, in humans, LF powers are reduced by either parasympathetic or sympathetic blockade; parasympathetic blockade by atropine eliminates most HR fluctuations at high frequency (HF; 0.15–0.4 Hz); thus, HRV at HF is a satisfactory, although partly incomplete, measure of vagal cardiac control, whereas LF components reflect both sympathetic and parasympathetic modulation, without excluding a role of humoral factors, gender and age. The LF/HF ratio was proposed as measure of the sympatho-vagal balance [210, 188] and was also effective to study autonomic control in those clinical conditions associated with an increase sympathetic and reduced vagal modulation of sinus node such as, for example, the acute phase of myocardial infarction or the initial phases of heart failure [157]. Since the beginning, however, it was evident that the physiological interpretation of LF and HF components and of LF/HF ratio was progressively more problematic when moving from short-term to 24 hour recordings, and recently it has been suggested that spectral analysis of HRV must be restricted to short term recordings under controlled conditions in order to measure more correctly and to interpret more safely LF and HF components [157].

The origin and the interpretation of the LF rhythm of heart rate variability, is by far the most controversial. It is known to be related to Mayer's wave, oscillations of arterial pressure lower than respiration with a period of approximately 10 s [135]. Several data suggest that heart rate oscillations buffer Mayer's wave [135]. Unfortunately, the function as well as physiological determinants of Mayer's wave frequency and amplitude are still largely unknown [135].

Clinical relevance: The clinical relevance of HRV analysis is related to the well-established link between autonomic cardiac control and cardiovascular mortality, including sudden cardiac death, with HRV being a key marker of such a relationship. In fact, reduced HRV is associated with increased mortality after myocardial infarction and increased risk of sudden arrhythmic death [215]. One of the basic assumptions used to explain the negative predictive value of reduced HRV was the concept that overall HRV was largely dependent on vagal mechanisms and that a reduction in HRV could reflect an increased sympathetic and a reduced vagal modulation of sinus node; i.e., an autonomic imbalance favouring cardiac electrical instability [157]. Changes in HRV have been also shown to identify favorable changes in cardiac autonomic control after cardiac resynchronization therapy in patients with severely symptomatic heart failure [215]. These observations strongly suggest that HRV, in addition to representing a research tool, should become a more widely employed clinical parameter [215].

Criticisms: The usefulness of HRV indices has been seriously criticized by some authors. Criticisms do not deny the clinical relevance of HRV, but they question its

Table 1.4: Indices of HRV, from [1]. NN=NN intervals corresponding to heart period during sinus rhythm; SD=Standard deviation

Variable (Units)	Description
Time-domain	
SDNN (ms)	SD of all NN
SDANN (ms)	SD of the averages of NN in all 5-min segments of the entire recording
RMSSD (ms)	The square root of the mean of the sum of the squares of differences between adjacent NN
SDNN index (ms)	Mean of the SD of all NN for all 5-min segments of the entire recording
SDSD (ms)	SD of differences between adjacent NN
NN50 count	Number of pairs of adjacent NN differing by more than 50 ms in the entire recording
pNN50 (%)	NN50 count divided by the total number of all NN
HRV triangular index	Total number of all NN divided by the height of the histogram of all NN measured on a discrete scale with bins of 7.8125 ms (1/128 seconds)
TINN (ms)	Baseline width of the minimum square difference triangular interpolation of the highest peak of the histogram of all NN
Differential index (ms)	Difference between the widths of the histogram of differences between adjacent NN measured at selected heights
Logarithmic index	Coefficient ϕ of the negative exponential curve $ke^{-\phi\,t}$, which is the best approximation of the histogram of absolute differences between adjacent NN
Variable (Units)	Description
Frequency-domain	
power (ms^2)	The variance of NN over 5 min
VLF (ms^2)	Power in VLF range ($f \leq 0.04$ Hz)
LF (ms^2)	Power in LF range ($f \in [0.04 - 0.15]$ Hz)
LF norm (nu)	LF power in norm units LF/(total power-VLF)x100
HF (ms^2)	Power in HF range ($f \in [0.15 - 0.4]$ Hz)
HF norm (nu)	HF power in norm units HF/(total power-VLF)x100
LF/HF	Ratio LF(ms^2)/HF(ms^2)

physiological interpretation. In 1997, Dr Ekberg wrote a critical review [78] that support the opinion that calculations of sympathovagal balance, proposed ten years before [210], may obscure rather than illuminate human physiology and pathophysiology. In the paper, Dr Ekberg claimed that the ratio of the LF power to HF power is not suitable to quantitatively evaluate autonomic nervous activity owing to the following reasons [78]:

– Vagal contributions to baseline LF RR-interval fluctuations are great, and evidence that baseline LF RR-interval spectral power is related quantitatively to sympathetic-cardiac nerve traffic is nonexistent.
– Most evidence refutes the notion that LF RR-interval spectral power tracks baroreflex-mediated changes of sympathetic nerve activity.
– Baseline respiratory-frequency RR-interval fluctuations are related significantly but imperfectly to the level of human vagal-cardiac nerve traffic.
– Moderate changes of arterial pressure, which alter vagal-cardiac nerve activity, do not change HF RR-interval fluctuations, and changes of breathing frequency and depth, which profoundly alter HF RR-interval fluctuations, may not change vagal-cardiac nerve activity at all.

Finally he questioned the hypothesis that sympathetic and parasympathetic nervous systems continuously interact [79], suggesting that the construct of sympatho-vagal balance imposes attributes on physiological regulatory mechanisms that they do not possess [78].
This critical appraisal caused many of the members of the task force [1] to answer to these criticisms to support the usefulness of HRV indices in cardiovascular control analysis [172, 237, 169].
Ten years later, a series of editorial papers about whether cardiovascular variability is or is not an index of autonomic control of circulation [215, 170] refocused the debate about the role of HRV indices in physiology. All authors agreed that neither low frequency (< 0.15 Hz) nor high frequency (> 0.15 Hz) indices can be used as exclusive markers of sympathetic and parasympathetic activity, respectively [170]. And some of them suggested that heart rate variability provides only a qualitative marker of cardiac parasympathetic regulation through respiratory sinus arrhythmia (RSA). In the debate, on one side, Taylor and Studinger [215, 170] argued that quantification of autonomic activity has not been achieved, and suggested that efforts should be focused on establishing more direct links to underlying physiology. For these authors, the point is that there is more to be learned from cardiovascular periodicities than what they may or not say regarding baseline levels of autonomic nerve traffic [215, 170]. On the other side, Parati et al. [215, 170] claimed that HRV analysis has already established a basis for autonomic interpretation of results and that future modeling will expose underlying physiology.
These debates and discussions, which should include the more recent debate about the origin of respiratory sinus arrhythmia [141, 81] and Mayer's Wave [135], show that research in cardiovascular variability is far from being over and much effort is needed in multi-signal analysis.

Representations of heart rate variability

In the literature, several methodologies to mathematically describe heart rate variability have been proposed. Here we report a brief description of the most common ones:

- Interpolation: Heart rate variability can be estimated just by evenly resampling the inverse interval function, i.e. the reciprocal of the heart period. In the interpolation process, the n-th heart period should be arbitrarily assign to a given temporal instant, which usually is the time of occurrence of one of the two QRS complexes which determine the beginning and the end of the heart period. This procedure is not based on a physiological model. The representation of a discrete unevenly sampled time series as a continuous signal is often a requirement of many signal processing techniques, among which there is time-frequency analysis.

- Autoregressive model: Autoregressive models as well as ARMA and ARMAX models are widely used to describe heart rate variability and the interactions of cardiovascular signals [165, 167, 31]. Again, the use of these models is not motivated by cardiovascular physiology, but is principally due to the possibility of using very powerful methodologies of time series spectral and cross spectral analysis. Although the use of these models is rarely based on cardiovascular physiology, it offers the possibility of using very powerful methodologies of time series spectral and cross spectral analysis.

- IPFM: The integral pulse frequency modulation (IPFM) model has been used to explain the mechanisms used by the autonomic system to control the heart rate [179, 178, 221]. The IPFM model is based on the hypothesis that the sympathetic and parasympathetic influences on the sino-atrial node can be represented by a single modulating signal, and the beat trigger impulse is generated when the integral of this function reaches a threshold. The heart timing signal, which assume the IPFM model, has been demonstrated to provide an unbiased estimation of the ANS modulation, even in the presence of isolated ectopic beats [179, 178]. Recently, a time-varying threshold IPFM model was proposed to be used in situations in which the mean heart period is time varying, as during exercise stress testing [18].

- Point process: Recently, a point process model has been also used to study heart rate and heart rate variability [29, 28]. A point process is a random process for which any realization consists of a set of isolated points in time. In this framework, the waiting time until the next R-wave event or, equivalently, the length of the next R-R interval, obeys an history-dependent inverse Gaussian process probability density. The time-varying parameters of this model are estimated by local maximum likelihood and assessed by model goodness-of-fit by Kolmogorov-Smirnov tests based on the time-rescaling theorem [28, 55]. The mean and the standard deviation of the probability density function are used to give instantaneous estimates of heart rate and heart rate variability. Recently, this point process framework has been combined with bi-variate autoregressive

models to include the influence of respiration and to assess cardiovascular interactions [63, 62].

1.2.4 Respiratory sinus arrhythmia

Cardiorespiratory interactions are mediated by both mechanical effects related to hemodynamics, and neural control mainly related to vagal (parasympathetic) activity. Respiratory sinus arrhythmia (RSA) is the variation in heart rate that occurs during a breathing cycle, or heart rate variability in synchrony with respiration. In short-term HRV, RSA is the most prominent and consistent component. It appears in power spectrum of RR interval as a peak within the so-called HF band (0.15–0.4 Hz) or, more appropriately, as a peak at respiratory frequency. It is believed that RSA is mediated solely by vagus due to the difference in frequency characteristics of signal transfer between sympathetic and vagal modulation of heart rate. Because the magnitude of RSA is attenuating with progressive suppression of cardiac vagal activity and abolished by complete vagal blockage with atropine, RSA has been proposed and widely used as a quantitative index of cardiac vagal function [117, 2, 229].

The magnitude of RSA increases with rest and decreases with strain or tension. RSA is increased in the supine position and decreased in the upright position [211]. It becomes greatest during sleep and is greater during slow wave sleep than REM sleep. It also increases with relaxation and decreases with physical and mental stresses [117]. Moreover, RSA decreases with advancing age and severity of cardiac diseases. In particular, in patients with coronary artery disease, RSA at rest decreases progressively with advancing severity of coronary artery disease [117].

Although RSA was already studied at the beginning of XXth century, it is still far from being completely understood, and it is consider a complex phenomenon whose physiological role is still a matter of debate [246].

The importance of RSA is motivated by the following reasons: (i) It is frequently employed as an index of cardiac vagal tone or even believed to be a direct measure of vagal tone. For this reason RSA is classically described as a vagally mediated increase and decrease in heart rate concurrent with inspiration and expiration, respectively. (ii) It is used to index disease risk or severity [113]; (iii) It is a central point in the evolution theory of neural control of cardiorespiratory interactions [112]. However, there are many concerns regarding the interpretation of RSA, which are described in the following section.

Interpretation of RSA: The simple magnitude of RSA is often assumed to be a valid index of cardiac parasympathetic control. However, as explained in [112], there are many significant caveats regarding vagal tone interpretation. The main concerns are:

(i) Respiratory parameters of rate and volume can confound relations between RSA and cardiac vagal tone. Alterations in respiration rate and tidal volume had profound effects upon RSA magnitude: RSA magnitude under steady-state conditions is inversely related to respiration rate and directly related to tidal volume. However, these effect have been reported to be unrelated to directly determined

levels of cardiac vagal tone [113]. A number of laboratory studies document that within-individual changes in respiratory parameters of rate and tidal volume can seriously confound the association of RSA and cardiac vagal tone. Respiratory influences upon RSA amplitude become a problem for assessment of cardiac vagal tone whenever respiratory rate and/or tidal volume substantially differ between groups or conditions, and whenever RSA, respiratory parameters and cardiac vagal tone all do not systematically covary with each other [112]. The most likely explanation for the RSA variations due to changes of respiration rate and volume, is that they are related to phasic patterning of vagal effects upon heart rate, owning to respiratory gating [80]. Therefore, in this case RSA cannot be used to quantitatively measure vagal tone.

To exclude respiratory confounding effects from RSA, subjects are sometimes asked to breath at a paced rate [113]. Another technique is to adjust for the influence of tidal volume. The measure is simply RSA divided by tidal volume when time domain-measures are used [113], or the transfer function from cross-spectral analysis of the RRI and respiratory time series when spectral analysis is employed [62]. In both cases, it characterizes the amount of RSA amplitude change per liter tidal volume. Due to the reciprocal relation between rate and tidal volume, this adjustment may dampen or even eliminate the RSA dependency upon respiration rate [112]. Finally, experts suggest that the only way to ascertain whether RSA differences are related to respiratory parameters in a particular study is to measure both respiration and RSA, as well as to examine relations between the two [112].

(ii) Although within-subject relations between RSA and cardiac vagal control are often strong, between-subject associations may be relatively weak [112]. Furthermore, it is not clear what exactly individual differences in RSA represent.

(iii) RSA measurement is strongly influenced by concurrent levels of momentary physical activity, which can bias estimation of individual differences in vagal tone. Therefore, it is plausible that even small laboratory differences in movement during baseline measurement may produce effects upon RSA that could be wrongly inferred as evidence of constitutional differences in autonomic control [112].

(iv) RSA amplitude is affected by beta-adrenergic tone and may not be a pure vagal measure. RSA was shown to be sensitive to variations in cardiac vagal tone when cardiac sympathetic tone was absent, or was relatively low and stable. However, there is not confirmation about the parasympathetic specificity of RSA, i.e. that RSA always specifically reflects cardiac vagal control independently from how cardiac sympathetic activity changes [112]. However, it has been shown that R-R interval correction of RSA can reduce or eliminate the influence of basal levels of cardiac sympathetic tone. Concerning possible sympathetic effects on RSA, it is worth mention that a pronounced decrease in RSA magnitude may signify true reduction of vagal outflow from brain to heart, or a primary increase in sympathetic tone that leads to an interaction with vagal activity, or both.

(v) RSA and cardiac vagal tone may dissociate under certain circumstances. Dis-

sociation has been observed in experiments in which phenylephrine was used to activate vagal baroreflex response. The relation between RSA and vagal tone was relatively proportional and linear until heart rate slows down to very low levels. As heart rate further decreases, so does magnitude of RSA [105]. Some results suggest that the relation between RSA and vagal tone is quadratic across the entire range of vagally mediated heart change [105].

Another instance of dissociation between cardiac vagal tone and RSA appears to occur during stimulation of the carbon dioxide chemoreceptors [112].

Recently, it was suggested that the apparent associations between RSA and cardiac vagal tone can be explained as indirect consequences; i.e., whenever the cardiac vagal tone changes in response to the resting level of the cardiopulmonary system, RSA appears to change parallel to it [117]. This hypothesis, which supports the idea that the degree of respiratory modulation of cardiac vagal outflow and cardiac vagal tone may be regulated separately and independently of each other, can explain the possible dissociation between the respiratory cardiac vagal modulation and cardiac vagal tone under certain conditions. According to this hypothesis, RSA should be considered as an intrinsic resting function of cardiopulmonary system [117].

Origin of RSA: Three main hypothesis exist to explain the origin of RSA. According to them, RSA is due to (i) a central mechanism [81], (ii) the barobaroreflex [75, 141, 142], (iii) the mechanical stretching of the sinoatrial node [44, 186]; (iv) or a mixture of them [136].

Those who support the central origin for RSA, pointed out that vagal-cardiac motoneuron membrane potentials fluctuate at respiratory frequencies, modulate responsiveness of vagal motoneurons to arterial baroreceptor inputs, and impose a respiratory rhythm on vagal-cardiac nerve traffic and heart periods. Therefore, central respiratory gating of vagal motoneuron responsiveness [80] is sufficient to explain respiratory sinus arrhythmia [81]. According to this hypothesis, the strong correlation between systolic pressure and RR intervals at respiratory frequencies reflects the influence of respiration on these two measures, rather than arterial baroreflex physiology [80, 15]. A central mechanism is thought to be more likely than baroreflex also due to the observation that the latencies between a change in the respiratory component of the arterial pressure and a related change in the respiratory component of th RR (i.e. RSA) reported in the literature is too short to be due to baroreflex mechanisms. Moreover, RSA is still present in subjects with baroreflex failure [136], and causal analysis also support the hypothesis that baroreflex can not be considered as the unique origin of RSA [218, 247, 219, 136].

The hypothesis that RSA is mainly a reflex phenomenon, driven by incoming information from baroreceptors, relies on a model [75, 47, 48]. According to this hypothesis the RSA is due to respiratory induced blood pressure oscillations (mainly due to variations in the stroke volume following intrathoracic pressure changes) that are translated into heart rate by the baroreflex [141]. Consequently, RSA would reduce diastolic pressure variability. This hypothesis does not refute animal experiments that show respiration to modulate centrally the blood pressure to heart period reflex, but it suggests that in awake humans this phenomenon is insufficient to explain respiration-to-heart rate
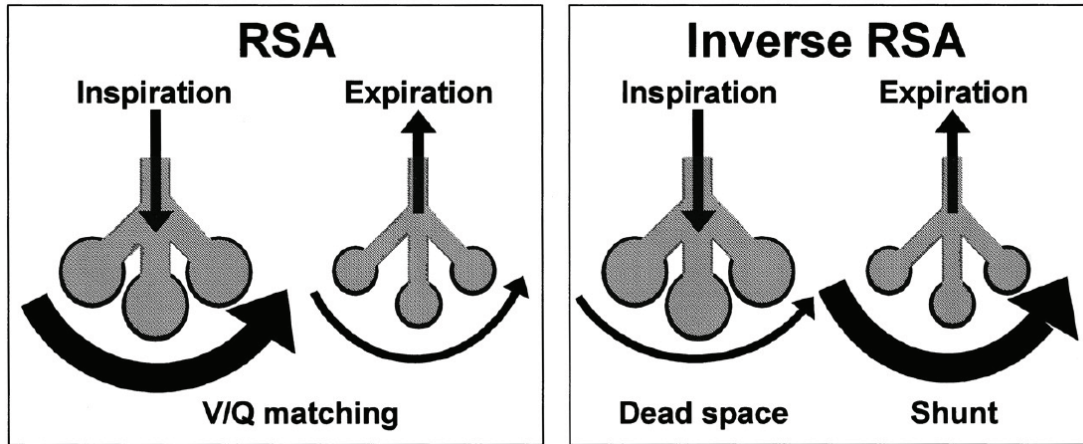
Figure 1.5: Schema showing the effects of RSA and its inversion (inverse RSA) on the relationship between alveolar gas volume and capillary blood flow during inspiration and expiration. Horizontal bows and vertical arrows indicate the volume of blood flow and the direction of gas flow, respectively. RSA improves respiratory gas exchange efficiency though matching between alveolar ventilation and capillary perfusion throughout respiratory cycle, while inverse RSA results in increased alveolar dead space (wasted ventilation) and increased intrapulmonary shunt. (From [118, 117, 258])

relations [141].

A third hypothesis suggests that, given the complexity of human cardio-respiratory physiology, RSA should be the results of many causes. Among others, there are the feedback from the lungs and, possibly, atrial stretch receptors [142].

This debate points out the need of improved methodologies that undertake the limitation of classical temporal or spectral analysis [236].

Physiological role of RSA Respiratory sinus arrhythmia is a physiologic phenomenon reflecting respiratory-circulatory interactions universally observed among vertebrates. Some studies have shown that the efficiency of pulmonary gas exchange is improved by RSA, suggesting that RSA may play an active physiologic role [118, 258]. As shown in the schema of Fig. 1.5, the matched timing of alveolar ventilation and its perfusion with RSA within each respiratory cycle could save energy expenditure by suppressing unnecessary heartbeats during expiration and ineffective ventilation during the ebb of perfusion. Thus RSA may have a positive influence on gas exchange at the level of the lung via efficient ventilation/perfusion matching [258, 117]. This hypothesis is in agreement with the definition of the RSA as an "intrinsic resting function of cardiopulmonary system" previously mentioned [117].

However, recent results [246] have been presented that do not support the hypothesis that RSA optimizes pulmonary gas exchange efficiency via clustering of heart beats in inspiration. In that study [246], contrary to assumptions in the literature, no significant clustering of heart beats was observed, even with high levels of RSA enhanced by slow breathing [246]. It is suggested that some process other than the clustering of heart beats may be responsible for previously reported associations between RSA

and indexes of pulmonary gas exchange efficiency. Authors speculate that the enhancement of gas exchange may be mediated by mechanical effects. The falling intra thoracic pressure associated with spontaneous inspiratory efforts lowers right atrial pressure and facilitates blood flow to the right ventricle because the rate of venous return changes inversely with right atrial pressure. This bolus-increased venous return during inhalation may be transmitted to the pulmonary artery on subsequent beats, resulting in a matched increase in both pulmonary capillary blood flow and alveolar ventilation. This thoracic pump effect, which is distinct from RSA, may be greater during slower breathing and may confound the apparent relationship between RSA and pulmonary gas exchange efficiency [246].

1.3 Methodological aspects

In this section we give a short and non exhaustive description of different methodologies currently used to analyze the time-varying spectral content of time series. In the last decades, a vast number of time-varying/time-frequency techniques has been applied to biomedical signals, mainly related to cardiovascular or neural systems [165, 31, 46, 255]. Broadly speaking, most of these techniques can be divided in two categories, which include parametric and non-parametric analysis. In the following, we briefly introduce these techniques.

1.3.1 Parametric autoregressive approaches

A time-series $y_1(n)$ can be seen as a realization of a stochastic process of type:

$$y_1(n) = -\sum_{k=1}^{P} a_{11}(n,k)y_1(n-k) + \sum_{k=1}^{P} a_{12}(n,k)y_2(n-k) + \ldots + \sum_{k=1}^{P} a_{1M}(n,k)y_M(n-k) + \xi_1(n)$$

(1.2)

In this expression, $y_1(n)$ is seen as the results of a linear combination of its own previous values, trough coefficients $a_{11}(n,k)$; a linear combination of previous values of other stochastic processes $y_j(n)$, with $j \in \{2, \ldots, M\}$, through coefficients $a_{1j}(n,k)$; a white noise noise $\xi_1(n)$, which confers to the time series its stochastic behavior and accounts for the phenomena that cannot be explained by the model. Indices n and k are time instant, that can be both evenly and unevenly spaced on the temporal axis. Uneven regressions are sometimes used to describe discrete events as heart rate or systolic and diastolic arterial pressure [27, 31, 4].

Writing the relationships of type (1.2) for the rest of time-series $y_j(n)$, we can describe a linear multivariate system as [168]:

$$\mathbf{Y}(n) = \sum_{k=1}^{P} \mathbf{A}(n,k)\mathbf{Y}(n-k) + \mathbf{\Xi}(n)$$

(1.3)

where $\mathbf{A}(n,k)$ is a $M \times M$ matrix which contains coefficients $a_{ij}(n,k)$. In this formulation, time-varying properties of the system are captured by time-varying coefficients $a_{ij}(n,k)$, which account for the influence that, at a given time instant $n_0 - k_0$, the

signal $y_j(n)$ execrts over the signal $y_i(n)$ at time n_0.

The maximum number of samples considered in the regression, i.e. p, is the order of the model, and it plays an important role in the fitting capability of the model.

Once that the coefficients of the model have been estimated, owing to the $\mathcal{Z}$ transform, it is possible to obtain the transfer functions that characterize the response of each part of the system in the frequency domain . From the transfer functions, it is then straightforward to obtain spectral and cross spectral densities of time series $y_i(n)$.

Thus, the primary reasons of the great success of autoregressive modeling of time-series are: (i) The possibility of estimating the (time-varying) power spectral densities of the analyzed signals; (ii) The possibility of automatically decomposing the spectra in different components, which describe the separate contributions that underlying sources has on the global system; (iii) The possibility of assessing mutual relationships between the spectral components of the system, even when closed loop are present in the system [255, 261, 84, 46]. In the presence of closed loop, multivariate autoregressive analysis can provide an assessment of direct and indirect causal interactions. Interest in causal analysis has been the objective of many recently studies [14, 87, 83, 85, 194, 193, 217]. Autoregressive parametric analysis should include two main steps: identification and validation. The coefficients of the model are usually identified by minimizing the estimation error. The most used procedures for time-varying identification include recursive least square algorithm, Kalman filters and local maximum likelihood [165, 29]. An alternative option, which is supposed to reduce the great variance of recursive least square algorithms, consists in performing an (off-line) expansion of the coefficients onto a set of predetermined basis functions [89, 186]. The set up of a multivariate model requires some information about the system being described. Prior information about the input/output relationships between the different signals of the systems should be included in the model. The order of the model is a very important parameter. Although sometimes the selection of the order of the model is based on physiological assumptions [4], the most of the time it is selected following the optimization of some ad-hoc criteria. The most used one is probably the Akaike information criterion, which measures the trade off between accuracy and complexity of the model. The identification procedure provides an approximation of the true coefficients. The goodness of this approximation depends on practical factors, such as the length of the data, and on the parameters used in the identification procedure itself. Thus, it is of primary importance to quantify the goodness of fit of the model to demonstrate its validity. Common validation procedures aim at verifying the whiteness and uncorrelation of the residuals of the model [85, 255].

The model described in (1.3) is often reduced to a monovariate one, with $M = 1$, to perform time-varying spectral analysis of a single time-series. Although multivariate autoregressive models can be used to described complex systems, they are not the most general ones. For instance, one can include a dependence of $y_j(n)$ on past values of the white noises that enter in the model as input. When a regression on past values of $\xi_j(n)$ is included, the model is called autoregressive moving average (ARMA) model [204]. A monovariate time-varying ARMA model is used in §2 to generate real-like HRV signals with predetermined spectral properties. Exogenous inputs with a colored spectrum can also be added to the model, thus providing the so called ARX or AR-

MAX models. Although more and more complex models can be appealing since they may be used to explain more and more detailed interactions, caution should be used in increasing their complexity, since the more complex the model is, the less reliable their estimated coefficients can be.

Multivariate autoregressive models are linear in their coefficients. Although non-linear models may better describe systems in which non-linear behaviors as hysteresis and saturation have been observed, linear models may be preferable, because they are much more intuitive and may therefore be more useful in gaining insight into neural regulatory functioning [255]. Recently, some approach for time-frequency identification that include both time and frequency shift have been proposed [129].

1.3.2 Non-parametric approach

Non-parametric methodologies have been mainly used to give a joint time-frequency representation of a signal. Although these methodologies usually assume a deterministic structure for the signals being analyzed, they can also be used to infer second order properties of non-stationary random processes [182].

Non-parametric multivariate analysis is usually limited to the simultaneous processing of couples of signals, in which a signal is seen as the input and the other as the output of an implicit open loop model. Cross time-frequency analysis, which allows assessing these input/output interactions, is a very recent domain of research [252, 181, 110, 144]. Much of the work presented in this dissertation aims at extending cross-time frequency analysis to the study of cardiovascular interactions, by means of time-frequency coherence (see §4) and phase difference spectrum (see §5) based on a particular representation called smoothed pseudo Wigner-Ville distribution.

Time-frequency representations can be grouped in linear and quadratic (or bilinear) distributions [123, 92, 8].

Linear time-frequency distributions: Linear time-frequency distributions include very popular techniques, such as the spectrogram and the continuous wavelet transform. Spectrogram is defined as the squared magnitude of the short-time Fourier transform:

$$S^{\mathrm{s}}(t, f) = \left| \int_{-\infty}^{+\infty} x(\tau) h(\tau - t) e^{j2\pi f \tau} d\tau \right|^2 \tag{1.4}$$

where $h(t)$ is a sliding window. Spectrogram provides uniform resolution in the time-frequency domain, and it is characterized by a severe trade-off between time and frequency resolution. That is, the better the signal is described in time direction, the worse it is described in frequency direction. The multitaper spectrogram, which is obtained by averaging different spectrograms estimated by using orthogonal sliding windows, will be used in §4.4. Please refer to §4.4 for a more detailed discussion of advantages an drawbacks of the spectrogram.

Continuous wavelet transform is obtained by projecting a signal on a family of zero-mean functions (the wavelets) deduced from an elementary function (the mother

wavelet) by translations and dilations [10]:

$$\mathcal{W}(t,a) = \int_{-\infty}^{+\infty} x(\tau)\Psi_{t,a}(\tau)d\tau \tag{1.5}$$

$$\Psi(\tau) = \frac{1}{\sqrt{|a|}}\Psi(\frac{\tau - t}{a}) \tag{1.6}$$

The variable a is a scale factor, in the sense that $|a| > 1$ dilates and $|a| < 1$ compresses $\Psi_{t,a}(t)$. By definition, the wavelet transform is more a time-scale than a time-frequency representation. However, for wavelets which are well localized around a non-zero frequency f_0 at scale $a = 1$, a time-frequency interpretation is possible thanks to the formal identification $f = \frac{f_0}{a}$. The squared magnitude of the continuous wavelet transform, $|\mathcal{W}(t,a)|^2$, also called scalogram, can be used to estimate the time varying spectral density of a signal. Since when the scale factor a changes both the bandwidth and the duration of the wavelets $\Psi_{t,a}(t)$ change, the continuous wavelet transform uses short windows at high frequencies and long windows at low frequencies [10]. Therefore, contrary to the spectrogram that uses a fixed window $h(t)$, $\mathcal{W}(t,a)$ is characterized by a non uniform time-frequency resolution. A better time resolution is used to represent high frequency components, while a better frequency resolution is used to represent low frequency components.

Continuous wavelet transform has been used in heart rate variability analysis [245], and more recently it has been applied to characterize cardiovascular and cardiorespiratory interactions [144, 145, 97, 66]. Note that in §4.6 a comparison between wavelet coherence and a new time-frequency coherence function proposed in this dissertation is carried out.

Quadratic time-frequency distributions: Quadratic, or bilinear, distribution are used in §3–§5. Please, refer to §3.1 for an introduction of these particular class of representation.

Here, we just would like to stress that both linear and quadratic time-frequency distributions can be obtained as a convolution of a time-frequency kernel function with a particular distribution called Wigner-Ville distribution (see (3.7)) [92]. Therefore, wavelets, spectrograms and quadratic time-frequency representations should not be seen as independent analytical tools, and their performance is mainly due to the shape of the kernel functions.

Other non-stationary approaches: Empirical mode decomposition (EMD) is a recent tool, proposed for analyzing non-stationary signals. As suggested by its name, EMD is more like an algorithm (an empirical approach), rather than a theoretical tool. The EMD reduces any given time-series into a collection of intrinsic mode functions (IMF). An IMF is defined as a function that satisfies the following requirements: (i) In the whole time series, the number of extrema and the number of zero-crossings must either be equal or differ at most by one. (ii) At any point, the mean value of the envelope defined by the local maxima and the envelope defined by the local minima is zero. Therefore, contrary to Fourier analysis, which is based on harmonic functions

that are constant both in amplitude and frequency, EMD provides a decomposition of the signal on simple oscillatory modes, which can have variable amplitude and frequency along the time axis.

After having decomposed a signal into its IMF, one can apply Hilbert spectral analysis to obtain instantaneous frequency and amplitude of the IMF, thus characterizing the time-frequency structure of the signal. This combination of EMD and Hilbert spectral analysis is called Hilbert-Huang transform [127]. Alternatively, one can also analyze the IMF by means of time-frequency distributions and subsequently reconstruct the entire time-frequency spectrum of the signal.

Applications of empirical mode decomposition to cardiovascular analysis can be find in [191, 239, 97, 163].

Recently, a bivariate extension of EMD has been proposed [224]. In this framework, a simultaneous decomposition of two signals is realized by first considering the two signals as the real and imaginary part of a complex signal, and then by extracting zero-mean rotating intrinsic components. This methodology could be applied to the simultaneous analysis of cardiovascular signals.

1.4   Outline of the manuscript

Chapter §2:   In this chapter, we address the problem of generating signals with a predetermined time-frequency structure. We present two methodologies to generate real-like heart rate variability signals by means of time-varying ARMA models.
Part of the work presented in this chapter has been published in:

[204] Orini, M., Bailón, R., Mainardi, L., Laguna, P.: Synthesis of hrv signals characterized by predetermined time-frequency structure by means of time-varying arma models. Biomedical Signal Processing and Control, In Press, – (2011)
[203] Orini, M., Bailón, R., Laguna, P., Mainardi, L.T.: Modeling and estimation of time-varying heart rate variability during stress test by parametric and non parametric analysis. In: Proc. Computers in Cardiology, pp. 29–32 (2007)

Chapter §3:   In this chapter, we address the problem of reliably characterizing the time-frequency structure of the heart rate variability signal. This chapter includes an introduction to the distributions belonging to the Cohen's class and a description of the interference terms geometry. The smoothed pseudo Wigner-Ville distribution is evaluated by using signals generated with a framework presented in §2. Finally, a method that performs a parametric decomposition of the Wigner-Ville distribution is presented.

Chapter §4:   In this chapter, we address the problem of quantifying the local coupling between the spectral components of non-stationary cardiovascular signals. The chapter includes: Two methodology to estimate time-frequency coherence by smoothed pseudo Wigner-Ville distribution and error analysis by means of a simulation study; a methodology to estimate time-frequency coherence based on multitaper spectrogram; two methods to estimate a threshold function to assess the statistical significance of the

local coupling; a comparative study between coherence by smoothed pseudo Wigner-Ville distribution, multitaper spectrogram and wavelet transform, which also includes the analysis of physiological signals.
Part of the methodologies presented in this chapter has been published in:

[205] Orini, M., Bailón, R., Mainardi, L., Laguna, P., Flandrin, P.: Characterization of the dynamic interactions between cardiovascular signals by time-frequency coherence. IEEE Trans. Biomed. Eng., In Press (2011)

[206] Orini, M., Bailón, R., Mainardi, L.T., Mincholé, A., Laguna, P.: Continuous quantification of spectral coherence using quadratic time-frequency distributions: error analysis and application. Proc. Computers in Cardiology (2009)

[202] Orini, M., Bailón, R., Gil, E., Minardi, L.T., Laguna, P.: Framework for continuous quantification of spectral coherence using quadratic time-frequency distributions: exploring cardiovascular coupling. International Journal of Bioelectromagnetism **12**, 177–182 (2010)

Chapter §5: In this chapter, we address the problem of estimating phase difference and time delay between the spectral components of two non-stationary cardiovascular signals. This represent an extension of the cross time-frequency analysis presented in §4. The phase difference spectrum is estimated by means of smoothed pseudo Wigner-Ville distribution and the time course of cross spectral indices is estimated in specific signal-dependent time-frequency regions. Different simulation studies are carried out to assess the performance of the presented estimators. Part of the work presented in this chapter has been published in:

[207] Orini, M., Bailón, R., Mainardi, L.T., Laguna, P.: Time-frequency phase differences and phase locking to characterize dynamic interactions between cardiovascular signals. Conf Proc IEEE Eng Med Biol Soc (2011)

[208] Orini, M. and Laguna, P. and Mainardi, L.T. and Bailón, R.: Characterization of the dynamic interactions between cardiovascular signals by cross time-frequency analysis: phase differences, time delay and phase locking. Proc. Conf. on numerical method in engineering (2011)

Chapter §6: In this chapter, we characterize the pattern of response of the autonomic modulation of heart rate to musical stimuli characterized by different emotional valence but same arousal. Additionally, we also explore music-induced changes in the respiratory rate and in the cardio-respiratory coupling. Part of the work presented in this chapter has been published in:

[201] Orini, M., Bailón, R., Enk, R., Koelsch, S., Mainardi, L.T., Laguna, P.: A method for continuously assessing the autonomic response to music-induced emotions through HRV analysis. Med. Biol. Eng. Comput. **48**(5), 423–433 (2010)

Chapter §7: In this chapter, we compare the time-frequency structure of heart rate variability and pulse rate variability derived from photoplethysmography signal, during tilt table test. The goal is to assess whether the pulse rate can be used as an

alternative measurement of heart rate variability in non-stationary conditions. Time-frequency and time-frequency coherence analysis are used. Part of the work presented in this chapter has been published in:

[100] Gil, E., Orini, M., Bailón, R., Vergara, J.M., Mainardi, L.T., Laguna, P.: Photoplethysmography pulse rate variability as a surrogate measurement of heart rate variability during non-stationary conditions. Physiol. Meas. **31**(9), 1271 (2010)
[101] Gil, E., Orini, M., Bailón, R., Vergara, J.M., Mainardi, L.T., Laguna, P.: Time-varying spectral analysis for comparison of HRV and PPG variability during tilt table test. Conf Proc IEEE Eng Med Biol Soc **2010**, 3579–3582 (2010)

Chapter §8: In this chapter, we use the methodology of cross time-frequency analysis presented throughout chapters §4–§5 to study the dynamic interactions between R–R variability and arterial pressure variability during tilt table test and during rest. The goals of the study are: characterize the temporal evolution of the coupling and phase difference between the two signals; track the changes of the baroreflex sensitivity during tilt; assess the usefulness of time-varying signal processing to analyze signals recorded in conditions usually supposed to be stationary. Part of the work presented in this chapter has been published in:

Orini, M., Laguna, P., Mainardi, L.T., Bailón, R.: Assessment of the dynamic interactions between heart rate and arterial pressure by cross timefrequency analysis. Physiol. Meas. In Press (2011)

Part I

Methodologies

Chapter 2

Time-frequency synthesis for HRV

Contents

2.1   Introduction

As already mention in the previous chapter, spectral analysis of heart rate variability (HRV) is a non invasive tool widely used to assess the regulation of the autonomous nervous system over the heart [1]. The spectrum of HRV is characterized by two main spectral components: the low frequency (LF) component, defined in [0.04, 0.15] Hz, and the high frequency (HF) component, defined in [0.15, 0.4] Hz. The power in the HF band is considered a measure of parasympathetic activity. The power in the LF band is considered a measure of sympathetic and parasympathetic activity, being its interpretation controversial when, e.g. the respiratory frequency lies in the LF band. For a more in depth description of the physiological mechanisms determining HRV, please refer to §1.2.3.

Traditional spectral analysis requires stationarity and can not be applied in a wide range of clinical and physiological studies, such as exercise stress testing, tilt table test, experiments of induced emotions, etc., in which time-frequency (TF) techniques should be preferred. Given that the number of HRV studies which involve TF analysis is increasing [165] and non-stationary signal processing is becoming the rule in cardiovascular analysis, there is a need of evaluation procedures to assess the performance of TF techniques on each specific application. This can be done by analyzing simulated HRV signals characterized by predetermined real-like time-varying (TV) spectral patterns. In simulation studies, signals related to the autonomic modulation are often modeled as the sum of two deterministic tones embedded in noise [164, 58, 146, 19, 216]. Nevertheless, the nature of biological signals is not completely deterministic [104], and TV autoregressive models are widely used to estimate HRV spectral indices as well as to describe the interactions between cardiovascular signals [33, 42, 46, 71, 88, 87, 156, 165, 166, 187, 261].

In this chapter, we propose to use TV autoregressive models to create HRV signals with known and controlled TF structure with the purpose of providing a useful tool for the assessment of different TF methodologies before being used in clinical applications. In the validation of these techniques, the use of non-stationary stochastic processes is complementary to the use of synthetic signals created by using deterministic models. Our attention is focused on the modeling of exercise stress testing and experiments of music-induced emotions. Exercise stress testing [19, 187] is a common test during which cardiovascular parameters vary quickly within a wide range of values. Recently, indices of HRV during this test have been used in the diagnosis of coronary artery diseases [21, 22, 248]. The validation of TF techniques used in HRV analysis during experiments of music-induced emotions deserves attention since in recent years the interest in therapeutic applications of music has increased, as well as the effort to understand the relationship between music features and physiological patterns [39, 40, 106, 107, 201].

In §3, this framework will be used to evaluate the performance of the smoothed pseudo Wigner-Ville distribution in non-stationary HRV analysis.

2.2 Methods for the synthesis of non-stationary HRV signals by TV-ARMA models

2.2.1 General framework

A time-varying autoregressive moving average (TV-ARMA) model can be used to describe non stationary signals:

$$x(n) = -\sum_{k=1}^{\tilde{p}} a_k(n)x(n-k) + \sum_{k=0}^{\tilde{q}} b_k(n)\xi(n-k) \tag{2.1}$$

where $a_k(n)$ and $b_k(n)$ are TV coefficients, $\tilde{p}$ and $\tilde{q}$ are the orders of the AR and MA part of the model, respectively, and $\xi(n)$ is a zero-mean unit-variance white Gaussian noise. The TV transfer function of (2.1), $H(n,z)$, and the TF model function of the random process $x(n)$, $S(n,\mathfrak{f})$, can be derived from the coefficients of the model as:

$$H(n,z) = \frac{\sum_{k=0}^{\tilde{q}} b_k(n)z^{-k}}{1 + \sum_{k=1}^{\tilde{p}} a_k(n)z^{-k}} = \frac{\prod_{k=1}^{\tilde{q}}\left(z - z_k(n)\right)}{\prod_{k=1}^{\tilde{p}}\left(z - p_k(n)\right)} b_0(n) z^{(\tilde{p}-\tilde{q})} \tag{2.2}$$

$$S(n,\mathfrak{f}) = |H(n,\mathfrak{f})|^2 = \left[\frac{b_0^2(n)\prod_{k=1}^{\tilde{q}}|z - z_k(n)|^2}{\prod_{k=1}^{\tilde{p}}|z - p_k(n)|^2}\right]_{z=e^{j2\pi\mathfrak{f}}} \tag{2.3}$$

where $\mathfrak{f} \in [-0.5, 0.5]$ is the normalized frequency; $z_k(n) = |z_k(n)|e^{j\angle z_k(n)}$ and $p_k(n) = |p_k(n)|e^{j\angle p_k(n)}$ are the zeros and poles of $H(n,z)$, whose magnitude and phase are denoted as $|\cdot|$ and $\angle\cdot$, respectively. Poles and zeros are numbered in increasing order according to their phase (i.e., as $0, ..., \angle p_1(n), \angle p_2(n), ..., 2\pi$).

When a complex pole is sufficiently close to the unit circle and far from other poles, its power is given by the pole residue [134, 33]:

$$P_i(n) = \Re\left[\frac{\prod_{k=1}^{\tilde{q}}\left(p_i(n) - z_k(n)\right)\prod_{k=1}^{\tilde{q}}\left(p_i^{-1}(n) - z_k^*(n)\right)b_0^2(n)}{p_i(n)\left(p_i^{-1}(n) - p_i^*(n)\right)\prod_{\substack{k=1 \\ k \neq i}}^{\tilde{p}}\left(p_i - p_k(n)\right)\left(p_i^{-1}(n) - p_k^*(n)\right)}\right] \tag{2.4}$$

Given a predetermined $S(n,\mathfrak{f})$, one of the goal of this chapter is to obtain simple closed-form expressions that allow to estimate the polar configuration of the corresponding transfer function $H(n,z)$. The rational for searching these closed-form expressions is to easily design any suitable spectral pattern for the stochastic processes being used in simulation studies.

The simulation process involves three steps: (a) Choice of the desired TF structure of signal $x(n)$, which is defined by a set of design parameters; (b) Estimation of the corresponding $H(n,z)$ and (c) Synthesis of the desired signals, by regressing the model coefficients with the white noise $\xi(n)$ as in (2.1).

Two general frameworks, which differ in the choice of the parameters that characterize the TF structure of the signals, are proposed. The first framework (I-FS) is proposed

to reproduce signals characterized by a desired TF model function $S(n, \mathfrak{f})$, while the second one (II-FP) is proposed to generate signals characterized by predetermined instantaneous frequencies and powers. Since in TF analysis HRV usually presents at least two well defined spectral peaks, corresponding to the LF and HF components, we only considered zero-pole configurations yielding $S(n, \mathfrak{f})$ with two well resolved narrow-band spectral peaks.

2.2.2 Framework I-FS

In framework I-FS, TV-ARMA models are used to reproduce a predetermined TF model function $S(n, \mathfrak{f})$ composed by spectral peaks of instantaneous amplitude $S(n, \mathfrak{f}_i(n))$ and normalized frequency $\mathfrak{f}_i(n)$, with $i \in \{1, \ldots, \tilde{p}\}$. The desired shape of $S(n, \mathfrak{f})$ is approximated by $\mathfrak{f}_i(n)$, $S(n, \mathfrak{f}_i(n))$ and by appropriately positioning the zeros $z_k(n)$ in the polar plane (see §2.2.4 for details). To estimate $H(n, z)$, (2.3) should be solved with respect to $p_k(n)$. This is done by considering that the amplitude of a spectral peak centered on $\mathfrak{f}_i(n)$ is:

$$S(n, \mathfrak{f}_i(n)) = \left[\frac{\prod_{k=1}^{\tilde{q}} |z - z_k(n)|^2}{\prod_{k=1}^{\tilde{p}} |z - p_k(n)|^2} b_0^2(n) \right]_{z = e^{j2\pi \mathfrak{f}_i(n)}} \quad (2.5)$$

where $|z - p_k(n)|$ represents the distance between the point $z = e^{j2\pi \mathfrak{f}_i(n)}$, located on the unit circle at phase $2\pi \mathfrak{f}_i(n)$, and the pole $p_k(n)$. Every pole is assumed to correspond to a spectral peak. Given that $z_k(n)$ are design parameters, the numerator of (2.5) is a known quantity $N_i(n)$, while the terms in the denominator are estimated by means of the cosine formula:

$$\left| e^{j2\pi \mathfrak{f}_i(n)} - p_k(n) \right|^2 = |p_k(n)|^2 + A_{i,k}(n)|p_k(n)| + 1 \quad (2.6)$$

$$A_{i,k}(n) = -2\cos\big(2\pi \mathfrak{f}_i(n) - \angle p_k(n)\big); \quad i, k \in \{1, \ldots, \tilde{p}\} \quad (2.7)$$

Inserting (2.6) in (2.5), we obtain a set of equations $\mathbb{E}_i$:

$$\mathbb{E}_i : \prod_{k=1}^{\tilde{p}} \left(|p_k(n)|^2 + A_{i,k}(n)|p_k(n)| + 1 \right) = \frac{N_i(n)}{S(n, \mathfrak{f}_i(n))} b_0^2(n), \quad (2.8)$$

with $i \in \{1, \ldots, \tilde{p}\}$. The solution of the system (2.8) provides the value of the parameters $|p_k(n)|$ and $b_0(n)$ which define the pole configuration of $H(n, z)$ and consequently the coefficients $a_k(n)$ and $b_k(n)$.

To model the HRV, which in short-term analysis is characterized by the simultaneous presence of two main spectral components, four poles are used ($\tilde{p} = 4$). In Fig. 2.1, the graphic representation of (2.5) for a model of order $(\tilde{p}, \tilde{q}) = (4, 2)$ evaluated at $\mathfrak{f}_i(n_0) = \mathfrak{f}_{\mathrm{LF}}(n_0)$ is shown. Black and gray arrows represent the factors that appear in the denominator and in the numerator of (2.5), respectively. The model includes two complex conjugate poles associated to the LF component, namely $p_{\mathrm{LF}}(n) = p_1(n) = p_4^*(n)$, and two complex conjugate poles associated to the HF component, namely $p_{\mathrm{HF}}(n) = p_2(n) = p_3^*(n)$. Thus, in this example $z_1(n)$ and $z_2(n)$ are placed on the unit circle and constrain the spectrum to vanish at frequency $\pm \frac{1}{2\pi} \angle z_1(n)$. The
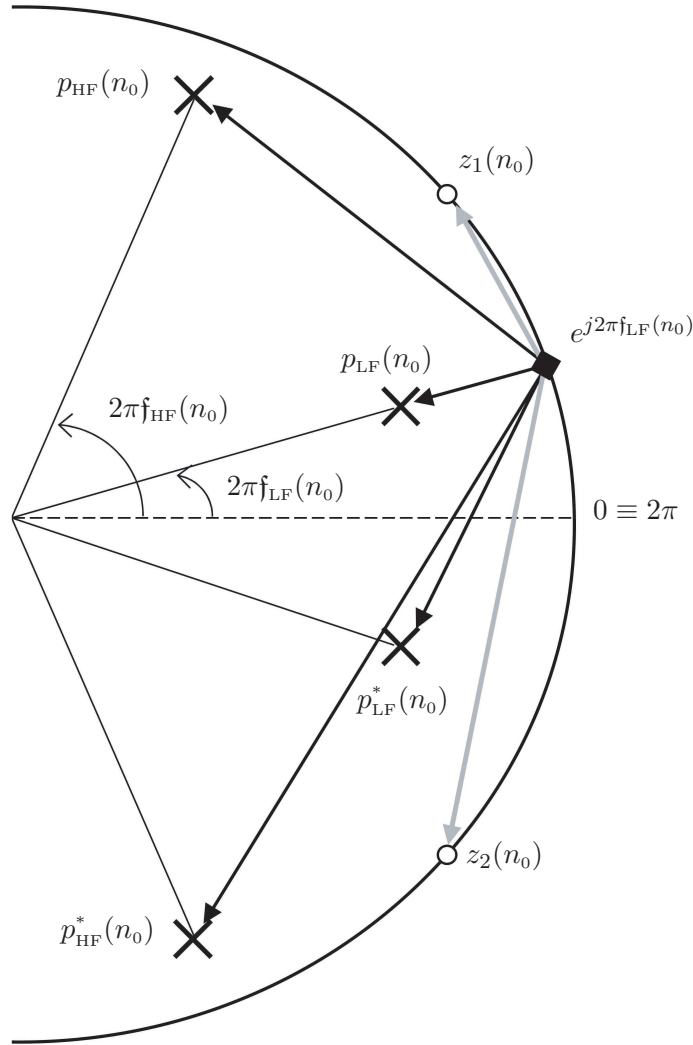
Figure 2.1: Configuration of a TV-ARMA model of order (4,2) for a given time instant $n = n_0$. Crosses and circles represent poles and zeros, respectively, while black and gray arrows correspond to the term in the denominator and numerator of (2.5), respectively.

design parameters are: $\mathfrak{f}_{\text{LF}}(n)$, $\mathfrak{f}_{\text{HF}}(n)$, $S(n, \mathfrak{f}_{\text{LF}}(n))$, $S(n, \mathfrak{f}_{\text{HF}}(n))$ and $z_k(n)$, while the unknown quantities are $|p_k(n)|$ and $b_0(n)$. After rearrangement, system (2.8) can be written:

$$
\begin{cases}
\dfrac{\prod_{k=1}^{4} \left(|p_k(n)|^2 + A_{\text{LF,k}}(n)|p_k(n)| + 1 \right)}{\prod_{k=1}^{4} \left(|p_k(n)|^2 + A_{\text{HF,k}}(n)p_k(n) + 1 \right)} = \dfrac{N_{\text{LF}}(n)S(n, \mathfrak{f}_{\text{HF}}(n))}{N_{\text{HF}}(n)S(n, \mathfrak{f}_{\text{LF}}(n))} \\[4mm]
b_0^2(n) = \dfrac{S(n, \mathfrak{f}_{\text{HF}}(n))}{N_{\text{HF}}(n)} \prod_{k=1}^{4} \left(|p_k(n)|^2 + A_{\text{HF,k}}(n)|p_k(n)| + 1 \right)
\end{cases}
\tag{2.9}
$$

A restriction should be introduced to match the number of equations with the number of unknowns. To this end, the magnitude of two complex conjugate poles is fixed to a constant value. As shown in the following, this restriction gives the possibility to further increase the control of $S(n, \mathfrak{f})$. Fixing the magnitude of the LF poles to a constant value $|p_1(n)| = |p_4(n)| = |p_{\text{LF}}|$ the first equation of system (2.9) takes the closed-form of a quartic equation:

$$
|p_{\text{HF}}(n)|^4 + C_1(n)|p_{\text{HF}}(n)|^3 + C_2(n)|p_{\text{HF}}(n)|^2 + C_1(n)|p_{\text{HF}}(n)| + 1 = 0
\tag{2.10}
$$

where:

$$
C_1(n) = \frac{(A_{\text{LF},2}(n) + A_{\text{LF},3}(n)) - \alpha(n)(A_{\text{HF},2}(n) + A_{\text{HF},3}(n))}{1 - \alpha(n)}
\tag{2.11}
$$

$$
C_2(n) = \frac{(2 + A_{\text{LF},2}(n)A_{\text{LF},3}(n)) - \alpha(n)(2 + A_{\text{HF},2}(n)A_{\text{HF},3}(n))}{1 - \alpha(n)}
\tag{2.12}
$$

$$
\alpha(n) = \frac{S(n, \mathfrak{f}_{\text{HF}}(n))N_{\text{LF}}(n) \prod_{k=\{1,4\}}(|p_{\text{LF}}|^2 + A_{\text{HF,k}}(n)|p_{\text{LF}}| + 1)}{S(n, \mathfrak{f}_{\text{LF}}(n))N_{\text{HF}}(n) \prod_{k=\{1,4\}}(|p_{\text{LF}}|^2 + A_{\text{LF,k}}(n)|p_{\text{LF}}| + 1)}
\tag{2.13}
$$

Properties of equation (2.10) are studied in the following.
Once that the magnitude of the HF poles, $|p_{\text{HF}}(n)|$, has been estimated from (2.10), the parameter $b_0(n)$ is obtained by replacing $|p_{\text{HF}}(n)|$ in the second equation of (2.9). In the case in which the magnitude of the HF poles $|p_2(n)| = |p_3(n)| = |p_{\text{HF}}|$ was used as design parameter, $|p_1(n)| = |p_4(n)|$ would be obtained using (2.10)–(2.13) and replacing $A_{\text{i},2}$ with $A_{\text{i},1}$, and $A_{\text{i},3}$ with $A_{\text{i},4}$, with $i \in \{\text{LF,HF}\}$, respectively.

Solutions of equation (2.10):
By omitting the temporal index and by replacing $y = |p_{\text{HF}}|$, eq. (2.10) reads as:

$$
y^4 + C_1 y^3 + C_2 y^2 + C_1 y + 1 = 0
\tag{2.14}
$$

where parameters C_1 and C_2 are defined in (2.11)-(2.12).
Equation (2.10) is a quasi-symmetric quartic equation, and it can be solved by following a procedure which consists of:
Divide (2.14) by y^2:

$$
\left(y^2 + \frac{1}{y^2} \right) + C_1 \left(y + \frac{1}{y} \right) + C_2 = 0
\tag{2.15}
$$

Use the variable change $s = y + \frac{1}{y}$ to obtain:

$$s^2 + C_1 s + C_2 - 2 = 0 \tag{2.16}$$

whose roots are:

$$s_{1,2} = \frac{\left[-C_1 \pm \sqrt{C_1^2 - 4(C_2 - 2)} \right]}{2(C_2 - 2)}; \quad \text{with } s_1 < s_2 \tag{2.17}$$

The four roots of (2.14) are then given solving:

$$y^2 - sy + 1 = 0 \tag{2.18}$$

$$y_{1,2} = \frac{1}{2} \left(s_1 \pm \sqrt{s_1^2 - 4} \right) \tag{2.19}$$

$$y_{3,4} = \frac{1}{2} \left(s_2 \pm \sqrt{s_2^2 - 4} \right) \tag{2.20}$$

From (2.19)–(2.20) follows that $y_1 y_2 = y_3 y_4 = 1$, which implies that if $|y_1| > 1$, $0 < |y_2| < 1$.

Three situations may occur:

- a) All $y \in \mathbb{C}$.

  In this case no real solution exist and no pole-zero configuration can be found to reproduce the desired spectral properties. Equation (2.14) do not have real solutions for:

  $$(s_2^2 - 4) = \left[\frac{1}{2} \left(-C_1 + \sqrt{C_1^2 - 4(C_2 - 2)} \right) \right]^2 - 4 < 0 \tag{2.21}$$

  Nevertheless, a real solution for (2.14) can still be found by changing z_k and $|p_{\mathrm{LF}}|$.

- b) $y_1 = \frac{1}{y_2} \in \mathbb{C}$ and $y_3 = \frac{1}{y_4} \in \mathbb{R}_+$.

  In this case (2.14) has 2 equivalent solutions. We will use $y = |p_{\mathrm{HF}}| < 1$. Case (b) occurs when:

  $$\begin{cases} (s_1^2 - 4) = \left[\frac{1}{2} \left(-C_1 - \sqrt{C_1^2 - 4(C_2 - 2)} \right) \right]^2 - 4 < 0 \\ (s_2^2 - 4) = \left[\frac{1}{2} \left(-C_1 + \sqrt{C_1^2 - 4(C_2 - 2)} \right) \right]^2 - 4 > 0 \end{cases} \tag{2.22}$$

- c) $y_1, y_2, y_3, y_4 \in \mathbb{R}$.

  This is the case in which (2.14) has 4 equivalent real solutions. We will use the solution which satisfies $y \in [0, 1]$. In the case in which this condition is satisfied by 2 roots, we will choose the higher one. Case (c) occurs when:

  $$(s_1^2 - 4) = \left[\frac{1}{2} \left(-C_1 - \sqrt{C_1^2 - 4(C_2 - 2)} \right) \right]^2 - 4 > 0 \tag{2.23}$$

41

2.2.3 Framework II-FP

In this framework, the TF structure of the signals is predetermined by fixing instantaneous frequencies $\mathfrak{f}_i(n)$ and powers $P_i(n)$, rather than $\mathfrak{f}_i(n)$ and $S(n, \mathfrak{f}_i(n))$, as in I-FS. The pole-zero configuration associated to $\mathfrak{f}_i(n)$ and $P_i(n)$ can be estimated by using the formula of the pole residue given in (2.4). At every time instant n, the power associated to the pole $p_i(n)$ depends on the whole pole-zero configuration, i.e. on the whole set of complex numbers $p_i(n) - p_k(n)$, $p_i^{-1}(n) - p_k^*(n)$, $p_i(n) - z_k(n)$ and $p_i^{-1}(n) - z_k^*(n)$, and the explicit form of (2.4) is highly non-linear in $|p_i(n)|e^{i\angle p_i(n)}$. Nevertheless, as shown in [134], under certain conditions described in the following, the residue formula (2.4) can be approximated as:

$$P_i(n) \approx \frac{b_0^2(n)}{\left(|p_i(n)| - \frac{1}{|p_i(n)|}\right) \prod_{\substack{k=1 \\ k\neq i}}^{\tilde{p}} |p_i(n) - p_k(n)|^2}; \quad i = \{1, \ldots, \tilde{p}\}; \tag{2.24}$$

To obtain this expression from (2.4) one should: (i) reduce the ARMA model to an AR one: if zeros $z_k(n)$ are not considered the numerator of (2.4) is just $b_0^2(n)$; (ii) assume that poles are placed very close to the unit circle $(1 - |p_i(n)| << 1)$, so that $p_i^{-1}(n) \approx p_i^*(n)$. This allows to approximate the factors in the denominator of (2.4) as:

$$\left(p_i(n) - p_k(n)\right)\left(p_i^{-1}(n) - p_k^*(n)\right) \approx |p_i(n) - p_k(n)|^2; \tag{2.25}$$

$$p_i(n)\left(p_i(n)^{-1} - p_i^*(n)\right) = |p_i(n)|\left(1/|p_i(n)| - |p_i(n)|\right) \approx \left(1/|p_i(n)| - |p_i(n)|\right) \tag{2.26}$$

To generate signals with a LF and HF components, the order of the model is $\tilde{p} = 4$. In this case (2.24) represents a system of 2 equations in $|p_{\text{LF}}(n)|$, $|p_{\text{HF}}(n)|$ and $|b_0(n)|$:

$$\begin{cases} P_{\text{LF}}(n) = \dfrac{b_0^2(n)\sigma^2}{\left|p_{\text{LF}}(n) - p_{\text{HF}}(n)\right|^2\left|p_{\text{LF}}(n) - p_{\text{HF}}^*(n)\right|^2} \times \\ \qquad\qquad \times \dfrac{1}{\left|p_{\text{LF}}(n) - p_{\text{LF}}^*(n)\right|^2\left(1/|p_{\text{LF}}(n)| - |p_{\text{LF}}(n)|\right)} \\ P_{\text{HF}}(n) = \dfrac{b_0^2(n)\sigma^2}{\left|p_{\text{HF}}(n) - p_{\text{LF}}(n)\right|^2\left|p_{\text{HF}}(n) - p_{\text{HF}}^*(n)\right|^2} \times \\ \qquad\qquad \times \dfrac{1}{\left|p_{\text{HF}}(n) - p_{\text{LF}}^*(n)\right|^2\left(1/|p_{\text{HF}}(n)| - |p_{\text{HF}}(n)|\right)} \end{cases} \tag{2.27}$$

Dividing $P_{\text{LF}}(n)$ by $P_{\text{HF}}(n)$ we get:

$$\frac{P_{\text{LF}}(n)}{P_{\text{HF}}(n)} = \frac{|p_{\text{HF}}(n) - p_{\text{HF}}^*(n)|^2(1/|p_{\text{HF}}(n)| - |p_{\text{HF}}(n)|)}{|p_{\text{LF}}(n) - p_{\text{LF}}^*(n)|^2(1/|p_{\text{LF}}(n)| - |p_{\text{LF}}(n)|)} \tag{2.28}$$

and rearranging:

$$\frac{P_{\text{LF}}(n)}{P_{\text{HF}}(n)}\left(\left|p_{\text{LF}}(n) - p_{\text{LF}}^*(n)\right|^2\left(1/|p_{\text{LF}}(n)| - |p_{\text{LF}}(n)|\right)\right) = \tag{2.29}$$

$$= \left|p_{\text{HF}}(n) - p_{\text{HF}}^*(n)\right|^2\left(1/|p_{\text{HF}}(n)| - |p_{\text{HF}}(n)|\right)$$

By using the cosine formula:

$$\left|p_{\text{LF}}(n) - p_{\text{LF}}^*(n)\right|^2 = \left[2|p_{\text{LF}}(n)|\sin(\angle p_{\text{LF}}(n))\right]^2 = \left[2|p_{\text{LF}}(n)|\sin(2\pi\mathfrak{f}_{\text{LF}}(n))\right]^2 \tag{2.30}$$

$$\left|p_{\text{HF}}(n) - p_{\text{HF}}^*(n)\right|^2 = \left[2|p_{\text{HF}}(n)|\sin(\angle p_{\text{HF}}(n))\right]^2 = \left[2|p_{\text{HF}}(n)|\sin(2\pi\mathfrak{f}_{\text{HF}}(n))\right]^2 \tag{2.31}$$

it is possible to rewrite (2.29) as:

$$\frac{P_{\mathrm{LF}}(n)}{P_{\mathrm{HF}}(n)}\sin^2(\angle\ p_{\mathrm{LF}}(n))\big(|p_{\mathrm{LF}}(n)| - |p_{\mathrm{LF}}(n)|^3\big) - \sin^2(\angle p_{\mathrm{LF}}(n))\big(|p_{\mathrm{HF}}(n)| - |p_{\mathrm{HF}}(n)|^3\big) = 0;$$
$$(2.32)$$

Finally, by fixing the magnitude of one of the two couple of complex conjugate poles, which are used as design parameters, it is then possible to find the magnitude of the other couple of complex conjugate poles. For example, if $|p_{\mathrm{LF}}(n)| = |p_{\mathrm{LF}}|$, $|p_{\mathrm{HF}}(n)|$ is find by solving the following incomplete cubic equation:

$$|p_{\mathrm{HF}}(n)|^3 - |p_{\mathrm{HF}}(n)| + C(n) = 0; \qquad (2.33)$$

where

$$
\begin{aligned}
C(n) &= \frac{P_{\mathrm{LF}}(n)}{P_{\mathrm{HF}}(n)}\left(\frac{\sin(\angle p_{\mathrm{LF}}(n))}{\sin(\angle p_{\mathrm{HF}}(n))}\right)^2 (|p_{\mathrm{LF}}| - |p_{\mathrm{LF}}|^3) = \qquad (2.34)\\
&= \frac{P_{\mathrm{LF}}(n)}{P_{\mathrm{HF}}(n)}\left(\frac{\sin(2\pi\mathfrak{f}_{\mathrm{LF}}(n))}{\sin(2\pi\mathfrak{f}_{\mathrm{HF}}(n))}\right)^2 (|p_{\mathrm{LF}}| - |p_{\mathrm{LF}}|^3)
\end{aligned}
$$

The incomplete cubic equation (2.33) has a solution with physiological meaning for those n for which $C(n) \in (-2/\sqrt{27}, 2/\sqrt{27})$.

In the case in which $|p_2(n)| = |p_3(n)| = |p_{\mathrm{HF}}|$ was used as design parameter, $|p_1(n)| = |p_4(n)| = |p_{\mathrm{LF}}(n)|$ would be obtained using (2.33)–(2.34) and replacing subscript LF with HF and subscript HF with LF.

2.2.4 Design parameters

The design parameters necessary to define the desired TF structure of the signals are:

- In I-FS framework : $\mathfrak{f}_i(n)$, $S(n, \mathfrak{f}_i(n))$ and $z_k(n)$;
- In II-FS framework: $\mathfrak{f}_i(n)$, $P_i(n)$.

with $i = \{LF, HF\}$. In both cases, the magnitude of one of the two complex-conjugate poles is fixed and the other one is estimated. The positioning of the poles used as design parameters can be used to improve the control of the shape of the model function $S(n, \mathfrak{f})$: by moving the poles closer to the unit circle the spectral peaks get sharper and their bandwidth is reduced.

In the case of framework I-FS, zeros are used to predetermine desirable spectral features. As shown in Fig. 2.2, they can be used to control the degree of overlapping of the spectral peaks. In these graphics, the model functions shown on the same line (on the left and on the right side of the graphic) share the same peak frequency $\mathfrak{f}_i(n_0)$, and peak amplitude $S(n_0, \mathfrak{f}_i(n_0))$ as well as the magnitude of the poles used as design parameters. Those on the left are obtained by means of AR models, while those on the right by means of an ARMA model of order (4,10). In these graphics, circles represent the frequency associated to the phase of zeros $z_k(n_0)$, with $k = \{1, 2, 3\}$. It is shown that without changing the magnitude of the pole used as design parameter, and by moving $z_k(n)$ closer to the unit circle, $S(n_0, \mathfrak{f})$ takes lower values at frequency $\frac{1}{2\pi}\angle z_k(n)$ and the spectral peaks are better resolved.
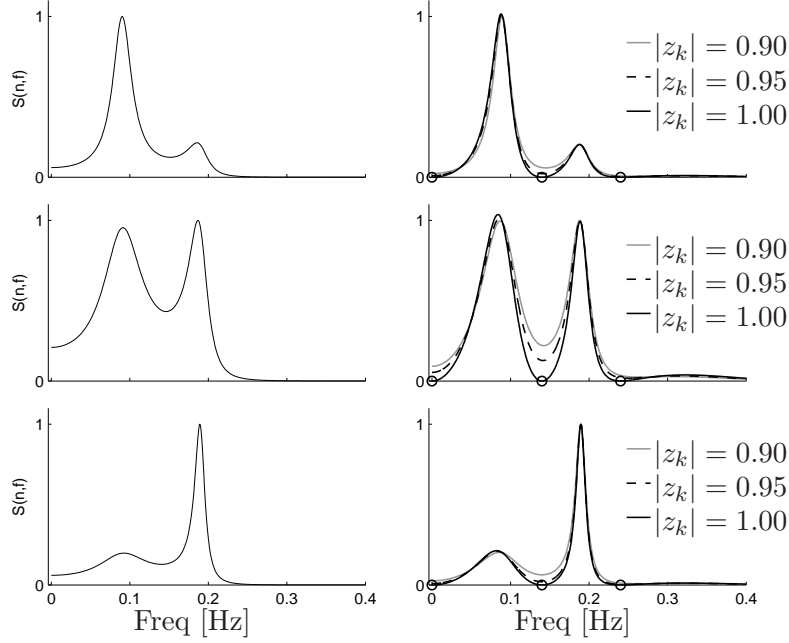
Figure 2.2: Influence of $z_k(n)$ on the model function. $S(n_0, \mathfrak{f})$ are modeled by means of AR models (left) and ARMA models of order (4,10) (right). In the right-side panels, circles represent the phase of $z_k(n_0)$, with k={1, 2, 3}. The magnitude of the zeros $|z_k(n_0)|$ is reported in the legend. Zeros $z_k(n_0)$, with $k > 3$, are associated to a frequency $f > 0.4$ Hz and are not shown.

2.2.5   Measures for the evaluation of the models

Due to the stochastic nature of the signals and to the limited number of realizations of the model, the estimated TF distribution of the stochastic process, obtained by averaging among realizations, is always characterized by an estimation error. always presents a fluctuation around $S(n, \mathfrak{f})$. This fluctuation represents a sort of intrinsic uncertainty of the simulated signals and is quantified by means of two measures.

The first one is a spectral distance, defined as the normalized L1–norm of the difference between $S(n, \mathfrak{f})$ and the estimated TF distribution of the stochastic process $\overline{W}_x(n, \mathfrak{f})$:

$$d_{\mathrm{w}} = \frac{||\overline{W}_x(n, \mathfrak{f}) - S(n, \mathfrak{f})||_{l_1}}{||S(n, \mathfrak{f})||_{l_1}} \tag{2.35}$$

$$\overline{W}_x(n, \mathfrak{f}) = \frac{1}{R} \sum_{r=1}^{R} W_x(n, \mathfrak{f}; r) \tag{2.36}$$

where $W_x(n, \mathfrak{f}; r)$ is the Wigner-Ville distribution (see §3.1) of one realization of the processa $x(n; r)$ [175, 92]. Distance d_{w} is specially sensitive to the correct TF localization of the spectral components.

The second measure is obtained by comparing the total power $P_{\mathrm{TOT}}(n)$, obtained by integrating $S(n, \mathfrak{f})$ with respect to $\mathfrak{f}$, with the instantaneous powers of the simulated

signals:

$$e(n) = \frac{\frac{1}{R}\sum_{r=1}^{R} x^2(n;r) - P_{\mathrm{TOT}}(n)}{P_{\mathrm{TOT}}(n)} \tag{2.37}$$

The temporal mean and standard deviation of $e(n)$, denoted as μ_e and σ_e, is used to assess the capability of the model to generate signals characterized by the desired instantaneous power.

For a given number of realizations R, measures d_{W} and $e(n)$ depend on the pole-zero configuration given by $p_k(n)$, $z_k(n)$, $b_0(n)$ and will be used in the following sections to assess the effect of the design parameters as well as to compare the frameworks.

2.3 Applications & Validations

In this section, the dynamics observed in HRV during exercise stress testing (EST) and experiments of music-induced emotions (MIE) are modeled. In both situations, the evaluation of frameworks I-FS and II-FP is done as follow:

(i) Framework I-FS is used: signals are modeled by fixing $\mathfrak{f}_i(n)$, $S(n, \mathfrak{f}_i(n))$ and by choosing $z_k(n)$ and $|p_{\mathrm{LF}}|$ as to obtain the desired model function $S(n, \mathfrak{f})$, which will be used in the evaluation;

(ii) The instantaneous power of LF and HF components, $P_{\mathrm{LF}}(n)$ and $P_{\mathrm{HF}}(n)$, are estimated from this model function;

(iii) They are used as design parameters of framework II-FP, whose model function will be estimated and used to assess the uncertainty of the simulated signals generated by framework II-FP.

The TF structure of the simulated signals is shown in Fig. 2.3-2.4, where $f_i(n) = \mathfrak{f}_i(n)f_s$, being f_s the sampling rate. In both cases, signals are characterized by epochs of mild and abrupt variations (indicated as T_1 and T_2, respectively), which correspond to different degrees of non-stationarity. The degree of non-stationarity, reported in Table 2.1, is quantified by:

$$\bar{F}'_i = \frac{f_s}{N_{\mathrm{T}}} \sum_{n=n_b}^{n_b+N_{\mathrm{T}}-1} |f_i(n) - f_i(n-1)|, \ [\mathrm{Hz\ s^{-1}}] \tag{2.38}$$

$$\bar{S}'_i = \frac{f_s}{N_{\mathrm{T}}} \sum_{n=n_b}^{n_b+N_{\mathrm{T}}-1} \frac{|S(n, \mathfrak{f}_i(n)) - S(n-1, \mathfrak{f}_i(n-1))|}{S(n_0, \mathfrak{f}_i(n_0))}, \ [\% \ \mathrm{s^{-1}}] \tag{2.39}$$

where N_{T} is the number of time samples of intervals T_1 or T_2, n_b is the first time sample of each interval, $i \in \{\mathrm{LF, HF}\}$ and $n_0 = 1$.

2.3.1 Exercise stress testing (EST)

As shown in Fig. 2.3, in this simulation, HRV spectral components are assumed to vary linearly [19]. The central frequency of the LF spectral component, $f_{\mathrm{LF}}(n)$, is constant over time, while $f_{\mathrm{HF}}(n)$ increases and decreases during effort (T_1) and recovery (T_2),

Table 2.1: Simulation setup

Parameters of I-FS framework				
	EST		MIE	
	T_1	T_2	T_1	T_2
Length [s]	360	150	38	42
$\bar{F}'_{\mathrm{LF}}$ [mHz s^{-1}]	0	0	0.9	1.6
$\bar{F}'_{\mathrm{HF}}$ [mHz s^{-1}]	1.1	2.2	0.3	3.2
$\bar{S}'_{\mathrm{LF}}$ [% s^{-1}]	0.14	0.28	1.14	2.3
$\bar{S}'_{\mathrm{HF}}$ [% s^{-1}]	0.25	0.28	0.8	1.4

respectively. The changes in the amplitude $S(n, \mathfrak{f}_{\mathrm{HF}}(n))$ simulates the withdrawal of the parasympathetic modulation (-70% in the first 3 min) and the restoration of baseline values during recovery (+50% in 3 min). From 3 min before the peak stress until reaching it, $S(n, \mathfrak{f}_{\mathrm{HF}}(n))$ slightly increases, simulating the effect of the stretch of the sinus node due to respiration [44, 19]. The order of the model used in this application was $(\tilde{p}, \tilde{q}) = (4, 8)$, while the design parameter $|p_{\mathrm{LF}}|$ varied in $\{0.880, 0.885, ..., 0.980\}$. Zeros are placed on the unit circle and have TV phase. The configuration of the poles and zeros at time $n_0 = 0$ is given in Fig. 2.5. In this graphic, it is shown that $z_1(n)$, fixed at DC, cancels the contribution around 0 Hz, which in TF analysis is usually filtered out; $z_2(n) = z_8^*(n)$, with phase $\pi(\mathfrak{f}_{\mathrm{LF}}(n) + \mathfrak{f}_{\mathrm{HF}}(n))$, lies in between LF and HF poles, to separate the spectral peaks, which otherwise would overlap; $z_3(n) = z_7^*(n)$, with phase $\pi(3\mathfrak{f}_{\mathrm{HF}}(n) - \mathfrak{f}_{\mathrm{LF}}(n))$, is symmetric to $z_2(n)$ with respect to $\mathfrak{f}_{\mathrm{HF}}(n)$ and makes the HF peak symmetric; zero $z_4(n) = z_6^*(n)$, with phase $\frac{\pi}{2}(3\mathfrak{f}_{\mathrm{HF}}(n) - \mathfrak{f}_{\mathrm{LF}}(n) + 1)$ and $z_5(n) = \pi$, cancel undesired contributions introduced by the other ones in $f > \mathfrak{f}_{\mathrm{HF}}(n)$.

2.3.2 Experiments of music-induced emotions (MIE)

Parameters $f_i(n)$ and $S(n, \mathfrak{f}_i(n))$ were derived from the time-course of the LF and HF components of an original HRV signal recorded during an experiment of music-induced emotions [201]. In that experiment, participants listened to different kinds of musical stimuli, each one of a duration of about 90 s, and characterized by different emotional valence. The pattern of response of HRV, shown in Fig. 2.4, is characterized by two phases: an early fast epoch in which abrupt changes occur (T_2), and a later epoch of adaptation in which spectral parameters changed gradually (T_1). The time-course of spectral indices of Fig. 2.4 is derived by low-pass filtering the time-course of the parameters obtained by TF analysis of the HRV of a subject listening to an excerpt of pleasant music [201]. As also reported in Table 2.1, changes in T_2 are particularly abrupt: $S(n, \mathfrak{f}_{\mathrm{LF}}(n))$ and $S(n, \mathfrak{f}_{\mathrm{HF}}(n))$ decreases by about 70% and 40% in the first 13 s. The order of the model used to simulate these variations was $(\tilde{p}, \tilde{q}) = (4, 10)$, while the design parameter $|p_{\mathrm{LF}}|$ varied in $\{0.880, 0.885, ..., 0.980\}$. Zeros are placed on the unit circle and have TV phase. Zeros $z_1(n)$, $z_2(n) = z_{10}^*(n)$ and $z_3(n) = z_9^*(n)$ are located as in simulation EST (see also Fig. 2.5), while, in order to cancel contributions
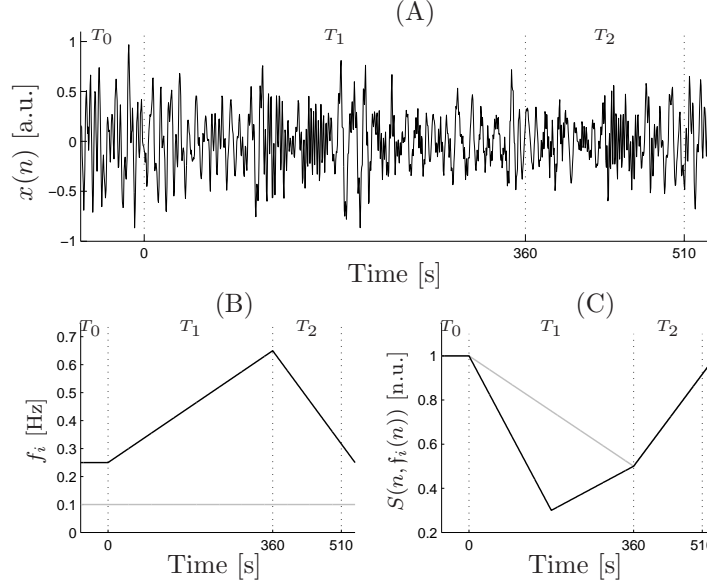
Figure 2.3: HRV during: Exercise stress testing (EST). (A) A simulated HRV signal $x(n)$; (B) Instantaneous frequency and (C) spectral amplitude of the LF (in gray) and HF (in black) components. T_0, T_1 and T_2 represent epochs of stationarity, slow and fast variations, respectively. Note that temporal axes are different from Fig. 2.4.

in $f > \mathfrak{f}_{\mathrm{HF}}(n)$, $z_4(n) = z_8^*(n)$, $z_5(n) = z_7^*(n)$ and $z_6(n)$ are evenly distributed between $z_3(n)$ and π, i.e. with phases equal to $\frac{\pi}{3}(6\mathfrak{f}_{\mathrm{HF}}(n) - 2\mathfrak{f}_{\mathrm{LF}}(n) + 1)$, $\frac{\pi}{3}(3\mathfrak{f}_{\mathrm{HF}}(n) - \mathfrak{f}_{\mathrm{LF}}(n) + 2)$ and π, respectively.

2.3.3 Evaluation of the models

In Figure 2.6, the intrinsic uncertainty of signals obtained by means of frameworks I-FS and II-FP is shown for both simulations EST and MIE. The uncertainty was assessed by measures d_{W} and $e(n)$, estimated from (2.35)–(2.37), where, for each framework, the corresponding model function $S(n, \mathfrak{f})$ was used.

As shown in Fig. 2.6, the intrinsic uncertainty of the simulated signals always decreased with decreasing $|p_{\mathrm{LF}}|$, i.e. the magnitude of the pole used as design parameter. This indicates that signals characterized by wide spectral peaks are generated more reliably than signals characterized by narrow spectral peaks. As a rule of thumb, to minimize the intrinsic uncertainty of the signals, one should give to the poles used as design parameters the lowest magnitude which at the same time allows the generation of a model function that complies with the specifications. This heuristic method was used to select the values of $|p_{\mathrm{LF}}|$ used in simulation EST and MIE. Comparison of results reported in column (A) and (B) of Fig. 2.6 shows that the spectral distance d_{W} as well as the mean and the standard deviation of $e(n)$ were lower for signals obtained by using framework I-FS than II-FP. As shown in Fig. 2.6, by increasing the number of realizations of the model, R, the intrinsic uncertainty decreased. The comparison between $P_{\mathrm{TOT}}(n)$ and the power estimated directly from the signal as in (2.37) is reported in the lower graphic of Fig. 2.6 and shows that the simulated signals
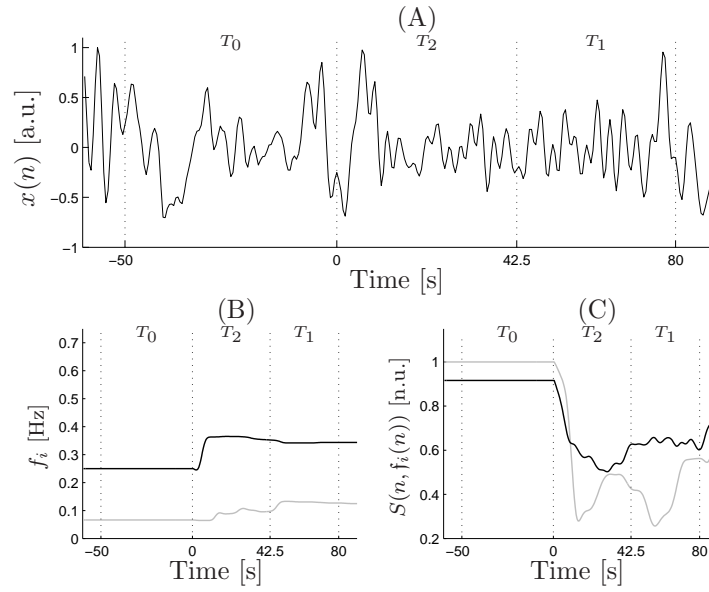
Figure 2.4: Modeling HRV during: Experiment of music-induced emotions (MIE). (A) A simulated HRV signal $x(n)$; (B) Instantaneous frequency and (C) spectral amplitude of the LF (in gray) and HF (in black) components. T_0, T_1 and T_2 represent epochs of stationarity, slow and fast variations. Note that temporal axes are different from Fig. 2.3
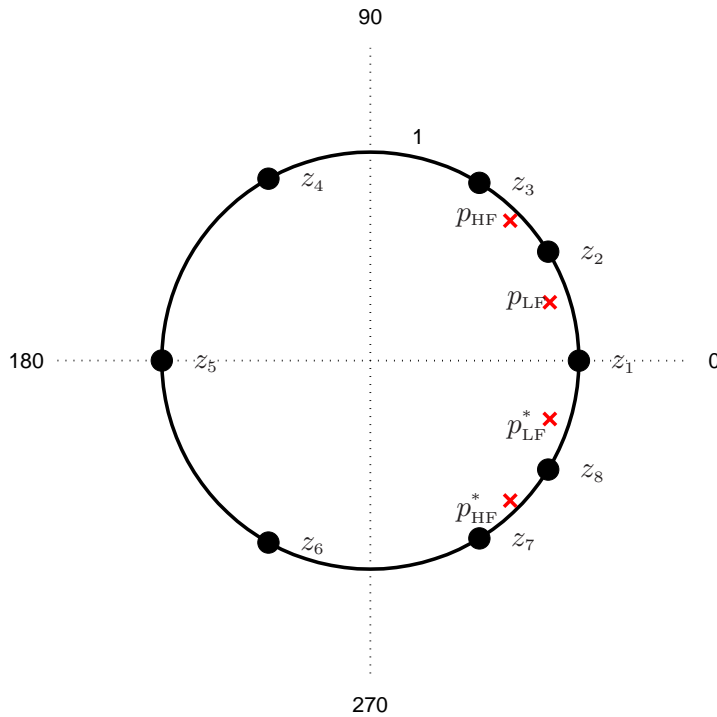
Figure 2.5: Configuration of poles $p_i(n)$ and zeros $z_k(n)$ used in the simulation of exercise stress testing patterns, for $n = 0$. Poles and zeros are represented by $\times$ and $\bullet$, respectively. For details see §2.3.1
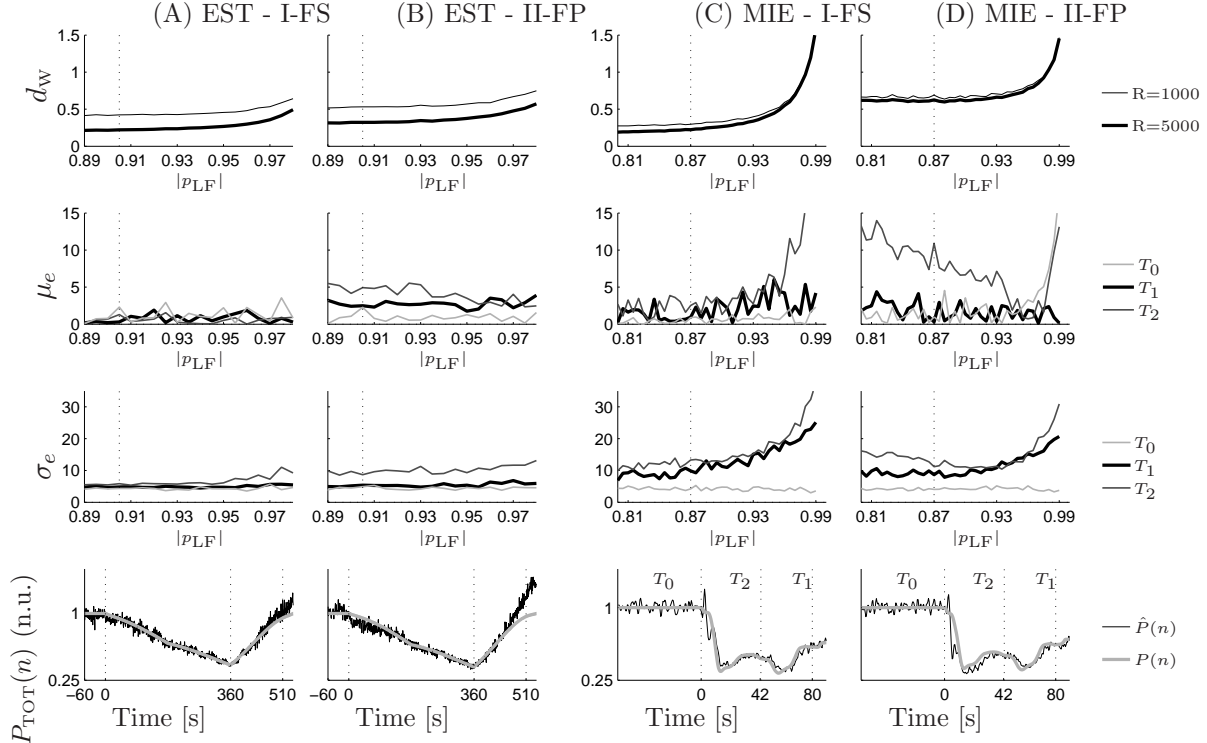
Figure 2.6: Model evaluation: (A)–(B) exercise stress testing; (C)–(D) experiment of music-induced emotions; (A) and (C) I-FS framework; (B) and (D) II-FS framework; The intrinsic uncertainty of the simulated signals is evaluated by means of the spectral distance d_{w} (top graphic) and the mean and the standard deviation of $e(n)$ (second and third lines of graphics). Vertical dotted lines marked the value of the design parameter $|p_{\mathrm{LF}}|$ which will be used in the following chapter to generate signals for the evaluation of the smoothed pseudo Wigner-Ville distribution. Lower graphics: $P_{\mathrm{TOT}}(n)$ estimated from $S(n, \mathfrak{f})$ and power estimated form the signals with $R = 1000$. See §2.2.5 for details.

followed on average the desired dynamics, even in epoch T_2 of simulation MIE, during which the instantaneous power dramatically decreased while $f_{\mathrm{HF}}(n)$ increased almost stepwise.

Assessment of the robustness

To assess whether the presented methodology can reproduce a much wider range of spectral configurations than those considered here, and to assess how the use of zeros affects the intrinsic uncertainty of the models, simulations EST and MIE were modified and different configurations were tested. In the description of the following results, index n is omitted. Spectral parameters were chosen as : f_{LF}=0.09 Hz, $f_{\mathrm{HF}} = \{0.15, 0.16, ..., 0.5\}$ Hz and $\log_{10}\left(S(\mathfrak{f}_{\mathrm{LF}})/S(\mathfrak{f}_{\mathrm{HF}})\right) = \{-2, -1.8, ..., 2\}$. The magnitude of one couple of complex-conjugate poles was fixed at $\{0.850, 0.855, ..., 0.995\}$ and the magnitude of the other poles was estimated by using the closed-form expressions of framework I-FS (2.10). Models with the following configurations were tested: AR model, ARMA (4,8) as in simulation EST, and ARMA (4,10) as in simulation MIE. To accept $|p_{\mathrm{HF}}|$ (or $|p_{\mathrm{LF}}|$) as a possible solution, the corresponding model function should verify the following conditions:

  – Very LF component is low $S(0) \leq 0.15\mathrm{min}[S(\mathfrak{f}_{\mathrm{LF}}), S(\mathfrak{f}_{\mathrm{HF}})]$;
  – LF and HF spectral peaks are well resolved: $S((\mathfrak{f}_{\mathrm{LF}} + \mathfrak{f}_{\mathrm{HF}})/2) \leq 0.25\min\{S(\mathfrak{f}_{\mathrm{LF}}), S(\mathfrak{f}_{\mathrm{HF}})\}$;
  – Components with central frequency higher than HF are low $S(f > \mathfrak{f}_{\mathrm{HF}}) \leq 0.15\min\{S(\mathfrak{f}_{\mathrm{LF}}), S(\mathfrak{f}_{\mathrm{HF}})\}$.

Figure 2.6 shows that, whenever possible, solutions characterized by a polar configuration with poles of low magnitude should be preferred to configurations with poles of high magnitude, since the lower the magnitude of the poles, the better the simulated signals will reproduce the desired spectral patterns. Results reported in Fig. 2.7 give, for the whole set of configurations, the lowest magnitude of the poles used as design parameter for which a suitable solution existed. Results reported on the left (right) correspond to the case in which $|p_{\mathrm{LF}}|$ ($|p_{\mathrm{HF}}|$) was used as design parameter and $|p_{\mathrm{HF}}|$ ($|p_{\mathrm{LF}}|$) was estimated. In the clack regions no suitable solution was found, either because (2.10) had no solution or because $S(n, \mathfrak{f})$ did not complies with the specifications. Figure 2.7 shows that:

 (i) Framework I-FS is robust: the only few cases in which a suitable solution was not found corresponded to extreme configurations for which HRV may be better modeled as monocomponent;
 (ii) For a same configuration, ARMA models allowed to use poles with lower magnitude than AR models, which in turn allows one to generate signals characterized by lower uncertainty;
(iii) Solutions for low f_{HF} are possible only with poles of high magnitude;
(iv) To model HRV signals in which $S(\mathfrak{f}_{\mathrm{LF}})$>>$S(\mathfrak{f}_{\mathrm{HF}})$, it is preferable to use as design parameter $|p_{\mathrm{HF}}|$ and estimate $|p_{\mathrm{LF}}|$, since, as shown in the right-side panels, in this way it is possible to find appropriate polar configurations by using poles with lower magnitude than if $|p_{\mathrm{LF}}|$ was used as design parameter and $|p_{\mathrm{HF}}|$ was estimated (as in the left-side panels).
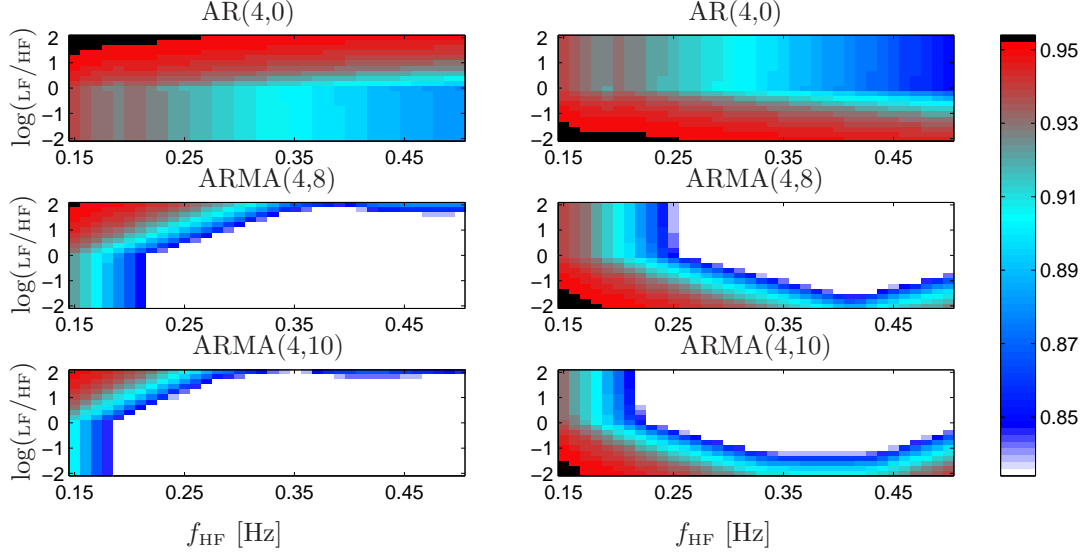
Figure 2.7: Robustness and contribution of z_k for the I-FS framework. The lowest design parameter $|p_{\mathrm{LF}}|$ (on left panels) and the lowest design parameter $|p_{\mathrm{HF}}|$ (on right panels) that allowed to reproduce real-like HRV signals are color coded. Black color means that no suitable solution is available. Upper, middle and lower graphics refer to models of order (4,0), (4,8) and (4,10). In y-label $\log(LF/HF)$ stands for $\log_{10}(S(\mathfrak{f}_{\mathrm{LF}})/S(\mathfrak{f}_{\mathrm{HF}}))$

2.4   Discussion

Applications of TF methods of analysis in biomedical signal processing have increased in the last years [165]. Nevertheless, the problem of how to generate signals with a given TF model function has been less studied. Only a small number of methods for the synthesis of non stationary processes whose TF representation was closest, in a least squares sense, to a given model function $S(n, \mathfrak{f})$ were presented in the literature [52, 126]. The importance of these studies lies in that models that allow to reproduce real-like signals with predetermined TF characteristics can be used to validate and compare different non-stationary signal processing techniques. Another application of the presented framework may concern the generation of controlled TV surrogate data to assess non linearity in non stationary time series or the significance of TV coherence function [261, 86, 89].

In this chapter, two robust and flexible frameworks for generating non-stationary HRV signals following predetermined spectral patterns have been presented. Signals are modeled as time-varying stochastic processes characterized either by spectral components with controlled instantaneous powers and frequencies or by a given time-frequency model function, whose shape can be controlled by tuning several design parameters. Using these methods we were able to simulate stochastic signals whose spectral components changed both linearly and non-linearly during time, with different rates of variation, going from slow variations to sudden and very sharp transitions. We modeled HRV dynamics during exercise stress testing and experiments of music-induced emotions. These frameworks can be used in all those studies which require

the generation of simulated HRV signals. Moreover, even if in this study we only considered HRV dynamics, they could also be used to simulate any of those cardiovascular signals which present at least a LF or a HF component, e.g. arterial pressure variability, pulse transit time, respiratory signal etc.

A traditional approach to generate synthetic signals consists in using a sum of sinusoids with time-varying amplitude and frequency and adding noise. Despite its simplicity, this deterministic method, which will be widely used also within this dissertation, is still a valid approach. However, we believe that to fully evaluate time-frequency methods of analysis, this deterministic method and the proposed stochastic framework, should be both considered because they are complementary. A stochastic approach is particularly important in the validation of those time-frequency techniques which are known to be optimal for the estimation of chirps (as the Wigner-Ville distribution) or of those techniques which assume a deterministic model for the signals (as the one proposed in [19]). In these cases, a validation based on a deterministic model is likely to provide positively biased results. Conversely, a validation based on deterministic signals can be used to assess techniques of analysis based on autoregressive methods. In §3.2.1 stochastic signals generated by means of the presented framework will be used to evaluate the smoothed pseudo Wigner-Ville distribution.

2.4.1 Models for non-stationary HRV generation

The presented methodologies are based on the identification of the polar configuration associated to a model function whose geometry can be controlled by the design parameters introduced in §2.2.4. The identification problem has a closed-form solution which is exact in the case of I-FS and approximate in the case of II-FP framework. Therefore, once that the design parameters have been chosen, the solution of (2.10), or (2.33), directly provides the parameters of the model used to generate signals characterized by the desired properties. Framework II-FP has the advantage of allowing to directly control the instantaneous power of LF and HF components, but, being based on a TV-AR model, it can not provide much control on the shape of $S(n, \mathfrak{f})$ which is constrained to be a sum of Lorentzian functions. The capability of tuning the shape of the model function $S(n, \mathfrak{f})$ by properly choosing parameters $z_k(n)$, gives a great flexibility to the I-FS framework, which additionally was observed to generate signals whose spectral patterns followed more reliably the desired ones. The quantification of the intrinsic uncertainty of the simulated signals through the estimation of d_{w} and $e(n)$ allows one to evaluate the signals before using them to assess a method of analysis. It was shown that the uncertainty increases with the magnitude of the poles. Thus, one should give to the magnitude of the poles used as design parameter the lowest value which at the same time provides a $S(n, \mathfrak{f})$ which complies with the specifications.

A correct positioning of zeros $z_k(n)$ increases the number of possible $S(n, \mathfrak{f})$ which can be modeled. For example, as shown in Fig. 2.2, $z_k(n)$ can be used to control the degree of overlapping of LF and HF spectral peaks when their central frequencies are close. To separate the LF and HF spectral peaks without using $z_k(n)$, one could move $|p_{\mathrm{LF}}|$ toward the unit circle which, in turn, has the undesirable effect of increasing the uncertainty of the signals. Thus, the use of TV-ARMA models instead of the simpler

TV-AR models is crucial not only to improve the control of $S(n, \mathfrak{f})$ but also to reduce the intrinsic uncertainty of the simulated signals. In some configurations, additional $z_k(n)$ should be used to compensate for the introduction of undesirable components in $S(n, \mathfrak{f})$. In the applications presented in this chapter, $z_k(n)$ were placed on the unit circle. In those applications where this constrain is too restrictive, $S(n, \mathfrak{f})$ could be forced to a non-zero value by placing the $z_k(n)$ inside the unit circle, as shown in Fig. 2.2.

The model sampling rate f_s is another important parameter. It should be high enough to ensure a good time resolution but not too high, in order to spend the degrees of freedom of the model to describe relevant signal components and not modeling noise presents in high frequency band.

Finally, the presented framework have been shown to be robust: as shown in Fig. 2.7 it was possible to find a pole-zero configuration for almost any kind of possible combination of HRV spectral indices.

Chapter 3

Time-frequency analysis for HRV

Contents

3.1 Time-frequency representations: the Cohen's Class

The time-frequency (TF) representations which belong to the Cohen's class [67, 92] are covariant under time and frequency translations. The property of covariance under time and frequency translations states that:

$$y(t) = x(t - t_0)e^{j2\pi f_0} \Rightarrow C_y(t, f) = C_x(t - t_0, f - f_0) \qquad (3.1)$$

where $C_x(t, f)$ and $C_y(t, f)$ are TF representation of $x(t)$ and $y(t)$, respectively. The Cohen's class admits at least three equivalent definitions [8, 92]:

- *Time-delay* parametrization, via $\phi_{\text{t-d}}(t, \tau)$:

$$C(t, f) = \iint_{-\infty}^{-\infty} \phi_{\text{t-d}}(t - v, \tau)x\left(v + \frac{\tau}{2}\right)x^*\left(v - \frac{\tau}{2}\right)e^{-j2\pi f\tau}dvd\tau \qquad (3.2)$$

In this expression, the Cohen's class is seen as the Fourier transform of a non-stationary smoothed autocorrelation function:

$$s_x(t, \tau) = \int_{-\infty}^{-\infty} \phi_{\text{t-d}}(t - v, \tau)x\left(v + \frac{\tau}{2}\right)x^*\left(v - \frac{\tau}{2}\right)dv \qquad (3.3)$$

where $\phi_{\text{t-d}}(t, \tau)$ is a kernel (subscripts t-d stand for time-delay) whose function is explained in the following.

- *Delay–Doppler* parametrization, via $\phi_{\text{d-D}}(\tau, \nu)$:

$$C(t, f) = \iint_{-\infty}^{-\infty} \phi_{\text{d-D}}(\tau, \nu)A_x(\tau, \nu)e^{j2\pi(t\nu - f\tau)}d\nu d\tau \qquad (3.4)$$

In this expression, the Cohen's class is seen as the two-dimensional Fourier transform of a weighted version of the narrowband symmetric ambiguity function, $A_x(\tau, \nu)$, [93, 124, 68], defined as:

$$A_x(\tau, \nu) = \int_{-\infty}^{-\infty} x\left(t + \frac{\tau}{2}\right)x^*\left(t - \frac{\tau}{2}\right)e^{-j2\pi\nu t}dt \qquad (3.5)$$

- *Time-frequency* parametrization, via $\phi_{\text{t-f}}(t, f)$:

$$C(t, f) = \iint_{-\infty}^{-\infty} \phi_{\text{t-f}}(t - v, f - u)W_x(v, u)dvdu = \phi_{\text{t-f}}(t, f) \otimes W_x(t, f) \qquad (3.6)$$

In this expression, the Cohen's class is obtained by low-pass filtering (symbol $\otimes$ stands for convolution) in time and frequency the Wigner-Ville distribution (WVD), defined as the Fourier transform of the non-stationary autocorrelation function:

$$W_x(t, f) = \int_{-\infty}^{-\infty} x\left(t + \frac{\tau}{2}\right)x^*\left(t - \frac{\tau}{2}\right)e^{-j2\pi f\tau}d\tau \qquad (3.7)$$

Expression (3.6) shows that the WVD can be considered as the central element of the Cohen's class, i.e. the distribution from which all the other ones can be derived. The WVD (3.7) and the narrowband symmetric ambiguity function (3.5) are related by two dimensional Fourier transform [8]:

$$A_x(\tau, \nu) = \iint\limits_{-\infty}^{-\infty} W_x(t, f) e^{-j2\pi(\nu t - f\tau)} dt df \tag{3.8}$$

This implies that the WVD is itself a member of the Cohen's class, characterized by $\phi_{\text{d-D}}(\tau, \nu) = 1$ and consequently $\phi_{\text{t-f}}(t, f) = \delta(0, 0)$.

Every representation belonging to the Cohen's class is perfectly characterized by one of the three functions $\phi_{\text{t-d}}(t, \tau)$, $\phi_{\text{d-D}}(\tau, \nu)$ or $\phi_{\text{t-f}}(t, f)$, which are usually called kernels. These kernels completely define the properties of the TF distributions and are mutually related by the Fourier transform [8]:

$$\phi_{\text{d-D}}(\tau, \nu) = \int_{-\infty}^{\infty} \phi_{\text{t-d}}(t, \tau) e^{-j2\pi\nu t} dt = \iint\limits_{-\infty}^{+\infty} \phi_{\text{t-f}}(t, f) e^{j2\pi(\tau f - \nu t)} dt df \tag{3.9}$$

$$\phi_{\text{t-f}}(t, f) = \int_{-\infty}^{\infty} \phi_{\text{t-d}}(t, \tau) e^{-j2\pi f\tau} d\tau = \iint\limits_{-\infty}^{+\infty} \phi_{\text{d-D}}(\tau, \nu) e^{j2\pi(t\nu - \tau f)} d\tau d\nu \tag{3.10}$$

The main function of the kernels is to reduce the interference terms that affect the WVD and they have been extensively studied since the early Nineties [133, 25, 26, 73, 72, 7, 13, 249].

3.1.1 Interference terms

Interferences are oscillatory terms inherent to the quadratic structure of the WVD, which are not due to spectral components of the signal but are due to their mutual interactions [122, 125]. Therefore, they are usually considered as noise which should be eliminated, or at least reduced, in order to improve the readability of the distribution. Ideally, the distribution should only be composed of autoterms, i.e. terms due to the signal components taken independently. Given that the interference terms are oscillatory, they can be attenuated by filtering the WVD with kernels which acts as low-pass filters. In turn, the interpretation of these kernels as low-pass filters imposes geometrical constraints on their design [13, 25, 26, 72, 73].

Interference terms of the WVD are a consequence of the WVD's bilinear (or quadratic) structure; they occur in the case of multicomponent signals and can be identified mathematically with quadratic cross terms [90, 122]. They appear whenever a signal can be described as the sum of different spectral components. For example, the WVD of the signal $x(t) = x_1(t) + x_2(t)$, is:

$$W_x(t, f) = W_1^{(\text{S})}(t, f) + W_2^{(\text{S})}(t, f) + 2\Re[W_{12}^{(\text{I})}(t, f)] \tag{3.11}$$

where $W_1^{(\text{S})}(t, f)$ and $W_2^{(\text{S})}(t, f)$ are the autoterms that refer to signal components, while $W_{12}^{(\text{I})}(t, f)$ is an interference term which oscillates with a frequency and in a direction

which depend on the relative position of the autoterms in the TF plane [122, 125, 124]. As shown in Fig. 3.1, the interference geometry can be explained considering 2 points in the TF plane (t_1, f_1) and (t_2, f_2), which represent 2 signal components perfectly localized in time and frequency. They give rise to an outer interference located at $(t_{12}, f_{12}) = (\frac{t_2 + t_1}{2}, \frac{f_2 + f_1}{2})$ which oscillate in time direction with an oscillation frequency $\nu_{12} = (f_2 - f_1)$ and in frequency direction with oscillation frequency $\tau_{12} = (t_2 - t_1)$ [124, 125]. This implies that a large distance between the signal terms in the time (frequency) direction entails a faster interference oscillation in the frequency (time) direction and that, on the other hand, if the signal components occupy essentially the same time-frequency region, the interference terms will not oscillate.

Interference terms are sometimes divided in two groups: outer and inner interferences.

Outer interferences appear in multicomponent signals, as the result of the interactions between two different spectral component which are simultaneously present at the same time. Outer interferences are usually located at midway between the two components and mainly oscillate in time direction. An example of outer interference is shown in Fig. 3.2.

Inner interferences are due to non linearities in the law of instantaneous frequency of each spectral component and they also appear in monocomponent signals. Their structure obeys the same geometric laws of outer interferences. An example of inner interference is shown in Fig. 3.3.

Quadratic time-frequency distributions, such as the WVD, of signals related to the autonomic modulation of the heart are expected to present both outer and inner interferences [125]. The classification of the interference terms in inner and outer is useful for their description but is somehow arbitrary, since a strict definition of a non-stationary spectral component does not exist and mono component signals can always be split in several components.

The geometrical properties of the interference terms will be used in §4.3.2 to design a signal-dependent kernel.

Beside the use of particular kernel functions $\phi_{\text{t-d}}(t, \tau)$, $\phi_{\text{d-D}}(\tau, \nu)$ or $\phi_{\text{t-f}}(t, f)$, the complex analytic representation of the signal is often used instead of the original signal to further reduce the interference terms. Indeed, the power spectral density of the analytic representation of a signal vanishes for $f < 0$. Thus, the use of the complex analytic signal assures that positive and negative spectral components do not produce any interference term, thus improving the readability of the TF distribution.

3.1.2 Time-frequency resolution

Why it matters

A general scheme for the time-frequency analysis of biomedical signals can be divided in three major tasks:
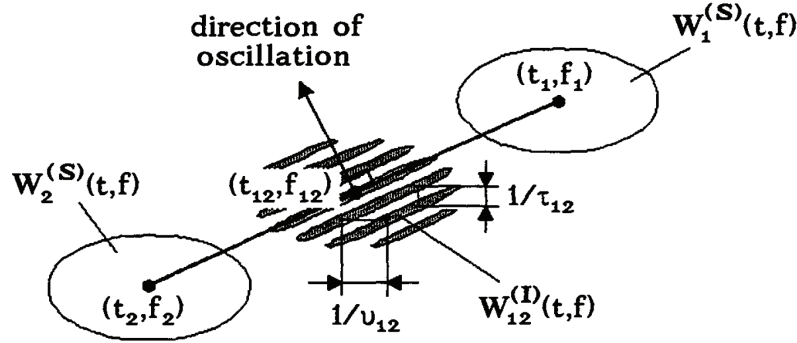
Figure 3.1: Geometry of interferences. Interferences created by the interactions between 2 atomic structures in the TF plane. $x_1(t)$ and $x_2(t)$ are located at (t_1, f_1) and (t_2, f_2). They generate an interference term centered at $(t_{12}, f_{12}) = (\frac{t_2 + t_1}{2}, \frac{f_2 + f_1}{2})$ which oscillate in time direction with an oscillation frequency $\nu_{12} = (f_2 - f_1)$ and in frequency direction with oscillation frequency $\tau_{12} = (t_2 - t_1)$ (Figure from [124, 125]).
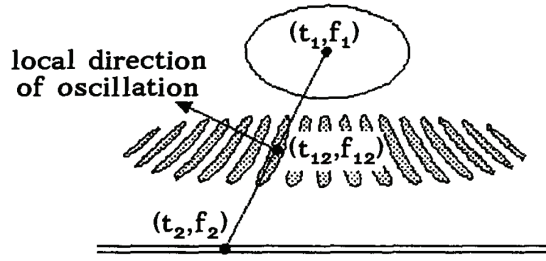
Figure 3.2: Geometry of outer interferences. Note that the interference terms are generated owing to the presence of 2 different spectral component and it mainly oscillate in time direction (Figure from [125])
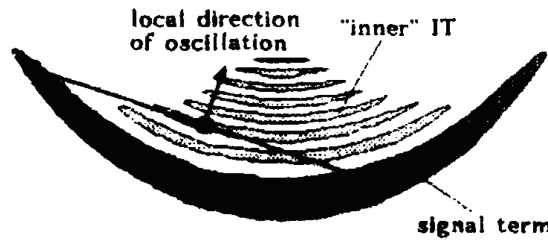
Figure 3.3: Geometry of inner interferences. Note that the interference terms are generated owing to non linearities in the instantaneous frequency of a monocomponent signal. The interference terms mainly oscillate in frequency direction (Figure from [125])

(i) Representation of the signal in the joint time-frequency domain.
(ii) Localization of relevant patterns in the joint time-frequency domain.
(iii) Quantification of the information, usually by reducing it to the time-course of a physiological index or to a scalar value.

As it appears from this scheme, the final result of the analysis is strictly related to the capability of the time-frequency distribution to represent the signal with a fine resolution. In the analysis of the signals related to the autonomic modulation, such as heart rate variability and systolic arterial pressure variability, frequency resolution should be fine enough to separate the LF and the HF components, even when low respiratory rate makes them closer. At the same time, time resolution should be fine enough to follow quick variations, typically of the order of few seconds.

The time-frequency resolution of a distribution belonging to the Cohen's class depends on the degree of filtering provided by the kernel function, which, in turn, depends on its geometrical properties. The Wigner-Ville distribution, with kernel function $\phi_{\text{t-f}}(t, f) = \delta(0, 0)$, has the best TF resolution.

Due to the Heisenberg principle, when a given TF distribution is used to estimate a non-stationary spectral density function, the time and frequency resolutions cannot be jointly arbitrarily low, but they are inversely related. This kind of trade-off affects the spectrogram and in general the positive distributions. The amount of smoothing also depend on the signals, being higher for those signals which present more interference terms [125, 182].

The quantification of the resolution is important in two aspects:

– It allows to compare the performance of different possible distributions and to chose the most appropriate for a given application.
– The quantification of the resolution can help to correctly interpret the results.

Indeed, before claiming that, for example, a given stimulus provokes a pattern of response characterized by a given latency, or that it provokes a change in a given spectral band, it is necessary to know the effect of the smoothing kernel on the localization of the time-frequency observed features.

How the time-frequency resolution is estimated

The resolution of the time-frequency distribution is given by the shape of the kernel function, which should be quantified by some relevant parameters.

Within this manuscript, we propose to quantify time resolution by the full width at half maximum of $\phi_{\text{t-f}}(t, 0)$, $\Delta_{\text{t}}^{\text{m}}$, or alternatively by the full width at $a\%$ of the total area of $\phi_{\text{t-f}}(t, 0)$, $\Delta_{\text{t}}^{(a\%)}$. Dually, frequency resolution is quantified by the full width at half maximum of $\phi_{\text{t-f}}(0, f)$, $\Delta_{\text{f}}^{\text{m}}$, or alternatively by the full width at $a\%$ of the total area of $\phi_{\text{t-f}}(0, f)$, $\Delta_{\text{f}}^{(a\%)}$.

These quantities measure the degree of spreading of a line in the TF domain: $\Delta_{\text{t}}^{\text{m}}$ and $\Delta_{\text{f}}^{\text{m}}$ are equal to the full width at half maximum of the given time-frequency distribution of a Dirac impulse, evaluated along t, and of a sinusoid, evaluated along f, whose ideal TF representations would be straight lines. Parameters Δ^{m}
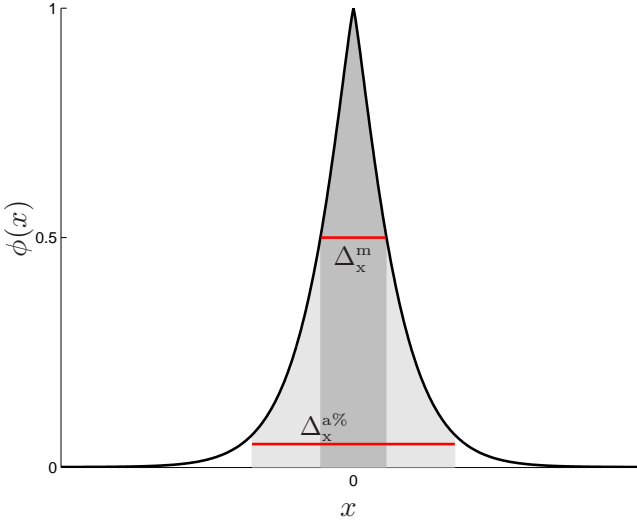
Figure 3.4: Quantification of the time-frequency resolution by the full width at half maximum (Δ_x^m), or by the full width at $a\%$ ($\Delta_\text{x}^{(\text{a}\%)}$), with $a = 95\%$, of the total area of $\phi(x)$. Here x is a variable which can represent both time and frequency, as well as $\phi(x)$ can represent both $\phi_\text{t-f}(t,0)$ and $\phi_\text{t-f}(0,f)$.

and $\Delta^{(\text{a}\%)}$, with $a = 95\%$, obtained from a general kernel function are shown in Fig. 3.4.

Time resolution: Let's consider the smoothed pseudo Winer-Ville distribution of a temporal impulse, such as a delta function $x(t) = \delta(t - t_0)$. From (3.6), we get:

$$S(t,f) = W_x(t,f) \otimes \phi_\text{t-f}(t,f) = \delta(t-t_0) \otimes \phi_\text{t-u}(t,f) = \int_{-\infty}^{\infty} \phi_\text{t-f}(t-t_0, f-u)du \quad (3.12)$$

If $\phi_\text{t-f}(t,f)$ is a separable function, such that $\phi_\text{t-f}(t,f) = \phi_\text{t}(t)\phi_\text{f}(f)$ then, evaluating $S(t,f)$ along t we get $S(t,f) = k\phi_\text{t}(t-t_0)$, where k is a scale factor.

Frequency resolution: Let's consider the smoothed pseudo Winer-Ville distribution of a complex exponential $x(t) = \exp(j2\pi f_0 t)$. From (3.6), we get:

$$S(t,f) = W_x(t,f) \otimes \phi_\text{t-f}(t,f) = \delta(f-f_0) \otimes \phi_\text{t-f}(t,f) = \int_{-\infty}^{\infty} \phi_\text{t-f}(t-v, f-f_0)dv \quad (3.13)$$

If $\phi_\text{t-f}(t,f)$ is a separable function, such that $\phi_\text{t-f}(t,f) = \phi_\text{t}(t)\phi_\text{f}(f)$ then, evaluating $S(t,f)$ along f we get $S(t,f) = k\phi_\text{f}(f-f_0)$, where k is a scale factor.

Note that Δ^m mainly depends on the sharpness of $\phi_\text{t-f}(t,f)$ around its maximum, while it is slightly affected by its tails. On the other hand, a measure such as $\Delta^{(\text{a}\%)}$, is more affected by the values that $\phi_\text{t-f}(t,f)$ takes far from its maximum. Thus, the ratio $\Delta^\text{m}/\Delta^{(\text{a}\%)}$ can be used to quantify and compare the capability of the distribution of concentrating the energy of the signal in the time-frequency domain. For $\Delta^\text{m}/\Delta^{(\text{a}\%)} \leq 1$ the kernel localizes the energy of the signal in very limited TF regions, since the kernel has almost no tails.

3.2 The smoothed-pseudo Wigner-Ville distribution (SPWVD)

The WVD (3.7) provides an excellent localization of spectral components in TF domain, but its applicability is limited by the unavoidable presence of interference terms, which are not inherent to the signal and which oscillate in the TF plane [92, 124, 125]. Several filtered versions of the WVD have been proposed to reduce the interference terms while maintaining a good TF resolution. Among those that have been applied to the study of the cardiovascular variability [166, 165, 216], the smoothed pseudo Wigner-Ville distribution (SPWVD) is one of the most interesting, since it provides an independent control over the time and frequency resolution. The SPWVD is the only member of the Cohen's class which makes use of separable kernels, i.e. $\phi_{\text{t-f}}(t, f) = \phi_{\text{t}}(t)\phi_{\text{f}}(f)$, and gives the possibility to independently control the amount of time and frequency filtering [175, 92, 67]. Given its great potentiality [216], the assessment of the performance of the SPWVD in non-stationary HRV analysis is of interest.

The SPWVD of a signal $x(t)$ can be estimated in the time-lag domain (t, τ) by means of (3.2) and by using the separable kernel $\phi_{\text{t-d}}(t, \tau) = \phi_{\text{t}}(t)\phi_{\text{d}}(\tau)$:

$$C(t, f) = \int_{-\infty}^{-\infty} \phi_{\text{d}}(\tau) \left[\int_{-\infty}^{-\infty} \phi_{\text{t}}(t - v)x \left(v + \frac{\tau}{2} \right) x^* \left(v - \frac{\tau}{2} \right) dv \right] e^{-j2\pi f \tau} d\tau \qquad (3.14)$$

In this expression, the term in the brackets, represent a smoothed version of the deterministic autocorrelation function. From what pointed out in the previous section, the time and the frequency resolution of the SPWVD will be separately given by the shape of $\phi_{\text{t}}(t)$ and by the shape of (the Fourier transform of) $\phi_{\text{d}}(\tau)$, respectively.

In Fig. 3.5, an illustrative example of the effect of the smoothing is given. Panels (a)–(b) represent a signal composed of 4 Gaussian atoms, i.e. 4 complex exponentials modulated by Gaussian functions. Graphics (c)–(f) show 4 different TF distributions of this signal. The centers of the TF atoms are localized by black crosses. In panel (c), the Wigner-Ville distribution is shown. The 4 TF atoms are well localized both in time and frequency. However, several interference terms also appear in the TF distributions. Importantly, these interference terms have an amplitude higher than the autoterms. In panel (d) and (e) the Wigner-Ville distribution is only filtered in frequency and time, respectively. It is shown that the filtering in frequency cancels the interference terms owing to the interaction of TF atoms with the same frequency and that oscillate in frequency directions (see panel (d)), while filtering in time cancels the interferences terms owing to the interactions of TF atoms that appear at the same time instant and that oscillate in time direction ((see panel (e))). If we compare the distributions in (d)–(e) with the Wigner-Ville distribution in (c), we observe that the filtering makes the TF representations less localized in frequency and time, respectively. Finally, in panel (f), the smoothed pseudo Wigner-Ville distribution obtained by combining the time and frequency filtering used in (d) and (e) is shown. All the interference terms have been eliminated. Furthermore, the smoothing applied to the distribution shown in (f) was sufficient to make the smoothed pseudo Wigner-Ville positive, so that it can now be considered as an estimate of the non-stationary spectrum of signal $x(t)$.
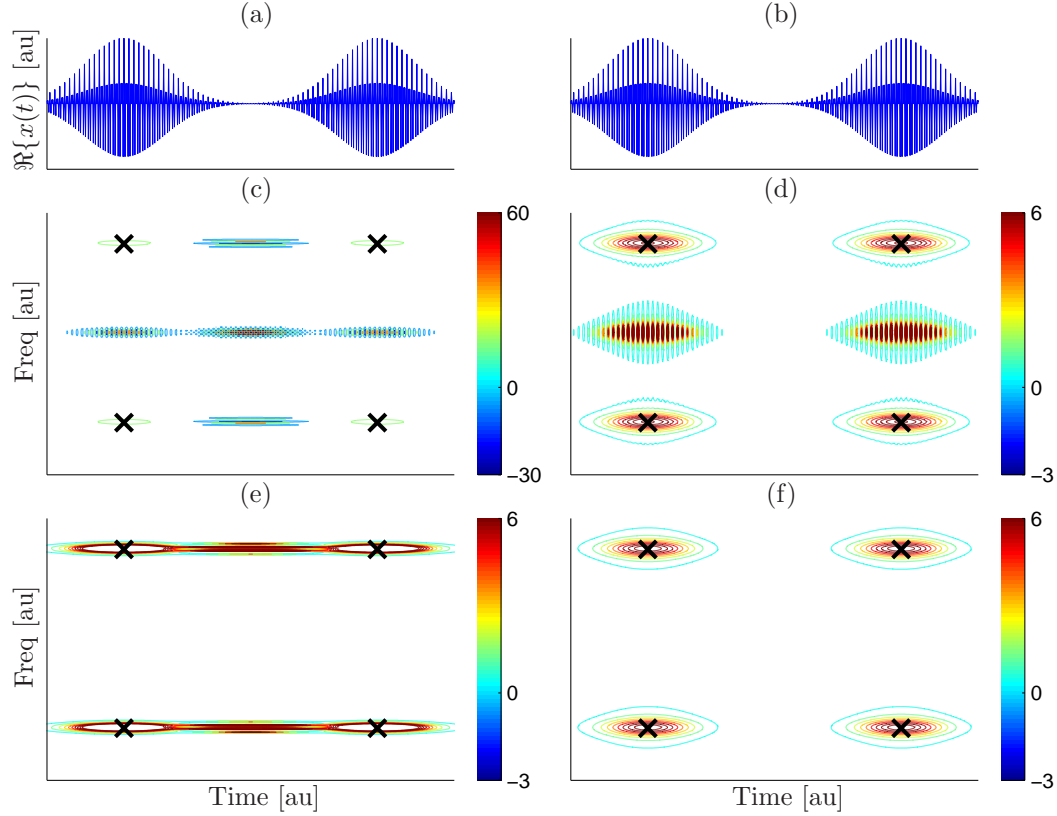
Figure 3.5: Effect of TF smoothing. (a)–(b): A signal composed of 4 Gaussian atoms. (c): Wigner-Ville distribution. (d): Pseudo Wigner-Ville distribution (frequency smoothing only). Note that interference terms oscillating in frequency have been removed. (e): Smoothed Wigner-Ville distribution (time smoothing only). Note that interference terms oscillating in time have been removed. (f): Smoothed pseudo Wigner-Ville distribution (both time and frequency smoothing). Black cross localize the center of the Gaussian atoms in the TF domain. TF distributions are normalized to the total energy of the signal. Iso-contours of graphics in (d)–(f) represent the same values.

3.2.1 Evaluation by a simulation study

Materials

To assess the performance of the SPWVD in the analysis of non-stationary signals related to the autonomic modulation, we generated stochastic signals that mimic real heart rate variability (HRV) patterns by means of the methodology described in the previous chapter. More in detail, signals were obtained by means of the I-FS framework (see §2.2.2) and reproduced possible dynamics of HRV during exercise stress test (EST, §2.3.1) and during experiments of music-induced emotions (MIE, §2.3.2). The time-course of the instantaneous frequencies and powers of the spectral components during EST and MIE are reported in Fig. 2.3–2.4, and the parameters which quantifies the degree of non-stationarity of these signals are given in Table 2.1.

Signals were generated with a sampling rate, F_s, equal to 2 Hz and global results were obtained by using $R{=}1000$ realizations of the models. For simulation EST, the model includes 4 poles and 8 zeros, i.e. the order of the TV-ARMA model was (4,8), and the magnitude of the LF pole used as design parameter, $|p_\mathrm{LF}|$, was equal to 0.905. For simulation MIE, the model order was (4,10) and $|p_\mathrm{LF}| = 0.870$. These values of $|p_\mathrm{LF}|$ were chosen based on the results shown in Fig. 2.6.

Time-frequency analysis

The non-stationary spectral density function, $\hat{S}(t, f)$, was estimated by means of the smoothed pseudo Wigner-Ville distribution (3.14). The time and frequency smoothing were provided by a rectangular window $\phi_\mathrm{t}(t)$ of length $2N - 1$ and an exponential function $\phi_\mathrm{d}(\tau)$ with damping factor $\delta|$. The width of $\phi_\mathrm{t}(t)$ gave a time resolution of about $\{20.5, 35.5, 50.5\}$ and $\{5.5, 15.5, 25.5\}$ seconds for simulation EST and MIE, respectively, while in both simulations $\phi_\mathrm{d}(\tau)$ gave a frequency resolution of $\{0, 7, 13\}$ mHz. Time and frequency resolutions are given as the full-width at half maximum of $\phi_\mathrm{t}(t)$ $(\Delta_\mathrm{t}^\mathrm{m})$ and of the Fourier transform of $\phi_\mathrm{d}(\tau)$ $(\Delta_\mathrm{f}^\mathrm{m})$, respectively.

To estimate the time-course of the HRV spectral indices the traditional LF band, $B_\mathrm{LF} = [0.04, 0.15]$ Hz and a TV respiration-dependent HF band[1], centered on the respiratory rate $F_\mathrm{resp}(t)$, $B_\mathrm{HF}(t) = F_\mathrm{resp}(t) + [-0.125, 0.125]$ Hz, are used [16]. Here, the respiratory rate $F_\mathrm{resp}(t)$ is assumed to be equal to $F_\mathrm{HF}(t)$. However, in real data analysis a direct or ECG-derived estimation of respiratory rate could be used to dynamically adjust the HF band [24].

Instantaneous frequencies from the model, $F_\mathrm{LF}(t)$ and $F_\mathrm{HF}(t)$, and from TF analysis, $\hat{F}_\mathrm{LF}(t)$ and $\hat{F}_\mathrm{HF}(t)$, are obtained as the peak frequency of the TF model function, defined in (2.3), and of the SPWVD, defined in (3.14), in B_LF, $B_\mathrm{HF}(t)$, respectively.

Instantaneous powers, $P_\mathrm{LF}(t)$, $P_\mathrm{HF}(t)$, $P_\mathrm{TOT}(t)$ and $\hat{P}_\mathrm{LF}(t)$, $\hat{P}_\mathrm{HF}(t)$, $\hat{P}_\mathrm{TOT}(t)$ are obtained by integrating the model function and the estimated SPWVD in B_LF, $B_\mathrm{HF}(t)$ and on the entire spectrum, respectively.

The estimation error between the time-course of a general HRV index $\mathcal{I}(t)$ and its

---

[1]The use of dynamic boundaries for the HF components will be discussed in §6.3.4, where it is used in a physiological study.

estimate $\hat{\mathcal{I}}(t)$ is calculated as:

$$E_{\mathcal{I}}(t) = \frac{\frac{1}{R}\left(\sum_{r=1}^{R}\hat{\mathcal{I}}_r(t)\right) - \mathcal{I}(t)}{\mathcal{I}(t)} \tag{3.15}$$

where $\mathcal{I}(t) \in \{F_{\mathrm{LF}}(t), F_{\mathrm{HF}}(t), P_{\mathrm{LF}}(t), P_{\mathrm{HF}}(t), P_{\mathrm{TOT}}(t)\}$ and $R = 1000$ is the number of realizations of the model.

Results & Discussion:

Representative examples of TF estimates and estimation errors are given in Fig. 3.6. A comparison between the TF model functions, reported in the first column, and the SPWVD obtained by averaging the distributions of each realization of the model, reported in the second column, shows that the SPWVD provides a representation of the TF structure of the simulated signals which is well localized both in time and in frequency. This is confirmed by the quantification of the instantaneous frequencies and powers reported in the last two columns of Fig. 3.6. It is shown that in simulation EST the estimated parameters perfectly followed the transitory, with a mean estimation error $|\bar{E}_{\mathcal{I}}| < 2.8\%$ in T_1 and $|\bar{E}_{\mathcal{I}}| < 3.6\%$ in T_2. In simulation MIE, which is characterized by much stronger rates of variation, the indices estimated using the SPWVD followed the theoretical changes, even if with a higher percentual error. Global results, obtained by using all the 9 different kernels, are detailed in Table 3.1 and summarized in Fig. 3.7. During both simulations EST and MIE, the SPWVD estimated the dynamics of the simulated signals with a median error which, in the worst case, did not exceed the 10%. Results should be compared to the intrinsic uncertainty of the simulated signals (see §2.2.5), whose distribution is reported in the last column of Fig. 3.7. The estimation error $E_{\mathcal{I}}(t)$ increased by increasing the rate of variation of the spectral components. For simulation EST, the estimation error was always very low, both for epochs T_1 and T_2. The time-course of $F_{\mathrm{LF}}(t)$, $F_{\mathrm{HF}}(t)$ and $P_{\mathrm{LF}}(t)$ was estimated with an estimation error whose median and interquartile range were bounded between 0.78% and 5.52% and between 0.29% and 5.16%, respectively. During T_2, the interquartile range of the estimation error of $\hat{P}_{\mathrm{HF}}(t)$ was higher, but still comparable with that of $e(t)$, which measures the intrinsic uncertainty. The temporal evolution of the total power was estimated with an error whose median and interquartile range were bounded between 0.11% and 0.65% and between 2.11% and 4.55%, respectevely. For simulation MIE, the estimation error was higher, especially during T_2. Nevertheless, in Fig. 3.6, it is shown that $\hat{P}_{\mathrm{LF}}(t)$ and $\hat{P}_{\mathrm{HF}}(t)$ correctly followed the temporal evolution of $P_{\mathrm{LF}}(t)$ and $P_{\mathrm{HF}}(t)$ even during T_2. In this simulation, the estimation of $P_{\mathrm{LF}}(t)$ worsened by increasing the degree of the time smoothing. To correctly track the changes of the HRV spectral indices, one should always pay attention to the TF resolution fixed by the kernels. Concerning the effect of the TF filtering, it is shown that the estimation error of $P_{\mathrm{TOT}}(t)$ only depended on the filtering in time, and that for a given time resolution, $E_{\mathcal{I}}(t)$ decreased by increasing the degree of the frequency filtering. This was particularly evident for the estimation of HF instantaneous power and frequency, where misestimations due to residual interference terms are more frequent. The use of a time-varying respiration-dependent boundaries [16]
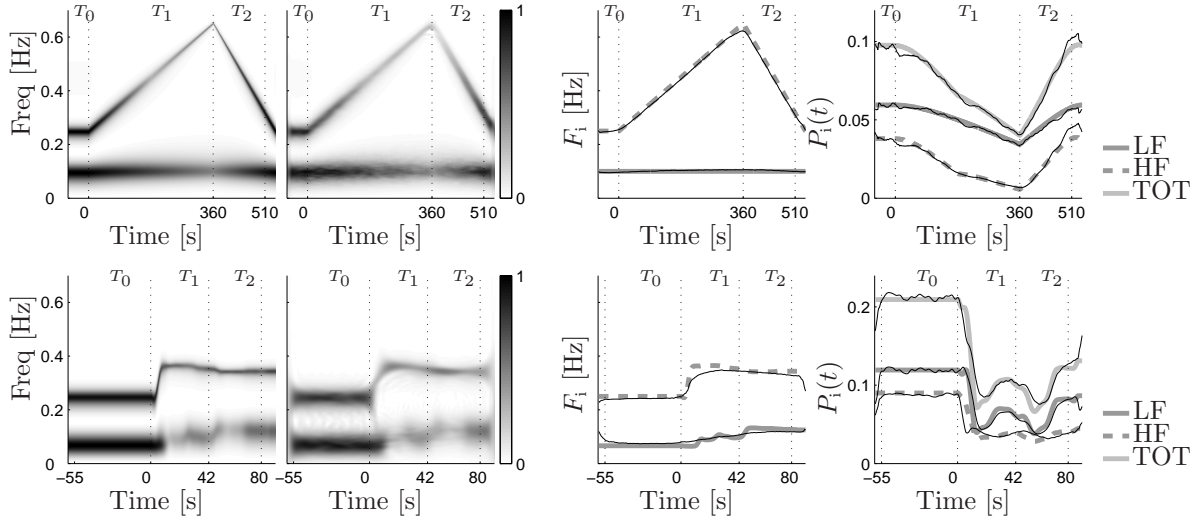
Figure 3.6: Model and estimated spectral patterns. Upper graphic: simulation EST; Lower graphic: simulation MIE; From left to right, columns refer to: model function $S(t,f)$; averaged SPWVD $\hat{S}(t,f)$; instantaneous frequencies and instantaneous powers. Estimated $\hat{F}_i(t)$ and $\hat{P}_i(t)$ are reported in black, values of the model in gray. Time-frequency resolution was {20s,7mHz} and {5s,13mHz} for EST and MIE simulations. R=1000 realizations were used.
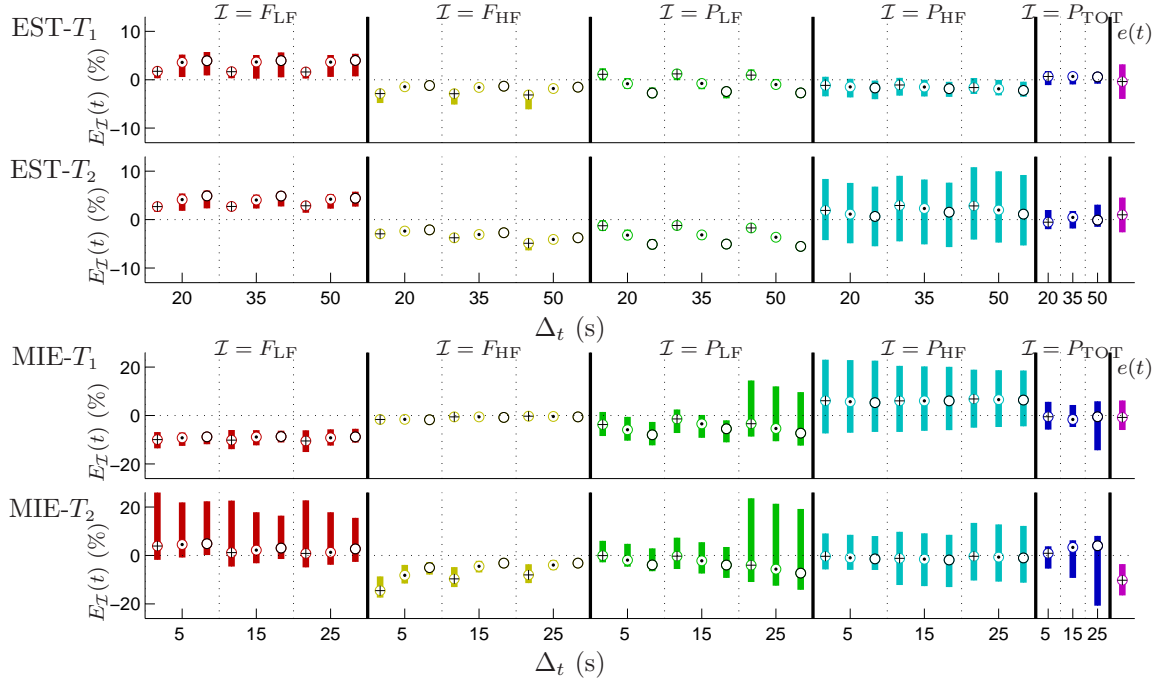
Figure 3.7: Distribution of the estimation error $E_{\mathcal{I}}(t)$ for parameters $\mathcal{I} = \{F_{\text{LF}}(t), F_{\text{HF}}(t), P_{\text{LF}}(t), P_{\text{HF}}(t), P_{\text{TOT}}(t)\}$. Symbols represent the median values and the box the 25th and the 75th percentiles. In the last column the statistical distribution of the uncertainty $e(t)$ is reported. Results obtained with a frequency resolution $\Delta_{\text{f}}^{\text{m}} = \{0, 7, 13\}$ mHz are reported with a cross, a point and a circle, respectively.

was very effective to improve the estimation of the HF component, which otherwise would have required a much higher degree of filtering.

In this study we used a rather basic TF analysis, which involves a TF filtering of the WVD by means of time-invariant kernels that were arbitrary chosen, and an estimation of spectral indices by integrating $\hat{S}(t, f)$ in B_{LF} and $B_{\mathrm{HF}}(t)$. More sophisticated techniques have been presented in the literature to improve the spectral characterization of non-stationary signals. An interesting possibility is to make the TF filtering of the WVD time-varying or signal-dependent [25]. Another possibility, described in the following section §3.3, is to perform a parametric decomposition of the generalized autocorrelation function [164]. A method, which combines parametric decomposition of the autocorrelation function with a dynamic adjustment of the TF filtering which depends to the rate of variation of the spectral components of the signal, has been recently proposed [19]. All these methodologies were assessed by means of deterministic signals embedded in noise and the frameworks presented in §2 could be used, in further studies, to compare their performance.

3.3 Combining parametric and non-parametric methods

To improve the capability of the SPWVD to localize and quantify the temporal evolution of the spectral components of a signal, the parametric decomposition of the non-stationary autocorrelation function (ACF), $s_x(t, \tau)$, whose expression is given in (3.3), was proposed in [164]. This method allows to separate information that is considered inherent to the signal from noise. In this section, it is combined with the estimation of the respiratory information to improve the tracking of the HF component [20].

This methodology will be used in §6 to characterize the changes that different kinds of music provoked on the autonomic modulation of heart rate [201].

Parameter extraction

The time course of the HRV spectral parameters, such as instantaneous central frequencies, $F_{\mathrm{LF}}(t)$ and $F_{\mathrm{HF}}(t)$, and instantaneous powers, $P_{\mathrm{LF}}(t)$ and $P_{\mathrm{HF}}(t)$, can be obtained by combining the parametric decomposition of the non-stationary ACF [164] with the estimation of the respiratory rate, which is use to estimate the HF component [20]. The method of decomposition described here is an extension of the Prony modeling [174], designed to estimate the parameters of damped sinusoids embedded in noise [148]. Briefly, the non-stationary ACF (3.3), $s_x(t, \tau)$, is modeled, for every time-instant t_0, as the sum of q damped sinusoids which are in strict relation with the instantaneous LF and HF components:

$$s_x(t_0, \tau) \approx \sum_{i=1}^{q} A_i(t_0) e^{j2\pi f_i(t_0)\tau + d_i(t_0)|\tau|} + \xi(t_0, \tau) \tag{3.16}$$

where τ is the time lag. In (3.16), $\xi(t_0, \tau)$ is a white gaussian noise, which takes into account both background noise and model inaccuracies, $A_i(t_0)$, $d_i(t_0)$ and $f_i(t_0)$ are the

Table 3.1: Simulation EST and MIE - Estimation error $E_{\mathcal{I}}(t)$ in mean±standard deviation

$2N$ samp	Δ_t^m s	δ samp^{-1}	Δ_f^m Hz	$F_{LF}(t)$ %	$F_{HF}(t)$ %	$P_{LF}(t)$ %	$P_{HF}(t)$ %	$P_{TOT}(t)$ %
				– Exercise stress testing T_1 – Uncertainty $\mu_e \pm \sigma_e = 0.31 \pm 4.81$ [%]				
		0	0	1.19 ± 1.62	-4.48 ± 4.04	0.90 ± 1.72	-0.89 ± 5.36	
42	20.5	1/64	0.007	2.77 ± 2.72	-1.32 ± 0.72	-1.03 ± 1.66	-1.11 ± 5.29	0.05 ± 2.09
		1/32	0.013	3.15 ± 3.02	-1.07 ± 0.52	-2.92 ± 1.62	-1.33 ± 5.24	
		0	0	1.11 ± 1.60	-4.62 ± 3.95	0.95 ± 1.41	-0.79 ± 5.40	
72	35.5	1/64	0.007	2.75 ± 2.76	-1.49 ± 0.72	-0.97 ± 1.35	-1.02 ± 5.33	0.13 ± 1.91
		1/32	0.013	3.07 ± 2.95	-1.18 ± 0.57	-2.87 ± 1.32	-1.25 ± 5.28	
		0	0	1.06 ± 1.55	-4.82 ± 3.75	1.00 ± 1.23	-0.62 ± 5.69	
102	55.5	1/64	0.007	2.70 ± 2.77	-1.67 ± 0.78	-0.93 ± 1.17	-0.87 ± 5.63	0.21 ± 1.87
		1/32	0.013	2.98 ± 2.89	-1.35 ± 0.66	-2.82 ± 1.14	-1.11 ± 5.57	
				– Exercise stress testing T_2 – Uncertainty $\mu_e \pm \sigma_e = 1.29 \pm 5.82$ [%]				
$2N$ samp	Δ_t^m s	δ samp^{-1}	Δ_f^m Hz	$F_{LF}(t)$ %	$F_{HF}(t)$ %	$P_{LF}(t)$ %	$P_{HF}(t)$ %	$P_{TOT}(t)$ %
		0	0	2.30 ± 1.16	-4.12 ± 2.56	-1.33 ± 1.44	2.49 ± 9.55	
42	20.5	1/64	0.007	3.59 ± 2.02	-2.44 ± 0.31	-3.24 ± 1.43	1.95 ± 9.48	0.50 ± 3.31
		1/32	0.013	4.07 ± 2.22	-2.11 ± 0.29	-5.12 ± 1.41	1.41 ± 9.41	
		0	0	2.36 ± 1.04	-4.59 ± 1.99	-1.31 ± 1.16	3.01 ± 8.67	
72	35.5	1/64	0.007	3.61 ± 1.83	-3.03 ± 0.32	-3.21 ± 1.13	2.42 ± 8.63	0.63 ± 2.92
		1/32	0.013	4.06 ± 2.02	-2.65 ± 0.37	-5.08 ± 1.11	1.84 ± 8.60	
		0	0	2.35 ± 1.12	-5.29 ± 1.64	-1.25 ± 1.38	3.75 ± 8.00	
102	55.5	1/64	0.007	3.54 ± 1.88	-3.91 ± 0.57	-3.15 ± 1.32	3.10 ± 8.00	0.84 ± 2.77
		1/32	0.013	3.95 ± 2.02	-3.54 ± 0.57	-5.02 ± 1.28	2.45 ± 8.01	

$2N$ samp	Δ_t^m s	δ samp^{-1}	Δ_f^m Hz	$F_{LF}(t)$ %	$F_{HF}(t)$ %	$P_{LF}(t)$ %	$P_{HF}(t)$ %	$P_{TOT}(t)$ %
				Music-induced emotions T_1 – Uncertainty $\mu_e \pm \sigma_e = -9.80 \pm 8.98$ [%]				
		0	0	1.34 ± 3.30	-1.11 ± 0.98	6.09 ± 10.33	-16.27 ± 8.46	
12	5.5	1/64	0.007	1.54 ± 3.03	-0.77 ± 0.32	4.58 ± 10.28	-16.95 ± 8.33	-8.90 ± 8.32
		1/32	0.013	1.84 ± 2.71	-0.71 ± 0.12	3.09 ± 10.24	-17.63 ± 8.20	
		0	0	1.58 ± 3.31	-0.58 ± 0.21	5.86 ± 11.95	-16.43 ± 8.20	
32	5.5	1/64	0.007	1.55 ± 3.07	-0.43 ± 0.06	4.35 ± 11.88	-17.11 ± 8.07	-9.09 ± 8.70
		1/32	0.013	1.67 ± 2.73	-0.39 ± 0.07	2.87 ± 11.81	-17.78 ± 7.95	
		0	0	2.09 ± 4.05	-0.60 ± 0.19	10.35 ± 35.67	-15.81 ± 10.72	
52	5.5	1/64	0.007	2.01 ± 3.66	-0.47 ± 0.26	8.80 ± 35.28	-16.48 ± 10.63	-6.47 ± 20.26
		1/32	0.013	2.06 ± 3.42	-0.43 ± 0.31	7.27 ± 34.91	-17.15 ± 10.55	
				Music-induced emotions T_2 – Uncertainty $\mu_e \pm \sigma_e = 9.61 \pm 15.42$ [%]				
$2N$ samp	Δ_t^m s	δ samp^{-1}	Δ_f^m Hz	$F_{LF}(t)$ %	$F_{HF}(t)$ %	$P_{LF}(t)$ %	$P_{HF}(t)$ %	$P_{TOT}(t)$ %
		0	0	-6.38 ± 0.67	-4.41 ± 8.56	21.19 ± 18.03	-2.69 ± 25.23	
12	5.5	1/64	0.007	-4.80 ± 0.61	-3.12 ± 5.66	19.54 ± 17.50	-3.23 ± 24.85	10.90 ± 17.28
		1/32	0.013	-3.72 ± 0.65	-2.43 ± 4.35	17.84 ± 17.02	-3.74 ± 24.48	
		0	0	-8.85 ± 1.42	3.05 ± 5.22	28.52 ± 29.44	-0.30 ± 22.12	
32	15.5	1/64	0.007	-6.91 ± 1.48	0.21 ± 2.58	26.83 ± 28.75	-0.89 ± 22.13	15.22 ± 22.95
		1/32	0.013	-5.40 ± 1.52	-0.99 ± 2.56	25.04 ± 28.04	-1.45 ± 22.14	
		0	0	-8.83 ± 1.62	2.85 ± 4.21	42.59 ± 49.87	4.74 ± 21.50	
52	25.5	1/64	0.007	-6.90 ± 1.94	-0.66 ± 3.27	40.77 ± 48.80	4.01 ± 21.98	23.84 ± 33.52
		1/32	0.013	-5.50 ± 1.96	-2.08 ± 3.93	38.85 ± 47.70	3.34 ± 22.40	
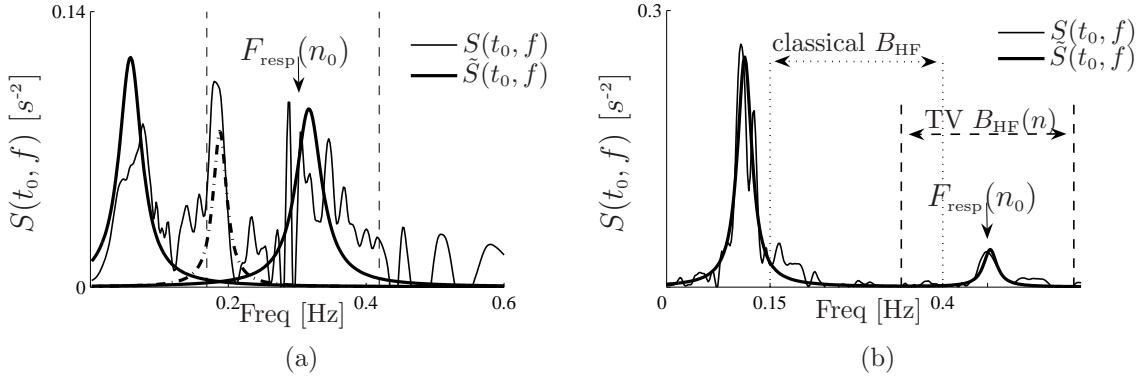
Figure 3.8: Combining TF analysis with parametric decomposition: in continuous line the SPWVD, $S(t_0, f)$, computed at time n_0. In bold line: the spectrum components, $\tilde{S}_{\mathrm{LF}}(t_0, f)$ and $\tilde{S}_{\mathrm{HF}}(t_0, f)$, reconstructed using the parametric decomposition. (a): The interference term, in dashed bold line, lies in between the LF and the HF components and can be discarded. (b): The importance of including the respiratory information in the definition of HF spectral band: traditional HF frequency band, in dotted vertical lines; TV respiration-dependent HF band, in dashed vertical lines.

amplitude, damping factor and frequency of the i-th damped complex sinusoid. The parameters $A_{\mathrm{i}}(t_0)$, $d_{\mathrm{i}}(t_0)$ and $f_{\mathrm{i}}(t_0)$ are obtained from $s_x(t_0, \tau)$ with $\tau > 0$, using the least square method described in [148], which provides accurate estimation of exponentially damped sinusoidal signals in noise. The method combines linear backward prediction and singular value decomposition to separate signal components from noise. If we take the Fourier transform of the instantaneous ACF described in (3.16), ignoring the noise term, we get a denoised estimate of the TV spectrum of signal $x(t)$:

$$\tilde{S}(t, f) = \sum_{i=1}^{q} \tilde{S}_{\mathrm{i}}(t, f) \tag{3.17}$$

where $\tilde{S}_{\mathrm{i}}(t, f)$ denotes the Fourier transform of each damped sinusoid in (3.16). In the following, it is shown that the power associated to a signal component whose instantaneous ACF is a complex damped sinusoid can be analytically obtained from coefficients $A_{\mathrm{i}}(t)$.

Consider a signal component $y(t)$, whose ACF is the damped complex sinusoid $s(\tau)$:

$$s(\tau) = Ae^{-d|\tau| + j2\pi f_0 \tau} \tag{3.18}$$

with $d > 0$, τ and $A \in \mathbb{R}$. The Fourier Transform of $s(\tau)$ is equal to:

$$S(f) = \int_{-\infty}^{\infty} Ae^{-d|\tau| + j2\pi(f_0 - f)\tau} d\tau = \frac{2Ad}{4\pi^2(f - f_0)^2 + d^2} \tag{3.19}$$

Note that $s(\tau)$ is an hermitian function and $S(f)$ is real. The function $S(f)$ is the power spectral density of $y(t)$ and has a Lorentian shape with a peak centered on

frequency f_0. The power of the signal component $y(t)$, P_y, is then closely related to coefficient A and it can be analytically obtained as the total area of $S(f)$:

$$P_y = \int_{-\infty}^{\infty} S(f)df = \int_{-\infty}^{\infty} \left[\frac{2Ad}{4\pi^2(f-f_0)^2 + d^2} \right] df = \tag{3.20}$$

$$= \frac{2Ad}{4\pi^2} \int_{-\infty}^{\infty} \left[\frac{1}{(f-f_0)^2 + \left(\frac{d}{2\pi}\right)^2} \right] df = \frac{2Ad}{4\pi^2} \frac{2\pi}{d} \left[\arctan\left(\frac{(f-f_0)2\pi}{d} \right) \right]_{-\infty}^{\infty} = A$$

After the decomposition, the LF component is selected as the sinusoid with highest power in LF range, while the HF component is selected as the sinusoid whose central frequency lies in the HF range and is closer to the respiratory rate. The use of these specific selection criteria for LF and HF components is particularly useful when the TF filtering is not sufficient to completely remove the interference terms. Indeed, in such a situation, the sinusoid that corresponds to the interference term, whose instantaneous central frequency lies in between the LF and the HF components [124], is automatically discarded from the instantaneous power and frequency estimation. This is shown in Fig. 3.8a, where we observe that the parametric decomposition of a highly noisy instantaneous spectrum $S(t_0, f)$ (in continuous line) allows to estimate LF and HF component (in bold line) and to discard the interference term (in dashed bold line).

Figure 3.8b shows an example in which a subject is breathing at $F_{\mathrm{resp}} = 0.465$ Hz. In this case, the use of a respiratory-dependent range (plotted in dashed vertical lines) allows to include the HF component, while the use of traditional HF range (dotted vertical lines) misses the HF component. This methodology will be used in §6 to analyze real non-stationary HRV signals. Further considerations about the results obtained by using this method, as well as time-varying respiratory boundaries, are given in §6.3.4.

Chapter 4

Time-frequency coherence analysis for cardiovascular signals

Contents

4.1 Introduction

Spectral coherence measures the degree of correlation between the spectral components of two signals [57]. This measure, which requires signals to be stationary, is inappropriate for studying non-stationary signals. In the analysis of cardiovascular signals, the estimation of spectral coherence in the joint time-frequency (TF) domain has many potential fields of application. For example, the localization of TF regions in which two signals are coupled can be applied in the time-varying characterization of baroreflex [76, 209, 145], or in the assessment of the degree of similarity between different signals, to validate the use of one signal, and its derived measures, as surrogates of original ones [100]. These applications will be the subject of the studies described in §7–8.

In recent years, different methods to estimate time-varying spectral coherence have been proposed. Most of them are based on parametric autoregressive modeling [168, 262, 261, 63]. The performance of these methods is related to the capability of fitting the appropriate underlying model and, in extremely non-stationary conditions, they have been observed to perform less accurately than non-parametric methods [216, 203].

Time-varying spectral coherence estimators based on non-parametric methods have the advantage of not requiring any assumption on the TF structure of the signals and are relatively easy to estimate. Among them, in biomedical applications, measures of time-scale coherence [110], based on the continuous wavelet transform, have been recently proposed to study cardiovascular dynamics [97, 144, 145] as well as neural connectivity [153, 260, 43, 54]. These methods are characterized by a non-homogeneous TF resolution and are suited for signals presenting high frequency components of short duration and low frequency components of long duration. In the late Nineties, estimators of time-frequency coherence based on multitaper spectrogram [254, 244] have been proposed to study the coupling between neuronal signals [256] and atrial fibrillation [158], but, to the extent of our knowledge, they have never been used in the analysis of cardiovascular variability.

In this chapter, two methods of time-frequency coherence analysis are described (see §4.3–4.4), with the purpose of showing their usefulness in the characterization of dynamic cardiovascular interactions. One is based on the smoothed pseudo Wigner-Ville distribution, while the other one on the multitaper spectrogram.

These methods include the possibility of automatic localizing TF regions in which spectral coherence is statistically significant. A methodology to numerically test the statistical significance of the time-frequency coherence estimates is described in §4.5. The accuracy in the localization of these regions is then assessed in a comparative study (see §4.6) based on simulated non-stationary signals. The comparison also include the assessment of wavelet coherence [110, 144].

To highlight the potentiality of the presented methods, time-frequency coherence analysis is used to characterize the changes which tilt table test provokes in the dynamic interactions between R–R variability (RRV) and systolic arterial pressure variability (SAPV), between RRV and respiration (RESP) and between RRV and pulse interval variability (PIV).

4.2 Time-frequency coherence

Spectral coherence function between two stationary zero-mean random processes $x(t)$ and $y(t)$ is a normalized version of the cross power spectral density, $S_{xy}(f)$. Its magnitude is defined as [57]:

$$\gamma(f) = \frac{|S_{xy}(f)|}{\sqrt{S_{xx}(f)S_{yy}(f)}}, \quad \gamma(f) \in [0, 1] \tag{4.1}$$

$$S_{xy}(f) = \mathcal{F}_{\tau \to f}\{\mathtt{E}[x(t)y^*(t - \tau)]\} \tag{4.2}$$

where $\mathcal{F}\{\cdot\}$ and $\mathtt{E}[\cdot]$ stand for the Fourier transform and the expectation operator, respectively. The magnitude of spectral coherence is one for those frequencies for which $x(t)$ and $y(t)$ are related by a linear time-invariant system and zero for those frequencies for which $x(t)$ and $y(t)$ are uncorrelated, i.e. when $S_{xy}(f) = 0$ [57, 181]. By analogy with the stationary case, the magnitude of time-frequency coherence (TFC) can be defined in non-stationary conditions as [252, 181]:

$$\gamma(t, f) = \frac{|S_{xy}(t, f)|}{\sqrt{S_{xx}(t, f)S_{yy}(t, f)}}, \quad \gamma(t, f) \in [0, 1] \tag{4.3}$$

where $S_{xy}(t, f)$ stands for some non-stationary cross spectrum.
Time-frequency coherence quantifies the strength of the local coupling between two non-stationary processes. The non-stationary spectrum used in (4.3) has not a unique definition. Nevertheless, the Wigner-Ville spectrum (WVS), defined as the Fourier transform of a non-stationary cross-correlation function [92]:

$$S_{xy}(t, f) = \mathcal{F}_{\tau \to f}\left\{\mathtt{E}\left[x\left(t + \frac{\tau}{2}\right)y^*\left(t - \frac{\tau}{2}\right)\right]\right\} \tag{4.4}$$

can be seen as a natural extension of the cross power spectral density in a non-stationary context. It can be shown that, under mild conditions, the Wigner-Ville spectrum (4.4) is equal to the ensemble average of the Wigner-Ville distributions (WVD), $W_{xy}(t, f)$, of the realizations of the processes [92]:

$$S_{xy}(t, f) = \mathtt{E}[W_{xy}(t, f)]; \tag{4.5}$$

$$W_{xy}(t, f) = \mathcal{F}_{\tau \to f}\left\{x\left(t + \frac{\tau}{2}\right)y^*\left(t - \frac{\tau}{2}\right)\right\}; \tag{4.6}$$

When only one observed realization is available, as in single-trial analysis, $S_{xy}(t, f)$ should be estimated by means of some estimator that replaces the expectation $\mathtt{E}[W_{xy}(t, f)]$ with local averaging:

$$\hat{S}_{xy}(t, f; \phi) = W_{xy}(t, f) \otimes \phi_{\text{t-f}}(t, f) \tag{4.7}$$

where $\otimes$ represents the 2D convolution on t and f, and $\phi_{\text{t-f}}(t, f)$ is the smoothing function, which, given (4.3), should guarantee the positiveness of the estimated spectra.
In this chapter, we always implicitly refer to single-trial coherence, since we are interested in characterizing cardiovascular interactions for a given subject. This contrasts

to inter-trial coherence, which is used to estimate the correlation throughout a given study population, by analyzing a batch of signals [260, 43].

Two different estimators of the Wigner-Ville spectrum are considered in this chapter to estimate the time-frequency coherence function, namely, the smoothed pseudo Wigner-Ville distribution (SPWVD) and the multitaper spectrogram (MTSP).

4.3 Time-frequency coherence by smoothed pseudo Wigner-Ville distribution (SPWV-TFC)

As also mentioned in §3.2, the SPWVD is a member of Cohen's class and corresponds to the particular case in which the kernel $\phi_{\text{t-f}}(t, f)$ is a separable function. It is defined as:

$$
\begin{aligned}
\hat{S}_{\text{xy}}^{\text{W}}(t, f) &= W_{\text{xy}}(t, f) \otimes \phi_{\text{t-f}}(t, f) = \mathcal{F}_{(\nu, \tau) \to (t, f)} \left\{ A_{\text{xy}}(\tau, \nu) \phi_{\text{d-D}}(\tau, \nu) \right\} \\
A_{\text{xy}}(\tau, \nu) &= \mathcal{F}_{t \to \nu} \left\{ x \left(t + \frac{\tau}{2} \right) y^* \left(t - \frac{\tau}{2} \right) \right\} \\
\phi_{\text{d-D}}(\tau, \nu) &= \mathcal{F}_{(t, f) \to (\tau, \nu)}^{-1} \left\{ \phi_{\text{t-f}}(t, f) \right\}
\end{aligned}
\tag{4.8}
$$

where $\mathcal{F}_{(\nu, \tau) \to (t, f)}$ is the 2D Fourier transform operator, used to pass from the ambiguity function domain to the TF domain, and $A_{\text{xy}}(\tau, \nu)$ is the cross ambiguity function of $x(t)$ and $y(t)$. The smoothing function can be seen as a 2D low pass filter which should be tuned in order to achieve a degree of smoothing sufficient to obtain meaningful estimates (i.e. $\hat{\gamma}(t, f) \in [0, 1]$), while maintaining at the same time a satisfactory TF resolution.

The SPWVD, $\hat{S}_{\text{xy}}^{\text{W}}(t, f)$, is not always positive and negative values are related to the presence of residual interference terms. These terms may cause the TFC to take values outside the range $[0, 1]$, thus losing its physical interpretation. This is shown by the Janssen's formula (also known as outer interference formula) [125, 92]:

$$
|W_{\text{xy}}(t, f)|^2 = \iint\limits_{-\infty}^{\infty} W_{\text{xx}} \left(t + \frac{\tau}{2}, f + \frac{\nu}{2} \right) W_{\text{yy}} \left(t - \frac{\tau}{2}, f - \frac{\nu}{2} \right) d\tau d\nu
\tag{4.9}
$$

This expression shows that for given TF point (t_0, f_0), it is possible to have $|W_{\text{xy}}(t_0, f_0)| \neq 0$ while $W_{\text{xx}}(t_0, f_0) = W_{\text{yy}}(t_0, f_0) \approx 0$, and consequently $\hat{\gamma}(t_0, f_0) > 1$.

To obtain meaningful TFC estimates, $\phi_{\text{t-f}}(t, f)$ should completely suppress the interference terms [181]. A necessary, but not sufficient, condition to have TFC estimates bounded between zero and one is the positiveness of the auto spectra. As long as the degree of TF filtering is strong enough, TF coherence by SPWVD (SPWV-TFC) is obtained as:

$$
\hat{\gamma}^{\text{W}}(t, f) = \frac{\left| \hat{S}_{\text{xy}}^{\text{W}}(t, f) \right|}{\sqrt{\hat{S}_{\text{xx}}^{\text{W}}(t, f) \hat{S}_{\text{yy}}^{\text{W}}(t, f)}}
\tag{4.10}
$$

In previous works which we published in [206, 100], a simplified version of the multiform–tiltable exponential kernel [72]:

$$\phi_{\text{d-D}}(\tau, \nu) = \exp \left\{ -\pi \left[\left(\frac{\nu}{\nu_0} \right)^2 + \left(\frac{\tau}{\tau_0} \right)^2 \right]^{2\lambda} \right\} \qquad (4.11)$$

was shown to provide reliable TFC estimates between cardiovascular signals. In the ambiguity function domain, the iso-contours of (4.11) are ellipses whose eccentricity depends on parameters ν_0 and τ_0. Parameters ν_0 and τ_0 are used to change the length of the ellipse axes aligned along ν (i.e. the degree of time filtering) and τ (i.e. the degree of frequency filtering), respectively. The parameter λ sets the roll off of the filter as well as the size of the tails of the kernel. This kernel function was used to obtain the TF distributions shown in the example of Fig. 3.5.

As described in §3.1.2, the time (frequency) resolution is given by the full width at half maximum $\Delta_{\text{t}}^{\text{m}}$ ($\Delta_{\text{f}}^{\text{m}}$) and the full width at $a\%$ of the total area $\Delta_{\text{t}}^{(\text{a\%})}$ ($\Delta_{\text{f}}^{(\text{a\%})}$) of $\phi_{\text{t-f}}(t, 0)$ ($\phi_{\text{t-f}}(0, f)$).

Two signal-dependent approaches, described in the following paragraphs, were proposed to determine an appropriate smoothing function $\phi_{\text{d-D}}(\tau, \nu)$.

4.3.1 Straightforward scheme for signal-dependent smoothing

According to this scheme, a signal-dependent kernel for time-frequency coherence analysis is obtained as follows.

First, the desired TF resolution ($\Delta_{\text{t}}^{\text{m}}$, $\Delta_{\text{f}}^{\text{m}}$), corresponding to the minimum amount of TF smoothing, is decided based on a-priori information about the signals and the experimental settings. The set of parameters $\{\tau_0, \nu_0, \lambda\}$ of the kernel in (4.11) that gives this TF resolution are used as starting point.

If using this set of parameters $\hat{\gamma}^{\text{wv}}(t, f) \notin [0, 1]$, the degree of time (or frequency) smoothing is maintained constant, while the frequency (or time) smoothing is increased until reaching meaningful estimates over the entire TF domain.

If at the end of the process, the frequency (or time) resolution is not satisfactory, the time (or frequency) resolution is decreased, i.e. the corresponding ν_0 (or τ_0) is increased, and the process iterates.

This process allows adjusting the TF filtering to the specific needs of analysis.

Despite the fact that in the SPWVD the degree of time and frequency filtering can be tuned independently, the resulting time and frequency resolution can not be set arbitrarily, since the condition of having $\hat{\gamma}^{\text{wv}}(t, f) \in [0, 1]$ imposes a sort of trade of on the minimum joint TF filtering.

This straightforward scheme was used in the applications described in §7 and §8. In particular, in §8, an illustrative example of how this procedure can be used to analyzed recorded physiological data will be given (see discussion of Fig. 8.1).

4.3.2 Geometrical scheme for signal-dependent smoothing

This second approach, which we proposed in [206, 202], is particularly suitable when no a-priori information about the signal is available. It makes use of geometrical relations between the TF structure of the signals and the interference terms to determine geometrical properties of $\phi_{\text{t-f}}(t, f)$. It also includes the restriction of the TF support of $\hat{\gamma}^{\text{WV}}(t, f)$ into regions of interest, defined as those TF regions where auto spectra are higher than a predetermined threshold. The use of TF regions of interest reduces the required degree of filtering, and it has been also used in a recent work [189].

Although in this section we apply this method to signals characterized by two non-stationary spectral components, it can be easily extended to the case of signals characterized by more spectral components. We denote the central frequencies of these components $f_{\text{B}}(t)$, with $B \in \{LF, HF\}$. As already described in §3.1.1, if we consider these spectral components as two time-frequency atoms, $(t_{\text{LF}}, f_{\text{LF}})$ and $(t_{\text{HF}}, f_{\text{HF}})$, we will observe an outer interference located at $(\frac{t_{\text{HF}}+t_{\text{LF}}}{2}, \frac{f_{\text{HF}}+f_{\text{LF}}}{2})$ which oscillates in time direction with oscillation frequency equal to the frequency lag $(f_{\text{HF}} - f_{\text{LF}})$, and in frequency direction with an oscillation frequency equal to the time lag $(t_{\text{HF}} - t_{\text{LF}})$ [124]. Due to Fourier transformation, an interference term that oscillates in time (or in frequency) direction is associated to a component located on the ν (or on the τ) axis of the ambiguity function. Furthermore, interference terms characterized by slow (fast) oscillations in the time-frequency domain, correspond to interference terms close to (far from) the origin of the ambiguity function.

Generalizing these local interactions, the outer interferences result to be located at midway between the 2 spectral components and they mainly oscillate in time direction with a time-varying frequency which is lower bounded by $\nu_{\text{min}} = \min \left[f_{\text{HF}}(t) - f_{\text{LF}}(t) \right]$ (see 3.2). The closer two signal components are, the slower the interference will oscillate in the time direction, and the closest the cross-component will be to the origin of the ambiguity plane. Therefore, in order to suppress outer interferences, the kernel should be able to filter out all $\nu > \nu_{\text{min}}$, where ν_{min} corresponds to the slowest outer interference term. To obtain ν_{min}, the estimation of $f_{\text{LF}}(t)$ and $f_{\text{HF}}(t)$ is required.

A direct or indirect estimation of respiratory rate can be used to approximate the instantaneous frequency of the HF component, $f_{\text{HF}}(t)$ [23, 24].

The central frequency of the LF component, $f_{\text{LF}}(t)$, is usually quite stable and can be therefore modeled as a straight line in the TF plane (as a sinusoid with constant frequency). To estimate $f_{\text{LF}}(t) = f_{\text{LF}}$, we use the Hough transform [65]. The Hough transform is a technique commonly used to detect line in an image. In the case in which the image domain is the ambiguity domain (τ, ν) and the Hough domain is characterized by parameters (a, b), the Hough transform parametrizes a line as:

$$\tau \cos(a) + \nu \sin(a) = b \tag{4.12}$$

So, the Hough transform associates all the points (τ, ν) with a pencil of sinusoids which intersect themselves in the plane (a, b). It is therefore possible to associate with each line of the ambiguity domain (τ, ν) a point (a, b) which is unique. If in the ambiguity function domain there is some structure concentrated along a straight line, we will observe in the domain of parameters (a, b) a peak whose coordinates are

directly related to the parameters of the line.

Given that the dual of a linear chirp $\delta(f - ct)$ in the ambiguity plane is perfectly concentrated along the line $\delta(\nu - c\tau)$, the Hough transform can be applied to the ambiguity function, $|A(\tau, \nu)|$, to detect the presence of this chirp. This has the advantage that, given that the ambiguity function is highly redundant, just a small part of the ambiguity plane, as for example the region $(\tau, \nu) > 0$, can be used, thus reducing the calculation time.

Once that $\nu_{\mathrm{min}} = \min\left[f_{\mathrm{HF}}(t) - f_{\mathrm{LF}}(t)\right]$ has been estimated, to find the value of ν_0 which assures the elimination of all the outer interferences, one should rewrite the kernel function (4.11) as:

$$\left(\frac{\nu}{\nu_0}\right)^2 + \left(\frac{\tau}{\tau_0}\right)^2 = \left(-\frac{\log(\phi_{\mathrm{d\text{-}D}}(\tau, \nu))}{\pi}\right)^{\frac{1}{2\lambda}} \tag{4.13}$$

The parameter ν_0 is then fixed by imposing that $\phi_{\mathrm{d\text{-}D}}(0, \nu_{\mathrm{min}}) = k << 1$. This conditions results in:

$$\nu_0 = \nu_{\mathrm{min}}\left(\frac{-\log(k)}{\pi}\right)^{-\frac{1}{4\lambda}} = \min\left[f_{\mathrm{HF}}(t) - f_{\mathrm{LF}}(t)\right]\left(\frac{-\log(k)}{\pi}\right)^{-\frac{1}{4\lambda}} \tag{4.14}$$

In the validation of this method, we used a value for $\lambda = 0.25$. With respect to a Gaussian kernel ($\lambda = 0.5$), this value gives a kernel which is sharper around the origin and with higher tails.

In Fig. 4.1, an example of the use of this kernel is shown. In panel (a), $\phi_{\mathrm{d\text{-}D}}(0, \nu)$ is plotted superimposed to the ambiguity function, $A_{\mathrm{xx}}(0, \nu)$, of a non-stationary simulated signal that mimics heart rate variability patterns. In the ambiguity function, the auto terms are concentrated around the origin of the axes, while the outer interference terms are located at $|\nu| > \nu_{\mathrm{min}}$. The kernel completely suppresses the outer interference, being $\phi_{\mathrm{d\text{-}D}}(0, \nu_{\mathrm{min}}) = k = 2 \cdot 10^{-3}$. In this case, the cross components located at $|\nu| > \nu_{\mathrm{min}}$ are completely removed. If a kernel function provides an insufficient smoothing, the outer interferences located around $\pm\nu_{\mathrm{min}}$ are not attenuated and will appear in the TF map. In panel (b), both the ambiguity function and the kernel are shown in the ambiguity domain. The most outer iso-contour of the kernel correspond to $\phi_{\mathrm{d\text{-}D}}(\tau, \nu) = k = 2 \cdot 10^{-3}$. Therefore the interference terms outside this iso-contour are suppressed and do not appear in the TF distribution.

As described in §3.1.1 and shown in Fig. 3.3, inner interferences appear in monocomponent signals and they obey the same geometrical laws as outer interferences. They appear in TF maps of signals whose instantaneous frequency varies non-linearly. Even if in signals related to the autonomic modulation inner interferences are usually smaller than outer ones, their suppression can be difficult due to their vicinity with the signal components. Given that the instantaneous frequency laws usually change gradually, they are observed to oscillate mainly in frequency direction (see Fig. 3.3) and the frequency smoothing (attenuation in τ direction via correct selection of parameter τ_0) is the main responsible of their attenuation.

The same scheme previously used to adjust the smoothing in time (i.e. in ν) can be

applied to adjust the smoothing in frequency (i.e. in τ). To do that, it is necessary to perform a previous analysis to estimate the value of $\tau_{\min}$, i.e. the minimal temporal distance between oscillations characterized by the same frequency. This is a very difficult task, since it requires to make the distinction between stationary or almost stationary oscillations, which are characterized by a null or almost null $\tau_{\min}$, and spectral components that vary non-linearly during time, which are those that generate the interference terms. Given that we are interested in a robust method, i.e. a method that always yields a kernel for which $\hat{\gamma}^{\text{WV}}(t, f) \in [0, 1]$, we opted for an other solution. In order to find a value for τ_0 that provides a good compromise between interferences suppression and TF resolution, an iterative process, similar to that described in the previous paragraph, is used. The parameter τ_0 is gradually reduced (increasing the frequency smoothing) until $\hat{\gamma}^{\text{WV}}(t, f) \in [0, 1]$ in the TF region of interest.

Examples of the use of a signal-dependent kernel obtained by following this geometrical scheme are shown in Fig. 4.1–4.2.

In Fig. 4.2, the effect of three different kernels on the SPWVD of two simulated signals is shown. These signals are simulated as the sum of two complex exponentials embedded in noise. The first exponential mimics an AM LF component, and the second one mimics an AM-FM HF component. In these figures, panels (a)–(b) represent the case of insufficient TF smoothing, provided by a kernel as that shown in Fig. 4.1 and reported in dotted line. Outer interferences are clearly visible at midway between the two components and, as expected, they are higher where the two signal spectral components are closer. In panels (c)–(d), the SPWVD estimated by using in the kernel the value ν_0 obtained by (4.14) is shown. It is free from outer interferences but not from inner ones, which are still well visible in panel (d), close to the HF spectral component. Finally, the SPWVD shown in panels (e)–(f) was obtained by using the same ν_0 as before and the value of parameter τ_0 associated to the lowest frequency smoothing which at the same time makes $\hat{\gamma}^{\text{WV}}(t, f) \in [0, 1]$ in the TF region of interest. As expected, this SPWVD is free from interference terms.

Time-frequency region of interest

The restriction of the TF support of $\hat{\gamma}^{\text{WV}}(t, f)$ to a region of interest is justified by the desire of reducing the TF filtering necessary to obtain $\hat{\gamma}^{\text{WV}}(t, f) \in [0, 1]$. The idea is to estimate time-frequency coherence only in those regions where it really matters, i.e. where both signals have spectral components. This reduces the chance of having to increase the filtering since $\hat{\gamma}^{\text{WV}}(t, f) \notin [0, 1]$ in regions where there is only noise. The TF region of interest is defined as the region $\Omega(t, f) = \Omega_{\text{x}}(t, f) \cap \Omega_{\text{y}}(t, f)$, where each $\Omega_{\text{i}}(t, f)$ is defined as:

$$\Omega_{\text{i}}(t, f) \equiv \left\{ (t, f) \in (\mathbb{R}^+, \mathbb{R}^+) \mid \hat{S}_{\text{i}}^{\text{WV}}(t, f) > a \cdot \max_{\text{f}} \left[\hat{S}_{\text{i}}^{\text{WV}}(t, f) \right] \right\} \tag{4.15}$$

with $a < 1$ and $i \in \{x, y\}$.

An alternative and less restrictive definition for the TF region of interest is $\Omega(t, f) = \Omega_{\text{x}}(t, f) \cup \Omega_{\text{y}}(t, f)$.
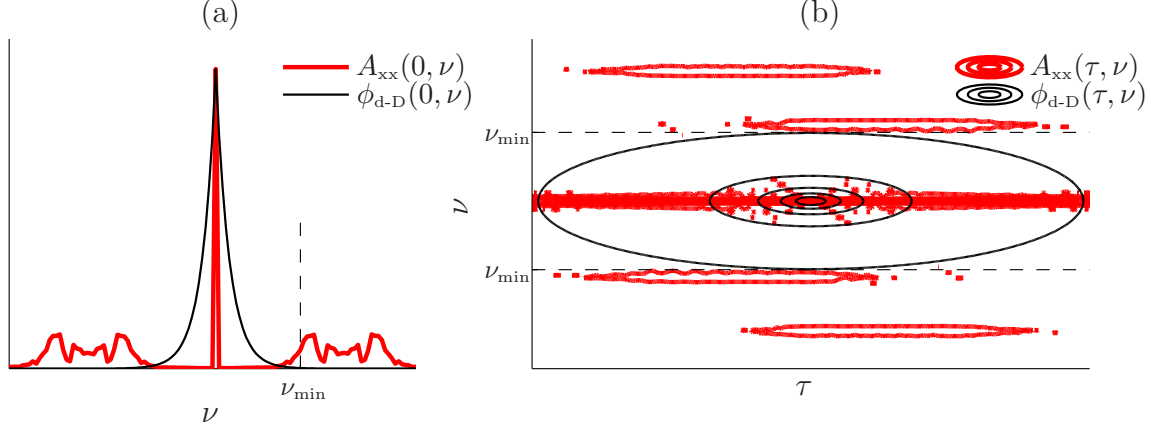
Figure 4.1: (a) kernel $\phi_{\text{d-D}}(0, \nu)$ for outer interferences attenuation. The kernel eliminates interference terms at $\nu > \nu_{\text{min}}$; (b) The iso-contours of the kernel and the ambiguity function reported in the ambiguity domain. The first 4 iso-contours of $\phi_{\text{d-D}}(\tau, \nu)$ correspond to 80%, 60%, 40% and 20%, while the most outer one corresponds to 0.2% of the maximum of $\phi_{\text{d-D}}(\tau, \nu)$.

4.3.3   Simulation study

In this section, we assess the estimation error of the band coherence. Band coherence is a time-varying index, obtained by averaging time-frequency coherence in a given time-frequency region. Its general expression reads as:

$$\gamma_{\text{B}}(t) = \int_B \gamma(t, f) df \Big/ \int_B df \tag{4.16}$$

where B represent a spectral band, which can be time-varying.
The bias, standard deviation and tracking capability of band coherence estimation have been assessed by means of synthetic signals characterized by known and controlled theoretical coupling. Pairs of signals $[x_1(t), x_2(t)]$ are created adding uncorrelated noises to an original signal $x(t)$:

$$x_1(t) = x(t) + \xi_1(t); \quad \xi_1(t) = \sigma_1(t)\eta_1(t) \tag{4.17}$$
$$x_2(t) = x(t) + \xi_2(t); \quad \xi_2(t) = \sigma_2(t)\eta_2(t) \tag{4.18}$$

where $\eta_i(t)$, with $i \in \{1, 2\}$, are zero-mean unit-variance white Gaussian noises.
The Wigner-Ville distributions of these signals are:

$$W_{11}(t, f) = W_{\text{xx}}(t, f) + W_{\xi_1\xi_1}(t, f) + 2\Re\left\{W_{x\xi_1}(t, f)\right\} \tag{4.19}$$
$$W_{22}(t, f) = W_{\text{xx}}(t, f) + W_{\xi_2\xi_2}(t, f) + 2\Re\left\{W_{x\xi_2}(t, f)\right\} \tag{4.20}$$
$$W_{12}(t, f) = W_{\text{xx}}(t, f) + W_{x\xi_1}(t, f) + W_{\xi_2 x}(t, f) + W_{\xi_2\xi_1}(t, f) \tag{4.21}$$

where $W_{x\xi_1}(t, f)$ is the cross WVD of the original signal $x(t)$ and $\xi_1(t)$. Considering that $\xi_1(t)$ and $\xi_2(t)$ are orthogonal and supposing that the smoothing function $\phi_{\text{t-f}}(t, f)$
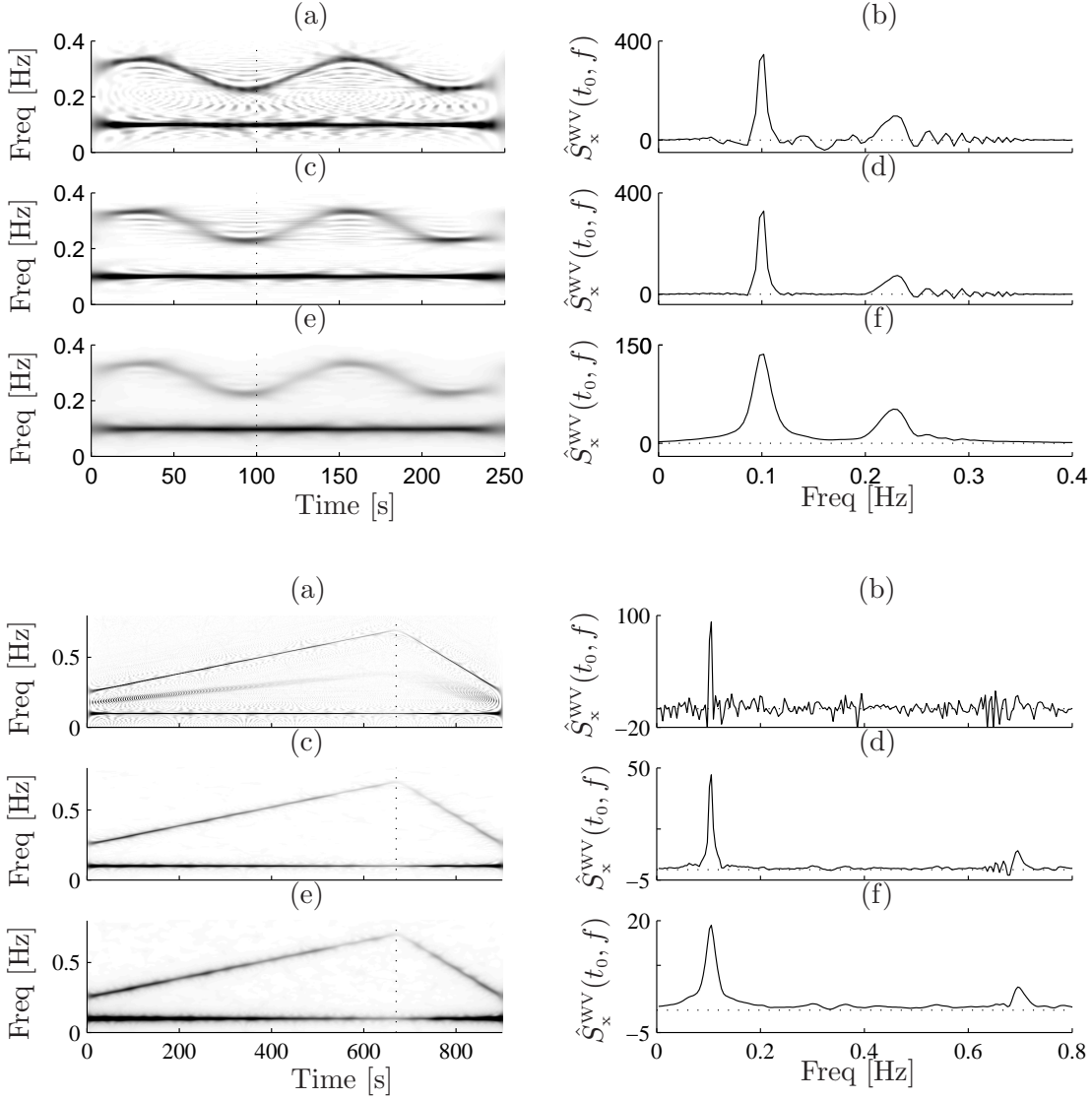
Figure 4.2: Two example of elimination of the interference terms of the SPWVD by adjusting the geometry of the kernel to the time-frequency structure of the signals. Left: auto TF spectra $\hat{S}_x^{\mathrm{wv}}(t, f)$; SNR=10dB; Right: $\hat{S}_x^{\mathrm{wv}}(t_0, f)$, with t_0 marked by a dotted line in the left panels. (a)–(b): insufficient smoothing. (c)–(d): smoothing performed with a kernel optimized for outer interferences suppression, as in (4.14). (e)–(f): smoothing performed with a kernel optimized for both outer and inner interferences attenuation. Outer interferences clearly appear in (a) between LF and HF components, while inner interferences clearly appear in (a)–(d) close to the HF peak. Note that y-axis in right side panels are different.

(a) (b)

— HF
...... LF
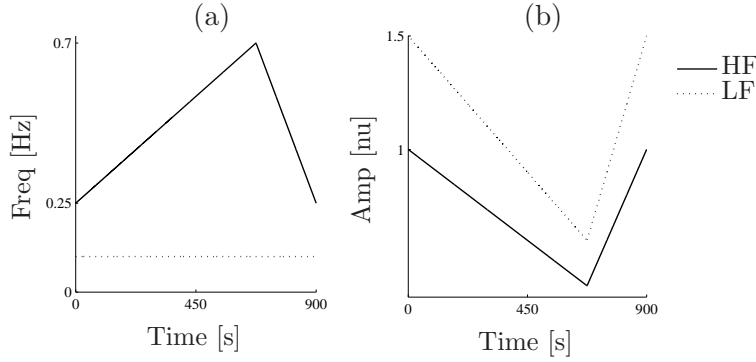
Figure 4.3: Time-course of the spectral components of the signals used in the simulation study to assess the TF coherence function based on the SPWVD

completely suppress the cross terms, it is possible to approximate the precedent relations as:

$$\hat{S}_{11}^{\mathrm{W}}(t,f) = \hat{S}_{\mathrm{xx}}^{\mathrm{W}}(t,f) + \hat{S}_{\xi_1\xi_1}^{\mathrm{W}}(t,f) \tag{4.22}$$

$$\hat{S}_{22}^{\mathrm{W}}(t,f) = \hat{S}_{\mathrm{xx}}^{\mathrm{W}}(t,f) + \hat{S}_{\xi_2\xi_2}^{\mathrm{W}}(t,f) \tag{4.23}$$

$$\hat{S}_{12}^{\mathrm{W}}(t,f) = \hat{S}_{\mathrm{xx}}^{\mathrm{W}}(t,f) \tag{4.24}$$

Imposing $\sigma_1(t) = \sigma_2(t) = \sigma(t)$, we have that $\hat{S}_{\xi_1\xi_1}^{\mathrm{WV}}(t,f) = \hat{S}_{\xi_2\xi_2}^{\mathrm{WV}}(t,f) = \sigma^2(t)$, and the theoretical time-frequency coherence is derived from (4.10):

$$\gamma^{\mathrm{WV}}(t,f) = \frac{\left|\hat{S}_{\mathrm{xx}}^{\mathrm{WV}}(t,f)\right|}{\sqrt{\left(\hat{S}_{\mathrm{xx}}^{\mathrm{WV}}(t,f)\right)^2 + 2\hat{S}_{\mathrm{xx}}^{\mathrm{WV}}(t,f)\sigma^2(t) + \sigma^4(t)}} \tag{4.25}$$

where $\hat{S}_{\mathrm{xx}}^{\mathrm{WV}}(t,f)$ is the SPWVD of $x(t)$. Expression (4.25) is used to assess the estimation error for different levels of coherence. In the following, the error in the band coherence estimation is evaluated. Theoretical band coherence, $\gamma_{\mathrm{B}}^{\mathrm{WV}}(t)$, and estimated band coherence, $\hat{\gamma}_{\mathrm{B}}^{\mathrm{WV}}(t)$, are obtained by averaging $\gamma^{\mathrm{WV}}(t,f)$ and $\hat{\gamma}^{\mathrm{WV}}(t,f)$ in a predetermined spectral band $B(t)$. The width of the spectral band $B(t)$, reported for each case in Table 4.1, is chosen requiring that up to 95% of the theoretical energy content of the spectral components of interest was concentrated in $B(t)$.

Specific situations, aiming at evaluating the performance of the time-frequency coherence estimator based on the signal-dependent filtering of the SPWVD, in different physiological contexts, have been modeled by means of signals of type (4.33):

- *I*. Band coherence $\gamma_{\mathrm{B}}^{\mathrm{WV}}(t)$ is constant over time:
  (*a*) The original signal $x(t)$ is a white noise.
  (*b*) The original signal $x(t)$ mimics a respiratory signal during stress testing, whose spectral component is described in Fig. 4.3 by continuous lines.
  (*c*) The original signal $x(t)$ mimics an AM-FM HRV signal during stress testing, whose spectral components are described in Fig. 4.3.
  Two hundred pairs of signals $[x_1(t), x_2(t)]$ have been created, for each theoretical coherence level, from 0.1 to 0.95 in steps of 0.05.

Table 4.1: simulation parameters

	$I(a)$	$I(b)$	$I(c)$	II
Type	T-inv	T-inv	T-inv	TV
$x(t)$	$\eta(t)$	RESP	HRV	HRV
$B(t)$ [Hz]	[0,2]	$f_{\mathrm{HF}}(t) \pm 0.075$	$f_{\mathrm{HF}}(t) \pm 0.05$	$f_{\mathrm{HF}}(t) \pm 0.05$

- *II*. Band coherence $\gamma_{\mathrm{B}}^{\mathrm{WV}}(t)$ is time-varying. Signal $x(t)$ is of type $I(c)$ (see Fig. 4.3) and three different time courses of band coherence $\gamma_{\mathrm{B}}^{\mathrm{WV}}(t)$ are modeled and described by gray line in Fig. 4.6:
  (a) $\gamma_{\mathrm{B}}^{\mathrm{WV}}(t)$ linearly decreases.
  (b) $\gamma_{\mathrm{B}}^{\mathrm{WV}}(t)$ decreases stepwise.
  (c) $\gamma_{\mathrm{B}}^{\mathrm{WV}}(t)$ is high except during short and abrupt decorrelating events.
  In these cases, 1000 pairs of signals $[x_1(t), x_2(t)]$ have been created and $\hat{\gamma}_{\mathrm{B}}^{\mathrm{WV}}(t)$ is estimated in mean and standard deviation over all realizations. Simulation parameters are summarized in Table 4.1.

Note that when $x(t)$ is a white noise (case $I(a)$), $\gamma_{\mathrm{B}}^{\mathrm{WV}}(t)$ represents a global (not localized in time and frequency) estimation, while in the other cases a localized band coherence estimation is performed. The knowledge of $f_{\mathrm{HF}}(t)$ is included in the kernel design to estimate ν_0 as in (4.14). This is not a strong assumption, given that it can be easily approximated by a direct or indirect estimation of respiratory rate. In the calculation, parameters a, λ and k were equal to 0.01, 0.25 and 0.002 respectively.

Results of case I are shown in Fig. 4.4–4.5 and results of case II are shown in Fig. 4.6.

In the simulations of case I, in which band coherence was constant over time, the bias was very low (< 0.05) for $\gamma_{\mathrm{B}}^{\mathrm{WV}}(t) > 0.5$, and the standard deviation was always small. In the simulations of case II, in which both the time-frequency structure of the signals and the band coherence were time-varying, the estimator performed very well for gradual and slow coherence changes (Fig. 4.6a). In case of abrupt changes (Fig. 4.6b) the estimator took few seconds to properly adjust to the new values, while when short decorrelating events appear (Fig 4.6c) the estimator was able to correctly localized them, even if with a higher bias.

4.4 Time-frequency coherence by multitaper spectrogram (MTSP-TFC)

The spectrogram is another estimator of the Wigner-Ville spectrum (4.4), defined as [124, 92]:

$$\hat{S}_{\mathrm{xy}}^{\mathrm{S}}(t,f) = \left[\mathcal{F}_{\tau \to f} \left\{ x(\tau) h(\tau - t) \right\} \right] \left[\mathcal{F}_{\tau \to f} \left\{ y(\tau) h(\tau - t) \right\} \right]^* \qquad (4.26)$$

where $h(t)$ is used to window the signal before taking its Fourier transform. As the SPWVD, the spectrogram can also be seen as a member of the Cohen's class, esti-
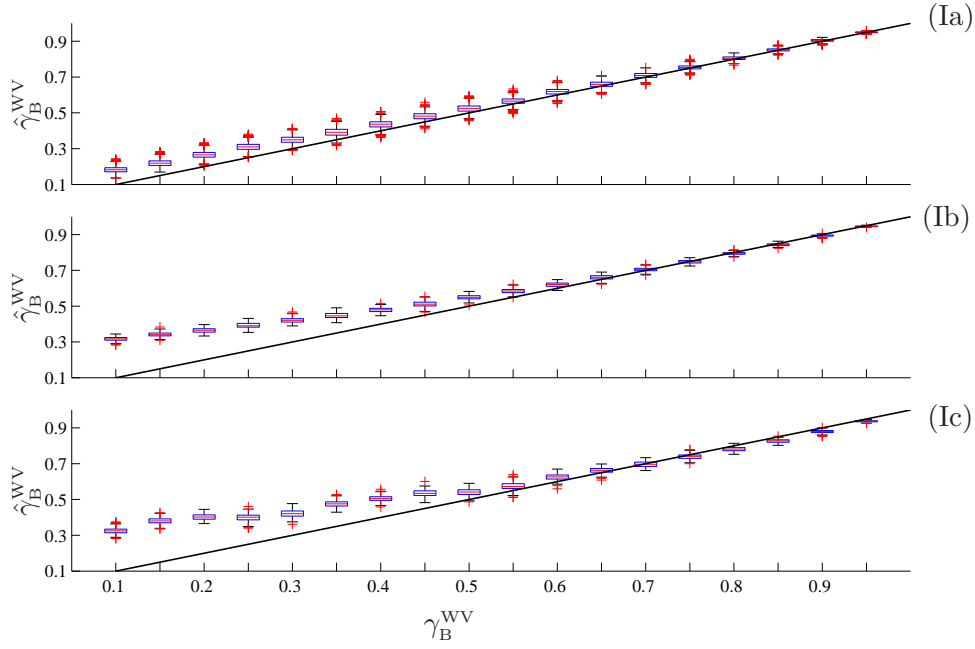
Figure 4.4: Results of the simulation study based on signals of Type I, to assess the TF coherence by SPWVD, obtained by the geometrical scheme (§4.3.2).
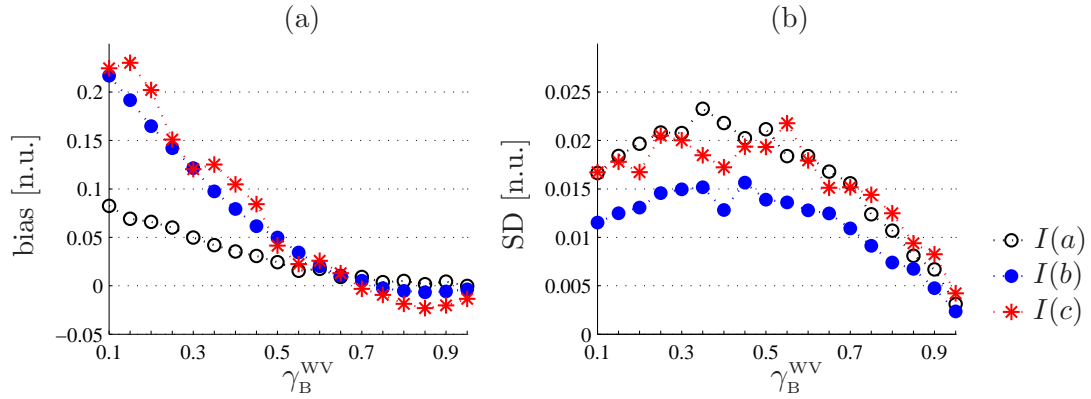
Figure 4.5: Results of the simulation study based on signals of Type I to assess the TF coherence function based on the SPWVD: bias (a) and SD (b).
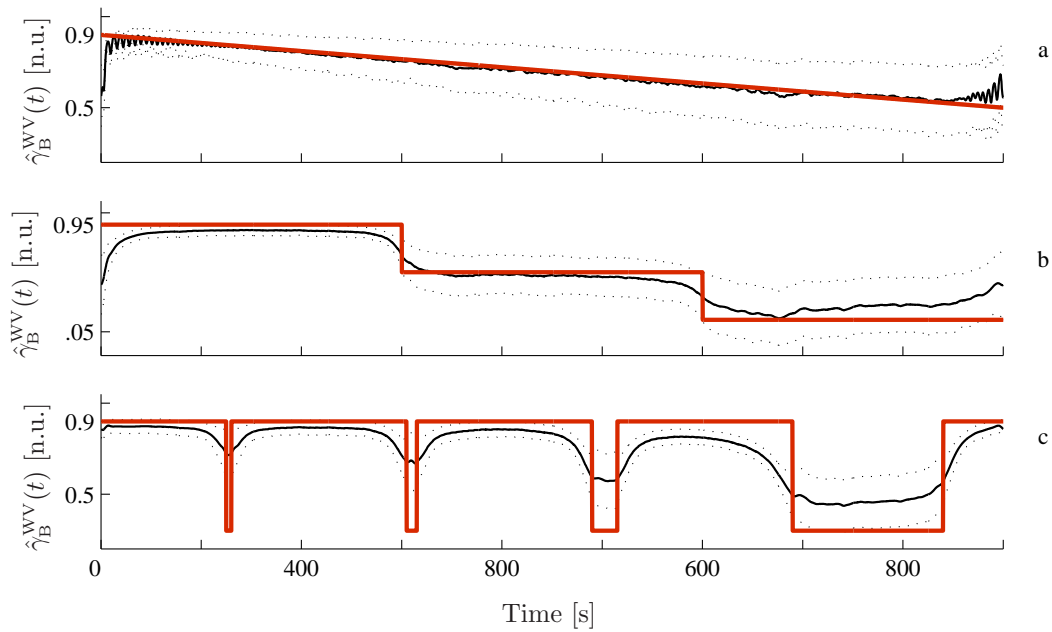
Figure 4.6: Results of the simulation study based on signals of Type II, to assess the TF coherence by SPWVD, obtained by the geometrical scheme (§4.3.2). Gray lines: $\gamma_B^{\mathrm{WV}}(t)$, black and dotted lines: mean trend $\pm$ SD of $\gamma_B^{\mathrm{WV}}(t)$
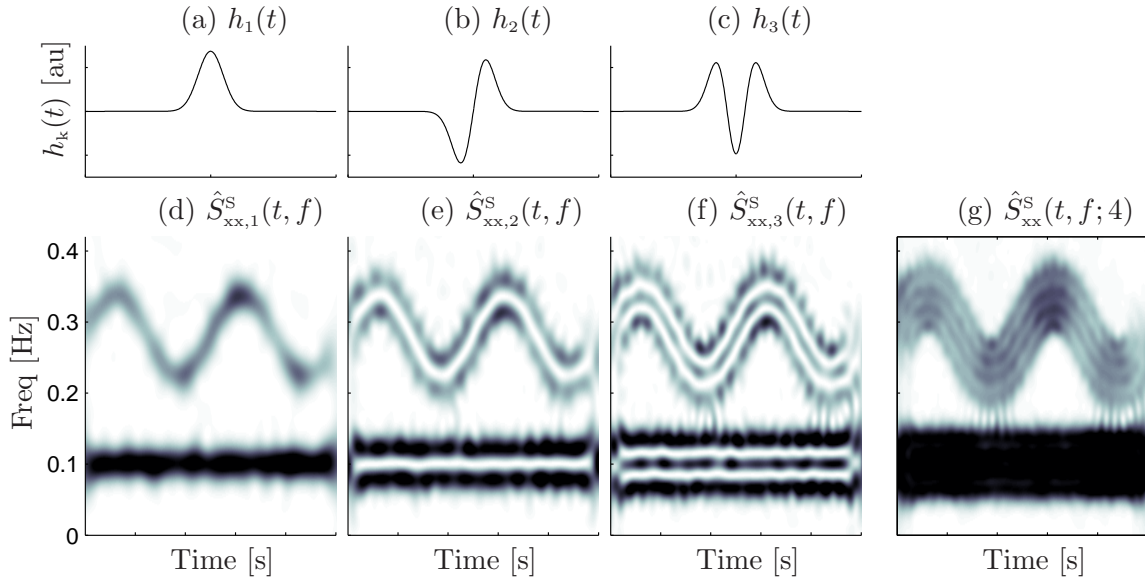
Figure 4.7: Example of estimation of multitaper spectrogram. (a)–(c) The first, second and third Hermite functions. (d)–(f) The spectrograms which correspond to the Hermite functions plotted above. (g) The multitaper spectrogram, $\hat{S}^{\mathrm{S}}(t, f)$ estimated by averaging 4 spectrograms (the three spectrograms shown in (d)–(f) and another one which is not shown).

mated by using (4.7) and replacing $\phi_{\text{t-f}}(t, f)$ with the WVD of $h(t)$, $W_{\text{hh}}(t, f)$.

The advantages of the spectrogram are the reduced level of interference terms and that it is non-negative. Shortcomings are related to the poor joint TF resolution given by $h(t)$: the impossibility of independently adjusting the smoothing in time and frequency leads to the well known trade-off for which the better a signal component is localized in time (or frequency), the worse it is localized in frequency (or time).

Moreover, spectrograms as defined in (4.26) can not be used in single-trial coherence analysis, since from (4.26) follows that $\left|\hat{S}^{\text{S}}_{\text{xy}}(t, f)\right|^2 = \hat{S}^{\text{S}}_{\text{xx}}(t, f)\hat{S}^{\text{S}}_{\text{yy}}(t, f)$ and the time-frequency coherence estimates given by the spectrogram are equal to one over the entire TF domain.

In a statistical sense, the spectrogram is an inconsistent estimator of the Wigner-Ville spectrum (4.4), with a variance of the order of the squared Wigner-Ville spectrum [92].

The multitaper spectrogram (MTSP) is a TF estimator introduced to improve the bias-variance trade-off of the traditional spectrogram [37, 36, 244]. It is based on a multitaper approach, originally proposed to improve the estimation of the power spectral density of a stationary process [242, 243]. The MTSP is computed by averaging different spectrograms, estimated by using a set of orthogonal windows $h_{\text{k}}(t)$, and is defined as [37]:

$$\hat{S}^{\text{S}}_{\text{xy}}(t, f; K) = \frac{1}{K}\sum_{\text{k}=1}^{\text{K}}\left[\mathcal{F}_{\tau \to f}\left\{x(\tau)h_{\text{k}}(\tau - t)\right\}\right]\left[\mathcal{F}_{\tau \to f}\left\{y(\tau)h_{\text{k}}(\tau - t)\right\}\right]^* \quad (4.27)$$

where $h_{\text{k}}(t)$ are Hermite functions, which are used since they are optimally concentrated in a circular TF region [256, 37]. They are estimated as [254]:

$$h_{\text{k}}(t) = e^{-\frac{t^2}{2}}\mathcal{H}_{\text{k}}(t)/\sqrt{\pi^{\frac{1}{2}}2^k k!} \quad (4.28)$$

where $\mathcal{H}_{\text{k}}(t)$, with $k \in \mathbb{N}$, stands for Hermite polynomials, which obey the recursion:

$$\mathcal{H}_{\text{k}}(t) = 2t\mathcal{H}_{\text{k-1}}(t) - 2(k - 2)\mathcal{H}_{\text{k-2}}(t), \quad k \geq 2 \quad (4.29)$$

with the initialization $\mathcal{H}_0(t)=1$, $\mathcal{H}_1(t)=2t$.

Time and frequency resolutions are quantified by indices Δ^{m} and $\Delta^{\text{(a\%)}}$ estimated from the MTSP of a Dirac impulse $\delta(t - t_0)$, $\hat{S}^{\text{S}}_{\delta\delta}(t, f_0) = \frac{1}{K}\sum_{\text{k}=1}^{\text{K}} h_{\text{k}}^2(t - t_0)$, and that of a complex exponential $e^{j2\pi f_0 t}$, $\hat{S}^{\text{S}}_{\text{ee}}(t_0, f) = \frac{1}{K}\sum_{\text{k}=1}^{\text{K}}|H_{\text{k}}(f - f_0)|^2$, where $H_{\text{k}}(f)$ is the Fourier transform of $h_{\text{k}}(t)$.

It is worth noting that the kernel function $\phi_{\text{t-f}}(t, f)$ of a spectrogram in which the sliding window $h_{\text{k}}(t)$ is a Hermite function is a Laguerre function [94, 37]:

$$W_{\text{h}_k \text{h}_k}(t, f) = \exp\left(-\frac{\pi}{2}(t^2 + f^2)\right)\sum_{\text{m}=0}^{\text{k}} \frac{k!}{(k - m)!m!}\frac{[-\pi(t^2 + f^2)]^{\text{m}}}{m!} \quad (4.30)$$

The kernel obtained by using only four Hermite functions, the sum of four Laguerre functions, well approximates the "top hat" function [37]. The representation of the kernel in the ambiguity function domain is also related to the Laguerre functions

[94, 103].

An illustrative example of how the multitaper spectrogram is estimated is shown in Fig. 4.7. In this example, synthetic signals obtained as the sum of two non-stationary complex exponentials embedded in noise are used. In the upper graphics, (a)–(c), the first, second and third Hermite functions are shown. In the lower graphics, (d)–(f), the spectrograms which correspond to the Hermite functions plotted above are shown. Finally, the multitaper spectrogram, $\hat{S}_{xx}^{s}(t, f)$ is shown in panel (g). This distribution is estimated by averaging $K = 4$ spectrograms (the three spectrograms shown in (d)–(f) and another one which is not shown).

Time-frequency coherence by multitaper spectrogram (MTSP-TFC) is obtained as:

$$\hat{\gamma}^{s}(t, f) = \frac{\left| \hat{S}_{xy}^{s}(t, f; K) \right|}{\sqrt{\hat{S}_{xx}^{s}(t, f; K) \hat{S}_{yy}^{s}(t, f; K)}} \tag{4.31}$$

4.5   Statistical analysis

As in stationary contest, time-frequency coherence estimates are not meaningful *per se*, but they strongly depend on the parameters used in its calculation [57, 86]. The local averaging provided by the smoothing function $\phi_{\text{t-f}}(t, f)$, causes the time-frequency coherence estimates of two uncorrelated signals to be higher than zero. This dependence introduces an uncertainty in the interpretation of the coherence level. The problem is that a given coherence estimate, although high, could be lower than that estimated between uncoupled processes. To reduce this uncertainty and to localize TF regions characterized by a significant coherence level, a hypothesis test is used. The test is based on the point-by-point comparison of the time-frequency coherence estimates, $\hat{\gamma}(t, f)$, with a threshold function, $\gamma_{\text{TH}}(t, f)$, obtained by estimating the time-frequency coherence between several realizations of locally uncoupled signals.

In the statistical procedure, the null hypothesis H_0 to be rejected states that two signals $x(t)$ and $y(t)$, with time-frequency coherence $\gamma(t, f)$, are uncorrelated around a point (t_0, f_0).

The procedure consists of the following steps:

(i) Generate uncorrelated test signals $\tilde{x}_{j}(t)$ and $\tilde{y}_{j}(t)$.

(ii) Compute the statistical distribution $\Gamma(t, f) = \{\hat{\gamma}_{1}(t, f), ..., \hat{\gamma}_{j}(t, f), ...\}$, where $\hat{\gamma}_{j}(t, f)$ is the TFC between the j-th realization of test signals $\tilde{x}_{j}(t)$ and $\tilde{y}_{j}(t)$;

(iii) Estimate the threshold $\gamma_{\text{TH}}(t, f; \alpha)$, corresponding to the desired significance level α. According to this framework, α is the probability of wrongly rejecting the null hypothesis, and $\gamma_{\text{TH}}(t, f; \alpha)$ is estimated point-by-point as the $(1 - \alpha)$-th percentile of $\Gamma(t, f)$;

(iv) Determine a TF mask $\mathcal{M}(t, f; \alpha)$ that identifies those regions in which the null hypothesis can be rejected:

$$\begin{cases} \mathcal{M}(t, f; \alpha) = 1, & \text{if } \hat{\gamma}(t, f) > \gamma_{\text{TH}}(t, f; \alpha) \text{ coupling} \\ \mathcal{M}(t, f; \alpha) = 0, & \text{if } \hat{\gamma}(t, f) \leq \gamma_{\text{TH}}(t, f; \alpha) \text{ no coupling} \end{cases} \tag{4.32}$$

A priori, the threshold function $\gamma_{\mathrm{TH}}(t, f; \alpha)$ should depend on the geometry of the kernel used in the calculation of time-frequency coherence and on the time-frequency structure of the analyzed signals.

In this study, a signal dependent and a signal independent threshold functions are used.

The approach proposed in this secction is based on surrogate data analysis [230]. This kind of techniques have been recently used in many aspects of spectral analysis [50, 51, 86, 89, 87].

Signal independent threshold (SITH)

Test signals $\tilde{x}_j(t)$ and $\tilde{y}_j(t)$ are white noises. In this case, the threshold $\gamma_{\mathrm{TH}}^{\mathrm{SI}}(t, f; \alpha)$ will only depend on the kernel and is expected to be constant over the entire time-frequency domain. This can be seen both as an inconvenience, since SITH is not specific for the signals being analyzed, and as an advantage, since it can be used to statistically assess the statistical level of any time-frequency coherence function obtained by using the same kernel. In a population study, this greatly reduces the computational cost of the analysis.

Signal dependent threshold (SDTH)

The estimation of SDTH involves three steps:

- (i) Estimate $\gamma_{\mathrm{TH}}^{\mathrm{X}}(t, f)$ from distribution $\Gamma_x(t, f) = \{\hat{\gamma}_{x,1}(t, f), \ldots, \hat{\gamma}_{x,j}(t, f), \ldots\}$, where $\hat{\gamma}_{x,j}(t, f)$ is the TFC between signal $x(t)$ and the j-th realization of a white noise.
- (ii) Estimate $\gamma_{\mathrm{TH}}^{\mathrm{Y}}(t, f)$ from distribution $\Gamma_y(t, f) = \{\hat{\gamma}_{y,1}(t, f), \ldots, \hat{\gamma}_{y,j}(t, f), \ldots\}$, where $\hat{\gamma}_{y,j}(t, f)$ is the TFC between signal $y(t)$ and the j-th realization of a white noise.
- (iii) Signal dependent threshold is obtained as $\gamma_{\mathrm{TH}}^{\mathrm{SD}}(t, f; \alpha) = \max\{\gamma_{\mathrm{TH}}^{\mathrm{X}}(t, f; \alpha), \gamma_{\mathrm{TH}}^{\mathrm{Y}}(t, f; \alpha)\}$.

4.6 A comparative study between time-frequency coherence by SPWVD and MTSP

A comparative study is carried on to assess the capability of the SPWVD (see §4.3) and MTSP (see §4.4) to provide coherence estimates that correctly localize time-frequency regions characterized by local coupling and/or characterized by the lack of local coupling. The overall aim of this comparison is to highlight advantages and drawbacks of both time-frequency estimators, in order to give to the users useful information to decide which methodology is more appropriate to analyze a given data set.

The comparison includes a simulation study as well as recorded physiological data analysis. Particular attention is paid to the quantification of the time-frequency resolution of both estimators. The wavelet coherence will be also considered in the comparison.

4.6.1 Simulation study

Signals affected by the autonomic nervous modulation, such as heart rate variability, blood pressure variability, respiratory signal, pulse transit time variability etc., may be modeled as the sum of complex exponentials showing both amplitude and frequency modulation, embedded in noise:

$$x(t) = A_{x,LF}(t)e^{i\theta_{x,LF}(t)} + A_{x,HF}(t)e^{i\theta_{x,HF}(t)} + \xi_x(t) \tag{4.33}$$
$$y(t) = A_{y,LF}(t)e^{i\theta_{y,LF}(t)} + A_{y,HF}(t)e^{i\theta_{y,HF}(t)} + \xi_y(t)$$

where $\xi_x(t)$ and $\xi_y(t)$ are two independent white Gaussian noises and subscripts LF and HF stay for low frequency and high frequency range. Instantaneous phases and frequencies are related by $f(t) = (d\theta(t)/dt)/(2\pi)$.

The time-course of the signal components used in this simulation are shown in Fig. 4.8a–d. Signals $x(t)$ and $y(t)$ can be seen as locally coupled, since their spectral components share the same instantaneous frequencies and their amplitudes vary slowly. They are expected to be coupled over all the time-frequency domain except in three localized regions.

- During T_1, which lasts 15 s, both LF and HF components are uncoupled, since $A_{y,LF}(T_1) = A_{y,HF}(T_1) = 0$.
- During T_2, which lasts 85 s, signals are uncoupled in LF, since $A_{y,LF}(T_2) = 0$.
- During T_3, which lasts 50 s, signals are uncoupled in HF, since $A_{y,HF}(T_3) = 0$.

The correct identification of the TF regions where signals are coupled/uncoupled is challenging since both instantaneous frequencies and amplitudes of the signals are time-varying. From a physiological viewpoint, the time-course of the instantaneous frequency of the HF components, $f_{x,HF}(t)$ and $f_{y,HF}(t)$, cover the range of possible respiratory frequencies observed in many autonomic tests, and it may correspond to a pattern observed during some respiratory disorders, such as periodic breathing. From a theoretic viewpoint, the tracking of time-varying spectral components characterized by sinusoidal frequency modulation is challenging, due to the high level of inner interference terms which characterizes signals with such a modulation [125]. Moreover, $f_{x,HF}(t)$ and $f_{y,HF}(t)$ reach values as low as 0.18 Hz (10.8 breaths/min), mimicking slow breathing. In such a situation, the localization of the LF and HF components is even more challenging and requires high TF resolution.

The capability of the time-frequency coherence estimators to track the changes described above is quantified in terms of accuracy. Gold standards are represented by functions $c_{LF}(t)$ and $c_{HF}(t)$, which by definition are equal to 1 when signals are coupled and to 0 when signals are uncoupled at $f = f_{LF}(t)$ and $f = f_{HF}(t)$, respectively (see Fig. 4.8e–f).

At each TF point $(t_0, f_B(t_0))$ outcomes are classified as true or false positive or negative according to the scheme shown in Table 4.2, in which $B = \{LF,HF\}$ and $\mathcal{M}(t, f; \alpha)$ is defined in (4.32).

According to this scheme, a low sensitivity (or specificity) corresponds to the identification of intervals of local coupling (or uncoupling) shorter than the true ones.

Accuracy is given by AC=(TP+TN)/(TP+TN+FP+FN).

Test outcome	Golden standard	
	$c_{\mathrm{B}}(t_0) = 1$	$c_{\mathrm{B}}(t_0) = 0$
$\mathcal{M}(t_0, f_{\mathrm{B}}(t_0); \alpha) = 1$	True positive (TP)	False positive (FP)
$\mathcal{M}(t_0, f_{\mathrm{B}}(t_0); \alpha) = 0$	False negative (FN)	True negative (TN)

Table 4.2: Detection scheme. $B = \{\mathrm{LF,HF}\}$ and $\mathcal{M}(t, f; \alpha)$ is defined in (4.32)
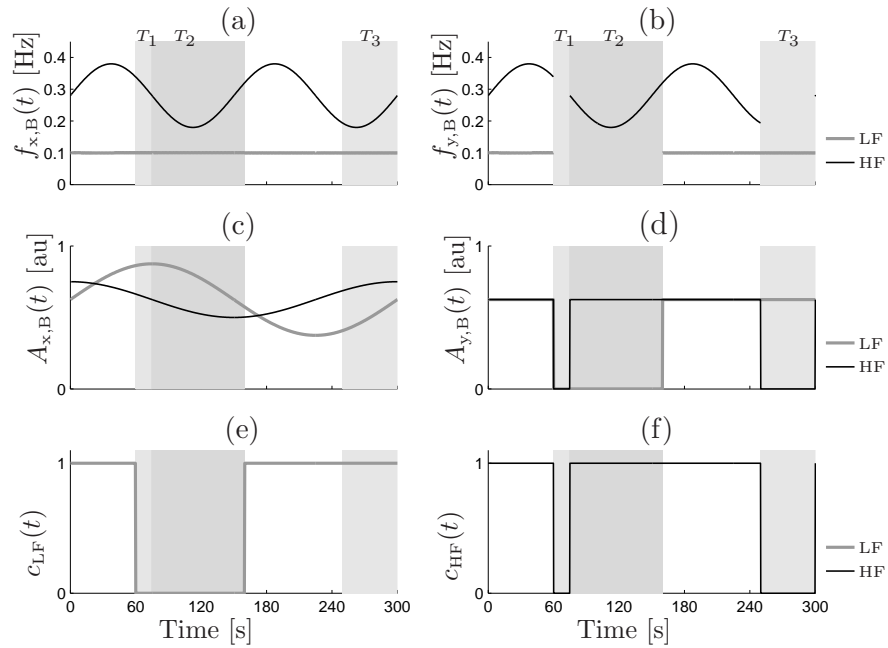
Figure 4.8: Simulation study. (a)–(d): Instantaneous frequencies, $f_{\mathrm{k,B}}(t)$, and amplitudes, $A_{\mathrm{k,B}}(t)$, of LF and HF components of signal $x(t)$ and $y(t)$ (4.33). (e)–(f) Theoretical coherence patterns $c_{\mathrm{B}}(t)$ in LF and HF bands. Shadowed areas correspond to interval of uncoupling in both LF and HF (T_1), in LF (T_2) and in HF (T_3).

The effect of the kernel on coherence estimates

Signal independent threshold: The relation between the mean value of the signal independent threshold function, $\overline{\gamma_{\text{TH}}^{\text{SI}}}$, and the TF resolution is shown in Fig. 4.9. $\overline{\gamma_{\text{TH}}^{\text{SI}}}$ was obtained by collecting the TFC of 250 couples of white noise, and with $\alpha = 5\%$. This figure reveals the strong dependence of the coherence estimates on the geometry of the kernel, thus confirming the need of a statistical test to assess the local coupling. Depending on the kernel, $\overline{\gamma_{\text{TH}}^{\text{SI}}}$ can take values as high as 0.9, and it is higher for lower degree of smoothing. This implies that, without an appropriate statistical test, it is easy to wrongly detect local coupling.

For each combination of time and frequency resolution, the coefficient of variation of $\gamma_{\text{TH}}^{\text{SI}}(t, f)$ never exceeded 3%, and $\overline{\gamma_{\text{TH}}^{\text{SI}}}$ stabilized after processing about 75 noise realizations. This shows that the threshold is uniform over the TF domain and suggests that only few pairs of white noises are necessary to reliably estimate the threshold value.

Figure 4.9a shows that for the time-frequency coherence obtained by MTSP, signal independent threshold, $\overline{\gamma_{\text{TH}}^{\text{SI}}}$, decreased by increasing the number of tapers K, while, for a given number of tapers, $\overline{\gamma_{\text{TH}}^{\text{SI}}}$ was almost independent from the different combinations of time and frequency resolution. This is likely due to the fact that, for a given taper k, the TF support of the kernel associated to different $h_{\text{k}}(t)$ is approximately the same (when the width of $h_{\text{k}}(t)$ increases, the width of $|H_{\text{k}}(f)|$ decreases).

Figure 4.9b shows that for the time-frequency coherence obtained by SPWVD, the signal independent threshold, $\overline{\gamma_{\text{TH}}^{\text{SI}}}$, was inversely related to the degree of TF smoothing. It is worth noting that not all the combinations of time and frequency smoothing provided a degree of filtering sufficient to get $\hat{\gamma}^{\text{W}}(t, f) \in [0, 1]$. For instance, when frequency resolution $\Delta_{\text{f}}^{\text{m}} = 0.031$ Hz (symbol $*$) was combined with a time resolution $\Delta_{\text{t}}^{\text{m}} < 18$ s, $\hat{\gamma}^{\text{W}}(t, f) \notin [0, 1]$. In this example, the finest resolution of the SPWVD were: $(\Delta_{\text{t}}^{\text{m}}, \Delta_{\text{f}}^{\text{m}}) \approx (18\text{s}, 0.031\text{Hz}), (12\text{s}, 0.047\text{Hz}), (9\text{s}, 0.086\text{Hz})$. For the same $\Delta_{\text{t}}^{\text{m}}$, the MTSP with $K = 4$ gave much lower $\Delta_{\text{f}}^{\text{m}}$, being $(\Delta_{\text{t}}^{\text{m}}, \Delta_{\text{f}}^{\text{m}}) \approx (18\text{s}, 0.203\text{Hz}), (12\text{s}, 0.305\text{Hz}), (9\text{s}, 0.402\text{Hz})$.

Signal dependent threshold. Figure 4.10 represents the signal dependent threshold, $\gamma_{\text{TH}}^{\text{SD}}(t, f)$, corresponding to signals described in Fig. 4.8, characterized by SNR equal to 20, 5 and -10 dB. Thresholds were obtained by using, for both $\Gamma_{\text{x}}(t, f)$ and $\Gamma_{\text{y}}(t, f)$, 250 realizations of test signals, and $\alpha = 5\%$. Threshold $\gamma_{\text{TH}}^{\text{SD}}(t, f)$ estimated by SPWVD reflects the narrow band structure of the signals, at least for high SNR level, while $\gamma_{\text{TH}}^{\text{SD}}(t, f)$ estimated by MTSP is constant over the TF domain. In the following, given that for MTSP $\gamma_{\text{TH}}^{\text{SD}}(t, f) \approx \gamma_{\text{TH}}^{\text{SI}}(t, f)$, the statistical test for MTSP-TFC will be performed by SITH only.

Results of the simulation study

The choice of the parameters for the kernel $\phi_{\text{t-f}}(t, f)$ and tapers $h_{\text{k}}(t)$ should be based on some a priori assumptions or on previous analysis about the time-frequency structure of the signals [206, 100]. Taking into account the time-course of the spectral components of signals $x(t)$ and $y(t)$ shown in Fig. 4.8, one could require to use a TF
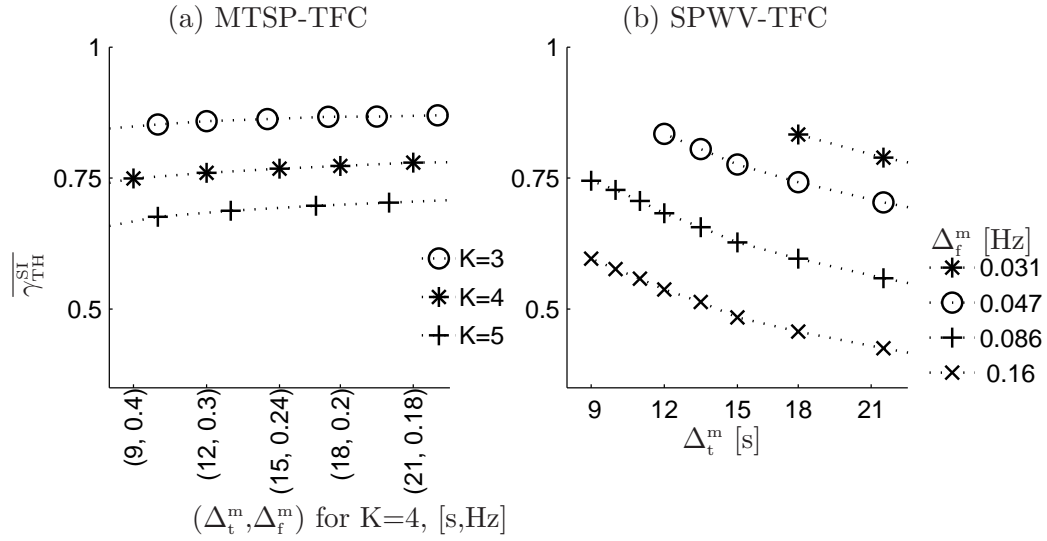
Figure 4.9: Signal independent thresholds $\overline{\gamma_{\mathrm{TH}}^{\mathrm{SI}}}$, with α=5%, corresponding to different TF resolutions. (a) $\overline{\gamma_{\mathrm{TH}}^{\mathrm{SI}}}$ by MTSP: Results are obtained by using $K=\{3,4,5\}$ Hermite functions. (b) $\overline{\gamma_{\mathrm{TH}}^{\mathrm{SI}}}$ by SPWV: Time resolution $\Delta_{\mathrm{t}}^{\mathrm{m}}$ is reported on the horizontal axis, frequency resolution $\Delta_{\mathrm{f}}^{\mathrm{m}}$ is coded by different symbols.
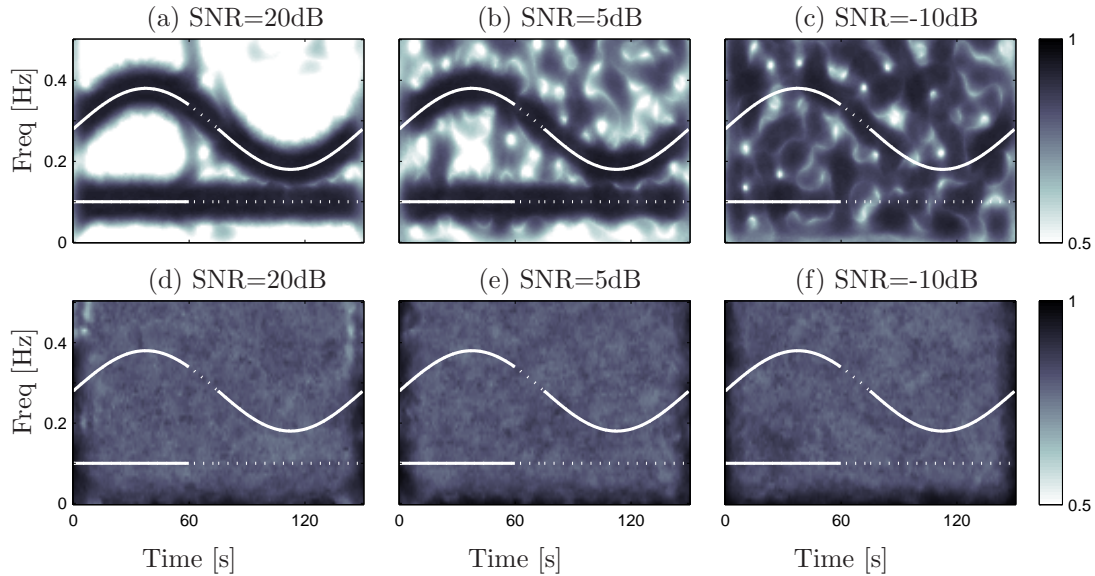
Figure 4.10: Signal-dependent threshold $\gamma_{\mathrm{TH}}^{\mathrm{SD}}(t, f)$ for (a)–(c) SPWV-TFC and (d)–(f) MTSP-TFC. Statistical level $\alpha = 5\%$. Signals are of the type described in Fig. 4.8 and are characterized for a SNR equal to 20, 5 and -10 dB. Instantaneous frequencies of $x(t)$ and $y(t)$ are reported in dotted and continuous line, respectively.
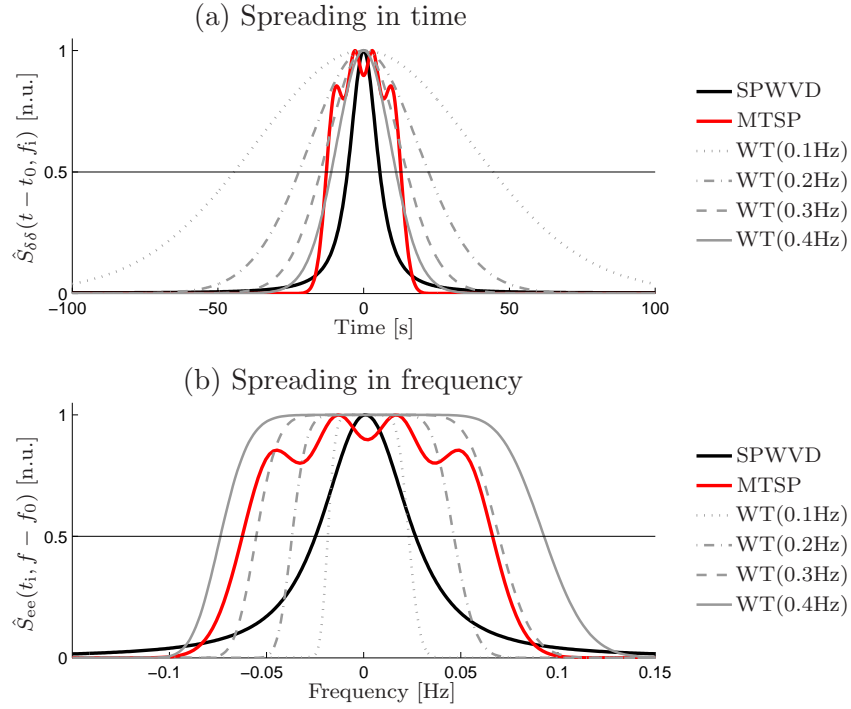
Figure 4.11: Time-frequency representations of: (a) Dirac impulse $x(t) = \delta(t - t_0)$, $\hat{S}_{\delta\delta}(t - t_0, f_{\mathrm{i}})$; (b) complex exponential $x(t) = e^{j2\pi f_0 t}$, $\hat{S}_{\mathrm{ee}}(t_{\mathrm{i}}, f - f_0)$. The SPWVD and MTSP are the same $\forall f$, while the wavelet transform (WT) is estimated for $f_0 \in \{0.1, 0.2, 0.3, 0.4\}$ Hz.
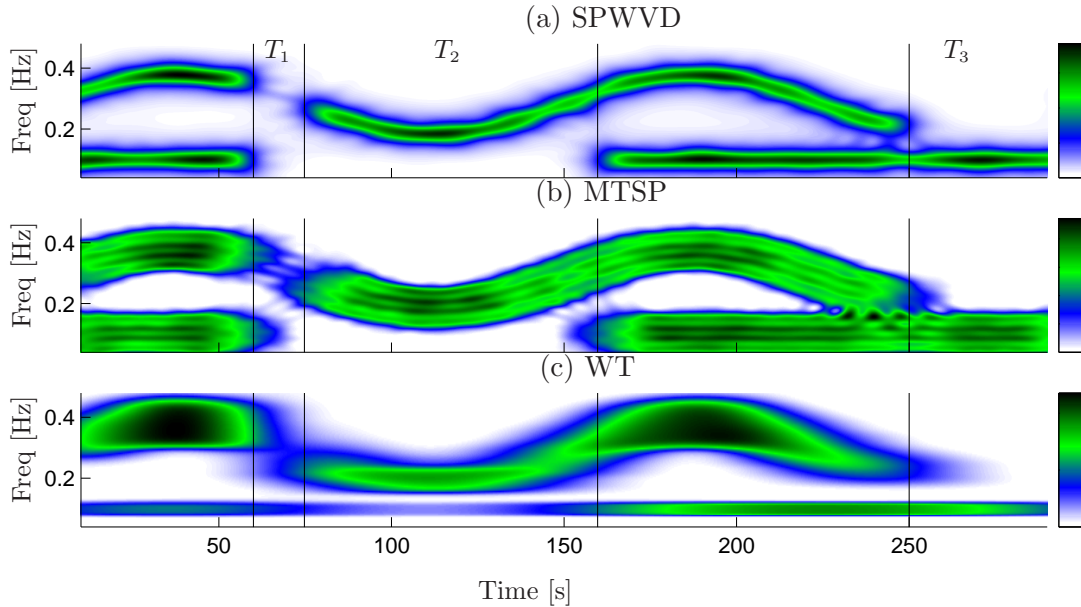
Figure 4.12: Time-frequency spectra of one realization of signal $x_2(t)$, characterized by SNR=10 dB, used in the simulation study. (a) SPWVD, $\hat{S}_{\mathrm{xx}}^{\mathrm{w}}(t, f)$; (b) MTSP, $\hat{S}_{\mathrm{xx}}^{\mathrm{s}}(t, f)$, with $K = 4$; (c) Wavelet transform. The kernels used to estimate these spectra are the same as those used in Fig. 4.11.

Table 4.3: Simulation study – TF resolution.

	Time Resolution (s)		Freq Resolution (Hz)	
	Δ_t^m	$\Delta_t^{(90\%)}$	Δ_f^m	$\Delta_f^{(90\%)}$
SPWVD	11.1	39.5	0.051	0.185
MTSP (K=4)	25.6	25.1	0.129	0.127
WT (0.1Hz)	89.0	124.2	0.041	0.042
WT (0.2Hz)	44.5	64.2	0.083	0.082
WT (0.3Hz)	29.6	42.8	0.124	0.122
WT (0.4Hz)	22.2	32.1	0.166	0.162

smoothing which gives $\Delta_t^m = 7.5$ s and $\Delta_f^m = 0.04$ Hz. These values correspond to half the duration of the shortest decorrelating interval, and half the minimal spectral distance between LF and HF component.

The parameters of the MTSP and the SPWVD that gave resolutions close to these values were chosen. The TF spectra of a Dirac impulse, $x(t) = \delta(t - t_0)$, and of a complex exponential, $x(t) = e^{j2\pi f_0 t}$, estimated by SPWVD and MTSP used in the simulation study, are shown in Fig. 4.11. For comparison, TF spectra estimated by wavelet transform are also shown. Wavelet spectra were obtained by using a specific toolbox for the estimation of wavelet coherence [110]. As suggested in [144], Morlet wavelet with $\omega_0 = 20$ is used, and a further smoothing is applied to obtain spectra that can be used in the estimation of wavelet coherence [144, 110]. Given that the resolution of the wavelet transform depends on frequency, the spectra of the Dirac impulse and of complex exponentials $x(t) = e^{j2\pi f_i t}$ were estimated for $f_i \in \{0.1, 0.2, 0.3, 0.4\}$ Hz. From the spectra shown in Fig. 4.11, indices Δ^m and $\Delta^{(a\%)}$ were estimated, and are reported in Table 4.3. The SPWVD was characterized by much better resolution than the MTSP: Δ_t^m and Δ_f^m of the SPWVD were about half Δ_t^m and Δ_f^m of the MTSP. Nevertheless, the Hermite functions, being $\Delta^{(90\%)}/\Delta^m < 1$ (i.e. $\frac{1}{4}\sum_1^4 |h_k(t)|^2$ and $\frac{1}{4}\sum_1^4 |H_k(f)|^2$ had practically no tails), made the smoothing of the MTSP well concentrated in the TF domain. The kernel used in the calculation of the SPWVD, was characterized by $\Delta^{(90\%)}/\Delta^m \approx 3$. The presence of tails in the kernel used to estimate the SPWVD (4.11) is necessary to find a good compromise between the elimination of the interference terms and the TF resolution. The SPWVD was also characterized by much better resolution than the wavelet transform, except for frequency resolution at $f = 0.1$ Hz, for which Δ_f^m of wavelet transform was slightly lower than Δ_f^m of SPWVD. Figure 4.12 depicts the TF spectra, estimated by SPWVD, MTSP and wavelet transform, of a signal used in the simulation study, characterized by SNR=10dB. The kernels used in this example were the same as those used in Fig. 4.11. It is shown that the SPWVD gave a more accurate localization of the time-varying spectral components of the signals. For $f \approx 0.1$ Hz, the SPWVD and wavelet transform were characterized by similar frequency resolution. However, around this frequency, the SPWVD offered a fine temporal resolution (see also Fig. 4.11 and Table 4.3), while the wavelet transform gave a very poor representation of the temporal changes of the LF component, which did not vanish during T_1 and T_2. Furthermore, in the wavelet transform, the
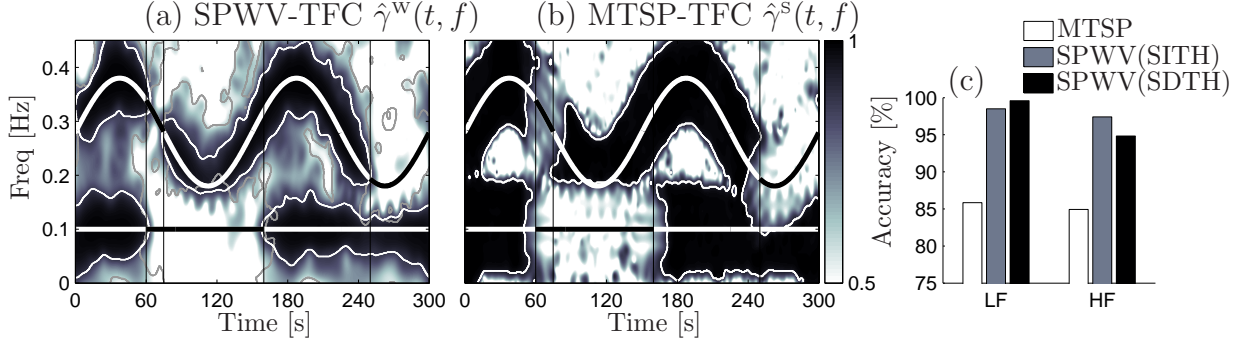
Figure 4.13: Simulation study: single-trial analysis for SNR=10 dB. (a) SPWV-TFC, $\hat{\gamma}^{\mathrm{w}}(t,f)$; (b) MTSP-TFC, $\hat{\gamma}^{\mathrm{s}}(t,f)$; White contours include the TF regions for which $\hat{\gamma}(t,f) > \overline{\gamma_{\mathrm{TH}}^{\mathrm{SI}}}$. In (a), gray contours include the TF regions for which $\hat{\gamma}(t,f) > \gamma_{\mathrm{TH}}^{\mathrm{SD}}(t,f)$; Thresholds are estimated at a significance level α=0.1%. (c) Accuracy in the localization of coupled/uncoupled TF regions. In panels (a)–(b) black and white lines represent TF regions where signals are uncoupled and coupled, respectively.

bandwidth of the HF component is much wider than the bandwidth of the LF one. However, this does not reflect the "real" structure of the signals, but it is due to the frequency-dependent resolution of wavelet transform.

In Fig. 4.13, results from a representative example of single-trial coherence analysis by SPWV and MTSP are shown. In this example, SNR=10 dB and $\alpha = 0.1\%$. Regions where $\hat{\gamma}(t,f) > \gamma_{\mathrm{TH}}^{\mathrm{SI}}(t,f)$ and $\hat{\gamma}(t,f) > \gamma_{\mathrm{TH}}^{\mathrm{SD}}(t,f)$ are encircled by white and gray contours, respectively. White and black lines represent the regions where signals are coupled, i.e. $c_{\mathrm{B}}(t)$=1, and uncoupled, i.e. $c_{\mathrm{B}}(t)$=0, respectively. By using both methods it was possible to identify regions characterized by local coupling. Intervals T_1 (decorrelation in both LF and HF), T_2 (decorrelation only in LF) and T_3 (decorrelation only in HF) were better localized by SPWV-TFC. As shown in the bar chart of Fig. 4.13c, MTSP-TFC was characterized by lower accuracy than the SPWV-TFC. The lower performance in the correct localization of the different TF regions was due to the lower resolution both in time, which led to overestimate the duration of T_1, T_2 and T_3, and in frequency, which led to incorrectly consider not significant the coupling in those TF regions where the LF and HF components were closer (see HF at about 120 s and LF at about 250 s). The SPWV-TFC was characterized by better detection rates also for $\alpha = 1\%$ and $\alpha = 5\%$ (not shown), even if the differences between the accuracy of $\hat{\gamma}^{\mathrm{w}}(t,f)$ and $\hat{\gamma}^{\mathrm{s}}(t,f)$ decreased by increasing α.

In Fig. 4.14, the maps of the significance level of the local coupling are shown for different SNRs. This kind of map provides a useful alternative representation of the results of single-trial coherence analysis. Regions in which the coupling is not significant are reported in white, while those regions in which the coupling is significant are reported in gray scale, with intensity which depend on the significance level. White and black lines represent the regions where signals are coupled, i.e. $c_{\mathrm{B}}(t)$=1, and uncoupled, i.e. $c_{\mathrm{B}}(t)$=0, respectively. Maps which correspond to the results shown in Fig. 4.13 are reported in the middle graphics.

The SPWVD localized coherence changes better, due to higher resolution both in
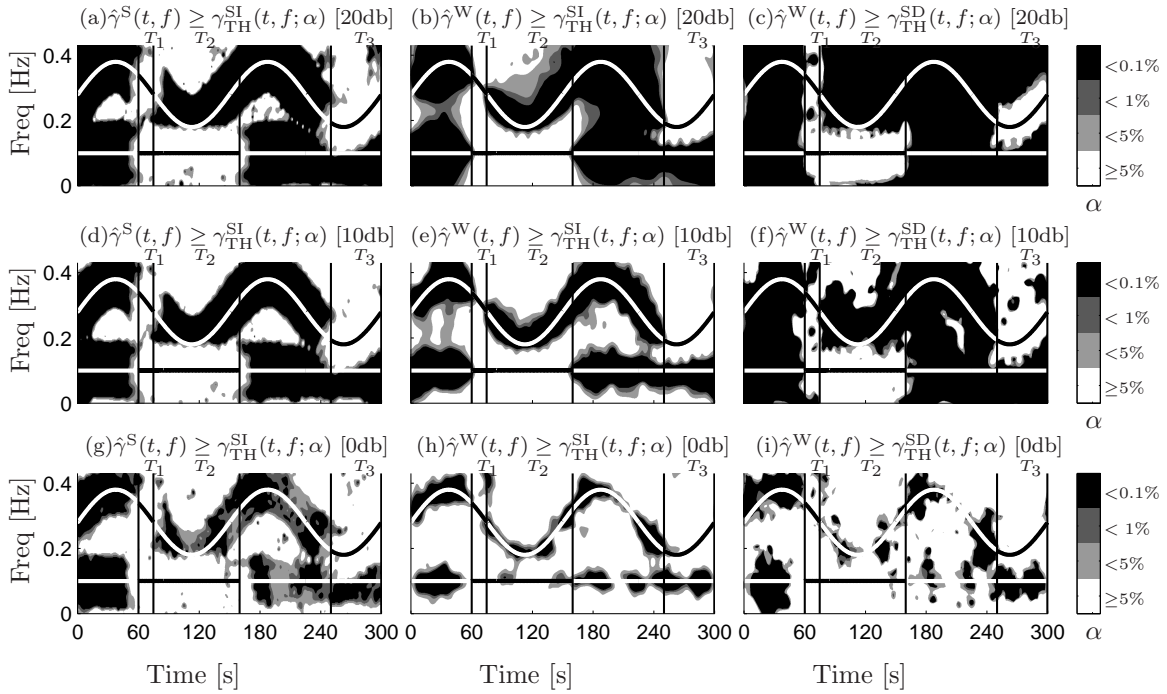
Figure 4.14: Simulation study: single-trial analysis. TF maps of the statistical significance level. First column: TFC by MTSP with signal independent threshold; Second column: TFC by SPWVD and signal independent threshold; Third column: TFC by SPWVD and signal dependent threshold; Upper (a)–(c), middle (d)–(f) and lower (g)–(i) graphics represent cases of SNR of 20 dB, 10 dB and 0 dB, respectively. Black and white lines represent regions characterized by presence and lack of coupling.

time and frequency. This led to the correct estimation of the duration of T_1, T_2 and T_3, and to separate the LF and HF components even when they were close. Results shown in Fig. 4.14c, obtained by comparing $\hat{\gamma}^w(t,f)$ to the SDTH, matched the ideal TFC distribution characterized by a coherence level that is not significant only in well-localized TF regions: during T_1 in both LF and HF bands, during T_2 in LF band, and during T_3 in HF band. In Fig. 4.14g, it is shown that for a SNR as low as 0 dB, the MTSP identifies larger regions characterized by local coupling.

Global results, given in terms of accuracy, are shown in Fig. 4.15. In these graphics, the influence of noise, type of threshold and significance level is assessed. For each combination of these parameters, 50 pairs of signals were processed.

The results depicted in the graphics of Fig. 4.15 shown that:

  (i) Time-frequency coherence by SPWVD is characterized by higher accuracy than that obtained by MTSP; for example, for SNR$\geq$0 and $\alpha = 0.1\%$, the global accuracy of the SPWV-TFC, estimated by averaging results obtained in LF and HF bands, was more than 11.8% higher than the accuracy of the MTSP-TFC.
 (ii) Accuracy of the time-frequency coherence obtained by SPWVD was very high for SNR$\geq$ 5 dB (AC>96.7%, averaging results in LF and HF ranges).
(iii) The differences between the accuracy of $\hat{\gamma}^w(t,f)$ and $\hat{\gamma}^s(t,f)$ decreased by increasing α.
(iv) The use of signal dependent threshold, instead of signal independent threshold, improved the accuracy of the localization of locally coupled/uncoupled regions given by SPWVD, but only for high SNR.

4.6.2   Physiological study

Fourteen subjects (aged 29 ± 3 years) underwent a tilt table test with the following protocol: 4 minutes in early supine position (T_{es}), 5 minutes head-up tilted to an angle of 70° (T_{ht}) and 4 minutes back to later supine position (T_{ls}).

These recordings are part of the data base described in the Appendix and more information about the signals can be find in §A. Beats from ECG and pulses from the pressure signal were detected to generate RR, pulse interval and systolic arterial pressure time series. All the time series were subsequently resampled at 4 Hz and R–R variability (RRV), pulse interval variability (PIV) from the finger pressure signal, and systolic arterial pressure variability (SAPV) signals were obtained by high-pass filtering the corresponding series with a cut-off frequency of 0.03 Hz. The degree of coupling between RRV and RESP, between RRV and SAPV, and between RRV and PIV was assessed.

These examples are interesting since:

  - RRV-RESP: the HF component of RRV is known to mainly reflect the respiratory activity. The change in RRV due to the respiration is called respiratory sinus arrhythmia [112, 258]. Despite the fact that this phenomenon is known since long time, it is not completely understood and it is currently matter of interest, both form the physiological [81] and methodological [62, 66] viewpoints.
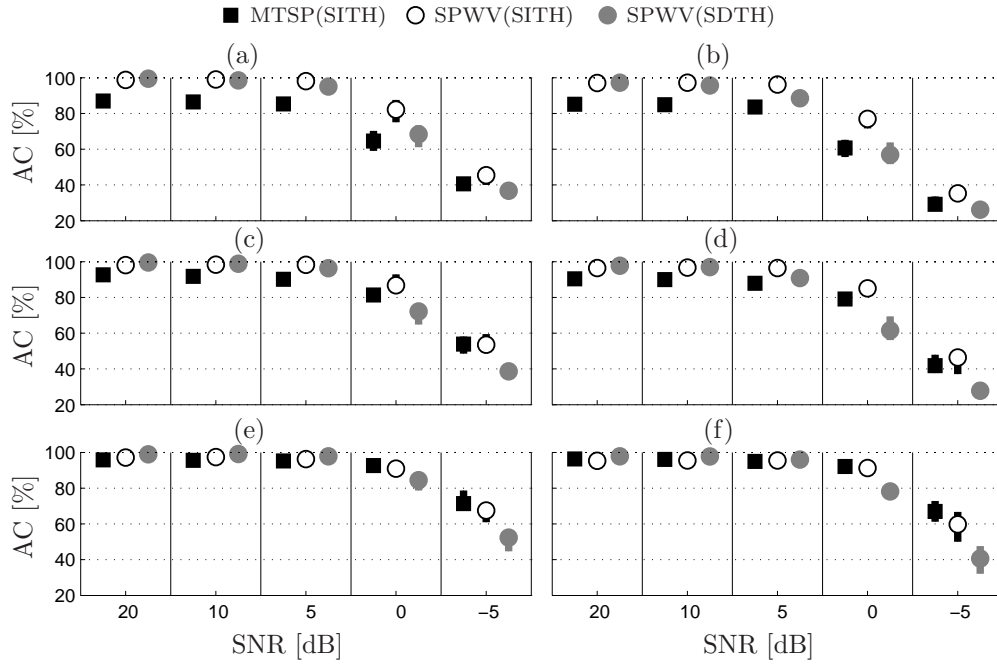
Figure 4.15: Simulation study: global results. Accuracy in the localization of TF regions where signal components are locally coupled/uncoupled. Fifty pairs of signals $x(t)$ and $y(t)$, characterized by different SNRs are processed and results are given as the 25th, 50th and 75th percentiles. Right and left panels concern LF and HF component. From top to bottom: thresholds used in the statistical analysis are associated to a significance level α of 0.1%, 1% and 5%.

- RRV-SAPV: the interactions between heart rate and arterial pressure are of crucial importance in the cardiovascular control and have been largely studied. We specifically approach this argument in §8.
- RRV-PIV: the pulse interval variability estimated in the finger has been proposed to be used as a surrogate for R–R variability estimated in the ECG. The estimation of time-frequency coherence which characterizes these two signals in non-stationary conditions can help to assess whether PIV can be considered as a reliable indirect measure of RRV. An analogous study is described in §7.

Results of the physiological study

In Fig. 4.16, the TF distributions of the RRV, PIV, SAPV and RESP signals, from a healthy subject (male, 27 years old) undergoing a tilt table test are shown. From visual inspection, it is already possible to detect some correlations between the non-stationary structure of the signals. Time-frequency spectral estimated by SPWVD are shown on the left, while those estimated by MTSP, with $K = 4$, are reported on the right. The resolution of the distributions was $(\Delta_t^m, \Delta_f^m) = (12s, 0.041Hz)$ for the SPWVD and $(26.5s, 0.12Hz)$ for the MTSP obtained with $K = 4$. Note that the use of only the first Hermite function ($K = 1$) gave a TF resolution of $(9.5s, 0.055Hz)$, close to that of the SPWVD. However, as already explained, spectrograms estimated without multitapering cannot be used in single-trial coherence analysis. At the beginning of the head-up tilt (epoch T_{ht}), the instantaneous power of the LF component of the RRV, PIV and SAPV signals quickly increased and maintained high value for about one minute. During the remaining part of T_{ht}, the instantaneous LF power first decreased and then increased again until supine position was restored. In all the signals, a component related to the respiration was present. During T_{ht}, the respiratory frequency was higher than the traditional upper limit of HF band (0.4 Hz), indicating that in non-stationary conditions spectral boundaries should be time-varying and respiratory-dependent [19]. The oscillation related to the respiration was more clearly represented in the PIV than in the RRV signal, probably due to the fact that the PIV signal is also affected by pulse transit time variability [100].

Time-frequency coherence analysis was performed between RRV–PIV, RRV–SAPV and RRV–RESP by both SPWV and MTSP. In Fig. 4.17, the maps of the significance level of the coupling, obtained by comparing the TFC to the corresponding signal independent threshold, are shown. The statistical significance of the coupling between the RRV and the SAPV signals increased during the head-up tilt, specially in the LF band. In this band, the proportional part of the TF plane in which time-frequency coherence by SPWVD was significant, was 64%, 88% and 69% during T_{es}, T_{ht} and T_{ls}, respectively. During T_{ht}, and around the respiratory rate (reported in red line), the significance of $\hat{\gamma}^w(t, f)$ was higher than that of $\hat{\gamma}^s(t, f)$. This is likely due to the finer resolution of the SPWVD, which better characterized the rapid changes of the HF components in both signals.

Finally, for this subject, the TFC between the RRV and the PIV signals was always very high, being only slightly less significant in HF.

To characterize the temporal evolution of the local coupling between the spectra

components of the signals, the index $\mathcal{C}_B(t)$ was defined as:

$$\mathcal{C}_B(t) = \int_B \hat{\gamma}(t,f)\mathcal{M}(t,f)df \Big/ \int_B df; \quad B \in \{LF, HF\} \tag{4.34}$$

where $\mathcal{M}(t,f)$ is defined in (4.32). This index takes into account both the spread and the magnitude of the local coupling, averaged in LF and HF spectral bands.

The ability to localize changes in the temporal evolution of the coherence between cardiovascular signals was assessed in the example shown in Fig. 4.18. This graphic shows the LF oscillations of the RRV and SAPV signals, whose TF spectra are shown in Fig. 4.16. These oscillations were obtained by low-pass filtering with a cut-off frequency of 0.16 Hz (see the box of Fig. 4.17). The LF oscillations of the RRV and SAPV signals were highly correlated, except during the interval bounded by two consecutive local minima of the SAPV oscillation, marked by a shadowed area. The interval corresponding to this shadowed area was determined empirically. The intervals during which the coherence, evaluated in the LF range by SPWVD and MTSP, were not statistically significant are bounded by vertical lines. These intervals are those for which $\mathcal{C}_{LF}(t) = 0$. As shown in this representative example, SPWVD localized the change in the strength of the local coupling more accurately than MTSP.
The median trend and the interquartile range of $\mathcal{C}_B(t)$, estimated among the entire study population, is shown in Fig. 4.19. Concerning the coupling between RRV-SAPV signals, the head-up tilt provoked a change in $\mathcal{C}_{LF}(t)$ composed of the following phases:

– (i) Instantaneous decrease during the upright movement of the automatic bed (interval in between vertical lines);
– (ii) Fast increase, up to values that are significantly higher than baseline ones (Wilcoxon rank-sum test, $p < 0.05$);
– (iii) Stabilization around baseline values.

In T_{ls}, the restoration of the supine position provoked a similar pattern, but characterized by lower $\mathcal{C}_{LF}(t)$. In panel (b), it is shown that, after head-up tilt, $\mathcal{C}_{HF}(t)$ first abruptly decreased and then quickly increased toward baseline values. The increase in the median $\mathcal{C}_B(t)$, observed in LF during T_{ht} and T_{ls}, and in HF during T_{ht}, had similar slopes (4.63, 4.86 and 4.17 10^{-3}s^{-1}, respectively).
The coupling between RRV-RESP signals (panels (c)–(d)) was not significantly affected by the head-up tilt.
The coupling between RRV-PIV signals was affected by the postural changes only in HF, while in LF, it was always close to one.

4.7 Discussion

In this chapter, the use of SPWVD and MTSP to reliably estimate the TF coherence between cardiovascular signals was assessed for the first time. It was shown that the combination of these methods with statistical analysis allows to accurately localize TF
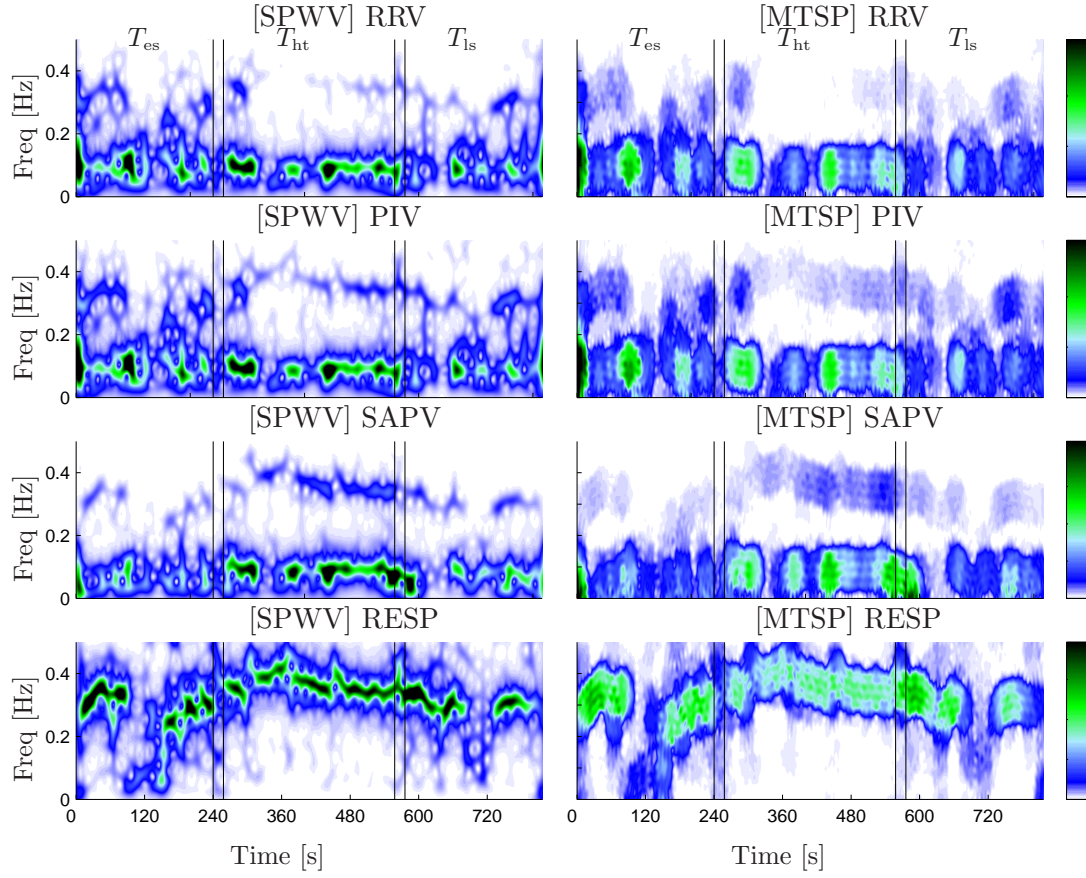
Figure 4.16: Recorded physiological data analysis. TF distributions. On the left: SPWVD; on the right: MTSP obtained by using four tapers. From top to bottom: RRV from ECG, PIV, SAPV and respiratory signal. Vertical lines mark the supine (T_es and T_ls) and the head-up tilt (T_ht) positions.
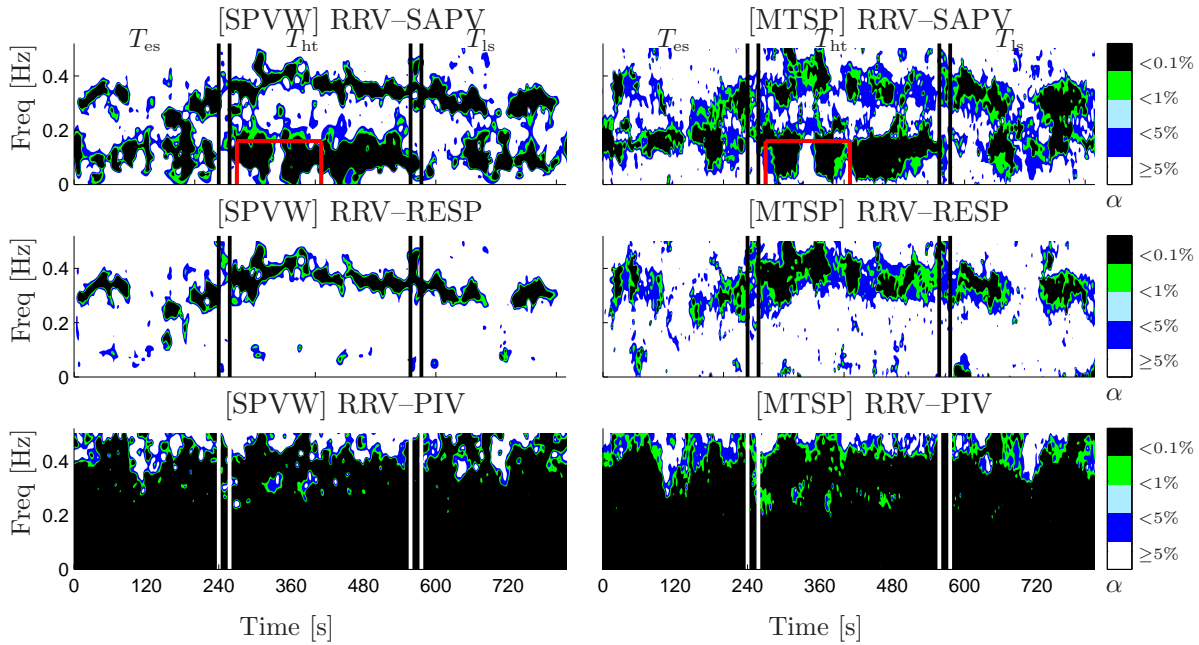
Figure 4.17: Recorded physiological data analysis. Maps of the significance level of the coupling. On the left: SPWVD-TFC; on the right: MTSP-TFC (K=4 tapers). From top to bottom: RRV–SAPV, RRV–RESP and RRV–PIV. Vertical lines mark the supine (T_{es} and T_{ls}) and the head-up tilt (T_{ht}) positions. The box reported in the upper graphics delimited the TF support of oscillations shown in Fig. 4.18.

regions where the coupling is significant.

It is worth noting that, in contrast with stationary spectral coherence, which quantifies the degree of global linearity, TF coherence quantifies the degree of local coupling. This is shown in the simulation study, where TF coherence was significant in a large part of the TF domain, although the signals were not globally linearly related (their amplitudes were not linearly related). This was due to the presence, in both signals, of locally synchronized oscillations. That is, TF coherence is significant whenever two signals share approximately the same instantaneous frequency.

In the study of cardiovascular control, TF coherence has many fields of application. For example, it can be used to reveal an impairment of the baroreflex, which results in a low degree of coupling between RRV and SAPV. Time-frequency coherence can be used as a measure of similarity to validate the use of one signal, and its derived measures, as surrogates of the original ones [100]. It can also be used to assess the pertinence of linear (or nonlinear) models to describe the relationship between different signals in the modeling of the cardiovascular system.

4.7.1 Statistical assessment

As for the stationary spectral coherence [57], TF coherence depends on the parameters used in its calculation. This dependence makes the use of some statistical analysis necessary to assess whether the TF coherence estimates are significant or not. The problem of interpreting the level of coherence correctly is especially important in non-

stationary analysis, since, as shown in Fig. 4.9, the finer the TF resolution, the higher should be the coherence estimates to be considered as statistically significant. Statistical analysis is based on the point-by-point comparison between coherence estimates and a threshold function. Two thresholds are defined: SITH, which only depends on the resolution of the TF spectra, and SDTH, which depends on both the resolution of the TF spectra and the TF structure of the signals. These thresholds have both pros and cons: on one hand, the use of a specific threshold that takes into account the TF structure of the signals is appealing, but on the other, in a population study, its use implies an increase in the computational cost of the analysis. As shown in Fig. 4.10, only the SPWVD gives the possibility of using a signal-dependent threshold. This is an advantage over the MTSP. Nevertheless, the results of the simulation study (Fig. 4.15) show that the use of SDTH improved the accuracy of localization only for signals characterized by high SNR.

4.7.2   Comparison between the methodologies

Although the theoretical properties of an estimator of coherence based on SPWVD were first discussed in [181, 252], it was never used in biomedical applications. In the SPWVD, the reduction of the interference terms [125] is crucial since they may cause the coherence estimates to lose their physical meaning. In this study, the appropriate degree of smoothing was determined by using the technique presented in §4.3.1, i.e. by first fixing a desired TF resolution, and then by iteratively increasing the degree of smoothing, until $\hat{\gamma}^{\mathrm{w}}(t, f) \in [0, 1]$. Another approach, presented in §4.3.2 [206], makes use of geometrical relations between the TF structure of the signals and the interference terms to determine the parameter of the kernel (4.11). In this approach, as in [189], the support of the TF coherence is limited to regions of interest to reduce the required degree of smoothing.

A first simulation study, described and commented in §4.3.3, showed that the SPWVD provides reliable estimates of the time-course of the coupling between synthetic real-like cardiovascular signals. The comparative study performed in §4.6 showed that by using both computer-generated and recorded physiological data, changes in the local coupling were better localized by SPWVD than MTSP. This is due to the same structural reason which makes the SPWVD more suitable than the spectrogram for the localization of TF features, namely, the possibility of independently setting the time and frequency filtering [92, 124]. Indeed, although the constraint of having a TF coherence bounded between zero and one imposes a sort of trade-off between time and frequency resolution, this option allows reducing the global amount of smoothing, thus yielding more accurate estimates. Nevertheless, the MTSP has some important features that could make it useful in coherence analysis. First, being based on spectrograms, which are non-negative, coherence estimates are always bounded between 0 and 1. Secondly, the use of Hermite functions, which are optimally concentrated in a circular TF region, offer a good trade-off between time and frequency resolution [91, 74]. Finally, as shown in Fig. 4.14, it is also possible to detect local coupling between signals characterized by a low SNR via MTSP.

Both SPWVD and MTSP are characterized by a constant resolution over the entire

TF domain. This is in contrast with other methodologies such as wavelet transform, in which the resolution depends on frequency. A uniform resolution makes the interpretation of the coherence function estimated by SPWVD and MTSP easier than the interpretation of wavelet coherence since the uncertainty due to smoothing does not change with frequency. Moreover, as shown in Fig. 4.11, the SPWVD used in the simulation study was characterized by a finer resolution than the Morlet wavelets used previously in coherence analysis [144]. A comprehensive comparison between wavelet coherence and the methodologies presented in this study is beyond the scope of this chapter. However, it is worth noting that although the resolution of the wavelet transform shown in Fig. 4.11 may be improved by choosing *ad hoc* parameters or other smoothing kernels [153], an improvement is likely to concern either time or frequency, since wavelet transform offers the same trade-off between time and frequency as methods based on Fourier analysis [56].

Given that the main goal of time-frequency coherence analysis is to provide accurate estimates of local coupling, and given that the correct localization in both time and frequency accounts for most of the accuracy of the estimates, indices Δ^m and $\Delta^{(a\%)}$ are used to quantify and compare the resolutions.

One of the differences between the SPWV-TFC and the TF coherence estimators based on spectrogram and continuous wavelet transform [144, 153, 260, 110], is that to estimate the SPWV-TFC, there is no need for further processing of the TF spectra. Indeed, by construction, the squared magnitude of the cross spectrogram (or scalogram) is equal to the product between the auto spectrograms (or scalograms). In single-trial coherence analysis, this implies that a further TF smoothing (a further decrease in TF resolution) than that used to estimate the spectra is required.

Spectrogram, wavelet and SPWVD provide a spectral analysis that is formally equivalent [56], and they can be obtained by processing the Wigner-Ville distribution [92]. As previously mentioned, the advantage of SPWVD is that it offers the possibility of determining the shape of the smoothing function both in time and frequency, which in turn allows for more accurate localization of cardiovascular dynamics.

Recently, time-varying autoregressive methods were also proposed to estimate the coherence function [262, 261]. Time-frequency and autoregressive analysis are very different and it is difficult to fairly compare them. However, TF analysis offers some advantages over autoregressive methods, which may deserve attention. In TF methods, the structure of the signals is characterized without imposing any assumption or model to the signals. No coefficient identification neither parameter initialization is needed. However, given that non-parametric TF methods are not based on a model, they do not allow disentangling feedback and feedforward mechanisms when systems interact in closed-loop [262, 261].

Physiological data analysis [1]

The analysis of recorded physiological data showed that the methodologies described in this study can be used to characterize the dynamic interactions between cardiovascular signals. Generally, these signals have a non-stationary structure, even during intervals of supine position. This confirms that stationarity is an exception rather than the rule, and highlights the importance of TF analysis which, unless stationarity is proved [51], should be preferred to traditional time-invariant analysis. For a statistically assessment of the degree of non-stationarity of this data set, see §8.

In this study population, time-frequency coherence analysis shows that, during tilt table test, cardiovascular rhythms, such as heart rate, systolic pressure and respiratory rate, were dynamically coupled. Head-up tilt provoked an increase of the TF coherence between RRV and SAPV. Moreover, it has been shown that the increase which followed the loss of coherence due to the postural changes (back and forth from supine position to head-up tilt), was characterized by similar slope. This may imply the presence of a common mechanism of resynchronization between RRV and SAPV.

The presence of some artefacts due to the recalibration of the finger pressure signal may also be responsible for the decrease of the coupling observed at the beginning of T_{ht} and T_{ls}. The RRV and SAPV signals were also coupled in HF band, around respiratory rate. The strength of this coupling was similar to that between the RRV and RESP signals. This coupling, which is due to respiratory sinus arrhythmia [112], was maintained even during head-up tilt. Finally, it is shown that the PIV signal can be used as a surrogate for the RRV signal, even if caution should be used in HF band, where a decrease of the coherence during the postural changes was observed. This may be due to a change in the vascular tone, which affects the pulse transit time and introduces a difference in the TF structure of the two signals [100]. The study of the degree of similarity between heart rate from ECG and pulse rate from the photoplethysmographic in non-stationary conditions is the subject of §7.

---

[1]In this chapter, the analysis of recorded physiological signals is performed to compare the estimators based on SPWVD and MTSP. For a more physiological discussion about the interactions between SAPV and RRV, please refer to §8.
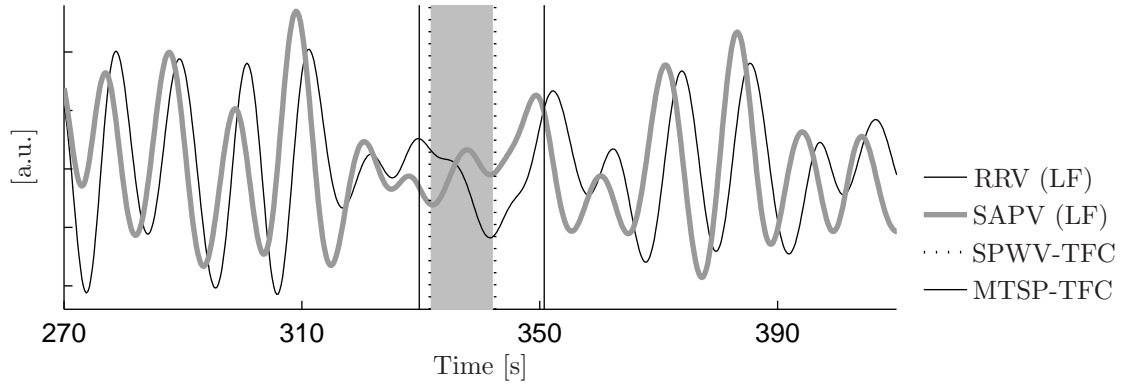
Figure 4.18: Low frequency oscillations of the SAPV and RRV signals, obtained by low–pass filtering (see the box in Fig. 4.17). Shadowed area: interval of decorrelation. Dashed and continuous vertical lines: interval of decorrelation detected by the SPWVD and MTSP, respectively.
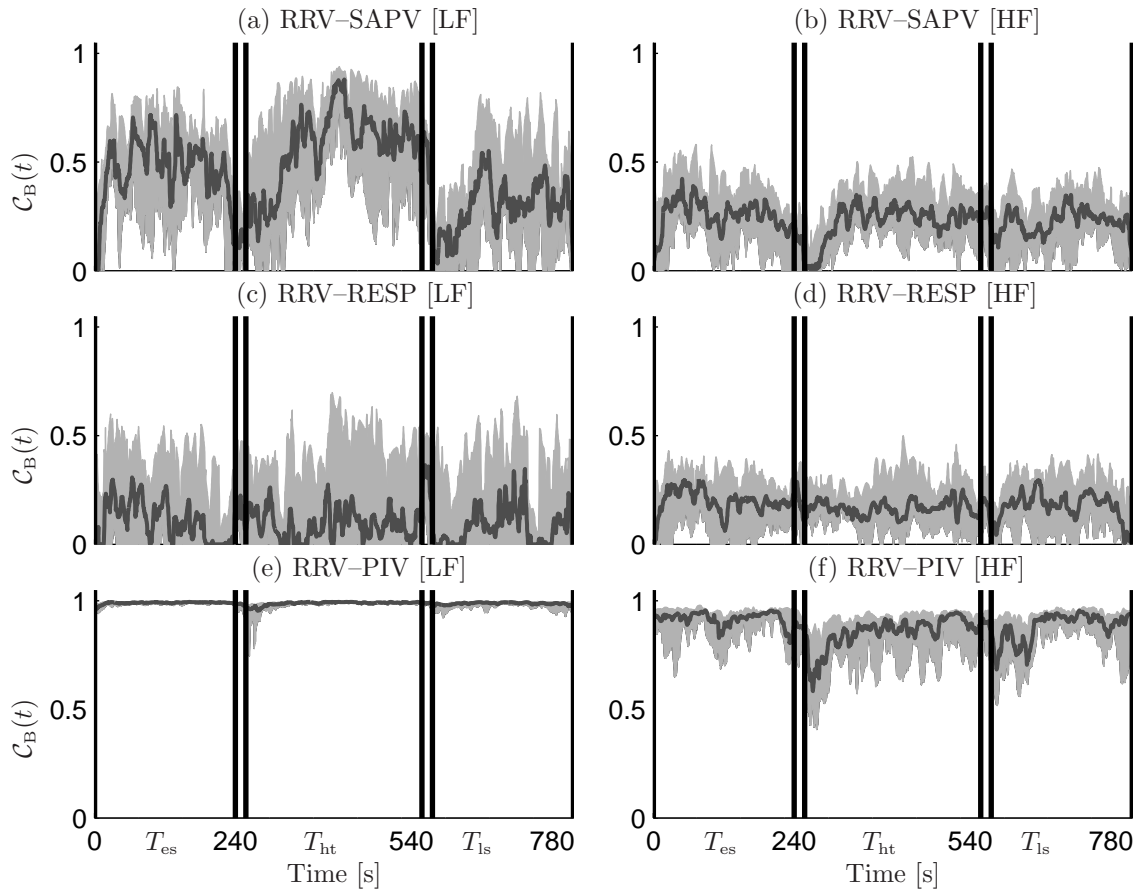
Figure 4.19: Global results: Strength and spread of the coupling, $\mathcal{C}_{\mathrm{B}}(t)$, between RRV–SAPV (above), RRV–RESP (middle) and RRV–PIV (below), estimated in LF (left) and HF ranges (right). Shadowed area: [25–75]th percentile of $\mathcal{C}_{\mathrm{B}}(t)$, estimated among subjects. Gray lines: median values.

Chapter 5

Time-frequency phase difference analysis for cardiovascular signals

Contents

5.1 Introduction

In this chapter, a methodology to dynamically quantify the degree of synchronization between signals related to the autonomic modulation is presented [207, 208]. This methodology provides estimates of phase difference, time delay and phase locking between the spectral components of two non-stationary signals. The estimation of these indices adds new valuable information to the time-frequency coherence presented in §4, and complements the assessment of the dynamic interactions between cardiovascular signals provided by cross time-frequency analysis.

As mentioned in the introduction (see §1.2), the short-term cardiovascular control involves several mechanisms which make arterial pressure, heart period and respiration dynamically coupled. These mechanisms are principally mediated by the autonomic nervous system [241, 173, 59]. A complex coordination exists between all the indices that characterize the cardiovascular system. This coordination involves a sequence of causal events which occur with a specific delay. Therefore, an impairment of the cardiovascular regulation may be reveled by an alteration of the degree of synchronization of these events.

From the phase difference estimate it is possible to obtain the time delay, the latencies, between the changes of the spectral features of two signals. The estimation of these latencies is relevant since they can help to gain some insight into the sequence of phenomena involved in the cardiovascular regulation. Although the quantification and the physiological interpretation of these latencies has been the subject of many physiological studies [240, 71, 231, 34, 78], the underlying mechanisms are still not completely understood. The method described in this chapter, which specifically aims at giving accurate estimates of the phase differences and temporal latencies between non-stationary signals, may help to clarify this debate. In recent years, some interesting reviews concerning the characterization of these interactions, and which specially focus on methodological issues, have also been published [31, 217, 255, 193, 76].

To the extent of our knowledge, in the literature, the estimation of the phase differences between non-stationary signals in the joint time-frequency domain was assessed and used in few studies. Among them, no one focuses on the characterization and description of cardiovascular dynamics. Phase differences have been estimated by wavelet transform [154, 152, 222, 227], by Rihaczek transform [11, 12] and by reduced interference distributions [235, 133]. In the comparative study presented in §4.6, it was shown that the SPWVD provided time-frequency coherence estimates which are well localized both in time and frequency. This paved the road for the study of the phase difference between cardiovascular signals by means of the SPWVD.

Note that the measures that are described and validated in this chapter will be then used in §8 to give a dynamic characterization of cardiovascular interactions.
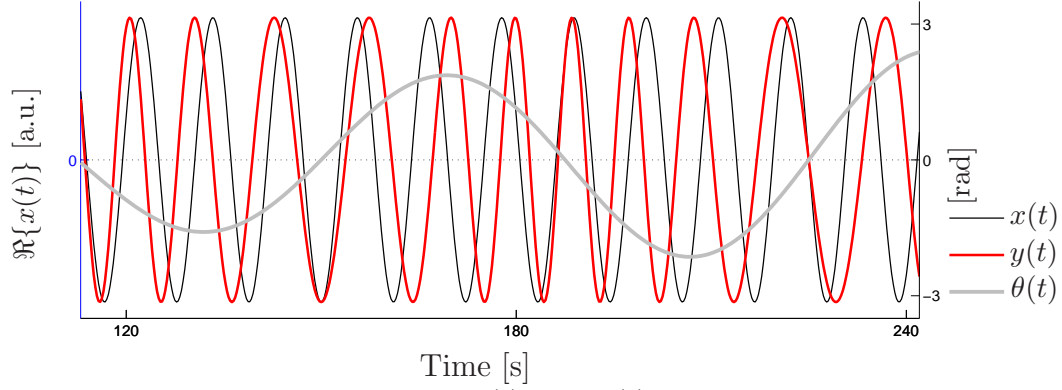
Figure 5.1: Two phase-shifted signals $x(t)$ and $y(t)$ which oscillate at typical Mayer wave frequency and characterized by a time-varying phase difference. Note that when $\theta(t) = 0$, $x(t)$ and $y(t)$ are in phase, while when $\theta(t) > 0$, $x(t)$ precedes $y(t)$.

5.2 Methods

5.2.1 Phase difference

To introduce the time-frequency phase difference and its estimation, let's rewrite the model for autonomic signals already used in the previous section, consisting in time-varying LF and HF components plus noise:

$$x(t) = A_{x,LF}(t)e^{j\theta_{x,LF}(t)} + A_{x,HF}(t)e^{j\theta_{x,HF}(t)} + \xi_x(t) \tag{5.1}$$
$$y(t) = A_{y,LF}(t)e^{j\theta_{y,LF}(t)} + A_{y,HF}(t)e^{j\theta_{y,HF}(t)} + \xi_y(t)$$

In these expressions, LF and HF indicate the low frequency component, traditionally inside [0.04, 0.15 Hz], and the high frequency component, traditionally inside [0.15, 0.4 Hz], respectively [1]; $\theta_{k,B}(t)$, with $B \in [LF, HF]$ and $k \in [x, y]$, is the instantaneous phase, related to the instantaneous frequency by $f_{k,B}(t) = (d\theta_{k,B}(t)/dt)/(2\pi)$; $\xi_k(t)$ is a white Gaussian noise (WGN).

Given that cardiovascular signals are usually non-stationary, the phase difference between each spectral component, $\theta_B(t) = \theta_{x,B}(t) - \theta_{y,B}(t)$, is also expected to be time-varying.

Given the expressions reported in (5.1), the time-course of the phase difference between two signals $x(t)$ and $y(t)$, evaluated for a specific spectral component B, can be estimated as:

$$\theta_B(t) = 2\pi \int_0^t [f_{x,B}(\tau) - f_{y,B}(\tau)]d\tau \tag{5.2}$$

An illustrative example of two oscillations that share similar instantaneous frequencies and are characterized by time-varying phase difference, is shown in Fig. 5.1. In this example, signals are: $x(t) = \exp(j2\pi 0.9t)$ (in black) and $y(t) = x(t)\exp(-j\theta(t))$ (in red). Phase difference, plotted in bold line, is $\theta(t) = 2\pi(0.1 + \sin(2\pi\frac{4}{T}t))$ rad, with $T = 300$ s. It is shown that at the beginning the signals are in phase, but they quickly lose their synchronization, with a phase difference $\theta(t)$ that increases and decreases

during time. This example may represent LF oscillations of R–R variability (RRV) and systolic arterial pressure variability (SAPV) during non-stationary conditions.
The sign of the phase difference estimates reveals which signal leads (or precedes) which, and can be used to study the causality of an interaction [193], by assessing the prevalent direction of the coupling [71, 219]. For example, in Fig. 5.1, it is shown that when the oscillation $x(t)$ lags behind (is delayed with respect to) $y(t)$, the phase difference is negative ($\theta(t) < 0$), while when $x(t)$ leads $y(t)$, the phase difference is positive ($\theta(t) > 0$). When $\theta(t) = 0$, the oscillations are perfectly synchronous, while when $\theta(t) = \pm\pi$ the oscillations have locally opposite phase.

5.2.2 Time-frequency representations

The estimation of the phase difference from the instantaneous frequencies of the spectral components of two signals, reported in (5.2), has two main drawbacks: it is very sensitive to estimation errors in $f_{k,B}(t)$, since an estimation error at t_0 affects all $\theta_B(t > t_0)$, and gives a quantification of the phase differences only at $f_{k,B}(t)$.
In the analysis of cardiovascular signals, these inconveniences are particularly serious, since biomedical signals are never perfectly narrow-band and an accurate estimation of the instantaneous frequencies is not always possible. Therefore, a simultaneous characterization of the phase differences in time and frequency may reveal important features which can be used to better describe the dynamic interactions between signals $x(t)$ and $y(t)$. This joint time-frequency characterization is given by cross time-frequency analysis.
Before defining the time-frequency phase difference distribution, let's rewrite the general expression of a cross time-frequency distribution belonging to the Cohen's class[1], as for example the SPWVD, equivalently defined in (3.14) or (4.8):

$$S_{xy}(t,f) = \iint\limits_{-\infty}^{\infty} \phi_{\text{d-D}}(\tau,\nu) A_{xy}(\tau,\nu) e^{j2\pi(t\nu - f\tau)} d\nu d\tau \qquad (5.3)$$

where $A_{xy}(\tau,\nu)$ is the narrow-band symmetric ambiguity function [93, 124] of signals $x(t)$ and $y(t)$, defined in (3.5).
The time-frequency phase difference (TFPD) spectrum is defined as:

$$\Theta(t,f) = \arg\left[S_{xy}(t,f)\right] = \arctan\left[\frac{\Im\left[S_{xy}(t,f)\right]}{\Re\left[S_{xy}(t,f)\right]}\right] \qquad (5.4)$$

This expression provides a quantification of the phase difference between the spectral components of two signals in the time-frequency domain and is bounded $\Theta(t,f) \in [-\pi, \pi]$.

---

[1]In all the expressions reported in the following, superscripts $^{\text{WV}}$ and $^{\text{S}}$, used in §4 to indicate estimates derived from the SPWVD and the spectrogram, respectively, are not longer used. Even if the methodology applies for any kind of distribution, in this chapter we focus on the SPWVD. Given that all the expressions of this chapter are estimated, the symbol ˆ is omitted.

Phase-locking

The time-frequency phase difference spectrum gives the possibility of estimating the degree of phase-locking between different signals [11, 12, 154, 152, 153]. In population studies, the phase locking is used to assess whether a determined stimulus provokes, among the subjects, similar changes in the time-frequency phase difference spectrum. Its time-frequency representation is:

$$\Psi(t,f) = \left| \frac{1}{L} \sum_{i=1}^{L} e^{j2\pi\Theta_i(t,f)} \right| = \left| \frac{1}{L} \sum_{i=1}^{L} \frac{S_{\mathrm{xy},i}(t,f)}{|S_{\mathrm{xy},i}(t,f)|} \right| \tag{5.5}$$

By construction, $\Psi(t,f)$ is bounded between 0 and 1, $\Psi(t,f) \in [0,1]$, being $\Psi(t,f) = 1$ if $\Theta_i(t,f)$ does not vary across subjects i, and being $\Psi(t,f) = 0$ if $\Theta_i(t,f)$ is characterized by a zero mean random distribution across i. Indeed, if for a given point (t_0, f_0), the complex terms in the summation in (5.5) maintain similar phase for all i, $\Psi(t_0, f_0) \approx 1$.

Therefore, the phase locking measures the degree of similarity of the time-frequency structure of a group of signals, by pairwise comparing their time-frequency phase differences $\Theta_i(t,f)$.

5.2.3 Extraction of time-varying indices

The time-varying index describing the temporal evolution of the phase difference between a given spectral component B of two signals is estimated by averaging the time-frequency phase difference spectrum in a specific time-frequency region $\Omega_{\mathrm{B}}^{(\theta)}$. Among a wide range of different possibilities, in this study we define $\Omega_{\mathrm{B}}^{(\theta)}$ as a time-frequency region centered around the instantaneous frequency of the spectral component, $f_{\mathrm{B}}^{(\mathrm{xy})}(t)$ (estimated as the maximum of the instantaneous spectral peak), and in which coherence is statistically significant. These conditions are necessary to obtain robust and accurate estimates since, in this context, the estimation of a phase difference is relevant only in those time intervals in which the two signals are approximately sharing the same instantaneous frequency.

First, the region where the time-frequency coherence estimates, $\gamma(t,f)$ (4.3), is significant is localized. This region is called Ω_{B} and is defined as:

$$\Omega_{\mathrm{B}} \equiv \left\{ (t,f) \in (\mathbb{R}^+ \times B) \mid \gamma(t,f) > \gamma_{\mathrm{TH}}(t,f) \right\}; \quad \text{with } B \in \{LF, HF\} \tag{5.6}$$

where $\gamma_{\mathrm{TH}}(t,f)$ is a threshold function which depends on the time-frequency resolution of the distributions used to estimate time-frequency coherence (see §4.5).

The instantaneous frequency of the spectral component B, around which $\Omega_{\mathrm{B}}^{(\theta)}$ is defined, can be estimated as the maximum of the magnitude of the cross time-frequency spectrum:

$$f_{\mathrm{B}}^{(\mathrm{xy})}(t) = \arg \max_{f \in B} |S_{\mathrm{xy}}(t,f)| \tag{5.7}$$

In some cases, it happens that the time-course of $f_{\mathrm{B}}^{(\mathrm{xy})}(t)$ is characterized by the presence of abrupt changes, such as stepwise increases (decreases) quickly followed

by stepwise decreases (increases). This is likely due to artifacts, noises or spurious components, rather than to actual instantaneous frequency variations. In this case, the following procedures can improve the estimation:

- Instantaneous frequency $f_B^{(xy)}(t)$ is estimated as the global maximum of $S_{xy}(t, f)$, within $f \in B$, as in (5.7).
- Intervals T_j during which an abrupt change of $f_B^{(xy)}(t)$, $\left|f_B^{(xy)}(t_{n-1}) - f_B^{(xy)}(t_n)\right| > \Delta f$, is followed in less than Δt by another abrupt change ($> \Delta f$) of opposite sign, are detected. Typically $\Delta f = 0.03$ Hz and $\Delta t = 10$ s.
- $\forall t_n \in T_j$, if another local maximum, or inflection point, exists and it is closer to the instantaneous frequency estimated at the previous time instant, $f_B^{(xy)}(t_{n-1})$, its frequency,$f_{B(2)}^{(xy)}(t_n)$, is selected.
- The new estimate replaces the older one, $f_B^{(xy)}(t_n) = f_{B(2)}^{(xy)}(t_n)$, if:

$$
\begin{cases}
\left|f_{B(2)}^{(xy)}(t_n) - f_B^{(xy)}(t_{n-1})\right| < \Delta f \\[2mm]
\dfrac{\left|S_{xy}(t_{n-1}, f_B^{(xy)}(t_{n-1})) - S_{xy}(t_n, f_{B(2)}^{(xy)}(t_n))\right|}{S_{xy}(t_{n-1}, f_B^{(xy)}(t_{n-1}))} < 0.1
\end{cases}
$$

otherwise, one can decide to maintain previous $f_B^{(xy)}(t_{n-1})$ or, alternatively, can take the more conservative decision of not providing any estimate for the instantaneous frequency at t_n.

Once that the instantaneous frequency has been estimated, the time-varying spectral bands centered around $f_B^{(xy)}(t)$ are defined as:

$$
\Omega_B^{(\gamma)} \equiv \left\{ (t, f) \in (\mathbb{R}^+ \times B) \mid f = f_B^{(xy)}(t) \pm \frac{\Delta_f^m}{2} \right\} \tag{5.8}
$$

where Δ_f^m is a term related to the frequency resolution of the TF distributions (see 3.1.2), which determines the maximum width of $\Omega_B^{(\theta)}$.
Finally, the region $\Omega_B^{(\theta)}$ is defined as:

$$
\Omega_B^{(\theta)} \equiv \left\{ \Omega_B^{(\gamma)} \cap \Omega_B \right\} \circ R(t, f); \ \ B \in \{LF, HF\} \tag{5.9}
$$

where $\circ$ denotes the opening (processing technique which involves erosion and dilation) and $R(t, f)$ is a rectangle which defines the minimum length and width of the subset which compose $\Omega_B^{(\theta)}$. The opening is used because it excludes from $\left\{\Omega_B^{(\gamma)} \cap \Omega_B\right\}$ the portions of TF domain which are smaller than $R(t, f)$, thus adding robustness to the final estimates.
The index that quantifies the phase difference, $\theta_B(t)$, is estimated (in radians) by averaging the time-frequency phase difference spectrum in $\Omega_B^{(\theta)}$:

$$
\theta_B(t) = \left[\int_{\Omega_B^{(\theta)}} \Theta(t, f) df \right] \Big/ \left[\int_{\Omega_B^{(\theta)}} df \right]; \ \ B \in \{LF, HF\} \tag{5.10}
$$

The time delay associated to $\theta_B(t)$ can be estimated (in seconds) by the index $\mathcal{D}_B(t)$, defined as:

$$
\mathcal{D}_B(t) = \frac{\theta_B(t)}{2\pi f_B^{(xy)}(t)} \tag{5.11}
$$

5.2.4   Analytical expressions of some case studies

Let's consider two linear chirps:

$$x(t) = \exp\big(j2\pi(\alpha_x t + \beta_x t^2)\big)$$
$$y(t) = \exp\big(j2\pi(\alpha_y t + \beta_y t^2) - j\theta(t)\big)$$

characterized by instantaneous frequencies $f_x(t) = 2\beta_x t + \alpha_x$, and $f_y(t) = 2\beta_y t + \alpha_y - (d\theta(t)/dt)/(2\pi)$.

The cross SPWVD distribution is:

$$S_{xy}(t,f) = W_{xy}(t,f) \otimes \phi_{\text{t-f}}(t,f)$$

where $W_{xy}(t,f)$ is the cross Wigner-Ville distribution and $\phi_{\text{t-f}}(t,f)$ a separable TF smoothing function. The cross Wigner-Ville distribution is:

$$W_{xy}(t,f) = \int_{-\infty}^{\infty} x\left(t+\frac{\tau}{2}\right) y^*\left(t-\frac{\tau}{2}\right)\exp(-j2\pi\tau f)d\tau = \qquad (5.12)$$

$$= \int_{-\infty}^{\infty} \exp\bigg(j2\pi\bigg((\beta_x - \beta_y)(t^2 + \frac{\tau^2}{4}) + (\alpha_x - \alpha_y)t +$$

$$+(\beta_x + \beta_y)t\tau + (\alpha_x + \alpha_y)\frac{\tau}{2} + \frac{1}{2\pi}\theta\left(t-\frac{\tau}{2}\right) - f\tau\bigg)\bigg)d\tau$$

Phase differences

Let's now consider the case in which the linear chirps are sharing approximately the same instantaneous frequency and the phase difference varies linearly with time:

$$\alpha_x = \alpha_y = \alpha; \quad \text{and} \quad \beta_x = \beta_y = \beta;$$
$$\theta(t) = 2\pi(\theta_1 t + \theta_0)$$

From expression (5.12), we get:

$$W_{xy}(t,f) = |W_{xy}(t,f)|\exp(j\Theta_{xy}(t,f)) = \qquad (5.13)$$

$$= \exp(j2\pi(\theta_1 t + \theta_0))\int_{-\infty}^{\infty} \exp\left(j2\pi\tau\left(2\beta t + \alpha - \frac{\theta_1}{2} - f\right)\right)d\tau$$

$$= \exp(j2\pi(\theta_1 t + \theta_0)) \cdot \delta\left(f - \left(2\beta t + \alpha - \frac{\theta_1}{2}\right)\right)$$

The phase of the cross-WVD is equal to $\Theta_{xy}(t,f) = 2\pi(\theta_1 t + \theta_0) = \theta(t)$.
In the case in which $x(t)$ leads $y(t)$, i.e. $y(t)$ lags behind $x(t)$, $\theta(t) > 0$ and the phase of the cross Wigner-Ville distribution is positive.
The magnitude of the cross-WVD is centered around $f^{(xy)}(t) = 2\beta t + \alpha - \frac{\theta_1}{2}$, in between $f^{(xx)}(t) = 2\beta t + \alpha$ and $f^{(yy)}(t) = 2\beta t + \alpha - \theta_1$. The same considerations hold for the spectral peaks of the SPWVD $S_{xx}(t,f)$, $S_{yy}(t,f)$, and $S_{xy}(t,f)$, since $\phi_{\text{t-f}}(t,f)$ is symmetric. It is then clear then the higher θ_1 is, the lower the coherence between

$x_1(t)$ and $x_2(t)$ would be.

The phase of the cross SPWVD would be affected by the smoothing function $\phi_{\text{t-f}}(t, f)$. It is worth noting that the estimation of the phase difference only in specific time-frequency regions in which the local coupling is significant is important in two aspects: (i) if for a given time instant $f_{\text{x,B}}(t) \approx f_{\text{y,B}}(t)$ does not hold (in this example if $\beta_1 \approx \beta_2$ does not hold), phase difference between spectral components B of signals $x(t)$ and $y(t)$, $\theta_{\text{B}}(t)$, is not estimated, since coherence is not statistically significant; (ii) The dependence of $\theta_{\text{B}}(t)$ on the degree of TF smoothing is reduced by using TV spectral bands $\Omega_{\text{B}}^{(\theta)}$ whose width is related to the frequency resolution, i.e. to $\Delta_{\text{f}}^{\text{m}}$.

Another important issue to give a correct interpretation of the estimates concerns the effect which the inversion of a signal has on the phase differences. Note that, given complex exponentials $x(t)$, $y(t)$ and $z(t)$, we get:

$$\text{If } z(t) = -y(t) \Rightarrow \Theta_{\text{xz}}(t, f) = \Theta_{\text{xy}}(t, f) \pm \pi \tag{5.14}$$

Therefore, if $x(t)$ leads $y(t)$ with a phase difference $\theta(t) < \pi$, the reciprocal and the opposite of $y(t)$ may lead $x(t)$. This is important when assessing cardiovascular and cardiorespiratory interactions that involve heart rate or heart period variability. Using one or another of the many existing representations of heart rate or heart period [238] may lead to completely different results.

Time-delay

We consider the case in which two linear chirps are related by a constant time-delay $\mathcal{T} > 0$:

$$x(t) = \exp(j2\pi(\alpha t + \beta t^2)) \tag{5.15}$$
$$y(t) = x(t - \mathcal{T}) = \exp(j2\pi(\alpha(t - \mathcal{T}) + \beta(t - \mathcal{T})^2)) \tag{5.16}$$

In this case $x(t)$ leads $y(t)$. The cross WVD distribution is:

$$W_{\text{xy}}(t, f) = |W_{\text{xy}}(t, f)|\exp(j\Theta_{\text{xy}}(t, f)) =$$
$$= \exp\left(j2\pi\left[(2\beta t + \alpha - \beta\mathcal{T})\mathcal{T}\right]\right) \cdot \delta\left(f - (2\beta t + \alpha - \beta\mathcal{T})\right)$$

If we take the definition of time-delay given in (5.11) we get:

$$\mathcal{D} = \frac{\Theta_{\text{xy}}(t, f)}{2\pi f^{(\text{xy})}(t)} = \frac{2\pi(2\beta t + \alpha - \beta\mathcal{T})\mathcal{T}}{2\pi(2\beta t + \alpha - \beta\mathcal{T})} = \mathcal{T} \tag{5.17}$$

Phase differences are estimated only in time-frequency regions in which the coherence level is statistically significant. This imply that the instantaneous frequencies of $x(t)$ and $y(t)$ should be approximately the same. Being $f^{(\text{xx})}(t) = 2\beta t + \alpha$ and $f^{(\text{yy})}(t) = 2\beta t + \alpha - 2\beta\mathcal{T}$, we get that $f^{(\text{xx})}(t) \approx f^{(\text{yy})}(t)$ if $\beta\mathcal{T} << \beta t + \frac{\alpha}{2}$.
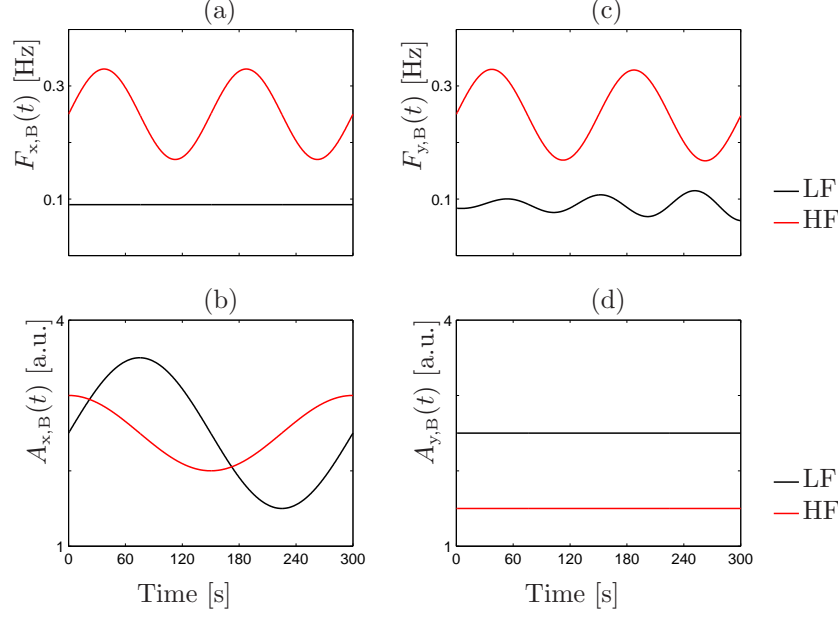
Figure 5.2: Time-frequency structure of signals of type (5.1) used in the simulation studies. (a)–(b): Instantaneous frequencies, (c)–(d): instantaneous amplitudes of the signals. (a) and (c): components of $x(t)$; (b) and (d): components of $y(t)$. Time-course of LF and HF spectral indices are in black and red, respectively.

5.3   Validations

5.3.1   Time course of the phase differences

Two simulation studies were carried on with the purpose of evaluating the estimator of the phase differences proposed in (5.10). The results obtained by cross time-frequency analysis are then compared to that obtained by the straightforward estimator given in (5.2).

Simulation 1 (SIM1) – Synthetic signals.

The first simulation study (SIM1) is based on synthetic signals. Simulated signals $x(t)$ and $y(t)$ are of type (5.1) and are characterized by the highly non-stationary TF structure reported in Fig. 5.2. These signals can be seen as locally coupled, since their spectral components share similar instantaneous frequencies and their amplitudes vary slowly. The phase difference between LF spectral components, $\theta_{\mathrm{LF}}(t)$, varies sinusoidally, while the phase difference between HF spectral components, $\theta_{\mathrm{HF}}(t)$, vary quadratically. Their mathematical expressions are:

$$\theta_{\mathrm{LF}}(t) = \theta_{\mathrm{y,LF}}(t) - \theta_{\mathrm{x,LF}}(t) = 2\pi \left(0.1 + 0.35\frac{t}{T}\right) \sin\left(2\pi\frac{3}{T}t\right) \text{ [radians]} \qquad (5.18)$$

$$\theta_{\mathrm{HF}}(t) = \theta_{\mathrm{y,HF}}(t) - \theta_{\mathrm{x,HF}}(t) = 0.9\pi \left(0.9\frac{t}{T} + 0.1\right)^2 \text{ [radians]} \qquad (5.19)$$

115

where $T = 300$ s is the length of the signals. In this non-stationary context, these phase differences cause the instantaneous frequencies of the signals to slightly differ. The time-frequency structure of the signals used in this simulation is similar to that used in the comparative study described in §4.6 (see Fig. 4.8). The same physiological and mathematical considerations apply in this case. In this simulation, the tracking of the phase differences is particularly challenging since all the parameters which determine the TF structure of the signals, i.e. $A_{k,B}(t)$, $f_{k,B}(t)$ and $\theta_B(t)$, vary quickly and simultaneously. The most prominent changes occur in LF, where the rate of variation of $\theta_{LF}(t)$ gives, for $t \approx 260$ s, $|f_{x,LF}(t) - f_{y,LF}(t)| \approx 0.025$ Hz.

The performance of the estimator of phase differences based on cross TF analysis, described through (5.3)–(5.10), is compared to the performance of the estimator based on the integration of the instantaneous frequencies, described in (5.2).

To assess whether the estimators of the phase differences are robust against noise, white Gaussian noise was added to signals $x(t)$ and $y(t)$ and the estimation was repeated for different levels of SNR, ranging from 0 to 20 dB. For every SNR level, 100 couples of signals were processed. Time-frequency spectra were estimated by using the kernel (4.11), which gave a time and frequency resolution of $\Delta_t^m \approx 12$ s and $\Delta_f^m \approx 0.04$ Hz.

Results: An illustrative example of a single-trial cross TF analysis of two signals $x(t)$ and $y(t)$ is given in Fig. 5.3. In panel (a) the signals as appear before adding the noises are shown. By visual inspection, it is already possible to recognize intervals during which the LF oscillation of $x(t)$ leads the LF oscillation of $y(t)$ and intervals in which the LF oscillation of $x(t)$ lags behind the LF oscillation of $y(t)$. In panel (b) the white Gaussian noises that give a SNR equal to 5 dB are shown. Time-frequency coherence and phase differences are reported in panels (c)–(d). Black contours encircle $\Omega_B^{(\theta)}$, the time-frequency region centered around $f_B^{(xy)}(t)$ in which phase differences are estimated. A narrowing of $\Omega_{LF}^{(\theta)}$ is observed around 200 and 260 s. This reflects a decrease of the local coupling due to the increasing of the difference between $f_{x,LF}(t)$ and $f_{y,LF}(t)$, which occurs for high values of $|d\theta_{LF}(t)/dt|$. In this particular study, we do not perform opening, i.e. $R(t, f) = \delta(0, 0)$ in (5.9), and no minimum size for the region $\Omega_B^{(\theta)}$ is required.

Finally, the time-course of estimates $\hat{\theta}_B(t)$, obtained by averaging in $\Omega_B^{(\theta)}$, is depicted in panels (e). It is shown that, despite the low SNR level and the non-stationary framework, the estimates accurately followed the time-course of the phase differences.

The global results of the first simulation are summarized in Fig. 5.4, where panels (a)–(d) and (e)–(h) show the results obtained by cross time-frequency analysis, as in (5.4)–(5.10), and by integration of the differences of the instantaneous frequencies, as in (5.2), respectively. In (5.2), the instantaneous frequencies of the spectral components of $x(t)$ and $y(t)$ were estimated as the frequencies corresponding to the maximum of the instantaneous auto TF spectra in both LF and HF bands. The time-course of the estimated phase differences between each component, $\hat{\theta}_B(t)$, is shown in panels (a)–(b) and (e)–(f), where results are given as the range between the lower and upper quartiles of the estimates. As shown, the estimator based on cross TF analysis gave a better characterization of the changes of the phase differences
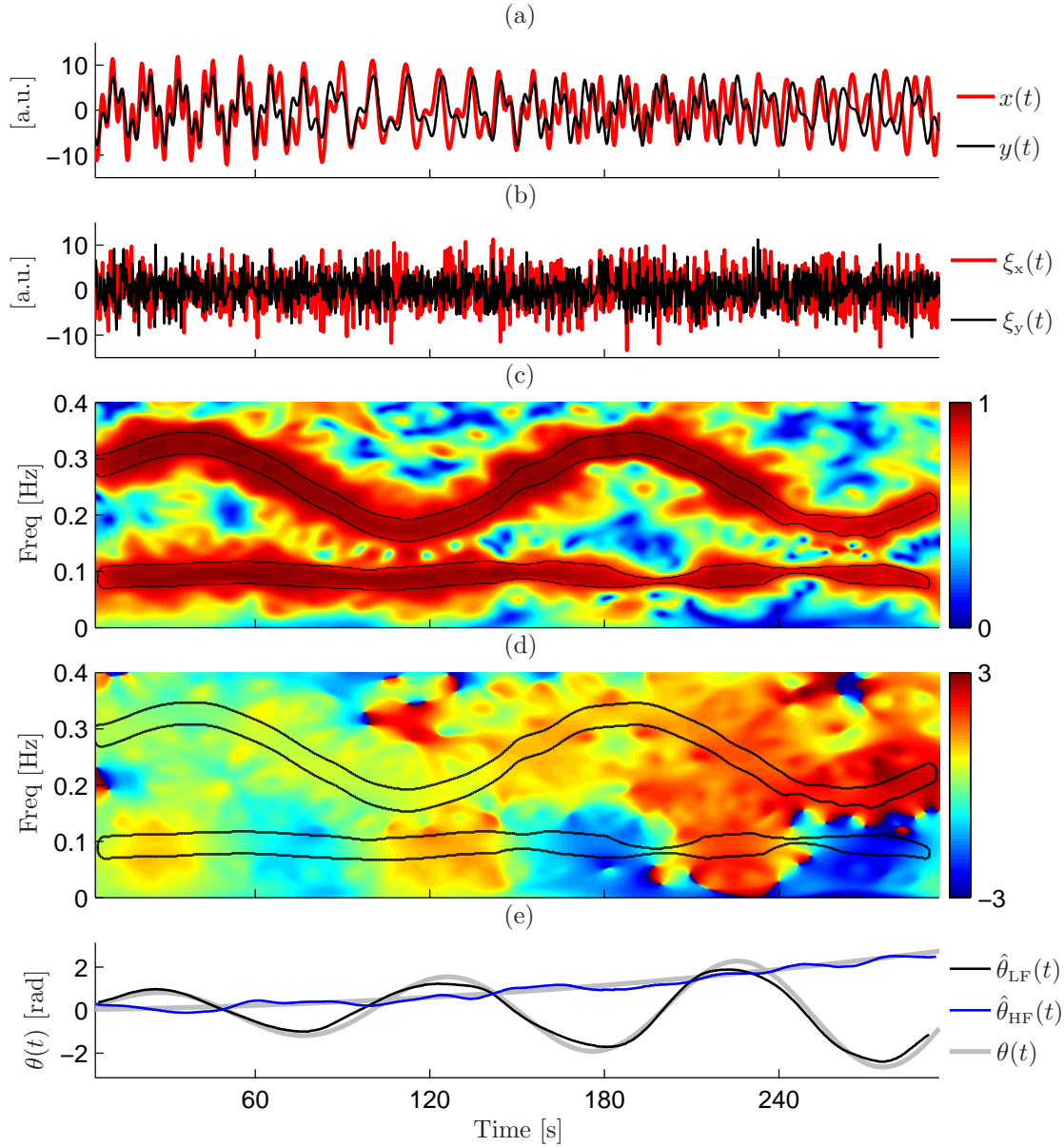
Figure 5.3: (a) Signals $x(t)$ and $y(t)$ without noise, whose TF structure is represented in Fig. 5.2; (b) White Gaussian noises giving SNR=5 dB; (c) Time-frequency coherence $\gamma(t, f)$, as in (4.10), of signals with SNR=5 dB; (d) Time-frequency phase spectrum $\Theta(t, f)$, as in (5.4); (e) Time courses of the phase differences in LF and HF spectral ranges, as in (5.18)–(5.19). Bold lines represent $\theta_{\mathrm{B}}(t)$. Contours reported in (c) and (d) encircle the time-frequency region $\Omega_{\mathrm{B}}^{(\theta)}$ where $\theta_{\mathrm{B}}(t)$ are estimated.

than the estimator based on the estimation of the instantaneous frequencies.

To quantify the goodness of the estimation, the median, and the lower and upper quartiles of the estimation errors, $\theta_\mathrm{B}(t) - \hat{\theta}_\mathrm{B}(t)$, were calculated for every iteration. The results of error analysis are given in panels (c)–(d) and (g)–(h), where circles and bars represent the average of the median and of the interquartile ranges of the estimation errors.

Numerical results are given in Table 5.1. Concerning the results obtained by cross TF analysis, it is shown that the median errors were always lower than 0.013 rad, even for SNR as low as 0 dB. The variability of the estimation depended on the SNR and on the rate of variation of $\theta_\mathrm{B}(t)$. For SNR=20 dB and for $\theta(t)$ varying quadratically, as in $\theta_\mathrm{HF}(t)$, the interquartile ranges were lower than 0.05 rad, less than 2% of the total range of variation of $\theta(t)$. For SNR=0 dB and for $\theta(t)$ varying sinusoidally, as in $\theta_\mathrm{LF}(t)$, the interquartile range was about 0.42 rad, about 8% of the total range of variation of $\theta(t)$.

The estimation of the phase differences by integration of the differences between the instantaneous frequencies gave results characterized by much lower accuracy. The estimation errors were characterized by interquartile ranges at least 34% higher than those obtained by cross TF analysis. For SNR equal to 0 dB, the interquartile ranges of the errors given by (5.2) were, in LF and HF bands, more than 200% and 800% higher than those obtained by the proposed method. The lower accuracy in estimating the phase differences by (5.2) with respect to (5.10), was mainly due to the difficulty of perfectly tracking the instantaneous frequencies of the signals, specially in presence of noise.

Simulation 2 (SIM2) – Real signals.

The second simulation study (SIM2) is based on recorded physiological signals. In this simulation, heart rate variability signals derived from ECGs acquired during a tilt table test (see the Appendix §A for details) are used. The signals used in the simulation are obtained as:

$$x(t) = a_\mathrm{RRV}(t) + \xi_\mathrm{x}(t) \quad \text{and} \quad y(t) = a_\mathrm{RRV}(t)\exp(-j\theta(t)) + \xi_\mathrm{y}(t) \tag{5.20}$$

where $a_\mathrm{RRV}(t)$ is the complex analytic signal representation of the RRV signal, and $\xi_\mathrm{K}(t)$ are complex white Gaussian noises. Complex analytic signals are obtained by using the Hilbert transform.

Two cases are simulated:

(i) In the first one, $\theta(t)$ changes sinusoidally (see Fig. 5.5a and 5.5e), as in (5.18).
(ii) In the second case $\theta(t)$ changes quadratically (see Fig. 5.5b and 5.5f) as in (5.19).

In this simulation, signals were longer than in the previous one, being $T \approx 800$ s. The estimation of $\theta_\mathrm{B}(t)$ was performed via cross time-frequency analysis as well as directly via the instantaneous frequency estimates as in (5.2), and it was repeated for different level of SNR, going from 20 to 0 dB. As in SIM1, time-frequency spectra were estimated by using the kernel (4.11), giving $\Delta_\mathrm{t}^\mathrm{m} \approx 12$ s and $\Delta_\mathrm{f}^\mathrm{m} \approx 0.04$ Hz.

Results: In these simulations, from each one of the 14 RRV signals, 50 couples of modified signals were generated for every SNR level. Given that $\theta_{\mathrm{LF}}(t) = \theta_{\mathrm{HF}}(t)$, the time course of $\hat{\theta}(t)$ was obtained by averaging between $\hat{\theta}_{\mathrm{LF}}(t)$ and $\hat{\theta}_{\mathrm{HF}}(t)$.

The results are summarized in Fig. 5.5, where panels (a)–(d) and (e)–(h) show the results obtained by cross TF analysis as in (5.10) and by integration of the differences of the instantaneous frequencies, as in (5.2), respectively.

The time-courses of the estimated phase differences, $\theta(t)$, are shown in panels (a)–(b) and (e)–(f), where results are given as the range between the lower and upper quartiles of the estimates. As shown, the estimator based on cross TF analysis was able to accurately track the changes of the phase differences in both the considered cases, while the estimator based on the estimation of the instantaneous frequencies did not provide a reliable characterization of these changes. The median, and the lower and upper quartiles of the estimation errors, $\theta_{\mathrm{B}}(t) - \hat{\theta}_{\mathrm{B}}(t)$, were calculated for every iteration. The results of error analysis are given in panels (c)–(d) and (g)–(h), where circles and bars represent the average of the median and of the interquartile ranges of the estimation errors.

Numerical results are given in Table 5.1. It is shown that the median errors were always lower than 0.01 rad, even for SNR as low as 0 dB. As for SIM1, the variability of the estimation depended on the SNR and on the rate of variation of $\theta(t)$. For SNR=20 dB and for $\theta(t)$ varying quadratically, the interquartile ranges were lower than 0.05 rad, less than 2% of the total range of variation of $\theta(t)$. While for SNR=0 dB and for $\theta(t)$ varying sinusoidally, the interquartile range was about 0.4 rad, less than 10% of the total range of variation of $\theta(t)$. The estimation of the phase differences by integration of the differences between the instantaneous frequencies gave results characterized by much lower accuracy. The estimation errors were characterized by interquartile ranges at least 20 times higher than those obtained by cross TF analysis (scales of panels (g)-(h) are 10 times higher than those of panels (c)-(d)).

The comparison between the results of SIM1 and SIM2 show that cross time-frequency analysis gave comparable results both on real and synthetic signals, while the methods based on the integration of the instantaneous frequencies gave much worse results when applied on recorded physiological signals. This was mainly due to the difficulty of reliably tracking the instantaneous frequencies of recorded physiological signals, specially in HF band.

5.3.2 Time delay

To assess the capability of the estimator (5.11) to correctly follow changes in the time delay of non-stationary signals, a simulation study is carried on. In this simulation, signals are synthetic and are obtained by the model described in (5.1). In particular:

- Signal $x(t)$ has the same time-frequency structure as $x(t)$ in SIM1 (see Fig. 5.2a–b).
- Signal $y(t)$ is obtained from $x(t)$, as $y(t) = x\left(t - \mathcal{D}(t)\right)$.

The time delay $\mathcal{D}(t)$ increased stepwise as shown in Fig. 5.6.
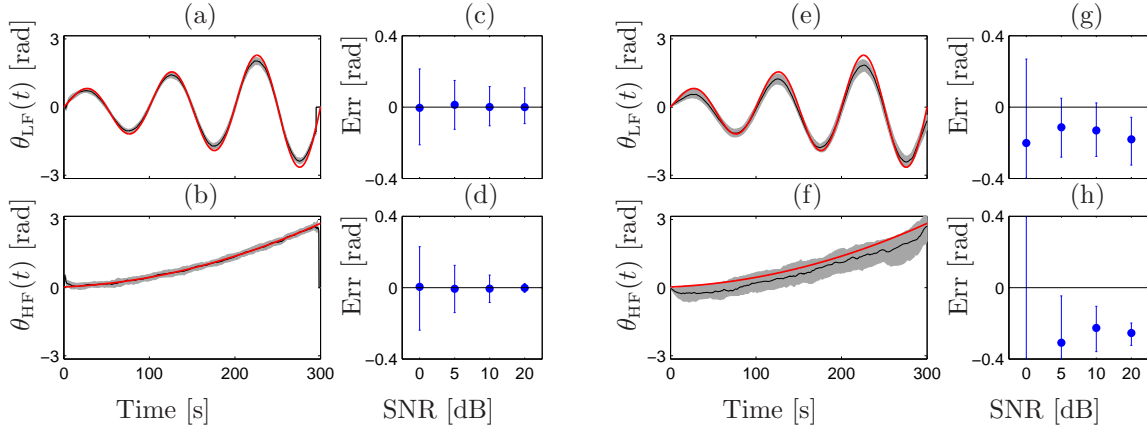
Figure 5.4: SIM I. (a)–(d): Results of cross time-frequency analysis; (e)–(h): Results obtained by instantaneous frequency estimates. (a)–(b) and (e)–(f): Red lines represent $\theta(t)$; shadowed areas represent the range between the lower and upper quartile of estimates $\theta(t)$. In these examples SNR=10 dB; (c)–(d) and (g)–(h): circles and bars represent the average of the I, II and III quartiles of the estimation errors.
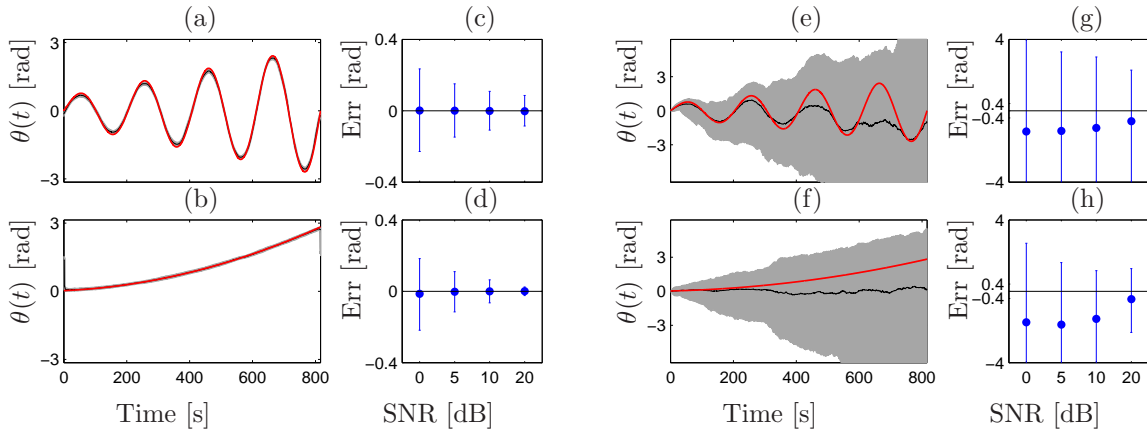
Figure 5.5: SIM2. See caption of Fig. 5.4 for a description of the graphic.
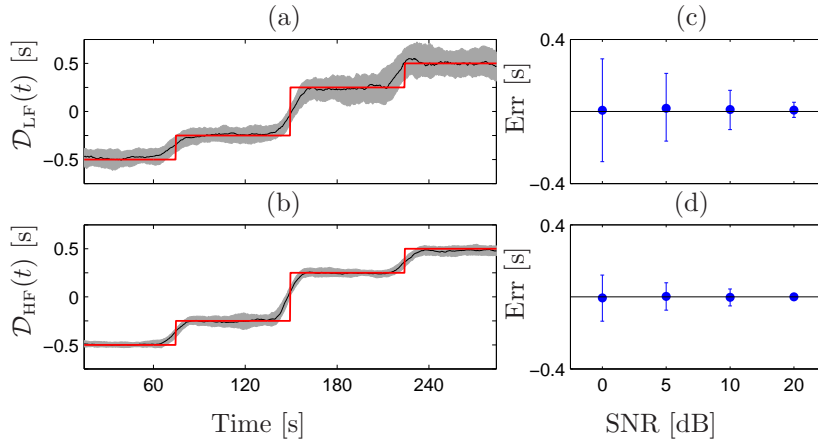
Figure 5.6: Time delay. (a)–(b): results of cross TF analysis; red lines represent $\mathcal{D}_{\mathrm{B}}(t)$; shadowed areas represent the range between I and III quartiles of $\mathcal{D}_{\mathrm{B}}(t)$. In these examples SNR=10 dB; (c)–(d): circles and bars represent the average of the I, II and III quartiles of the estimation errors.

Table 5.1: Simulation results. Results are reported as the average of the median $\pm$ the interquartile range of the estimation errors obtained at each iteration. Results concern the estimation errors shown in Fig. 5.4, Fig. 5.5 and Fig. 5.6.

Param	(eq.)	[unit]	20 dB	10 dB	5 dB	0 dB
			Phase differences – SIM1 – Synthetic signals			
$\theta_{\mathrm{LF}}(t)$	(5.10)	[Hz]	0.000 ± 0.200	0.000 ± 0.220	0.013 ± 0.274	-0.004 ± 0.426
	(5.2)	[Hz]	-0.180 ± 0.268	-0.131 ± 0.300	-0.113 ± 0.331	-0.201 ± 0.886
$\theta_{\mathrm{HF}}(t)$	(5.10)	[Hz]	-0.001 ± 0.049	-0.006 ± 0.153	-0.007 ± 0.264	0.005 ± 0.468
	(5.2)	[Hz]	-0.254 ± 0.126	-0.23 ± 0.253	-0.309 ± 0.551	-1.719 ± 3.923
			Phase differences – SIM2 – Real signals			
$\theta_{\mathrm{LF}}(t)$	(5.10)	[Hz]	-0.002 ± 0.171	-0.001 ± 0.217	0.000 ± 0.298	0.001 ± 0.463
	(5.2)	[Hz]	-0.591 ± 6.618	-1.150 ± 8.440	-1.412 ± 9.548	-1.536 ± 12.165
$\theta_{\mathrm{LF}}(t)$	(5.10)	[Hz]	0.000 ± 0.048	0.000 ± 0.129	-0.002 ± 0.226	-0.014 ± 0.402
	(5.2)	[Hz]	-0.439 ± 3.579	-1.664 ± 6.431	-2.017 ± 8.598	-2.112 ± 11.636
			Time delay – Synthetic signals			
$\mathcal{D}_{\mathrm{LF}}(t)$	(5.11)	[sec]	0.008 ± 0.084	0.011 ± 0.218	0.017 ± 0.376	0.006 ± 0.571
$\mathcal{D}_{\mathrm{HF}}(t)$	(5.11)	[sec]	0.000 ± 0.036	-0.002 ± 0.093	0.003 ± 0.151	-0.006 ± 0.256

Results: Time-frequency spectra were estimated by using the same kernel as that used in the previous simulations, which gave a time and frequency resolution of about 12 s and 0.04 Hz.

Results of this simulation are reported in Fig. 5.6 and Table 5.1.

The time delay $\mathcal{D}_{\mathrm{B}}(t)$ was estimated only by cross time-frequency analysis, as in (5.11). The time delay between the spectral components of $x(t)$ and $y(t)$ is the same in both LF and HF ranges. However, in contrast to what we did for SIM2, here we separately estimated $\mathcal{D}_{\mathrm{LF}}(t)$ and $\mathcal{D}_{\mathrm{HF}}(t)$, since the estimator $\mathcal{D}_{\mathrm{B}}(t)$ (5.11) also depends on the instantaneous frequency of the spectral components.

The results concerning $\mathcal{D}_{\mathrm{LF}}(t)$ are shown in panels (a) and (c), while the results concerning $\mathcal{D}_{\mathrm{HF}}(t)$ are shown in panels (b) and (d).

In panels (a)–(b) of Fig. 5.6, it is shown that the median trend of the estimates correctly tracked the abrupt changes of $\mathcal{D}_{\mathrm{B}}(t)$, with a time of adaptation, from the stepwise increase of $\mathcal{D}_{\mathrm{B}}(t)$ to the stabilization of the estimates, of about 10 s. As shown in Table 5.1, the variability of the estimates is greatly affected by the level of noise. The interquartile range of the error was higher in LF than in HF. This is likely due to the fact that the LF oscillation has a period of about 11 sec, about twice the minimum period of the HF component. This implies that an error in the estimation of the instantaneous frequency of the LF component causes $\mathcal{D}_{\mathrm{LF}}(t)$ estimates to vary greatly.

5.4 Discussion

In this chapter, a new methodology for the quantification of phase differences in non-stationary signals related to the cardiovascular and cardiorespiratory systems, based on cross TF analysis, is proposed. This methodology includes the estimation of the time-course of the phase differences, time delay and phase locking.

These estimates are relevant in the study of the cardiovascular interactions since they allow to infer which changes can be considered the cause and which the effect. Once that the prevalent direction of the coupling is determined, the characteristic latency of these changes is continuously quantified by the time delay.

A limitation of using the phase difference estimate to characterize the causal interactions between two spectral components is the intrinsic periodicity of the phase. Mathematically, the estimation of the phase difference $\theta(t)$ and the time delay $\mathcal{D}(t)$ are associated to the sets $\{\theta(t) \pm k(2\pi)\}$ and $\{\mathcal{D}(t) \pm kT(t)\}$, with $k \in \mathbb{N}$, and being $T(t)$ the time-varying period of the oscillations. However, the assessment of the strength of the local coupling and time delay of the observed interactions reduces this uncertainty. The fact that in the calculation only those time-frequency regions characterized by a significant level of coherence are considered implies that latencies much higher than the time resolution, $\mathcal{D}(t) >> \Delta_{\mathrm{t}}^{\mathrm{m}}$, should be discarded since they are not consistent with a high level of local coupling. Once that values of $\mathcal{D}(t)$ consistent with the local temporal scale of coherence analysis $\Delta_{\mathrm{t}}^{\mathrm{m}}$ has been determined, they should be compared with the range of latencies which are consistent with the physiological phenomenon under observation. An example of this kind of analysis is given in §8, where the time delay of the baroreflex is determined by considering those values consistent with a $\Delta_{\mathrm{t}} \approx 11$ s and the range of latencies [0.24, 3.00 s] which were experimentally estimated as typical of the baroreflex [71].

Among the different members of the Cohen's class, the SPWVD has been chosen since it provides auto and cross spectra characterized by high joint TF resolution [206], which can be independently adjusted in time and frequency. The localization of specific time-frequency regions in which the time-course of the indices is estimated is of crucial importance to obtain reliably estimates. This represents an improvement with respect to methodologies that make use of rigid time invariant spectral boundaries for extracting the time course of the indices. In practice, the use of rigid boundaries reduces the time-frequency analysis to a technique composed of a previous band-pass filtering followed by some traditional time invariant analysis. While the simultaneous localization of specific spectral ranges and time intervals from which indices are extracted allows to make the most of the joint time-frequency analysis.

In non-stationary contexts, this methodology was shown to provide accurate estimates also in presence of noise, and it outperformed straightforward techniques based on instantaneous frequency estimates.

Another widely used technique to assess phase differences is based on the estimation of the phase of the analytical representation of signals obtained by Hilbert transform [198]. This technique has the advantage to be rather simple and computationally fast. However, it is not appropriate to study multicomponent signals since it does not provide specific estimates of phase differences for different spectral components.

For a more in depth discussion about the use of the time-frequency phase difference spectrum and its derived measures in the analysis of dynamic interactions between the R–R variability and the systolic arterial pressure variability signal, please refer to §8.

Part II

Physiological studies

Chapter 6

Dynamic assessment of the autonomic response to music-induced emotions: HRV and respiration

Contents

6.1 Introduction

Almost everyone loves music because, among other reasons, it evokes particular emotional states. These emotional states are related to brain and autonomic nervous system activity, but the relationship between musical and autonomic features is far from being completely understood. The use of music for therapeutic purposes or, more generally, for improving our well-being, is a matter of increasing interest [39, 40, 106, 107, 128, 197, 228], but only little is known about how music can modulate physiological indices such as heart and breathing rate.

To continuously quantify and characterize the autonomic response to sound stimuli, an appropriate methodology is needed. In particular, this methodology should be able to track music-induced dynamics in the autonomic nervous system, and it should include an appropriate statistical study to assess whether different musical stimuli induce significantly different autonomic responses.

In this chapter, HRV is studied by TF analysis to characterize the autonomic response to musical stimuli. Time-frequency analysis has been performed since it provides a representation of a signal in both time and frequency domain simultaneously. The characterization of the dynamics induced by musical stimuli with different emotional valence on the autonomic modulation of heart rate is based on the methodology presented in §3.3.

The spectral analysis of HRV is a well established technique to assess autonomic activity [1] (see §1.2.3) and it was already proposed, in a stationary context, as a critical index for the assessment of autonomic effects elicited by music [128]. In non-stationary conditions, the tracking of the HRV spectral components (namely, the LF [0.04, 0.15] Hz and HF [0.15, 0.4] Hz components) provides the assessment of the autonomic dynamics, and different methods have been proposed for the TF analysis of HRV [166, 165]. In this section, we employ a TF approach based on the smoothed pseudo Wigner-Ville distribution (SPWVD) combined with a parametric decomposition (see §3.3) which allows to obtain a denoised spectrum and a robust estimation of HRV indices. To characterize the dynamic autonomic response to a given musical stimulus, individual response patterns for each subject are estimated and a sample-by-sample statistical analysis is performed.

After having characterized the time-course of the HRV indices, we study the effect that different musical stimuli have on the cardiorespiratory coupling. To this end, we apply time-frequency coherence and cross time-frequency analysis described in §4-§5.

6.2 Experimental procedure

Seventy five subjects without any formal musical education (age range: $18 - 35$ years, mean age: 24.5 ± 3.2 years, 36 female) participated in an experiment designed to characterize the effects of acoustic stimuli with different emotional valence. All subjects were right-handed with an handedness quotient >90 according to the 'Edinburgh Handedness Inventory 9' [199], and reported to have normal hearing.

During the experiment, four conditions were employed:

(i) *Pleasant condition* (P): six excerpts of joyful instrumental dance-tunes from the

last four centuries were used as pleasant stimuli (all major-minor tonal music, each had a duration of 90 s). The tempo of the excerpts, measured in beats per minute was 73, 105, 117, 124, 128, 169, mean $= 119.33\pm31.37$ bpm.

(ii) *Unpleasant condition* (U): six unpleasant stimuli were electronically manipulated counterparts of six musical pieces from the last four centuries (all major-minor tonal music with rather minor scales and slow tempo). For any of these stimuli, a new soundfile was created in which the original excerpt was recorded simultaneously with two pitch-shifted versions (one being one semitone above and the other a tritone below the original pitch), and subsequently recorded backwards in order to introduce many dissonant structures. To match the metre of these stimuli with the metre of the original pleasant ones, series of Shepard tones [234] were overlaid over the manipulated (unpleasant) musical excerpts. The Shepard tone had a stationary pitch and a duration of 100 ms, and each Shepard tone was one semitone higher than the previous Shepard tone (i.e., tones were perceived as a rising chromatic scale). Shepard tones were used to guarantee that the frequency spectrum of the stimuli was comparable, between the beginning and the end of the stimuli. The time interval between Shepard tones was chosen to match the tempo of the pleasant excerpts.

(iii) *Sequence of Shepard Tones* (X): Shepard tones were presented separately, i.e. without music, as control for the unpleasant stimuli. The purpose was to assess whether Shepard tones alone provoked the same effect as the more complex and dissonant unpleasant excerpts. The particular structure of the sequence creates the auditory illusion of a tone that continually ascends or descends in pitch, yet which ultimately seems to get no higher or lower. The time interval between tones was chosen to match the tempo of pleasant and unpleasant excerpts and six sequences were used.

(iv) *Resting condition* (R): in addition to these three stimulus categories, there were also six resting intervals of 90 s duration in which no acoustic stimulus was presented.

All stimuli (pleasant, unpleasant and Shepard tones) were matched for volume (average root mean square power = -21.12 $\pm$ 0.94 dB) and were presented as illustrated in Fig. 6.1. Each stimulus began with a start-signal-tone (four short ascending sine wave tones), and ended with an end-signal-tone (a high, short single sine wave tone). For the resting condition, after the start-signal-tone, trials were indicated by a new 100 ms, 400 Hz sine wave tone. Stimuli were presented to every subject in the same pseudo-randomized sequence, designed so that each experimental condition followed all other conditions with equal probability[1]. After the end-signal-tone of each trial, participants had to indicate how pleasant or unpleasant they felt at the end of the trial by pressing response buttons. The rating task was followed by a 10 s pause until the next start-signal-tone appeared. Participants were instructed to listen carefully to the auditory stimuli with eyes closed, and to tap the metre of the stimuli with their right

---

[1]More in detail, the entire sequence was: $X,U,P,X,U,R,X,P,R,U,X,P,U,X,R,P,U,R,P,X,R,U,P,R$.

index finger. This task was employed to control whether listeners paid attention not only to the pleasant but also to the unpleasant music and to the single tones sequence. No tapping was required during the resting condition.

6.2.1 Signal acquisition and preprocessing

Standard 12 lead electrocardiograms were measured using a 32 MREFA amplifier (Twente Medical Systems, Enschede, Netherlands) and digitized with a sampling rate of 1000 Hz. The recorded ECG signal was processed to derive the HRV signal and to estimate the respiratory frequency. After the detection of the QRS complexes, the instantaneous heart rate $d_{\mathrm{HR}}(t)$ was derived by integral pulse frequency modulation (IPFM) model, which also accounts for the presence of ectopic beats [180], and then evenly resampled at 4 Hz, using spline interpolation. The HRV signal $x(t)$ was then obtained by filtering $d_{\mathrm{HR}}(t)$ with a high-pass filter with a cut-off frequency of 0.03 Hz. By using the methodology explained in §3.3, the HRV signal was processed to estimate the HRV spectral indices, i.e. the instantaneous central frequencies $f_{\mathrm{LF}}(t)$ and $f_{\mathrm{HF}}(t)$ and powers $P_{\mathrm{LF}}(t)$ and $P_{\mathrm{HF}}(t)$ as well as the total instantaneous power, $P_{\mathrm{TOT}}(t) = P_{\mathrm{LF}}(t) + P_{\mathrm{HF}}(t)$ and a measure of the sympatho-vagal balance $P_{\mathrm{LFn}}(t) = \frac{P_{\mathrm{LF}}(t)}{P_{\mathrm{TOT}}(t)}$ [1]. The respiratory rate $f_{\mathrm{resp}}(t)$, necessary to make the HF band respiration-dependent, was indirectly estimated from the ECG derived respiratory signal, by using the method presented in [24].

6.3 Time-frequency analysis of the HRV signal

6.3.1 Dynamic adjustment of HF band

It is generally accepted that the HF component of HRV mainly reflects respiratory sinus arrhythmia [112] and therefore $f_{\mathrm{HF}}(t)$ can be considered an indirect estimation of the respiratory frequency $f_{\mathrm{resp}}(t)$. Thus, the knowledge of $f_{\mathrm{resp}}(t)$ is used to adjust the range of HF band and to improve the estimation of both LF and HF contributions. In traditional spectral analysis the HF range is usually fixed at [0.15, 0.4] Hz. Nevertheless, there are situations in which the use of this range leads to misestimation of the HF component, i.e. when respiratory rate decreases below 0.15 Hz (9 breaths per minute) or increases above 0.4 Hz (24 breaths per minute). In order to avoid these errors, the HF band is made time-varying and respiration-dependent [17]. The spectral boundaries are defined as:

$$\begin{cases} B_{\mathrm{LF}}(t) \in [0.04, 0.15] \text{ Hz} \\ B_{\mathrm{HF}}(t) \in f_{\mathrm{resp}}(t) \pm [-0.125, 0.125] \text{ Hz} \end{cases} \tag{6.1}$$

where $B_{\mathrm{LF}}(t)$ and $B_{\mathrm{HF}}(t)$ identify the LF and HF bands. In such a way, the HF band is dynamically adjusted around $f_{\mathrm{resp}}(t)$ and thus a correct quantification of HF component is obtained even when the respiratory rate lies outside the traditional HF range. An example is shown in Fig. 3.8b (in §3.3), where $f_{\mathrm{resp}} = 0.465$ Hz. In this case the use of a respiration-dependent range (plotted in dashed vertical lines) allows
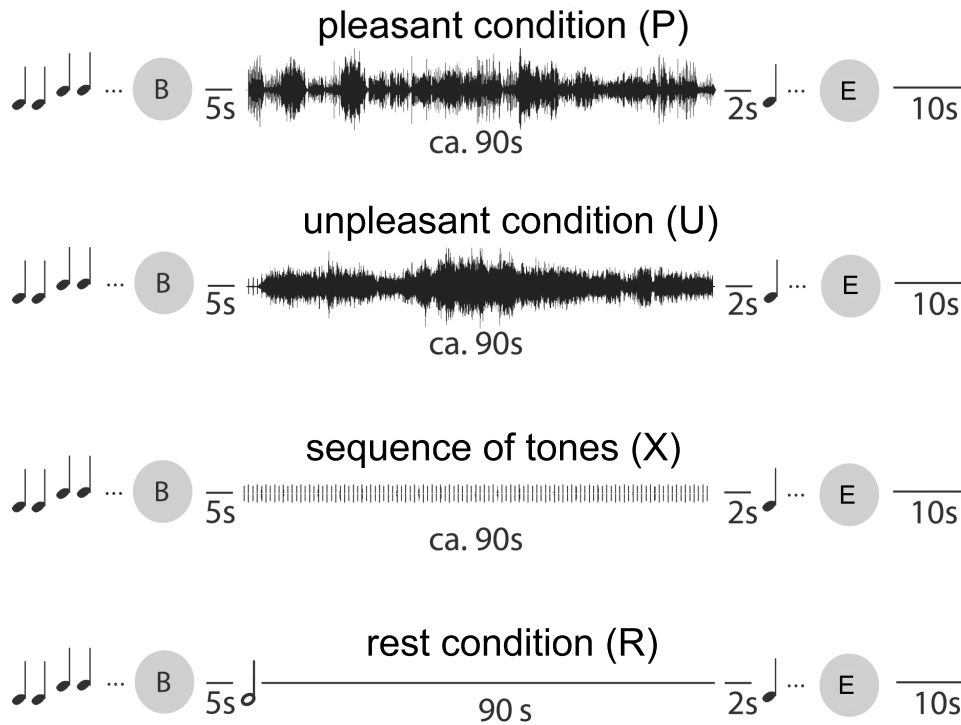
Figure 6.1: Experimental design - The trial begins (B) after a start-signal-tone. Musical pieces and silent period were followed by short signal tones that prompted participants to rate (E) their current emotional state. A 10 s pause was added before presentation of the next auditory cue.

to include the HF component, while the use of traditional HF range (dotted vertical lines) misses the HF component. When using the above rule, one has to pay attention to the fact that $B_{\mathrm{LF}}(t)$ and $B_{\mathrm{HF}}(t)$ partially overlap when $f_{\mathrm{resp}}(t) < 0.275$ Hz (16.5 breaths per minute). In this case, if in the spectrum there are two peaks, and at least one is in $B_{\mathrm{LF}}(t)$ and the other in $B_{\mathrm{HF}}(t)$, the one centered around the lower frequencies is considered the LF component and the one centered around the higher frequencies is considered the HF component. In those cases where $f_{\mathrm{resp}}(t)$ is much lower, the overlap between the two ranges increases and just one peak is usually observed. In such a situation, the separation of LF and HF components is not straightforward due to non-linear interactions between sympathetic and parasympathetic modulation [32].

6.3.2   Statistical Analysis

Statistical analysis was designed and performed to assess whether significant differences exist between the time-course of each physiological index in the four experimental conditions. Given that particular attention is paid to quantify the differences of the dynamic pattern of responses provoked by each musical stimulus, the statistical differences are quantified on a sample-by-sample basis.

The following notation is used: subjects are indexed with $i \in [1 : L]$, conditions with $E \in [P, U, X, R]$, stimuli which belong to the same condition with $j \in [1:6]$. A general physiological index is indicated with $\mathcal{I}(t)$. According to this notation, $\mathcal{I}_{\mathrm{i,E,j}}(t)$ represents the time-course of a physiological index during the j-th repetition of condition E for subject i.

We firstly assume that, for each subject, the median time-course over the six repetitions of the same musical condition is representative of the individual autonomic response pattern to that stimulus. This is defined as:

$$\mathcal{I}_{\mathrm{i,E}}^{\mathrm{c,m}}(t) = \mathrm{median} \left\{ \mathcal{I}_{\mathrm{i,E,j}}^{\mathrm{c}}(t) \right\}_{\mathrm{j=1}}^{6} \tag{6.2}$$

where $\mathcal{I}_{\mathrm{i,E,j}}^{\mathrm{c}}(t)$ is the baseline-corrected index computed as:

$$\mathcal{I}_{\mathrm{i,E,j}}^{\mathrm{c}}(t) = \mathcal{I}_{\mathrm{i,E,j}}(t) - \frac{1}{Tf_{\mathrm{s}}} \sum_{n=-Tf_{\mathrm{s}}}^{-1} \mathcal{I}_{\mathrm{i,E,j}}(t) \big|_{t=n/f_{\mathrm{s}}} \tag{6.3}$$

In this expression $f_{\mathrm{s}} = 4$ Hz is the sampling rate and $T = 12$ s is the duration of an interval preceding the onset of each j-th trial.

This particular normalization subtracts the mean values of the index, computed before the onset of each stimulus, from each index and it is used to highlight only the transient phenomena produced by the actual condition and not by the past history or by the different subject reference.

At every instant t_0, the value of $\mathcal{I}_{\mathrm{i,E}}^{\mathrm{c,m}}(t_0)$ for the subject i represents the i-th realization of a statistical population $\Gamma_{\mathrm{E},t_0} = \{\mathcal{I}_{\mathrm{1,E}}^{\mathrm{c,m}}(t_0), \mathcal{I}_{\mathrm{2,E}}^{\mathrm{c,m}}(t_0), ..., \mathcal{I}_{\mathrm{L,E}}^{\mathrm{c,m}}(t_0)\}$, obtained by collecting, from all the subjects, the same index, at the same time t_0.

By iteratively performing a pairwise comparison between the four statistical populations $\Gamma_{\mathrm{P},t}$, $\Gamma_{\mathrm{U},t}$, $\Gamma_{\mathrm{X},t}$ and $\Gamma_{\mathrm{R},t}$ (i.e. 6 pairwise comparisons), and repeating the test at
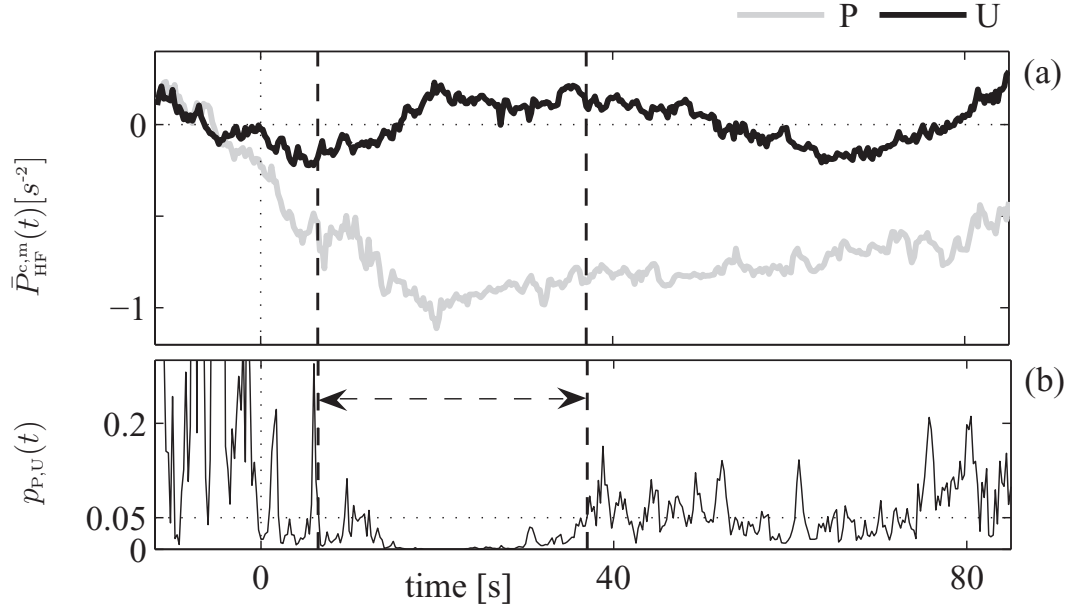
Figure 6.2: (a) Mean trend of $P_{\mathrm{HF}}^{\mathrm{c,m}}(t)$ during pleasant (P) and unpleasant (U) conditions. (b) Time course of the p-value quantifying the differences between $P_{\mathrm{HF,P}}^{\mathrm{c,m}}(t)$ and $P_{\mathrm{HF,U}}^{\mathrm{c,m}}(t)$. Vertical dashed lines mark the epoch (from about 6 to 38 s) in which response patterns are significantly different ($p < 0.05$).

any time instant t, the time-course of six p-values $p_{\mathrm{E}_k,\mathrm{E}_l}(t)$, $(E_{\mathrm{k}}, E_{\mathrm{l}}) \in [P, U, X, R]$ with $E_{\mathrm{k}} \neq E_{\mathrm{l}}$, is estimated. Given that the $\Gamma_{\mathrm{E,t}}$ are not normally distributed, the Man Whitney test is used. The continuous estimation of p-value $p_{\mathrm{E}_k,\mathrm{E}_l}(t)$ allows to assess the time after which the autonomic response to the different conditions differs, and for how long these differences are significant.

An example of this procedure is shown in Fig. 6.2, where the mean time-course of $P_{\mathrm{HF,i}}^{\mathrm{c,m}}(t)$, denoted $\bar{P}_{\mathrm{HF}}^{\mathrm{c,m}}(t)$, during pleasant and unpleasant conditions are reported. The resulting time-course of the p-value $p_{\mathrm{P,U}}(t)$, shown in Fig. 6.2b, allows one to identify the time epochs in which physiological responses are different.

6.3.3 Results

Time-frequency analysis that combines the SPWVD with parametric decomposition, as explained in §3.3, was used to track the dynamic response to music-induced emotion. The kernel of the SPWVD distribution was composed of functions $\phi_{\mathrm{t}}(t)$ and $\phi_{\mathrm{d}}(\tau)$ reported in §3.2.1. These kernels gave a resolution $\Delta_{\mathrm{t}}^{\mathrm{m}} = 25$ s and $\Delta_{\mathrm{f}}^{\mathrm{m}} = 7$ mHz. The traditional LF spectral range and a time-varying HF spectral range whose boundaries depended on the respiratory rate (6.1) were used.

A representative HRV signal segment and its TF representations are plotted in Fig. 6.3. The SPWVD and the TF distribution, $\tilde{S}(t, f)$, obtained through the parametric decomposition (3.17), are reported in Fig. 6.3b and 6.3c, respectively. The parametric decomposition of the autocorrelation function allows to discard the interference terms which were still present in the original SPWVD, $S(t, f)$. This improves the localiza-
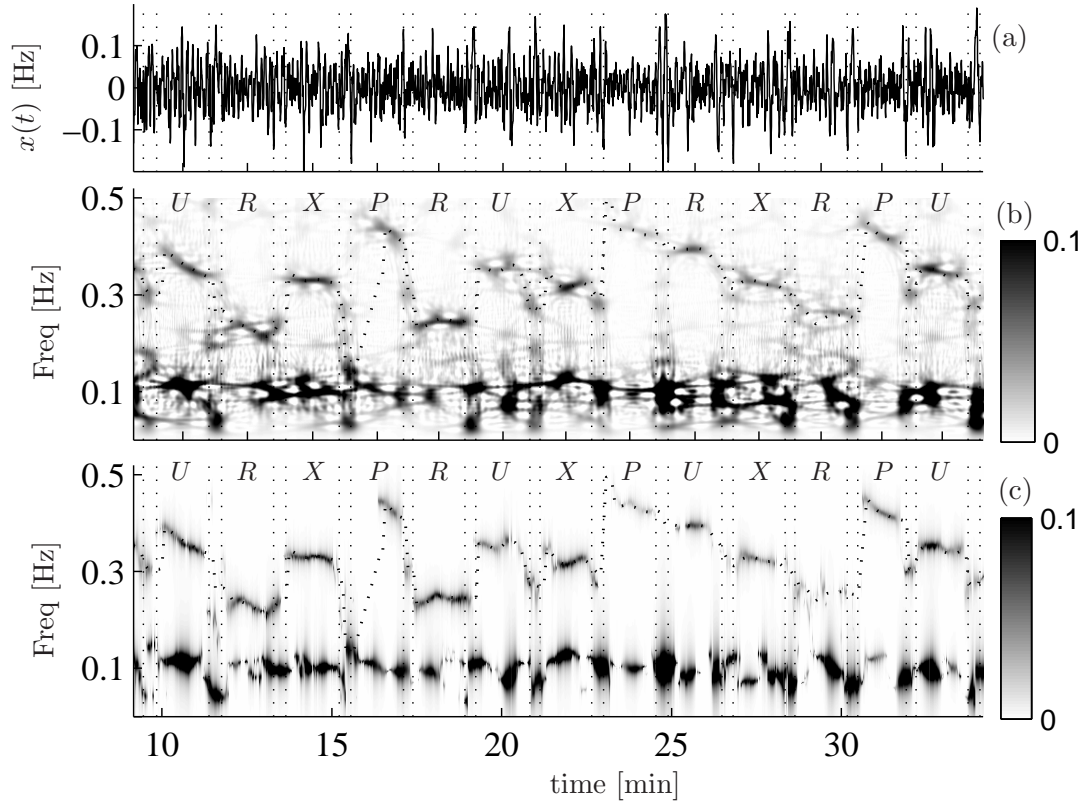
Figure 6.3: Improving the TF representations by parametric analysis. (a) Example of the HRV signal $x(t)$; (b) $S(t, f)$: smoothed pseudo Wigner Ville distribution; (c) $\tilde{S}(t, f)$: TF distribution reconstructed after the parametric decomposition illustrated in §3.3. In dotted line: the respiratory rate. Conditions: pleasant (P); unpleasant (U); sequence of Shepard tones (X); rest (R).

tion in the TF plane of the LF and HF components. From visual inspection of this representation is already possible to qualitatively characterize the patterns related to every particular condition. Low frequency component modulation, centered around 0.1 Hz, increased during the short intervals in between two conditions. As expected, the HF component followed the quick variation of the respiratory rate (reported in dotted line), with a time-course which appears to be highly condition-dependent: the instantaneous frequency of HF was higher during pleasant condition P and lower during rest R.

Differences in the dynamic response to the musical stimuli were continuously quantified through the statistical analysis illustrated in §6.3.2. An example is shown in Fig. 6.2, where the induced response patterns in $P_{\mathrm{HF}}(t)$ during pleasant and unpleasant conditions are shown. During pleasant condition, $P_{\mathrm{HF}}^{\mathrm{c,m}}(t)$ first decreased and, after about 20 s, it slowly increased toward baseline values, while during unpleasant condition it first slightly decreased for about 6 s, then it increased and it maintained higher values from 20 to 50 s from the beginning of the excerpt. The time course of the p-value, reported in Fig. 6.2b, shows that the response patterns were significantly different in

the temporal window 6–38 s after the onset of the stimuli (interval marked by vertical dashed lines). It is worth noting that, even if during pleasant and unpleasant conditions the mean trends were separated, differences were statistically significant only during the first part of the response. This shows the importance of the tracking of the p-value for a correct interpretation of the results.

The mean time course of the physiological indices are shown in Fig. 6.4 and described in the following section, while the results of the statistical analysis are summarized in Fig. 6.5.

In Fig. 6.5, the response patterns of the physiological indices to the experimental conditions are compared pairwise. Every column represents a physiological index $\mathcal{I}(t)$, and the column length represents the duration (% of stimuli duration) during which $\mathcal{I}_{\mathrm{E}_k}(t) > \mathcal{I}_{\mathrm{E}_l}(t)$, with $\mathrm{E} \in [\mathrm{P,U,X,R}]$ and for a significance level $p < 0.05$. A negative value for the column length indicates inverse relationship (i.e., $\mathcal{I}_{\mathrm{E}_k}(t) < \mathcal{I}_{\mathrm{E}_l}(t)$). For example, in the sixth column is reported that $P_{\mathrm{HF}}(t)$ is significantly lower during pleasant than during unpleasant condition, and this difference is maintained for 71% of the duration of the stimulus. Notably, some stimuli provoked index changes which were different for the entire duration of the stimulus. The strength of these differences is quantified by the median p-values estimated in the intervals of statistical significance. Symbols $*$ and $\circ$ indicate that median $p(t) < 0.005$ and median $p(t) < 5 \cdot 10^{-5}$, respectively.

Time course of physiological indices

Significant differences in the autonomic response patterns to pleasant music, unpleasant stimuli, sequence of tones and resting condition were observed. In the following, the changes observed for every physiological indices are described:

– $d_{\mathrm{HR}}(t)$: As shown in Fig. 6.4a, during the first 10 s the heart rate, $d_{\mathrm{HR}}(t)$, decreased for all the conditions, and after a transient of about 20 s it stabilized around values $d_{\mathrm{HR,R}}(t) < d_{\mathrm{HR,X}}(t) \approx d_{\mathrm{HR,U}}(t) < d_{\mathrm{HR,P}}(t)$. All the differences between the conditions were statistically significant (at least during more than 80% of their duration, as reported in Fig. 6.5), except between U and X. Between P and U the significance was reached after about 16 s, while between P and R and between U and R differences were significant from the first instants until the end of the conditions.

– $f_{\mathrm{LF}}(t)$: The mean trend of $f_{\mathrm{LF}}(t)$, reported in Fig. 6.4b, slightly increased from baseline for about 20-30 s, regardless of the kind of stimulus and no relevant difference was detected between the conditions.

– $f_{\mathrm{HF}}(t)$: This index, which is closely related to the respiratory rate $f_{\mathrm{resp}}(t)$, experienced the most marked differences among different musical stimuli. The time-course of the instantaneous frequency of the HF component and of the respiratory rate are shown in Fig. 6.4c and 6.4d, respectively. Their mean trend highly differed from a condition to another with little variability. Difference between $f_{\mathrm{HF,P}}(t)$ and $f_{\mathrm{HF,U}}(t)$ was significant after only 8 s, indicating that the response of $f_{\mathrm{HF}}(t)$ was faster than the one of $d_{\mathrm{HR}}(t)$. After 10–15 s, $f_{\mathrm{HF}}(t)$ reached

a stable state characterized by $f_{\mathrm{HF,R}}(t) < f_{\mathrm{HF,X}}(t) \approx f_{\mathrm{HF,U}}(t) < f_{\mathrm{HF,P}}(t)$. Between P and R and between U and R, differences were statistically significant during all the 90 s (with median p-value$< 10^{-10}$), mainly due to the fact that acoustic stimuli provoked an increase in $f_{\mathrm{HF}}(t)$, while the silence during resting condition was observed to provoke the opposite effect.

– $P_{\mathrm{LF}}(t)$: After the beginning of the trials, the power of the LF component, $P_{\mathrm{LF}}(t)$, was observed to decrease for any condition for about 15–20 s, before reaching a quasi stationary state (see Fig. 6.4e). Its decrease, which was statistically significant from the first seconds of the trials onset ($p <0.001$), had approximately the same rate for every condition. After the transients, it was observed that $P_{\mathrm{LF,P}}(t) < P_{\mathrm{LF,U}}(t) < P_{\mathrm{LF,X}}(t) \approx P_{\mathrm{LF,R}}(t)$. Even if the mean trend during pleasant condition was lower than during unpleasant, their great variability made this difference not statistically significant.

– $P_{\mathrm{HF}}(t)$: Fig. 6.4f depicts the pattern of response of the power of the HF components. It is shown that $P_{\mathrm{HF,X}}(t)$ and $P_{\mathrm{HF,U}}(t)$ fluctuated around baseline values, while $P_{\mathrm{HF,R}}(t)$ and $P_{\mathrm{HF,P}}(t)$ evidenced opposite trends, by increasing ($P_{\mathrm{HF,R}}(t)$) and decreasing ($P_{\mathrm{HF,P}}(t)$) in the first 20 s from the beginning of the stimulus. Almost immediately we observe that $P_{\mathrm{HF,P}}(t) < P_{\mathrm{HF,X}}(t) \approx P_{\mathrm{HF,U}}(t) < P_{\mathrm{HF,R}}(t)$. The differences between P and R and between unpleasant and resting conditions were almost instantaneously significant, while between pleasant and unpleasant conditions significance was reached after about 6 s and it was maintained for about 30 s (see also the example shown in Fig. 6.2).

– $P_{\mathrm{TOT}}(t)$: The total power was also estimated and its mean time-course is shown in Fig. 6.4g. During all the conditions $P_{\mathrm{TOT}}(t)$ tended to decrease from baseline values. During pleasant condition both $P_{\mathrm{LF}}(t)$ and $P_{\mathrm{HF}}(t)$ decreased and this is reflected on the strong reduction of $P_{\mathrm{TOT,P}}(t)$, while the increasing of $P_{\mathrm{HF}}(t)$ during resting condition made $P_{\mathrm{TOT,R}}(t)$ higher than during all the other conditions. The significance of the differences observed in $P_{\mathrm{TOT}}(t)$ were larger than for $P_{\mathrm{LF}}(t)$ but smaller than for $P_{\mathrm{HF}}(t)$.

– $P_{\mathrm{LFn}}(t)$: In Fig. 6.4h the mean baseline-corrected time-course of the sympatho–vagal balance $P_{\mathrm{LFn}}(t)$ is shown. It was observed that $P_{\mathrm{LFn}}(t)$ decreased during about 15 s, regardless of the specific condition and no significant differences were detected between its response patterns.

6.3.4 Discussion

In this section, we presented the results of a methodology designed to continuously quantify music-induced changes in HRV. This approach consists of three steps:

(i) The smoothed pseudo Wigner-Ville distribution is used to obtain a time-frequency representation of the HRV signal.
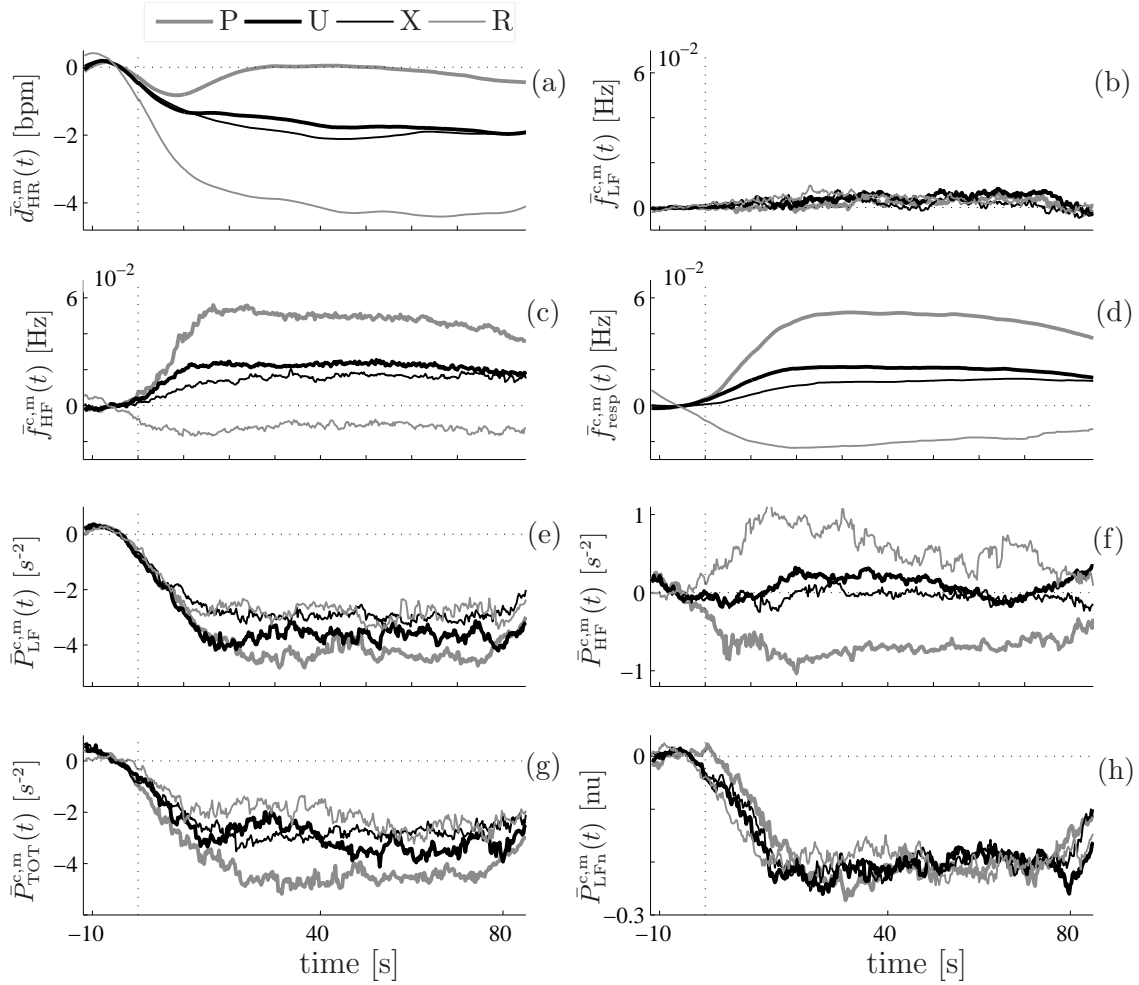
Figure 6.4: Mean trend, averaged over the entire population, of the changes provoked by pleasant (P), unpleasant (U), sequence of tones (X) and rest (R) conditions. Physiological indices from (a) to (h), as detailed in §6.2.1, are: (a) the mean heart rate $\bar{d}_{\mathrm{HR}}^{\mathrm{c,m}}(t)$; (b)-(c) the instantaneous frequency of LF and HF, $\bar{f}_{\mathrm{LF}}^{\mathrm{c,m}}(t)$ and $\bar{f}_{\mathrm{HF}}^{\mathrm{c,m}}(t)$; (d) the respiratory rate $\bar{f}_{\mathrm{resp}}^{\mathrm{c,m}}(t)$; (e)-(f) the instantaneous power of LF and HF, $\bar{P}_{\mathrm{LF}}^{\mathrm{c,m}}(t)$ and $\bar{P}_{\mathrm{HF}}^{\mathrm{c,m}}(t)$; (g) instantaneous total power $\bar{P}_{\mathrm{TOT}}^{\mathrm{c,m}}(t)$; (h) the sympatho–vagal balance $\bar{P}_{\mathrm{LFn}}^{\mathrm{c,m}}(t)$. Results are detailed in §6.3.3
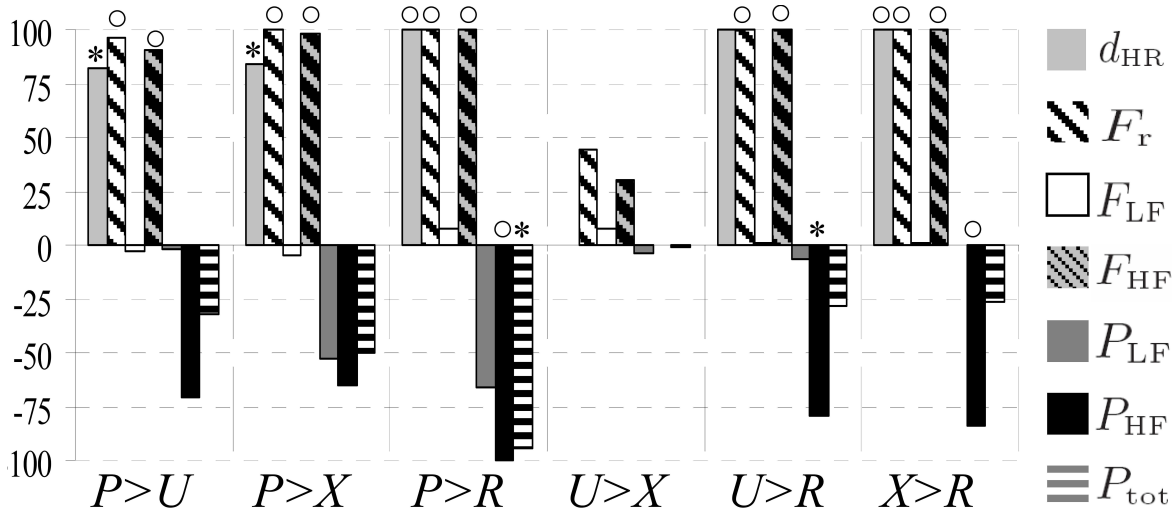
Figure 6.5: Results of the pairwise comparison between the conditions (see §6.3.2). Bar length represents the time duration (% of stimuli duration) in which $P > U$, $P > X$, $P > R$ etc. $(p(t) < 0.05)$. Negative values denote inverse relationship. $*$ and $\circ$: median p-values < 0.005 and $< 5 \cdot 10^{-5}$, respectively.

(ii) The time-course of physiological indices is estimated through a parametric decomposition which makes use of dynamical adjustment of HF range based on respiratory frequency.

(iii) A statistical population analysis is performed to continuously assess whether the dynamics involved in the autonomic response to different musical stimuli are significant or not.

The time-frequency framework

The response patterns of the autonomic nervous system are dynamic, and there is the need for an appropriate methodology capable of tracking these changes. Compared to other possibilities, such as continuous wavelet transform, spectrogram and time-varying autoregressive methods [165], the SPWVD has the advantage of an excellent joint TF resolution [124, 232]. In addition, the SPWVD was used, in a recent study [39], to estimate the changes in the instantaneous power spectrum of the respiratory signal induced by the listening to classical music excerpts.

In the TF analysis of HRV based on the WVD, the simultaneous presence of time-varying LF and HF components gives rise to interference terms [125] (see §3.1.1) which should be reduced using an appropriate kernel. In simulation studies, the smoothing function used in this study was shown to provide a reliable estimation of LF and HF dynamics, also in high non-stationary conditions [204, 203] (see also results shown in §3.2.1). Other kinds of kernels, capable of achieving a wide range of different shapes [72], or of automatically adjusting to the signal structure [25, 26, 19], have been proposed in the literature. However, a fixed kernel is used in this study to maintain the same time-frequency resolution for all subjects.

The parametric decomposition used to estimate the time-course of the spectral indices

allows to separate the information which is considered inherent to the signal from both noise and interference terms. This methodology was firstly proposed in [164] and here it was combined with the respiratory rate to improve the tracking of the HF component [20].

Dynamic HF band

The use of time-varying bands for a reliable estimation of HRV spectral components has been proposed in different applications. Most of these techniques make use of respiratory information to determine the spectral boundaries [130, 17, 19]. The inclusion of the respiratory rate in the definition of the HF range is specially important in time-frequency analysis.

In our results we observed marked variations in the respiratory rate due to the musical stimuli, which bring respiratory rate to frequencies higher than 0.4 Hz, as for example observed in Fig. 6.3 during pleasant condition. Thus, a dynamic adjustment is needed to correctly estimate these changes. The respiratory rate was obtained from the ECG-derived respiration estimated using [24]. This method exploits the oscillatory pattern of the rotation angles of the heart's electrical axis as induced by respiration, and it is particularly suitable when dealing with highly non-stationary and noisy ECG recordings. To corroborate the use of the technique described in [24] in this kind of studies, we compared our estimation of $f_{\mathrm{resp}}(t)$ with the respiratory frequency obtained from a direct measurement of respiration (performed through respiratory belt), which was only available in 58 subjects. The mean error was low (0.0001 ± 0.0045 Hz, equal to $-0.4 \pm 2.1\%$) and was in agreement with results reported in [24] for simulated signals. In this study the respiratory rate was always available. In those cases where respiratory frequency is not available (neither from respiratory signal nor from the ECG [23]), $B_{\mathrm{HF}}(t)$ may be automatically adjusted to the instantaneous spectral properties of the HRV signal [108].

Physiological index changes during music stimuli

The purpose of the experimental procedure was to characterize the effect of stimuli with different emotional valence on the heart rate modulation. There was agreement between the assumed valence of the stimuli and the emotional state as reported by the participants. All conditions were rated significantly differently. The pleasant condition was rated as the more pleasant and unpleasant condition as the more unpleasant. The results showed significant differences in the time-course of the HRV indices during the different conditions.

The mean trend of most of these indices, shown in Fig. 6.4, was characterized by two different phases: a first early short phase of about 15–20 s during which indices changed quickly, and a second longer phase during which indices approximatively maintained the same values or varied slowly. These considerations should be taken into account in the design of analogous experiments and should warn against the use of time-invariant methods in this kind of studies. Given that the autonomic response to music-induced emotions was observed to be transient and not instantaneous, too short stimuli could be insufficient to elicit significant differences. In addition, a pause between the end

of a trial and the beginning of the next one is strongly recommended to assure the restoration of appropriate baseline values.

The largest differences in autonomic responses were observed between pleasant and rest conditions: significantly different patterns were observed in all indices but $f_{\text{LF}}(t)$ (see column $P > R$ in Fig. 6.5).

More importantly, even the effects induced by pleasant and unpleasant excerpts, that is by two acoustic stimuli comparable in loudness and tempo, could be discriminated by tracking $d_{\text{HR}}(t)$, $f_{\text{resp}}(t)$, $f_{\text{HF}}(t)$, $P_{\text{HF}}(t)$ and, partially, by $P_{\text{TOT}}(t)$. This difference is likely to be due to the different emotional valence of the two types of stimuli (pleasant vs. unpleasant).

By contrast, unpleasant stimuli and the sequence of Shepard tones were observed to elicit rather comparable effects, and no physiological index could clearly discriminate between them. This similarity may be due to the absence of harmonic and melodic structures in both kinds of stimuli, or due to a predominant effect of the Shepard tones, which were present in both conditions, on the dissonant structures of the unpleasant excerpts.

Respiratory rate and $f_{\text{HF}}(t)$ showed the greatest sensitivity to music-induced stimuli: any kind of acoustic stimulus provoked almost instantaneous differences with respect to resting condition, and differences between pleasant and unpleasant conditions were reached in only 4–8 s after the stimulus onset. A fast response in HF component is in agreement with previous studies on the autonomic nervous system stimulation, such as response to tilt test [195, 168].

While the respiratory rate has been shown to be strongly affected by music [39, 40, 106, 107, 197], the role of heart rate is more controversial. In several works, heart rate was observed to be significantly affected by acoustic stimuli with different valence [40, 197, 228], while in others this influence was not observed [106, 128]. Here, unpleasant stimuli were observed to induce a stronger decrease in the heart rate, $d_{\text{HR}}(t)$, than pleasant music (see Fig. 6.4a). The triphasic waveform described in [53] and in [228] was also observed, even if here it appeared much smoother and longer: during pleasant condition $d_{\text{HR}}(t)$ initially decreased for about 10 s, then it slightly increased for about 10 s, before decreasing again.

Heart rate variability was already proposed as a critical index for the assessment of the music effect in [128], where the physiological response to exciting and sedative music was compared in a stationary context. That study reported that exciting music decreased the activation of the parasympathetic nervous system. Here, both LF and HF modulation, assessed by the instantaneous powers $P_{\text{LF}}(t)$ and $P_{\text{HF}}(t)$, were observed to be higher during resting condition than during acoustic stimuli listening, regardless of the internal structure of the excerpts. The power content in HF was higher during unpleasant than during pleasant condition, suggesting that the listening of pleasant music provoked a reduction of parasympathetic modulation. The pleasant excerpts elicited the opposite effect than resting condition, during which the vagal activity increased. The simultaneous decreasing of the heart and respiratory rates and the increasing of the power of HF modulation highlight the strong relaxing effect of silence, as already observed in [40].

As shown in Fig. 6.4e, when a condition began, the activation in LF band dramatically

decreased within about 15 s with respect to baseline values. The difference between $P_{\text{LF}}(t)$ values before and after each start–signal–tone are significant already after the first seconds of the trials. This pattern may be related to the expectation of a new coming stimulus (participants did not receive any previous information about the excerpts) and to the task of evaluation assigned to the participants, which may increase the sympathetic activity.

The decrease observed in the sympatho-vagal balance, which passed from a first LF predominance ($P_{\text{LFn}}(t) \approx 0.6$) to an equilibrium in which the modulation in HF was slightly higher ($P_{\text{LFn}}(t) \approx 0.4$), took about 20 s. This change was common to all the different conditions and no statistical differences were observed, among the subjects, in $P_{\text{LFn}}(t)$, suggesting that the sympatho-vagal balance is higher during attention.

Finally, it is worth noting that we focused our attention to HRV modification only. Nevertheless, the listening of music provokes changes also in other signals related to the autonomic nervous system [39, 40, 106, 107, 197, 228] and further studies should be therefore considered to achieve a comprehensive characterization of music-induced effects on the autonomic modulation. The statistical analysis performed in this study may also be applied in bivariate time-frequency analysis [144, 206] to assess whether different conditions provoke different dynamic interactions in cardiovascular or cardiorespiratory control, or to explore the relationship between physiological rhythm and musical profile as in [39].

6.4 Cross time-frequency analysis for the assessment of cardiorespiratory coupling

Cross time-frequency analysis was performed between the HRV signal and the respiratory signal in order to assess the effect of musical stimuli with different emotional valence on indices of synchronizations, such as band coherence, phase differences and time delay.

6.4.1 Methods

The time course of the indices of synchronization between the HRV and the respiratory signals was estimated by means of the methodology proposed in §4 and §5. We analyzed HRV $d_{\text{HRV}}(t)$ and respiratory signals from a sub-group of 58 subjects. In these subjects, the respiratory signal was acquired by means of a respiratory belt.

Briefly, the smoothed pseudo Wigner-Ville distribution was estimated by using a kernel function of type (4.11) which gave a time-frequency resolution $(\Delta_{\text{t}}^{\text{m}}, \Delta_{\text{f}}^{\text{m}}) = (10.9\,\text{s}, 39\,\text{mHz})$.

After having estimated the time-frequency spectra $S(t, f)$, time-frequency coherence $\gamma(t, f)$ and phase difference $\Theta(t, f)$, indices $\mathcal{I}(t)$ were estimated by averaging in specific time-frequency regions $\Omega_{\text{HF}}^{(\mathcal{I})}$, with HF $\in [0.15, 0.5]$. Indices $\mathcal{I}(t)$ were:

- The instantaneous frequency of the HF spectral component of the cross time-frequency spectrum, $f_{\text{HF}}^{(\text{xy})}(t)$, was estimated as in (5.7).

   – The time-course of the band coherence, $\gamma_{\mathrm{HF}}(t)$ was estimated by averaging $\gamma(t, f)$ in $\Omega^{(\gamma)}$, as defined in (5.8).

   – The time-course of the phase difference around the respiratory rate, $\theta_{\mathrm{HF}}(t)$, was estimated by averaging $\Theta(t, f)$ in $\Omega^{(\theta)}$, as defined in (5.9).

   – The temporal evolution of the time delay between the HF spectral components of the two signals, $\mathcal{D}_{\mathrm{HF}}(t)$, was obtained by using (5.11).

6.4.2 Results

The graphics of Fig. 6.6 represent the median trend and the interquartile range of the indices of synchronization, estimated along all the realizations of the stimulus and for all subjects (as described in §6.2, for each condition we have 6 stimuli × 58 subjects = 348 realizations). In Fig. 6.7, the median trends that characterized the response to each conditions are directly compared.

From the inspection of these two figures, we can make several considerations:

- Instantaneous frequency of the cross spectrum: the time-course of index $f_{\mathrm{HF}}^{(\mathrm{xy})}(t)$ is very close to that of the respiratory rate estimated in Fig. 6.4d. Musical stimuli provoked an increase of the respiratory rate, which was more evident during the listening to pleasant music, while the silence provoked a decrease of the respiratory rate. The median trends are well separated.

- Band coherence: the time-course of $\gamma_{\mathrm{HF}}(t)$ is similar during all the conditions. As shown in Fig. 6.7b, the median trends of the coherence are almost equal. Index $\gamma_{\mathrm{HF}}(t)$ is lower during the interval in between two consecutive stimuli and it increased afterwards, regardless the kind of condition. As for most of the spectral indices of the HRV, shown in Fig. 6.4, this increase is characterized by a short epochs of about 15–20 s in which the coherence estimates rapidly increased, followed by a longer epoch in which coherence estimates were almost stable. This behavior is observed also during the resting condition (R) and it should be related to the increase of the power of the LF component observed in the interval in between two consecutive stimuli (see Fig. 6.4e). The fact that, during the first seconds of musical stimulation the coherence between the two spectral components increased, while these spectral components were rapidly changing their instantaneous frequency, confirms that the methodology is perfectly suited for tracking non-stationary patterns.

- Phase difference: the time-course of indices $\theta_{\mathrm{HF}}(t)$ fluctuated around -0.2 rad regardless of the emotional valence of the condition. As shown in Fig. 6.7c, during pleasant conditions, the median trend of the phase differences were slightly lower (less negative) than during the rest of conditions. As shown in Fig. 6.6c, the inter-stimuli variability was characterized by an interquartile range lower than 0.6 rad (over a range of 6.28 rad). This suggests that the phase difference between the HF component of the HRV and the respiratory signals was not due to random fluctuations, but due to physiological mechanisms.

- Time delay: the time-course of indices $\mathcal{D}_{\mathrm{HF}}(t)$ increased immediately after the begin of pleasant condition, while $\mathcal{D}_{\mathrm{HF}}(t)$ during unpleasant, resting and control conditions were characterized by very similar median trends. The differences observed between phase differences (see Fig. 6.7c) and time delay (see Fig. 6.7d) were mainly due to the variation in the instantaneous frequency $f_{\mathrm{HF}}^{(\mathrm{xy})}(t)$.

6.4.3 Discussion

It is well known that an oscillation synchronous with the respiratory rate is present in the heart rate. As mentioned in §1.2.4, this phenomenon is called respiratory sinus arrhythmia [112, 258, 246], and it has both clinical and physiological relevance. In this study, we characterized the dynamic interactions between the heart rate variability and the respiratory signal by cross time-frequency analysis.

The results show that the HF component of the HRV signal was highly coupled to the respiration. The local coupling, quantified by coherence estimates, was high even when the respiratory rate quickly changed. Moreover, it was high also during the listening to pleasant music, which reduced the power of the HF component of the HRV signal (see Fig. 6.4f). Concerning the time-course of the coherence estimates, two issues deserve attention: the lower values of coherence during the interval in between two consecutive stimuli and the biphasic trends already observed in the spectral indices of the HRV signal. The lower coherence level during the interval in between two consecutive stimuli cannot be explained as an effect of the music, since also during resting condition we observe the same pattern. For the same reason, it cannot be due to the time-course of the instantaneous frequency and power of the HF component of the HRV signal. A decrease of the strength of the local coupling after and before musical stimulation is more likely due to the increase of the power of the LF component observed during these transitions. One can speculate that during the interval in between two consecutive stimuli, the task of rating the previous musical stimulus and the expectation of the next one, could both increase the sympathetic and reducing the parasympathetic modulation. This may imply a slightly reduction of the coupling around the respiratory rate. Another possibility is that the sudden increase of the power of LF spectral component observed after and before the musical stimulation was simply due to movement artifact.

The differences in the median trends of $\theta_{\mathrm{HF}}(t)$ observed in Fig. 6.7c, was enhanced after having normalized them by the corresponding instantaneous frequencies, as shown in Fig. 6.7d. This highlight the importance of studying the degree of synchronization between two components both in radians, by $\theta(t)$, and in seconds, by $\mathcal{D}(t)$. Given that in Fig. 6.6c the phase difference estimates were negative, and given that the respiration and the heart rate are in phase (an increase of the respiratory signal, i.e. an inspiration, is associated to an increase in the heart rate), the results confirmed that respiration leads (and in this open-loop relationship, causes) the HF component of the HRV signal. However, as pointed out in §8.5.4, phase differences and time delay estimates strongly depend on the specific representation used to estimate the HRV signal. We may conclude that the respiration was persistently reflected in the heart rate with a very short delay, likely about 0.1 seconds.
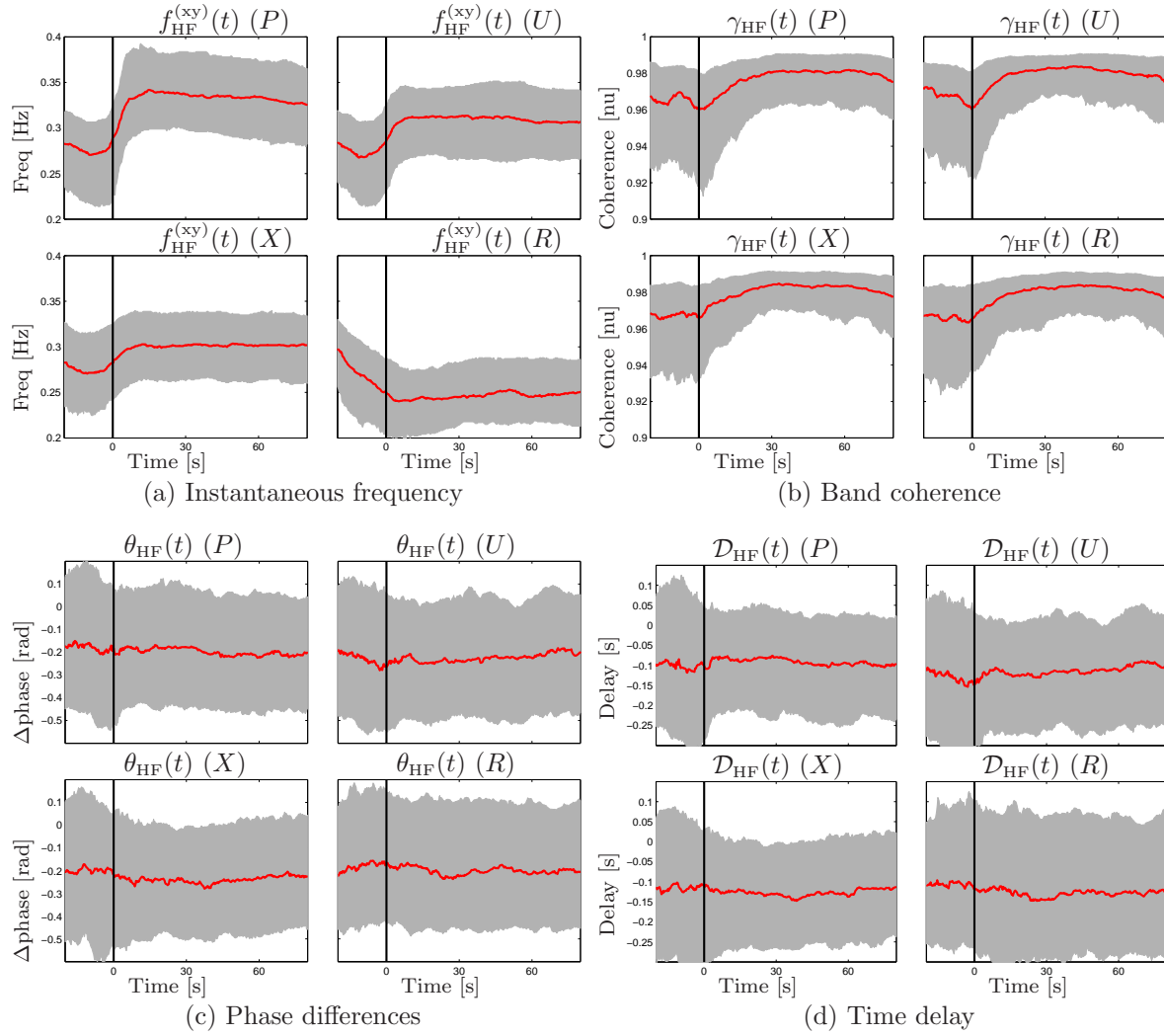
Figure 6.6: Results of the cross time-frequency analysis performed between the HRV signal and the respiratory signal. Time courses are estimated in specific TF regions defined in the respiratory band. Red lines and gray shadows represent the median trends and the interquartile ranges of the estimates. (a): Instantaneous frequency of the cross SPWVD, $f_{\mathrm{HF}}(t)$. (b): Band coherence $\gamma_{\mathrm{HF}}(t)$. (c): Phase differences $\theta_{\mathrm{HF}}(t)$. Time delay $\mathcal{D}_{\mathrm{HF}}(t)$. Conditions are: pleasant (P), unpleasant (U), sequence of tones (X) and rest (R).
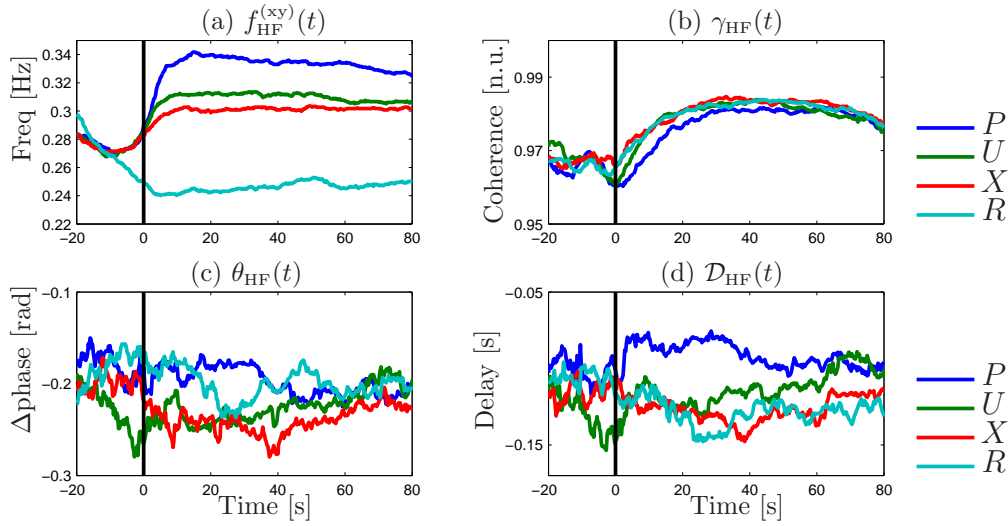
Figure 6.7: Median trends of the indices of synchronizations reported in Fig. 6.6. (a): Instantaneous frequency of the cross SPWVD, $f_{\text{HF}}(t)$. (b): Band coherence $\gamma_{\text{HF}}(t)$. (c): Phase differences $\theta_{\text{HF}}(t)$. Time delay $\mathcal{D}_{\text{HF}}(t)$. Conditions are: pleasant (P), unpleasant (U), sequence of tones (X) and rest (R).

Chapter 7

Time-frequency comparison between HRV and PRV from the PPG signal

Contents

7.1 Introduction

Pulse photoplethysmography (PPG), introduced by Hertzman [121], is a simple and useful method for measuring the relative blood volume changes in the microvascular bed of peripheral tissues and it can be used to evaluate peripheral circulation. This signal is obtained through non-invasive pulse oximetry systems and is based on blood light absorption [259, 183].

The PPG waveform contains both a DC and an AC component. The first one is due to the non-pulsatile blood volume component and the attenuation at the tissues surrounding the arteries, which produces a signal that changes slowly. The second one is attributable to the pulsatile component of the vessels, i.e. the arterial pulse, which is caused by the heart beat pumping.

Pulse photoplethysmography has been applied in many different clinical settings, including the monitoring of blood oxygen saturation, heart rate, blood pressure, cardiac output and respiration [5, 64]. Given its simplicity, low cost and that it is widely used in the clinical routine, it is desirable to maximize PPG potential by exploring additional measurements which can be derived from it. It is worth noting that oximetry systems have the potentiality of providing multiple information using only one sensor, making its use simpler, more comfortable and cheaper than multiple sensor devices.

It is generally accepted that photoplethysmography can provide valuable information about the cardiovascular system. The autonomic influences on the PPG signal have been analyzed in several studies [41, 192, 147] and recently pulse rate variability (PRV) extracted from the PPG signal has been studied as a potential surrogate of HRV [161, 160, 116, 233, 60]. The analysis of heart rate variability is one of the most widely used non-invasive techniques for the evaluation of the autonomic nervous system (ANS). The use of PRV as a surrogate of HRV could be useful in applications where ECG is not available or when it is beset with electrical artefacts [176]. Moreover, since PPG also allows to derive physiological parameters such as blood oxygenation and ventilatory rate, the use of the PRV instead of the HRV signal could be particularly suitable in those applications where the simultaneous acquisition of many signals is required, such as in sleep disorders studies, mainly for ambulatory sleep studies.

The main difference between HRV and PRV is the time it takes the pulse wave to travel from the heart to the finger. This time is called pulse transit time (PTT) and is typically measured as the difference between the occurrence of the peak of the R–wave on the ECG and the peak value of the corresponding pulse in the finger pad measured by PPG. Pulse transit time, which is tie-related to arterial compliance and blood pressure, changes beat to beat [61, 162, 190, 95, 98]. Thus, PRV is also affected by the variability in the PTT, i.e. the beat-to-beat changes in pulse wave velocity.

All the studies exploring the possibility of using PRV as an alternative measurement of HRV have been performed in stationary conditions using time-invariant analysis and generally showed that PRV is a good surrogate of HRV. However, there are many situations where significant changes in autonomic balance occur, as during orthostatic test, Valsalva maneuver, exercise stress testing and after pharmacologic interventions,
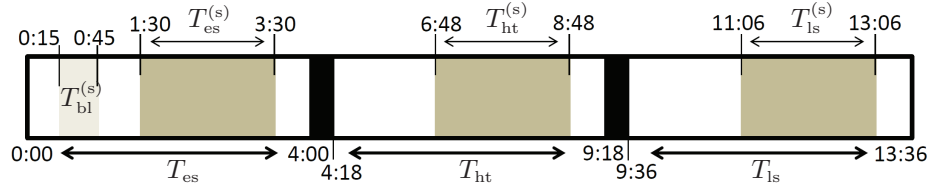
Figure 7.1: head up tilt test protocol. The automatic table takes 18 s to move from early supine position, during T_{es}, to head up tilt, during T_{ht}, as well as from T_{ht} to later supine position, during T_{ls}. This interval is marked as lined area. Windows $T_{es}^{(s)}$, $T_{ht}^{(s)}$ and $T_{ls}^{(s)}$ define the intervals where stationarity is assumed and time-invariant analysis was performed; $T_{bl}^{(s)}$ defines the interval where baseline was estimated for time-invariant physiological analysis.

which involve non-stationary processes. In such situations, the use of PRV as an alternative measurement of HRV could be of great interest.

In this chapter, we compare these signals during tilt table test. In tilt table test, after head up tilt, subjects undergo a progressive orthostatic stress and blood pressure is maintained thanks to cardiovascular regulation [137], which involves an increase in heart rate and a constriction of the blood vessels in the legs. This slight tachycardia and vasoconstriction are the result of sympathetic activation and vagal withdrawal [188]. When the supine position is restored, heart rate and vasoconstriction returns to previous basal values together with sympathetic tone.

The aim of the study presented in this chapter is to evaluate the usefulness of PRV as a surrogate of HRV analysis during non-stationary conditions, in particular during tilt table test. Time-frequency (TF) and TF coherence analysis were performed to asses whether PRV can be used in the analysis of the autonomic modulation of heart rate in non-stationary conditions [100, 101].

7.2 Material and methods

7.2.1 Data acquisition and signal preprocessing

Seventeen volunteers (aged 28.5± 2.8 years, 11 males) without any previous cardiovascular history underwent a head up tilt table test according to the following protocol: 4 minutes in early supine position (T_{es}), 5 minutes tilted head up to an angle of 70 degrees (T_{ht}) and 4 minutes back to later supine position (T_{ls}). The experimental protocol is illustrated in Fig. 7.1, where T_{es}, T_{ht} and T_{ls} mark the three epochs of early supine, head up tilt and later supine positions, respectively; $T_{es}^{(s)}$, $T_{ht}^{(s)}$ and $T_{ls}^{(s)}$ mark the interval in which time invariant analysis is applied; $T_{bl}^{(s)}$ marks the temporal window used as baseline in the statistical analysis. Table 7.1 shows database information. In this table, values of blood pressure were estimated from the finger during early supine position, T_{es}.

For more information about the protocol and the data acquisition, refer to Appendix §A. Briefly, the PPG signal was recorded from index finger with a sampling frequency

Table 7.1: Database information

Subject[1]	SAP[2]	DAP[3]	Subject[1]	SAP[2]	DAP[3]
s1 [28] ♀	113.5±5.4	64.2±3.1	s10 [29] ♂	130.4±6.5	86.9±2.6
s2 [26] ♂	125.2±6.6	82.3±4.1	s11 [26] ♀	95±2.7	48.5±2.7
s3 [27] ♂	69.1±4.7	34.7±3.7	s12 [24] ♂	105.5±7.1	67.5±3.1
s4 [27] ♂	120.1±5.5	69.5±2.6	s13 [30] ♂	104.9±7.6	56.2±3.2
s5 [27] ♂	122.6±6.9	61.1±4.3	s14 [31] ♂	104.9±4.1	54±3.2
s6 [34] ♀	124.5±6.4	64.5±2.9	s15 [34] ♂	124.5±3.9	78.2±2.6
s7 [27] ♀	118.1±5.7	43.2±3.1	s16 [29] ♂	-	-
s8 [31] ♀	104.6±5.3	59.2±2.3	s17 [30] ♂	137.9±3.6	74.7±2.1
s9 [26] ♀	117.1±2.8	60.5±2.2			
MEAN [28.5±2.8]	113.6±16.4	62.8±14.0			

[1] Number, [years], gender

[2,3] Systolic and Diastolic arterial pressure in the finger (mmHg) during T_{es}. mean±SD

of 250 Hz, whereas standard lead V4 ECG signal was recorded with a sampling frequency of 1000 Hz. Beats from ECG and pulses from PPG were detected to generate heart and pulse rate time series. The temporal location of each R wave in the ECG (t_{E_j}) was automatically determined using the algorithm described in [177]. The PPG signal was interpolated using cubic splines increasing the resolution in time up to an equivalent sampling rate of 1000 Hz to match the temporal resolution of both signals. Then, the temporal location of each pulse wave in the PPG (t_{P_j}) was detected as the maximum of the PPG signal within the interval $[t_{E_j}+150$ ms, $t_{E_{j+1}}]$, see Fig. 7.2. In addition, a PPG artefact detector [102] was applied to suppress pulses from PPG corresponding to artefacts and beat and pulse detections were manually supervised. Then, the effect of abnormal beats in both heart and pulse rate was corrected by applying a methodology based on the integral pulse frequency modulation model [180]. Heart rate and pulse rate signals, $d_{HR}(t)$ and $d_{PR}(t)$ respectively, were obtained by using a 5th order spline interpolation at 4 Hz of the inverse interval functions[1] (IIF) $d_{iif}(t_j)$:

$$d_{iif}^{ECG}(t_{E_j}) = \frac{1}{(t_{E_j} - t_{E_{j-1}})} \tag{7.1}$$

$$d_{iif}^{PPG}(t_{P_j}) = \frac{1}{(t_{P_j} - t_{P_{j-1}})}. \tag{7.2}$$

Finally, the HRV and PRV signals, $d_{HRV}(t)$ and $d_{PRV}(t)$, were calculated by suppressing the time-varying mean heart (pulse) rate from $d_{HR}(t)$ and $d_{PR}(t)$, respectively. Mean heart (pulse) rate were estimated by low-pass filtering $d_{HR}(t)$ and $d_{PR}(t)$, respectively, with a cut-off frequency of 0.03 Hz in order to suppress the DC and very low frequency

---

[1]In this chapter, we use this representation for heart rate variability to be consistent with the definition of the pulse rate variability. Please, note that in §6 signal $d_{HR}(t)$ was estimated by means of IPFM model.
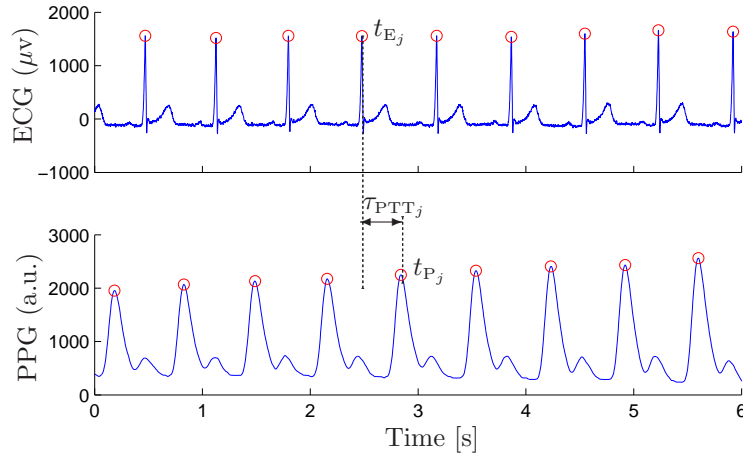
Figure 7.2: Beat and pulse detection example. Red circles correspond to t_{E_j} and t_{P_j}.

components of heart (pulse) rate.

7.2.2 Time-invariant analysis

Time-invariant analysis includes the quantification of the linear correlations between the indices derived from the HRV and PRV signals as well as spectral analysis. The Pearson's correlation coefficient, defined as:

$$\rho = \frac{C(\chi^{\mathrm{X}}(j), \chi^{\mathrm{Y}}(j))}{\sqrt{C(\chi^{\mathrm{X}}(j), \chi^{\mathrm{X}}(j))C(\chi^{\mathrm{Y}}(j), \chi^{\mathrm{Y}}(j))}}, \quad \mathrm{X,Y} \in \{\mathrm{HRV}, \mathrm{PRV}\} \qquad (7.3)$$

was used to quantify the linear strength between the HRV and PRV signals, as well as between several indices derived from HRV and PRV. In (7.3), $C(\cdot, \cdot)$ represents the covariance operator, while $\chi(j)$ is a general function of the independent variable j (which can represent subjects, time instants or frequency). The Pearson's correlation coefficient, $\rho_{\mathrm{d}}(k)$, between the variability signals, $\chi^{\mathrm{X}}(t) = d_{\mathrm{HRV}}(t)$ and $\chi^{\mathrm{Y}}(t) = d_{\mathrm{PRV}}(t)$ was calculated for each subject k to evaluate their linear relationship.

Classical time-invariant spectral analysis was performed in three windows ($T_{\mathrm{es}}^{(\mathrm{s})}$, $T_{\mathrm{ht}}^{(\mathrm{s})}$ and $T_{\mathrm{ls}}^{(\mathrm{s})}$) where stationarity is assumed [1]. As shown in Fig. 7.1, these windows had a length of 2 minutes and finished 30 seconds before any transition during the tilt test. Classical time domain and frequency domain indices were estimated in each window from both HRV and PRV [1, 211, 171]:

– Time domain: Mean normal to normal interval (NN), standard deviation of NN intervals (SDNN), root mean square of successive differences of adjacent NN intervals (RMSSD) and percentage of pairs of adjacent NN intervals differing by more than 50 ms (pNN50) were estimated.

– Frequency domain: fast Fourier transform algorithm with a frequency resolution of 0.0019 Hz was applied to $d_{\mathrm{HRV}}(t)$ and $d_{\mathrm{PRV}}(t)$ and the power in low fre-

quency band (P_{LF}), traditional high frequency band (P_{HF}) and the LF to HF ratio ($R_{\text{LF/HF}}$) were estimated.

Each index from PRV ($\mathcal{I}^{\text{PRV}}(k)$) was compared to the same index from HRV ($\mathcal{I}^{\text{HRV}}(k)$) for each subject k, with $\mathcal{I} \in \{\text{NN, SDNN, RMSSD, pNN50, } P_{\text{LF}}, P_{\text{HF}}, R_{\text{LF/HF}}\}$. Three additional indices were then estimated as:

(i) The difference between indices from HRV and PRV, $\delta_{\mathcal{I}}(k) = \mathcal{I}^{\text{PRV}}(k) - \mathcal{I}^{\text{HRV}}(k)$.

(ii) The p-value of the Student's t–test, used to assess whether indices $\mathcal{I}^{\text{PRV}}(k)$ and $\mathcal{I}^{\text{HRV}}(k)$ were statistically different. Before analysis, values of all variables were examined for deviations from normality by Kolmogorov-Smirnov test, founding in all cases that the hypothesis of normality could not be rejected ($p > 0.05$).

(iii) The Pearson's correlation coefficient, $\rho_{\mathcal{I}}$, between indices $\chi^{\text{X}}(k) = \mathcal{I}^{\text{HRV}}(k)$ and $\chi^{\text{Y}}(k) = \mathcal{I}^{\text{PRV}}(k)$ was used to measure their linear relationship.

7.2.3 Time-varying analysis

The SPWVD was used to estimate the time-varying spectral properties of the HRV and PRV signals, as well as to perform TF coherence analysis. A detailed explanation of time-frequency and time-frequency coherence analysis is given in §3 and §4, respectively.

Briefly, the cross-SPWVD of signals $x(t) = a_{\text{HRV}}(t)$ and $y(t) = a_{\text{PRV}}(t)$, where $a_{\text{HRV}}(t)$ and $a_{\text{PRV}}(t)$ are the complex analytic representations of the original real signals $d_{\text{HRV}}(t)$ and $d_{\text{PRV}}(t)$, was estimated as in (3.4):

$$S_{\text{xy}}^{\text{WV}}(t, f) = \iint_{-\infty}^{\infty} \phi_{\text{d-D}}(\tau, \nu) A_{\text{xy}}(\tau, \nu) e^{j2\pi(t\nu - f\tau)} d\nu d\tau \qquad (7.4)$$

The elliptical exponential kernel was the same as that defined in (4.11), with $\lambda = 0.25$:

$$\phi_{\text{d-D}}(\tau, \nu) = \exp\left\{-\pi\left[\left(\frac{\nu}{\nu_0}\right)^2 + \left(\frac{\tau}{\tau_0}\right)^2\right]^{\frac{1}{2}}\right\} \qquad (7.5)$$

Parameters τ_0 and ν_0 were selected to give a frequency resolution $\Delta_{\text{f}}^{\text{m}} = 0.0313$ Hz and a time resolution $\Delta_{\text{f}}^{\text{m}} = 15$ s (see §3.1.2).

For each subject k, the temporal evolution of the power content of HRV and PRV within each frequency band, $P_{\text{B}}^{\text{X}}(k, t)$, with X $\in$ {HRV, PRV}, was obtained integrating $S_{\text{xx}}^{\text{WV}}(t, f)$ in the frequency bands B $\in$ {LF, HF}.

The similarity between the temporal evolution of $d_{\text{HRV}}(t)$ and $d_{\text{PRV}}(t)$ was assessed by means of four indices:

(i) The Pearson's correlation coefficient, $\rho_{\mathcal{I}}(k)$, between $\chi^{\text{X}}(t) = P_{\text{B}}^{\text{HRV}}(k, t)$ and $\chi^{\text{Y}}(t) = P_{\text{B}}^{\text{PRV}}(k, t)$ and between $\chi^{\text{X}}(t) = R_{\text{LF/HF}}^{\text{HRV}}(k, t)$ and $\chi^{\text{Y}}(t) = R_{\text{LF/HF}}^{\text{PRV}}(k, t)$.

(ii) The difference between the instantaneous power of the two signals within each frequency band, $\delta_{\text{B}}(k, t) = P_{\text{B}}^{\text{PRV}}(k, t) - P_{\text{B}}^{\text{HRV}}(k, t)$. This index is used to compare the temporal evolution of the spectral content of the signals.

(iii) The Pearson's correlation coefficient, $\rho_{\mathrm{S}}(k,t)$, between instantaneous spectra of the two signals is estimated at every time instant $t=t_0$ as in (7.3) with $\chi^{\mathrm{X}}(f) = S_{a_{\mathrm{HRV}}}^{\mathrm{WV}}(t_0,f)$ and $\chi^{\mathrm{Y}}(f) = S_{a_{\mathrm{PRV}}}^{\mathrm{WV}}(t_0,f)$. This index is used to assess whether the signals are characterized by a similar distribution of energy with frequency.

(iv) Time-frequency coherence was obtained by the SPWVD as in (4.10):

$$\gamma(t,f) = \frac{\left|S_{\mathrm{xy}}^{\mathrm{WV}}(t,f)\right|}{\sqrt{S_{\mathrm{xx}}^{\mathrm{WV}}(t,f)S_{\mathrm{yy}}^{\mathrm{WV}}(t,f)}}; \quad x,y \in \{a_{\mathrm{HRV}}(t), a_{\mathrm{PRV}}(t)\}. \tag{7.6}$$

As explained in §4.3, time-frequency coherence gives a continuous quantification of spectral coherence over time, being one in epochs characterized by perfect linear coupling and zero when the two signals are completely uncorrelated. From $\gamma^2(t,f)$, we obtained the band coherence $\gamma_{\mathrm{B}}^2(k,t)$, with $B \in \{LF, HF\}$, by averaging $\gamma^2(t,f)$ in each spectral band for each subject k.

7.2.4 Physiological analysis

The tilt table test provokes changes in the autonomic modulation of heart rate and is used to study cardiovascular control [137, 188]. In this section, we assess the effect of replacing HRV estimation from the ECG with PRV estimation from the PPG, when the tilt table test is used to evaluate changes in the autonomic modulation of heart rate.

In time-invariant analysis, Student's t–test was performed to compare variations of spectral indices, $P_{\mathrm{B}}^{\mathrm{X}}(k)$, among windows $T_{\mathrm{es}}^{(\mathrm{s})}$, $T_{\mathrm{ht}}^{(\mathrm{s})}$ and $T_{\mathrm{ls}}^{(\mathrm{s})}$, estimated from both HRV and PRV signals. In time-varying analysis, we are interested in continuously monitoring the changes produced in the autonomic modulation of the heart rate during the tilt test. To this end, we quantified the statistical differences between the baseline power content $\overline{P_{\mathrm{B}}^{\mathrm{X}}}(k)$ and the power content at t_0, $P_{\mathrm{B}}^{\mathrm{X}}(k,t_0)$, by iteratively performing the Student's t–test. The baseline power content $\overline{P_{\mathrm{B}}^{\mathrm{X}}}(k)$ was estimated by averaging $P_{\mathrm{B}}^{\mathrm{X}}(k,t)$ in a reference window $T_{\mathrm{bl}}^{(\mathrm{s})}$, selected at T_{es} from 15 to 45 s (see Fig. 7.1). As result of the test we obtained a time-varying p-value, $p_{\mathrm{B}}^{\mathrm{X}}(t)$, for both HRV and PRV signals. Normality of the distributions was tested by Kolmogorov-Smirnov test, founding that the hypothesis of normality could not be rejected ($p > 0.05$) in 93% of the time.

7.3 Results

7.3.1 Time-invariant analysis

The correlation between $d_{\mathrm{HRV}}(t)$ and $d_{\mathrm{PRV}}(t)$, $\rho_{\mathrm{d}}(k)$, was 0.964 ± 0.030 (mean ± S.D.). The mean delay of $d_{\mathrm{PRV}}(t)$ with respect to $d_{\mathrm{HRV}}(t)$, introduced by the pulse wave travel to the periphery, was taken into account in the estimation of parameter $\rho_{\mathrm{d}}(k)$, to align $d_{\mathrm{HRV}}(t)$ and $d_{\mathrm{PRV}}(t)$.

Table 7.2 and Fig. 7.3 show the comparison of time and frequency indices derived from time-invariant analysis of HRV and PRV within each analysis window. All the indices

Table 7.2: Time-invariant analysis results

Condition	Index	HRV	PRV	difference $(\overline{\delta_{\mathcal{I}}(k)})$	p (T-test)	Correlation $(\rho_{\mathcal{I}})$
Supine $(T_{\text{es}}^{(\text{s})})$	NN (s)	0.988±0.195	0.988±0.195	-0.00038±0.00133	0.995	1.000
	SDNN (s)	0.056±0.022	0.057±0.022	0.00064±0.00187	0.933	0.997
	RMSSD (s)	0.049±0.028	0.05±0.027	0.00026±0.00186	0.978	0.998
	pNN50 (%)	24.509±19.151	23.819±18.067	-0.68969±2.31389	0.915	0.994
	LF (s^{-2})	0.002±0.001	0.002±0.002	0.00009±0.00015	0.859	0.997
	HF (s^{-2})	0.001±0.001	0.001±0.001	0.00008±0.00013	0.840	0.996
	LF (n.u)	0.657±0.164	0.653±0.159	-0.00467±0.01586	0.933	0.996
	HF (n.u.)	0.343±0.164	0.347±0.159	0.00467±0.01586	0.933	0.996
	LF/HF (n.u.)	2.652±1.834	2.531±1.718	-0.12034±0.19607	0.845	0.996
Upright $(T_{\text{ht}}^{(\text{s})})$	NN (s)	0.787±0.151	0.788±0.151	0.00116±0.00281	0.982	1.000
	SDNN (s)	0.056±0.031	0.058±0.031	0.00153±0.00256	0.886	0.997
	RMSSD (s)	0.036±0.025	0.038±0.024	0.00253±0.00195	0.765	0.998
	pNN50 (%)	13.72±15.429	15.307±16.572	1.58688±2.32206	0.774	0.992
	LF (s^{-2})	0.006±0.007	0.006±0.008	0.00033±0.00044	0.899	1.000
	HF (s^{-2})	0.001±0.001	0.002±0.002	0.0003±0.00038	0.565	0.981
	LF (n.u)	0.765±0.194	0.719±0.206	-0.04522±0.05137	0.515	0.969
	HF (n.u.)	0.235±0.194	0.281±0.206	0.04522±0.05137	0.515	0.969
	LF/HF (n.u.)	6.593±5.438	5.073±4.355	-1.51994±2.18202	0.375	0.924
Supine $(T_{\text{ls}}^{(\text{s})})$	NN (s)	1.008±0.193	1.01±0.195	0.00147±0.0041	0.983	1.000
	SDNN (s)	0.057±0.025	0.057±0.024	-0.00029±0.00458	0.972	0.984
	RMSSD (s)	0.049±0.03	0.049±0.025	-0.00042±0.00841	0.965	0.970
	pNN50 (%)	23.949±18.521	25.506±18.399	1.55752±2.02452	0.807	0.994
	LF (s^{-2})	0.001±0.001	0.001±0.001	0.00004±0.00009	0.932	0.998
	HF (s^{-2})	0.001±0.001	0.001±0.001	0.00006±0.00011	0.864	0.996
	LF (n.u)	0.568±0.201	0.558±0.201	-0.01014±0.01899	0.884	0.996
	HF (n.u.)	0.432±0.201	0.442±0.201	0.01014±0.01899	0.884	0.996
	LF/HF (n.u.)	1.843±1.324	1.739±1.215	-0.10394±0.24364	0.813	0.985

derived from PRV presented similar values to the indices derived from HRV. This was confirmed by the statistical test, which showed no significant differences between indices from HRV and PRV ($p > 0.05$). As shown in table 7.2, correlation coefficients indicated a strong correlation ($\rho_{\mathcal{I}} > 0.97$) for all indices but one ($R_{\text{LF/HF}}$ in $T_{\text{ht}}^{(\text{s})}$).

7.3.2 Time-varying analysis

An illustrative example of the results obtained by performing time-frequency and time-frequency coherence analysis for a subject (subject $k=17$, male, 30 years old) are reported in Fig. 7.4. Heart and pulse rates are reported in panel (a). The TF distribution of the HRV and PRV signals are shown in panels (b)–(c). The temporal evolution of the instantaneous power within the LF and HF bands, $P_{\text{B}}^{\text{x}}(k=17, t)$, is reported in panel (d). It is shown that the spectral properties of the HRV and PRV signals did follow the same trend. The main difference lies in the slight increase of the instantaneous power of the HF component estimated from the PRV signal, $P_{\text{HF}}^{\text{PRV}}(k=17, t)$, with respect to that estimated from the HRV signal, $P_{\text{HF}}^{\text{HRV}}(k=17, t)$. This difference was more pronounced during head up tilt. Panel (e) shows the correlation coefficient between instantaneous spectra of the two signals, $\rho_{\text{S}}(k=17, t)$. Results of TF coherence analysis are reported in panels (f)–(g). The quadratic TF coherence $\gamma^2(t, f)$, reported in panel (f), shows that during supine position T_{es} and T_{ls} the two signals presented
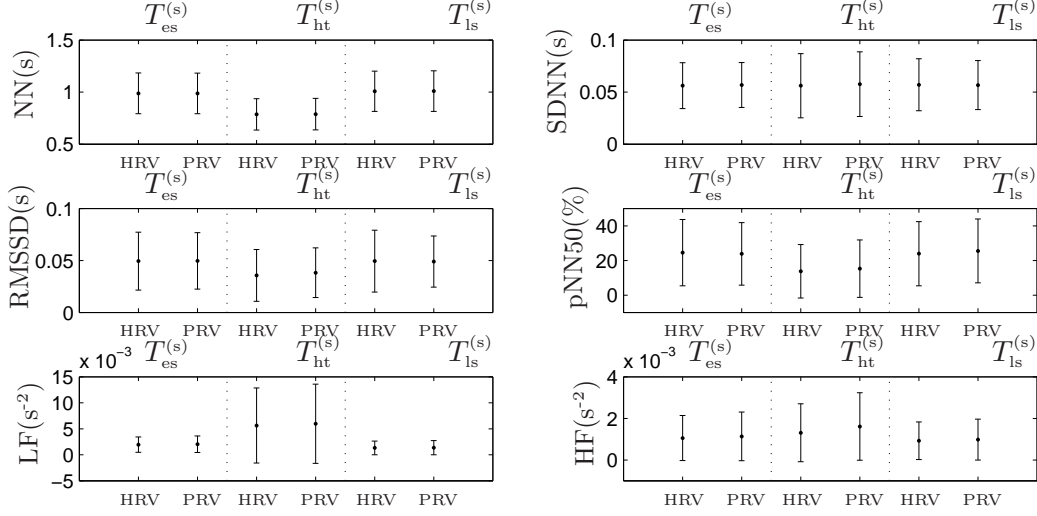
Figure 7.3: Time-invariant analysis to compare indices derived from HRV and PRV. Mean±SD of: normal to normal interval (NN), standard deviation of NN intervals (SDNN), root mean square of successive differences of adjacent NN intervals (RMSSD), percentage of pairs of adjacent NN intervals differing by more than 50 ms (pNN50); Power contents P_{LF} and P_{HF}. In intervals $T_{\mathrm{es}}^{(\mathrm{s})}$, $T_{\mathrm{ht}}^{(\mathrm{s})}$ and $T_{\mathrm{ls}}^{(\mathrm{s})}$ (see Fig. 7.1) stationarity was assumed.

almost a perfect correlation for all frequencies. Around 320 s, TF coherence decreased due to artefacts on the PPG signal (marked as black crosses). The temporal evolution of the band coherence $\gamma_{\mathrm{B}}^2(k{=}17, t)$, shown in panel (g), confirm the previous observations: HRV and PRV had an almost identical TF structure, at least in LF band.

It is worth noting that the example shown in Fig. 7.4 is a borderline case: subject $k{=}17$ had one of the highest $\delta_{\mathrm{HF}}(k, t)$ and the lowest $\gamma_{\mathrm{HF}}^2(k, t)$ in T_{ht}.

Table 7.3 shows that the index $\rho_{\mathcal{I}}(k)$, with $\mathcal{I} \in \{P_{\mathrm{LF}}^{\mathrm{X}}(k, t), P_{\mathrm{HF}}^{\mathrm{X}}(k, t), R_{\mathrm{LF/HF}}^{\mathrm{X}}(k, t)\}$, was close to one for almost all subjects.

Global results, obtained by averaging among subjects the indices presented in §7.2.3, are reported in Fig. 7.5. In panels (a)–(b), the instantaneous power within each frequency band from HRV and PRV and the corresponding instantaneous difference are shown, respectively. Note that the mean trend of the instantaneous power of LF and HF spectral components, obtained by averaged $P_{\mathrm{B}}^{\mathrm{HRV}}(k, t)$ and $P_{\mathrm{B}}^{\mathrm{PRV}}(k, t)$ among subjects k, presented the same temporal patterns, even if with a bias that increased during head up position. Panel (c) shows the mean trend of the instantaneous correlation $\rho_{\mathrm{S}}(k, t)$ between the power spectral density functions, estimated at each t_0 as $S_{a_{\mathrm{HRV}}}^{\mathrm{WV}}(t_0, f)$ and $S_{a_{\mathrm{PRV}}}^{\mathrm{WV}}(t_0, f)$. In the same panel we reported $\rho_{\mathrm{S}}(k{=}1, t)$ for the subject who presented the highest number of artefacts in the PPG signal, i.e. subject $k{=}1$. It is shown that artefacts provoked an abrupt decrease in $\rho_{\mathrm{S}}(k, t)$. Panel (d) shows the band coherence $\gamma_{\mathrm{B}}^2(k, t)$ in each spectral band.
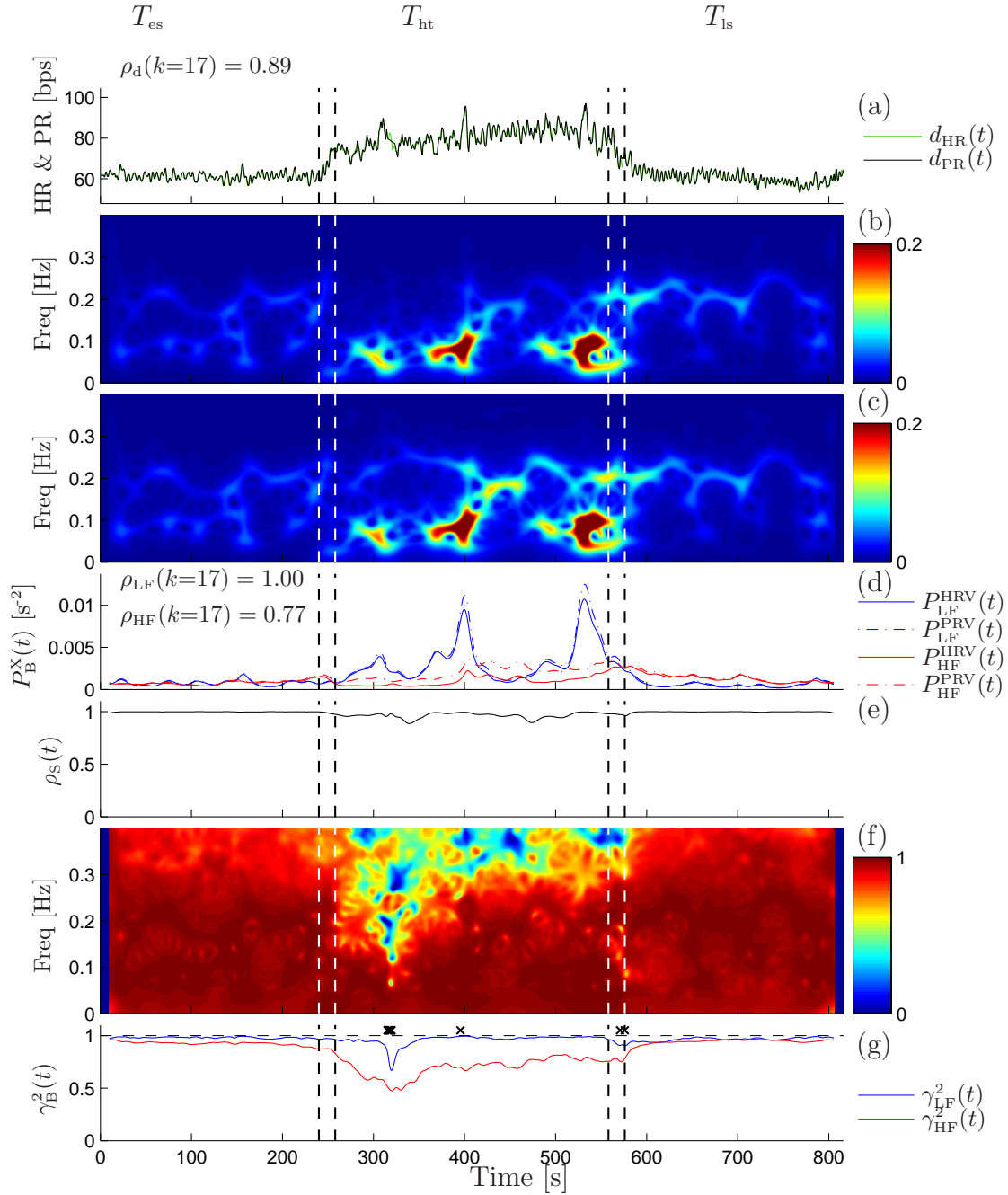
Figure 7.4: Results of TF and TF coherence analysis for one subject, $k = 17$. (a) Heart rate and pulse rate; (b) TF distribution of $a_{\mathrm{HRV}}(t)$; (c) TF distribution of $a_{\mathrm{PRV}}(t)$; (d) Temporal evolution of instantaneous power content $P_{\mathrm{B}}^{\mathrm{X}}(k{=}17, t)$ within spectral band $\mathrm{B} \in \{\mathrm{LF}, \mathrm{HF}\}$ for $\mathrm{X} \in \{\mathrm{HRV}, \mathrm{PRV}\}$; (e) Correlation coefficient between instantaneous spectra of the two signals, $\rho_{\mathrm{s}}(k{=}17, t)$. (f) Time-frequency coherence $\gamma^2(t, f)$. (g) Band coherence $\gamma_{\mathrm{B}}^2(k{=}17, t)$. Artefacts in PPG signal are marked as black crosses.
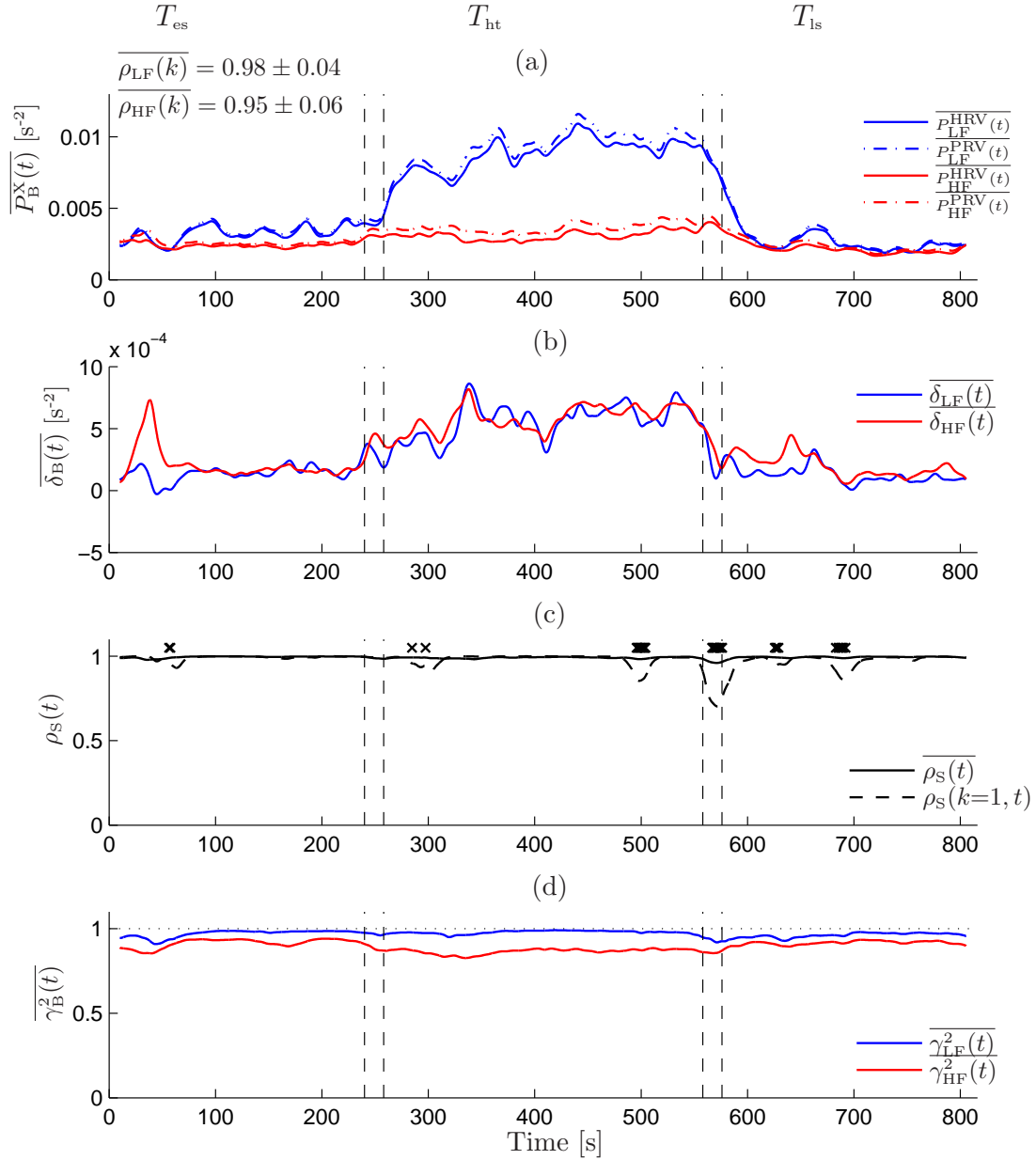
Figure 7.5: Global results of TF and TF coherence analysis. Mean trend estimated by averaging among subjects. (a) Time-course of the instantaneous power in each frequency band from HRV (continuous line) and PRV (dash-dotted line); (b) Instantaneous actual error in LF band (red line) and HF band (blue line); (c) Mean trend of the instantaneous correlation $\rho_S(k,t)$ between the power spectral density functions derived from HRV and from PRV (solid line). Index $\rho_S(k=1,t)$ and artefacts in PPG for subject 1 are reported in dashed line and cross marks, respectively; (d) Band coherence.

Table 7.3: Pearson's correlation $\rho_{\mathcal{I}}(k)$ between time-varying indices, $P_{\mathrm{LF}}^{\mathrm{X}}(k,t), P_{\mathrm{HF}}^{\mathrm{X}}(k,t), R_{\mathrm{LF/HF}}^{\mathrm{X}}(k,t)$ for each subject k.

k	1	2	3	4	5	6	7	8	9	10	11	12	13	14	15	16	17	**MEAN**
$\rho_{\mathrm{LF}}(k)$	0.84	0.95	0.99	1	1	0.99	1	1	1	1	0.99	0.99	1	1	1	1	1	**0.98±0.04**
$\rho_{\mathrm{HF}}(k)$	0.95	0.86	0.99	0.98	0.93	0.95	0.98	0.99	0.95	0.99	0.99	0.95	0.91	0.95	0.98	1	0.77	**0.95±0.06**
$\rho_{\mathrm{LF/HF}}(k)$	0.89	0.99	0.96	0.99	0.98	0.97	0.99	1	0.97	0.99	0.97	0.98	0.99	0.98	0.99	1	0.91	**0.97±0.03**

Table 7.4: Time-invariant physiological analysis results (p-values). Results of Student's t–test for time-invariant analysis comparing each pair of windows $T^{(\mathrm{s})}$.

$P_{\mathrm{LF}}^{\mathrm{HRV}}$	$T_{\mathrm{es}}^{(\mathrm{s})}$	$T_{\mathrm{ht}}^{(\mathrm{s})}$	$T_{\mathrm{ls}}^{(\mathrm{s})}$	$P_{\mathrm{HF}}^{\mathrm{HRV}}$	$T_{\mathrm{es}}^{(\mathrm{s})}$	$T_{\mathrm{ht}}^{(\mathrm{s})}$	$T_{\mathrm{ls}}^{(\mathrm{s})}$
$T_{\mathrm{es}}^{(\mathrm{s})}$	1	**0.047**	0.207	$T_{\mathrm{es}}^{(\mathrm{s})}$	1	0.569	0.7
$T_{\mathrm{ht}}^{(\mathrm{s})}$	-	1	**0.021**	$T_{\mathrm{ht}}^{(\mathrm{s})}$	-	1	0.352
$T_{\mathrm{ls}}^{(\mathrm{s})}$	-	-	1	$T_{\mathrm{ls}}^{(\mathrm{s})}$	-	-	1

$P_{\mathrm{LF}}^{\mathrm{PRV}}$	$T_{\mathrm{es}}^{(\mathrm{s})}$	$T_{\mathrm{ht}}^{(\mathrm{s})}$	$T_{\mathrm{ls}}^{(\mathrm{s})}$	$P_{\mathrm{HF}}^{\mathrm{PRV}}$	$T_{\mathrm{es}}^{(\mathrm{s})}$	$T_{\mathrm{ht}}^{(\mathrm{s})}$	$T_{\mathrm{ls}}^{(\mathrm{s})}$
$T_{\mathrm{es}}^{(\mathrm{s})}$	1	**0.046**	0.194	$T_{\mathrm{es}}^{(\mathrm{s})}$	1	0.342	0.677
$T_{\mathrm{ht}}^{(\mathrm{s})}$	-	1	**0.02**	$T_{\mathrm{ht}}^{(\mathrm{s})}$	-	1	0.184
$T_{\mathrm{ls}}^{(\mathrm{s})}$	-	-	1	$T_{\mathrm{ls}}^{(\mathrm{s})}$	-	-	1

7.3.3 Physiological analysis results

Results of the time-invariant analysis are reported in table 7.4. It is shown that $P_{\mathrm{LF}}(k)$ significantly increased as response to the orthostatic stress provoked by the head up tilt. Student's t–test presented similar results for both PRV and HRV signals.

Figure 7.6 shows the results of the time-varying analysis. It is shown that the time-course of the p-value estimated from HRV and PRV followed the same trend, being $p_{\mathrm{LF}}^{\mathrm{HRV}}(t)$ and $p_{\mathrm{LF}}^{\mathrm{PRV}}(t)$ almost equal. The variations observed in $P_{\mathrm{LF}}^{\mathrm{X}}(k,t)$ during the tilt table test, see Fig. 7.5a, caused $p_{\mathrm{LF}}^{\mathrm{X}}(t)$ to change. First, immediately after the head up tilt, $p_{\mathrm{LF}}^{\mathrm{X}}(t)$ dramatically decreased; then, during T_{ht}, $p_{\mathrm{LF}}^{\mathrm{X}}(t)$ continued gradually diminishing, reaching the threshold for statistical significance about 2 minutes later; finally, when the supine position was restored $p_{\mathrm{LF}}^{\mathrm{X}}(t)$ abruptly increased to previous values.
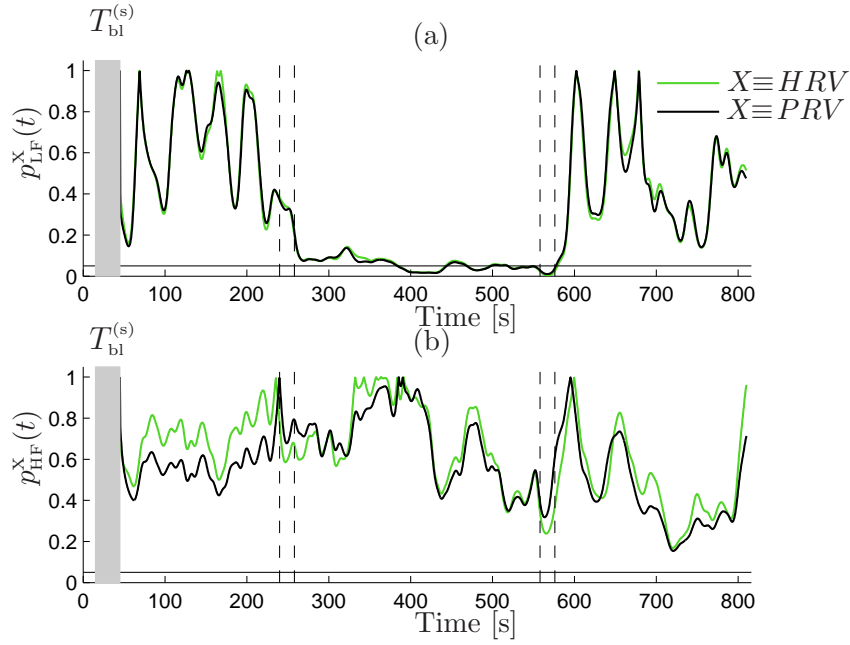
Figure 7.6: Time-varying physiological analysis. Temporal evolution of (a) the p-value $p_{\mathrm{LF}}^{\mathrm{X}}(t)$ and (b) $p_{\mathrm{HF}}^{\mathrm{X}}(t)$, which quantify the differences between actual values of $P_{\mathrm{B}}^{\mathrm{X}}(k,t)$ and baseline values, for $\mathrm{X} \in \{\mathrm{HRV}, \mathrm{PRV}\}$ and $\mathrm{B} \in \{\mathrm{LF}, \mathrm{HF}\}$. Baseline values were estimated in the reference window marked as gray area, $T_{\mathrm{bl}}^{(\mathrm{s})}$.

7.4 Relationship between HRV and PRV: the influence of PTTV

Using equations (7.1) and (7.2), it is possible to describe the relationship between HRV from ECG and PRV from PPG as:

$$
\begin{aligned}
d_{\mathrm{iif}}^{\mathrm{PPG}}(t_{\mathrm{P}_j}) =& \frac{1}{(t_{\mathrm{P}_j} - t_{\mathrm{P}_{j-1}})} = \frac{1}{(t_{\mathrm{E}_j} + \tau_{\mathrm{PTT}_j} + \xi_j) - (t_{\mathrm{E}_{j-1}} + \tau_{\mathrm{PTT}_{j-1}} + \xi_{j-1})} = \quad (7.7) \\
=& \frac{1}{(t_{\mathrm{E}_j} - t_{\mathrm{E}_{j-1}})} \cdot \frac{1}{1 + \frac{\tau_{\mathrm{PTT}_j} - \tau_{\mathrm{PTT}_{j-1}} + \xi_j - \xi_{j-1}}{t_{\mathrm{E}_j} - t_{\mathrm{E}_{j-1}}}} \approx \\
\approx& \frac{1}{(t_{\mathrm{E}_j} - t_{\mathrm{E}_{j-1}})} \left[1 - \frac{\tau_{\mathrm{PTT}_j} - \tau_{\mathrm{PTT}_{j-1}} + \xi_j - \xi_{j-1}}{t_{\mathrm{E}_j} - t_{\mathrm{E}_{j-1}}} \right] = \\
=& d_{\mathrm{iif}}^{\mathrm{ECG}}(t_{\mathrm{E}_j}) \left[1 - \left(\Delta_{\mathrm{PTT}_j}(t_{\mathrm{E}_j}) + \Delta_{\xi_j}(t_{\mathrm{E}_j}) \right) \cdot d_{\mathrm{iif}}^{\mathrm{ECG}}(t_{\mathrm{E}_j}) \right]
\end{aligned}
$$

In this expression τ_{PTT_j} is the PTT which corresponds to the jth beat; ξ_j is a stochastic variable which accounts for errors in location of t_{P_j}; this stochastic variable takes into account the fact that the fiducial point on the PPG signal is much less definite than the R peak of the ECG; $\Delta_{\mathrm{PTT}_j}(t_{\mathrm{E}_j}) = \tau_{\mathrm{PTT}_j} - \tau_{\mathrm{PTT}_{j-1}}$ and $\Delta_{\xi_j}(t_{\mathrm{E}_j}) = \xi_j - \xi_{j-1}$ are the PTT and the location error variabilities, respectively.

Note that in (7.7) it has been assumed that $(\Delta_{\mathrm{PTT}_j}(t_{\mathrm{E}_j}) + \Delta_{\xi_j}(t_{\mathrm{E}_j})) << t_{\mathrm{E}_j} - t_{\mathrm{E}_{j-1}}$ and t_{E_j} has no temporal jitter.

The beat–to–beat difference between HRV and PRV can be then written as:

$$d_{\mathrm{iif}}^{\mathrm{PPG}}(t_{\mathrm{P}_j}) - d_{\mathrm{iif}}^{\mathrm{ECG}}(t_{\mathrm{E}_j}) = -\left(\Delta_{\mathrm{PTT}_j}(t_{\mathrm{E}_j}) + \Delta_{\xi_j}(t_{\mathrm{E}_j})\right) \cdot \left(d_{\mathrm{iif}}^{\mathrm{ECG}}(t_{\mathrm{E}_j})\right)^2. \tag{7.8}$$

7.4.1 Simulation to test the effect of the PTTV

To test the isolated effect of ξ_j and to indirectly assess the role played by PPT in equation (7.8), a simulation study was carried out. In this simulation study, it was assumed that the difference between the HRV signal and the simulated PRV ($\mathrm{PRV_S}$) signal was only due to the jitter in the PPG fiducial point. This is equivalent to write $t_{\mathrm{P}_{\mathrm{S}_j}} = t_{\mathrm{E}_j} + \xi_j$. The stochastic variable ξ_j was modeled by zero-mean discrete uniform distributions and varying standard deviation. The inverse interval function for simulated PPG signals, $d_{\mathrm{iif}}^{\mathrm{PPG_S}}(t_{\mathrm{P}_{\mathrm{S}_j}})$, were computed for all patients,

$$d_{\mathrm{iif}}^{\mathrm{PPG_S}}(t_{\mathrm{P}_{\mathrm{S}_j}}) = \frac{1}{(t_{\mathrm{P}_{\mathrm{S}_j}} - t_{\mathrm{P}_{\mathrm{S}_{j-1}}})} = \frac{1}{(t_{\mathrm{E}_j} + \xi_j) - (t_{\mathrm{E}_{j-1}} + \xi_{j-1})}. \tag{7.9}$$

Simulated pulse rate variability signals $d_{\mathrm{PRV_S}}(t)$, were obtained after interpolation and DC suppression as previously described for obtaining the HRV and PRV signals.

In the simulation study, when the error in the location of the pulse in the PPG signal, ξ_j, was uniformly distributed between $\pm$ 8 ms (std = 4.9 ms), HF coherence toke similar values as those reported for real data, i.e. $\overline{\gamma_{\mathrm{HF}}^2(k,t)}$=0.89. The results for simulation study with this level of noise, obtained by averaging among subjects are shown in Fig. 7.7. As shown in panels (a)–(b), in this case, the isolated effect of the simulated jitter in the PPG fiducial point did not introduce a bias in the instantaneous power of the HF spectral components.

7.5 Discussion

The purpose of the study presented in this section was to evaluate the possibility of using PRV as an alternative measurement of HRV in non-stationary conditions. Similar results in the analysis performed on indices derived from $d_{\mathrm{HRV}}(t)$ and on indices derived from $d_{\mathrm{PRV}}(t)$ support the usefulness of the PRV signal as surrogate of the HRV signal.

The study is based on the analysis of the changes observed in the heart rate modulation of 17 young subjects during tilt table test. The analysis consists of three different parts:

(i) Classical indices of HRV analysis were estimated in three different time epochs during which stationarity was assumed.

(ii) Time-frequency and time-frequency coherence analysis were used to assess and compare the time-varying spectral properties of both signals.

(iii) A statistically analysis of the changes provoked by head up tilt with respect to baseline condition was performed by using both the HRV and PRV signals.
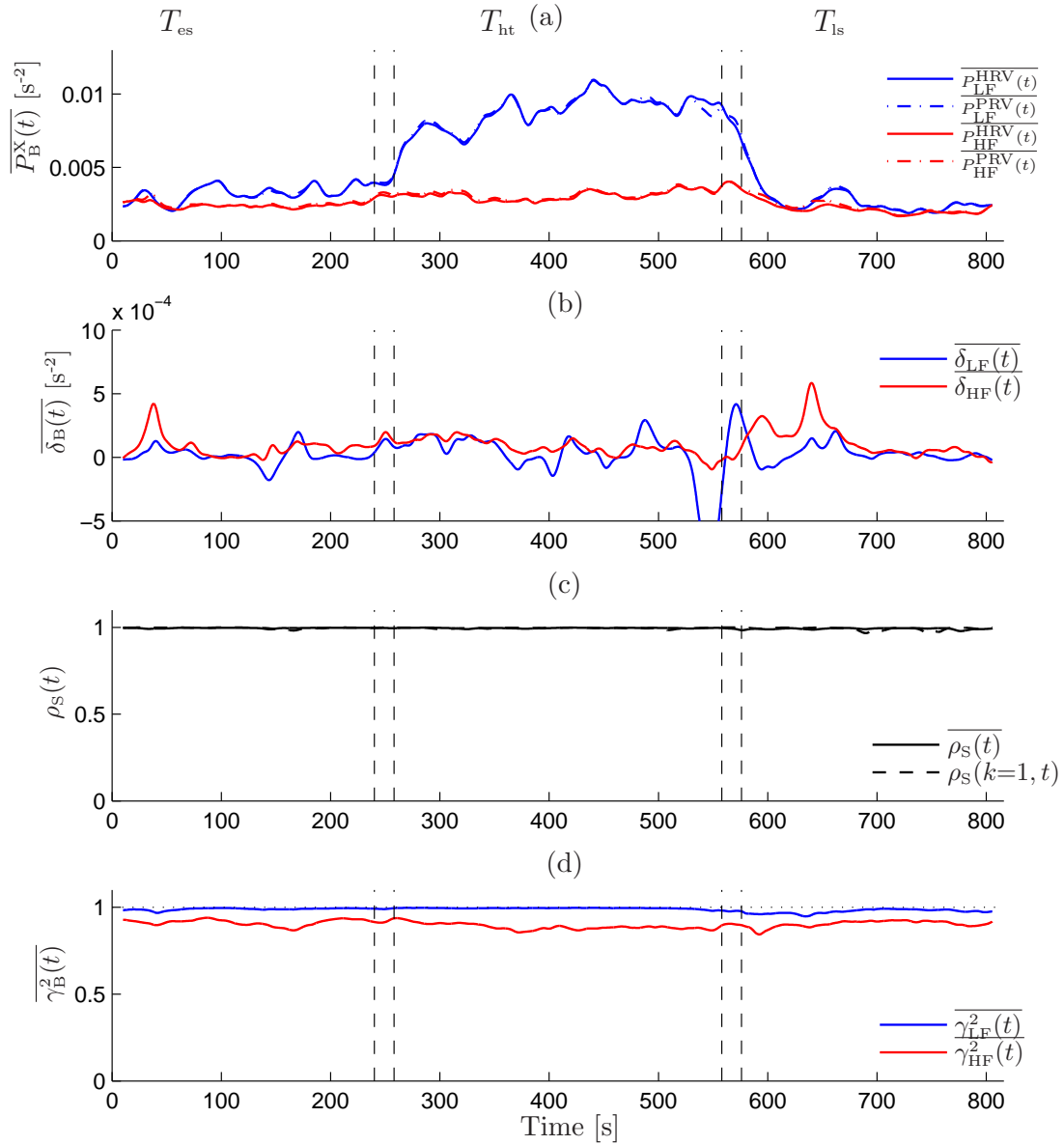
Figure 7.7: Simulation study: mean trend estimated by averaging among subjects. (a) Temporal evolution of the instantaneous power in each frequency band from HRV (continuous line) and PRV$_\text{S}$ (dash-dotted line); (b) Instantaneous actual error in LF band (red line) and HF band (blue line); (c) Mean trend of the instantaneous correlation $\rho_\text{S}(k,t)$ between the power spectral density functions derived from HRV and from PRV$_\text{S}$ (solid line). Index $\rho_\text{S}(k{=}1,t)$ for subject 1 is reported in dashed line; (d) Band coherence.

7.5.1 Time invariant analysis

A comparison between classical HRV and PRV analysis during tilt table test was presented. Table 7.2 and Fig. 7.3 show that classical time and frequency indices derived from PRV and HRV. No statistically significant differences between these indices ($p > 0.05$) was observed, whereas strong linear correlation ($\rho_{\mathcal{I}} > 0.9$) was measured. Generally, during early and later supine position we observed a higher similarity between these indices than during head up position. Additionally, a positive bias in the estimation of the power content from PRV is always present.

As already pointed out in [60, 70], this bias increases during head up tilt. This can be due to the effect of pulse transit time, and this point will be discussed in the following section. The results of time-invariant analysis are in agreement with previous works [161, 160, 116, 233, 49, 60], which suggested that PRV could be used as an alternative measurement of HRV during stationary conditions, at least in a resting position [60]. However, in a study with children [70] it was pointed out that the differences observed in HF band should be carefully considered.

7.5.2 Time-varying analysis

Different time-frequency and time-varying approaches have been proposed in the literature to quantify the dynamics of HRV in non-stationary conditions [165]. In this study we used the smoothed pseudo Wigner-Ville distribution since it is characterized by a high TF resolution and gives the possibility of performing an independent filtering in both time and frequency. The SPWVD has been used for the assessment of the time-varying spectral properties of HRV during different non-stationary conditions [131, 3, 19, 184, 99, 201] and has been considered as the best option for analysis of non-stationary HRV signals in a comparative study [216]. The choice of the kernel proposed in equation (7.5) was motivated by the results of [206], in which it was used to robustly estimate TF coherence. In our work, the degree of TF filtering (and interference terms reduction) was sufficient to provide a consistent estimation of TF coherence, i.e. $\gamma^2(t, f) \in [0, 1] \; \forall (t, f)$, for all subjects.

During tilt table test we observed high similarity between the patterns of response of HRV and PRV. The global results reported in Fig. 7.5 show that the instantaneous power content of the PRV was slightly higher ($\overline{\delta_{\mathrm{B}}(k, t)} < 10^{-3}$ s⁻²) than the instantaneous power content of the HRV signal. The temporal evolution of the index $\delta_{\mathrm{B}}(k, t)$ was almost the same in both frequency bands: during early and later supine position $\overline{\delta_{\mathrm{B}}(k, t)} < 0.25 \; 10^{-3}$ s⁻², whereas during head up position $\overline{\delta_{\mathrm{B}}(k, t)}$ increased up to a value of about $0.7 \; 10^{-3}$ s⁻². It is worth noting that during the highest non-stationary intervals (i.e. the transitions during which the table was tilted), $\delta_{\mathrm{B}}(k, t)$ did not increase. As reported in table 7.3, the time-course of the instantaneous power in LF and HF spectral bands, obtained from HRV and from PRV, was highly correlated, i.e. $P_{\mathrm{B}}^{\mathrm{HRV}}(k, t)$ and $P_{\mathrm{B}}^{\mathrm{PRV}}(k, t)$ followed the same trend.

The correlation between the instantaneous spectral densities of the two signals, $\rho_{\mathrm{S}}(k, t)$, was also very high, being the temporal average of the mean and standard deviation among subjects 0.99 ± 0.01. The small decreases of $\rho_{\mathrm{S}}(k, t)$ were due to the presence of some artefacts in the PRV signal.

The band coherence $\gamma_{\mathrm{B}}^2(k,t)$, showed that, despite of non-stationary conditions, the degree of linear coupling between the two signals was constant during time, and no relevant variations were observed even during upward and downward tilting. Band coherence in LF fluctuated around 0.97 ± 0.04 during the entire experimental procedure, while band coherence in HF fluctuated around 0.92 ± 0.06 and 0.87 ± 0.10 during supine (T_{es} and T_{ls}) and head up tilt (T_{ht}) position, respectively, being 0.89 ± 0.08 during the entire experimental procedure.

In both time-invariant and time-varying analysis we observed a positive bias in the measurement of spectral indices from PRV. This bias was observed to increase during head up tilt. As modeled in equation (7.8), differences between PRV and HRV are due to PTT variability and to the variability of the error in location of PPG fiducial point. Since there is no reason to expect an increase of the error committed in locating the PPG fiducial point during head up tilt, our hypothesis is that this bias observed in HF band could be due to the variability introduced by the PTT; this variability could increase during head up tilt. The observation of lower values in $\gamma_{\mathrm{HF}}^2(k,t)$ with respect to $\gamma_{\mathrm{LF}}^2(k,t)$ suggests that, due to PTT variability, respiration is slightly differently represented in PRV than in HRV. This is in agreement with [70]. Time-varying spectral indices estimated from PRV and HRV analysis did follow the same temporal patterns. Nevertheless, small differences exist between their values, mainly in the respiratory band. Thus, when a study aims at accurately estimating these time-varying spectral indices, caution should be used in replacing HRV by PRV. Equation (7.8) describes the relationship between HRV and PRV and shows that the difference between HRV and PRV is mainly due to PTT variability and to the variability of the jitter in the PPG fiducial point. To better understand the results presented in this work, a simulation study was carried out. We simulated the case in which the differences between HRV and PRV are only due to the jitter in the PPG fiducial point ξ_j. Similar values of HF band coherence as those observed in the analysis of real data could be obtained for ξ_j uniformly distributed between $\pm$ 8 ms (std = 4.9 ms). This simulation study showed that the jitter in the PPG fiducial point alone can not introduce a bias in the instantaneous error $\delta_{\mathrm{B}}(k,t)$. This observation corroborates the hypothesis that suggests that the difference between PRV and HRV showed in Fig. 7.5b is mainly due to PTT variability. The TF description of PTT variability goes beyond the purposes of this work, but further studies on this subject are needed.

7.5.3 Physiological analysis

From both time-invariant and time-varying analysis we observed a statistically significant increase of the power content in LF band of HRV and PRV during head up tilt. Results of table 7.4 show that differences in $P_{\mathrm{LF}}^{\mathrm{X}}(k)$ during $T_{\mathrm{ht}}^{(\mathrm{s})}$ and $T_{\mathrm{ls}}^{(\mathrm{s})}$ were statistically higher than differences during $T_{\mathrm{ht}}^{(\mathrm{s})}$ and $T_{\mathrm{es}}^{(\mathrm{s})}$. Simultaneous inspection of Fig. 7.5a and 7.6a reveals the transient nature of the autonomic response to orthostatic stress. It is shown that the variations in $P_{\mathrm{LF}}^{\mathrm{X}}(k,t)$ provoke changes in the temporal pattern of p-values. First, immediately after the head up tilt, the p-value $p_{\mathrm{LF}}^{\mathrm{X}}(t)$ dramatically decreased; then, during T_{ht}, $p_{\mathrm{LF}}^{\mathrm{X}}(t)$ continued gradually diminishing, reaching statisti-

cal significance about 2 minutes later; finally, when the supine position was restored $p_{\mathrm{LF}}^{\mathrm{x}}(t)$ abruptly increased to previous values. Moreover, as also shown in Fig. 7.6a the power content within LF band during early and later supine positions did not present any relevant difference, pointing out that recovery was fast. The power content in HF band did not present any significant change during the test. Finally, it is worth noting that there was agreement between the physiological analysis based on HRV and PRV. This suggests that, in this particular test, PRV could be used as a surrogate measurement of HRV to evaluate the autonomic modulation changes of the heart rate for both stationary and non-stationary analysis.

7.5.4 Limitations

It is well established that PPG measurements are quite sensitive to patient and/or probe-tissue movement artefact [5]. The presence of motion artefacts is one of the most important limitations of the use of the PRV signal as surrogate of the HRV signal [159]. Thus, automatic artefact detection [102, 257, 119] and replacement of correspondent corrupted signal segments are of crucial importance in PPG signal processing. In this study, a PPG artefact detector based on Hjorth parameters was used and subsequently PPG and ECG signals were manually supervised. The effect of errors in beat and pulse detection was corrected following the algorithm presented in [180]. Artefacted PPG pulses represented less than 1% of total pulses and, thanks to their detection and correction, did not significantly affected our global results. Nevertheless, their effect on the similarity indices of single subjects was still visible. In subject 17 an artefact provoked the decrease observed in TF coherence around 320 s (see Fig. 7.4). The PPG recording of subject 1 was that with the highest number of artefacts. In Fig. 7.5c, it is shown that artefacts provoked a decrease in the index $\rho_{\mathrm{s}}(k,t)$, being the most relevant decrease associated to artefacts during the downward motion of the automatic table (around 570 s). As also reported in [60, 159] high PPG signal quality and robust artefact removal are necessary for accurate PRV analysis.

The accuracy in detecting the fiducial point in PPG (t_{P_j}) is also essential in PRV analysis. It mainly depends on the sampling frequency and morphology of PPG pulse wave. According to [185], a low sampling frequency produces an increase in the power of the high frequency band, and generally at least a sampling frequency of 500 Hz is required to avoid some serious errors. In this study, the PPG signal was sampled at 250 Hz and later it was interpolated using cubic splines up to an equivalent sampling frequency of 1000 Hz in order to match the time resolution of HRV.

Photoplethysmographic pulse wave is less sharp than R wave in ECG. The rounded shape of the PPG pulse wave could introduce some inaccuracy in t_{P_j} detection. The effect of this error has been introduced in equation (7.7) by means of the stochastic variable ξ_j. The simulation study, which aimed at assessing the isolated effect of these inaccuracies pointed out that this jitter was not able to reproduce the bias observed in Fig. 7.5b. If the morphology of PPG pulse wave does not change along the recording, as in our data, the main difference between PRV and HRV will be due to PTT variability. If PPG pulse wave morphology changes other methods less sensitive to morphology for detecting t_{P_j} as for example methods based on mass center should

be considered. Taking into account the stability of the fiducial point on the PPG is important for PRV analysis in each application.

An important point to stress is that during tilt, the ANS reacts in such a way to keep blood pressure values as close as possible to the rest values. If some hypotensive events occurs during tilt, they are related to pre-syncopal/syncopal events which did not happen in our data. Thus changes in PRV could not be address to hypotensive events in our work.

In this study, beat detections from ECG have been used for determining the temporal location of each pulse wave in the PPG. A robust automatic detector of pulses from PPG independent from ECG and adapted to different possible kind of pulse wave morphology is needed for the application of PRV analysis in clinical routine. An extended study including more subjects and other physiological events associated to non-stationary conditions would be desirable to confirm our results. In addition, a study of the effect of aging as well as of changes in blood pressure on PRV would be interesting. It is well known that older subjects have increasing arterial stiffness, which results in increasingly faster pulse transmission to the periphery [6]. Thus, differences between HRV and PRV, which are mainly produced by PTT, could be dependent on aging.

Chapter 8

Characterization of the dynamic interactions between heart rate and arterial pressure by cross time-frequency analysis

Contents

8.1   Introduction

Short-term cardiovascular control involves homeostatic mechanisms for the maintenance of blood pressure, which make the blood pressure and heart rate to continuously interact. A change in the blood pressure causes a change in the heart rate through the feedback baroreceptor-cardiac reflex (baroreflex, see §1.2.2), while, in turn, a change in the heart rate causes a change in the blood pressure through feedforward mechanical effects. The assessment of baroreflex sensitivity (BRS), i.e. the change in the RR interval following a unitary change in the blood pressure, from non-invasive measurements is clinically relevant because a baroreflex impairment has been suggested to have diagnostic and prognostic relevance [76, 151].

In the last 20 years, different techniques have been proposed to estimate the spontaneous BRS [155, 212, 247, 225, 30, 109]. Among them, there is the cross-spectral analysis of systolic arterial pressure variability (SAPV) and RR variability (RRV) [76, 151]. In particular, the parameter α_{B} has been defined as the squared root of the ratio between the power of the RRV and SAPV series, and it is usually defined in both the LF and HF spectral bands, [212, 155]. Traditionally, this parameter is estimated whenever spectral coherence [57] between RRV and SAPV is higher than an arbitrary threshold. Although the first methodologies to estimate spontaneous BRS are not recent [225, 212, 168], in the last few years, the interest in improved methods has increased. Recently, much effort has been put into improving two issues: The capability of following changes in non-stationary conditions and the assessment of the prevalent direction of the coupling between RRV and SAPV. However, only few methodologies that combine non-stationary analysis and the assessment of causality have been applied in the study of cardiovascular interactions [63]. Non-stationary processing is important because in the cardiovascular system, stationarity is a rare exception rather than the rule.Recent non-stationary methods for the analysis of cardiovascular interactions are based on time-varying autoregressive models [45, 255, 63], continuous and discrete Wavelet transform [143, 145, 196, 253], and empirical mode decomposition [239, 97]. The assessment of the prevalent direction of the coupling is relevant because it can be used to infer which mechanism is primarily responsible for the changes observed in the signals and is necessary to assess spontaneous BRS [219]. To determine the prevalent direction of the coupling between RRV and SAPV [193], cross-spectral analysis has been traditionally used [71, 156]. Recently, parametric modeling [194, 35, 63] and non-linear indices [219, 132] have also been proposed to assess causality [193].

The main purpose of this chapter is to present a methodology to characterize the dynamic interactions between RRV and SAPV, which includes the assessment of both the strength and the prevalent direction of local coupling. This methodology is based on the SPWVD and provides TF representations of the signal power spectra, spectral coherence, and phase differences with fine joint TF resolution. It also allows estimating the time-course of the local coupling, phase differences, and time-delay between the LF and HF spectral components of the two signals. Robust estimates of the BRS are obtained owing to the localization of TF regions characterized by statistically significant coherence and in which the SAPV leads the RRV signal.

The capability of reliably estimating fast changes in these dynamic interactions is as-

sessed in a simulation study involving data recorded from healthy subjects.

A physiological study is carried out to characterize the cardiovascular dynamics during head-up tilt table test [168, 71, 250, 219], and the Eurobavar data set [155, 251, 109] is analyzed to assess whether the presented methodology can be considered as the generalization of traditional time-invariant methods. To highlight the importance of non-stationary signal processing in the assessment of short-term cardiovascular control, a test of stationarity [51] is applied to the signals analyzed in this chapter.

8.2 Methods

8.2.1 Assessment of non-stationarity

Stationarity is usually assumed based on some arbitrary considerations. Recently, Borgnat et al. proposed an operational framework for statistically testing stationarity relatively to an observation scale [51]. The test is based on the comparison between global and local time-frequency features. Stationarity happens if the local spectra at all different time instants are statistically similar to the global spectrum obtained by marginalization.

The procedure to statistically test stationarity [51], can be summarized as follows:

(i) A set of *stationarized* surrogate signals $s_j(t)$, with $j = \{1, ..., J\}$, is generated and used as reference. Signals are derived from the original signal by randomizing the phase of its Fourier transform and going back to the temporal domain.

(ii) The global frequency spectrum is obtained by averaging the multitaper spectrogram $S(t, f)$ [37, 254] at some given time instant n:

$$\overline{S(f)} = \frac{1}{N} \sum_{n=1}^{N} S(t_n, f) \tag{8.1}$$

In this study, the time in between two consecutive time samples depended on T_h, the width of the first Hermite function used in the calculation of the multitaper spectrogram. Parameter T_h varied in $T_h \in [\frac{T}{20}, \frac{T}{2}]$, with T length of the signal.

(iii) Estimates of some spectral distance $D(\cdot, \cdot)$ are collected as:

$$c_{s_j}(n) \equiv D\big(S_{s_j}(t_n, f), \overline{S_{s_j}(f)}\big), \ n = \{1, ..., N\} \tag{8.2}$$

$$c_x(n) \equiv D\big(S_x(t_n, f), \overline{S_x(f)}\big), \ n = \{1, ..., N\} \tag{8.3}$$

In this study, as proposed in [51], we used as spectral distance D a combination of the Kullback Leibler divergence (D_{KL}) and the logspectral deviation (D_{LSD}). These measures are derived as [51]:

$$D_{KL}(G_1, G_2) \equiv \int_A \big(G_1(f) - G_2(f)\big) \log \frac{G_1(f)}{G_2(f)} df \tag{8.4}$$

$$D_{LSD}(G_1, G_2) \equiv \int_A \left| \log \frac{G_1(f)}{G_2(f)} \right| df \tag{8.5}$$

$$D(G_1, G_2) = D_{KL}(G_1, G_2)\big(1 + D_{LSD}(G_1, G_2)\big) \tag{8.6}$$

In these expressions, the two distributions $G_1(f)$ and $G_2(f)$ are positive and normalized to unity over the domain A. The KL measure (8.4) performs poorer than the LSD (8.5) when signals are amplitude modulated, because of normalization. However, it behaves better when signals are frequency modulated, because of its recognized ability at discriminating distribution shapes [51]. Therefore, the use of the spectral distance $D(G_1, G_2)$ (8.6) is a good compromise for cardiovascular signals, which are expected to present both AM and FM modulations.

(iv) The dispersion of these distances under the null hypothesis of stationarity is given by:

$$\Theta_0(j) = \text{var}\big(c_{s_j}(n)\big), \ \ n = \{1, ..., N\}, \ \ j = \{1, ..., J\} \tag{8.7}$$

This distribution allows for the determination of a threshold γ above which the null hypothesis is rejected. This threshold is obtained by modeling $\Theta_0(j)$ as a Gamma distribution and fixing a false alarm rate of 0.05 [51]. The dispersion of the distances (8.3), which characterizes the original signal $x(n)$ is given by:

$$\theta_1 = \text{var}\big(c_x(n)\big), \ \ \{n = 1, ..., N\} \tag{8.8}$$

(v) The one-sided test is performed:

$$d(x) = \begin{cases} 1, & \text{if } \theta_1 > \gamma \text{ non-stationarity} \\ 0, & \text{if } \theta_1 \leq \gamma \text{ stationarity} \end{cases} \tag{8.9}$$

8.2.2 Cross time-frequency analysis

The methodology used in this study is detailed in §3–5. Here, we only provide a brief description of the framework used to analyze the signals.

Time-frequency representations

Auto and cross TF spectra, $S_{xy}(t, f)$, are estimated by SPWVD, as described in §3:

$$S_{xy}(t, f) = \iint\limits_{-\infty}^{+\infty} \phi_{\text{d-D}}(\tau, \nu) A_{xy}(\tau, \nu) e^{j2\pi(t\nu - \tau f)} d\nu d\tau \tag{8.10}$$

$$A_{xy}(\tau, \nu) = \int_{-\infty}^{\infty} x\left(t + \frac{\tau}{2}\right) y^*\left(t - \frac{\tau}{2}\right) e^{-j2\pi\nu t} dt \tag{8.11}$$

The kernel used in this study was an elliptical exponential function of type (4.11):

$$\phi_{\text{d-D}}(\tau, \nu) = \exp\left\{-\pi\left[\left(\frac{\nu}{\nu_0}\right)^2 + \left(\frac{\tau}{\tau_0}\right)^2\right]^{2\lambda}\right\} \tag{8.12}$$

$$\phi_{\text{t-f}}(t, f) = \iint\limits_{-\infty}^{+\infty} \phi_{\text{d-D}}(\tau, \nu) e^{j2\pi(t\nu - \tau f)} d\tau d\nu \tag{8.13}$$

time-frequency coherence was estimated as in (4.10):

$$\gamma(t, f) = \frac{|S_{xy}(t, f)|}{\sqrt{S_{xx}(t, f) S_{yy}(t, f)}}; \ \ \gamma(t, f) \in [0, 1] \tag{8.14}$$

In this study, the appropriate degree of time-frequency smoothing is determined by a straightforward scheme as that described in §4.3. It consists in fixing a desired TF resolution and by iteratively increasing the degree of smoothing, until reaching meaningful estimates over the entire TF domain. Results of this numerical process will be shown in the followings.

The statistical test to assess the significance of time-frequency coherence was based on the point-by-point comparison of the coherence estimates with a threshold function which depends on the geometrical properties of the kernel (the signal independent threshold described in §4.5).

The region where $\gamma(t, f)$ is significant, i.e. that where the two signals are sharing approximately the same instantaneous frequencies, is defined as:

$$\Omega_{\mathrm{B}} \equiv \left\{ (t, f) \in (\mathbb{R}^+ \times B) \mid \gamma(t, f) > \gamma_{\mathrm{TH}}(t, f) \right\}; \tag{8.15}$$

with $B \in \{LF, HF\}$.

The TF phase difference (TFPD) spectrum is given by (5.4):

$$\Theta(t, f) = \arctan \left[\frac{\Im\left[S_{\mathrm{xy}}(t, f)\right]}{\Re\left[S_{\mathrm{xy}}(t, f)\right]} \right]; \quad \Theta(t, f) \in [-\pi, \pi] \tag{8.16}$$

Time-course of the physiological indices

As detailed in §5.2.3, the time-course of the indices characterizing the dynamic interactions between cardiovascular signals is estimated in specific TF regions.

In the followings, the TF region from which the time-course of a general index $\mathcal{I}_{\mathrm{B}}(t)$ is extracted, is called $\Omega_{\mathrm{B}}^{(\mathcal{I})}$, with $B \in \{LF, HF\}$ indicating a spectral component. Time-varying spectral band centered around the instantaneous frequency of a components of the cross time-frequency spectrum, $f_{\mathrm{B}}^{(\mathrm{xy})}(t)$, is defined as:

$$\Omega_{\mathrm{B}}^{(\gamma)} \equiv \left\{ (t, f) \in (\mathbb{R}^+ \times B) \mid f = f_{\mathrm{B}}^{(\mathrm{xy})}(t) \pm \frac{\Delta_{\mathrm{f}}^{\mathrm{m}}}{2} \right\} \tag{8.17}$$

where $\Delta_{\mathrm{f}}^{\mathrm{m}}$ is a term related to the frequency resolution (see §3.1.2).

The time-course of the band coherence is then obtained by averaging $\gamma(t, f)$ in $\Omega_{\mathrm{B}}^{(\gamma)}$:

$$\gamma_{\mathrm{B}}(t) = \frac{1}{\Delta_{\mathrm{f}}^{\mathrm{m}}} \int_{\Omega_{\mathrm{B}}^{(\gamma)}} \gamma(t, f) df \tag{8.18}$$

Region $\Omega_{\mathrm{B}}^{(\theta)}$ is defined as:

$$\Omega_{\mathrm{B}}^{(\theta)} \equiv \left\{ \Omega_{\mathrm{B}}^{(\gamma)} \cap \Omega_{\mathrm{B}} \right\} \circ R(t, f); \tag{8.19}$$

where $R(t, f)$ is a rectangle of sides $2\mathrm{s} \times \frac{\Delta_{\mathrm{f}}^{\mathrm{m}}}{2}$ Hz and $\circ$ denotes the opening (processing technique which involves erosion and dilation). The opening excludes from $\left\{\Omega_{\mathrm{B}}^{(\gamma)} \cap \Omega_{\mathrm{B}}\right\}$ the portions of TF domain which are smaller than $R(t, f)$, thus adding robustness to

the final estimates.

Index $\theta_{\mathrm{B}}(t)$ is estimated (in radians) by averaging the TFPD spectrum in $\Omega_{\mathrm{B}}^{(\theta)}$ (5.10):

$$\theta_{\mathrm{B}}(t) = \left[\int_{\Omega_{\mathrm{B}}^{(\theta)}} \Theta(t,f)df\right] \bigg/ \left[\int_{\Omega_{\mathrm{B}}^{(\theta)}} df\right] \tag{8.20}$$

The time delay associated to $\theta_{\mathrm{B}}(t)$ is estimated (in seconds) by the index $\mathcal{D}_{\mathrm{B}}(t)$, defined as (5.11):

$$\mathcal{D}_{\mathrm{B}}(t) = \frac{\theta_{\mathrm{B}}(t)}{2\pi f_{\mathrm{B}}^{(\mathrm{xy})}(t)} \tag{8.21}$$

Baroreflex sensitivity

Index $\alpha_{\mathrm{B}}(t)$, which measures the changes in the spontaneous baroreflex sensitivity, is estimated in a TF region $\Omega_{\mathrm{B}}^{(\alpha)}$ centered around $f_{\mathrm{B}}^{(\mathrm{xy})}(t)$, where coherence is statistically significant and where a change in the SAPV precedes a correlated change in the RRV signal:

$$\Omega_{\mathrm{B}}^{(\alpha)} = \left\{(t,f) \in \Omega_{\mathrm{B}}^{(\theta)} \mid \Theta(t,f) < 0\right\} \tag{8.22}$$

According to the described framework, if we associate $x(t)$ and $y(t)$ to the RRV and SAPV signal, respectively, when the prevalent causal direction is that of the feedback baroreceptive path, i.e. with a change in the arterial pressure preceding a corresponding change in the heart period, the phase of $S_{\mathrm{xy}}(t,f)$ is negative, i.e $\Theta(t,f) < 0$ (see §5.2.4).

The time-course of the baroreflex sensitivity is estimated as:

$$\alpha_{\mathrm{B}}(t) = \sqrt{\int_{\Omega_{\mathrm{B}}^{(\alpha)}} S_{\mathrm{xx}}(t,f)df \bigg/ \int_{\Omega_{\mathrm{B}}^{(\alpha)}} S_{\mathrm{yy}}(t,f)df} \tag{8.23}$$

8.3 Material and study populations

The presented methodology is assessed in a simulation study and is used to analyze cardiovascular interactions in two different data set.

8.3.1 Simulation study

A simulation study was carried out with the purpose of validating the proposed methodology. The signals used in these simulations are modified versions of the RRV signals recorded during the tilt table test described in the following section. They are obtained as:

$$x(t) = a_{\mathrm{RRV}}(t) + \xi_{\mathrm{x}}(t) \tag{8.24}$$

$$y(t) = [\gamma_0(t)\alpha_0(t)\exp(j\theta_0(t))]a_{\mathrm{RRV}}(t) + \xi_{\mathrm{y}}(t) \tag{8.25}$$

where $a_{\mathrm{RRV}}(t)$ is the complex analytic signal representation of the RRV signal, and $\xi_{\mathrm{x}}(t)$ and $\xi_{\mathrm{y}}(t)$ are complex white Gaussian noises associate to a SNR = 10dB. Indices

$\gamma_0(t) \in \{0, 1\}$, $\theta_0(t) \in [-2.2, -0.8]$ rad and $\alpha_0(t) \in [5, 20]$ ms/mmHg represent the reference time-course of the local coupling, phase difference and baroreflex sensitivity (see Fig. 8.3). The reasons which make the estimation of these indices challenging are: the TF structure of the signals reflects the complexity of real non-stationary biomedical signals; the presence of epochs, the shortest lasting 30 s, during which signals are not locally coupled and during which $\theta_B(t)$ and $\alpha_B(t)$ should not be estimated; phase difference varies non-linearly with time; the baroreflex sensitivity first undergoes stepwise changes and then recovery toward higher values following a non-linear time-course; noise is added; finally, all these patterns imply simultaneous amplitude and frequency modulation of the signals.

8.3.2 Tilt table test analysis

Fourteen subjects (aged 29±3 years) underwent a tilt table test with the following protocol: 4 min in early supine position (T_{es}), 5 min head-up tilted to an angle of 70° (T_{ht}) and 4 min back to later supine position (T_{ls}) [100]. For a complete description of the data base, please refer to the Appendix §A. The ECG signals were recorded with a sampling frequency of 1 kHz. The temporal location of the nth QRS complex in the ECG, t_n^{QRS}, was automatically determined using the algorithm described in [177]. The RR series was estimated as $x_{RR}(n) = t_{n+1}^{QRS} - t_n^{QRS}$. The effect of abnormal RR intervals was corrected by applying a methodology described in [179]. The pressure signal was recorded in the finger by the Finometer® system with a sampling frequency of 250 Hz. The systolic arterial pressure series was obtained as the maximum of the pressure signal within a short interval following t_n^{QRS}. The time series were subsequently interpolated by fifth-order spline with a sampling frequency of 4 Hz, and the RRV and SAPV signals, namely $x_{RRV}(t)$ and $x_{SAPV}(t)$, were obtained by high-pass filtering with a cut-off frequency of 0.03 Hz.

8.3.3 Eurobavar study

The experimental setting is described in details in [155]. Briefly, 21 subjects (age 38.4±3.3 years) were included in the study. Subjects included 4 healthy volunteers, 12 normotensive outpatients, 3 hypertensive patients (1 untreated), one diabetic patient with cardiac autonomic neuropathy (DAN), and one subject who recently underwent heart transplantation (HTR). ECG and pressure signals were acquired with a sampling frequency of 500 Hz in supine and standing position (about 10 minutes).

8.4 Results

Although the SPWVD gives the possibility of using an independent filtering in time and frequency, the constraint of having $\gamma(t, f)$ bounded between zero and one imposes a sort of trade-off between time and frequency resolution, which can not be simultaneously arbitrarily fine. For a given set of signals, different combinations of time and frequency resolutions fulfill the condition $\gamma(t, f) \in [0, 1]$. This is shown in Fig. 8.1, where black circles represent the time and frequency resolution of the kernels of
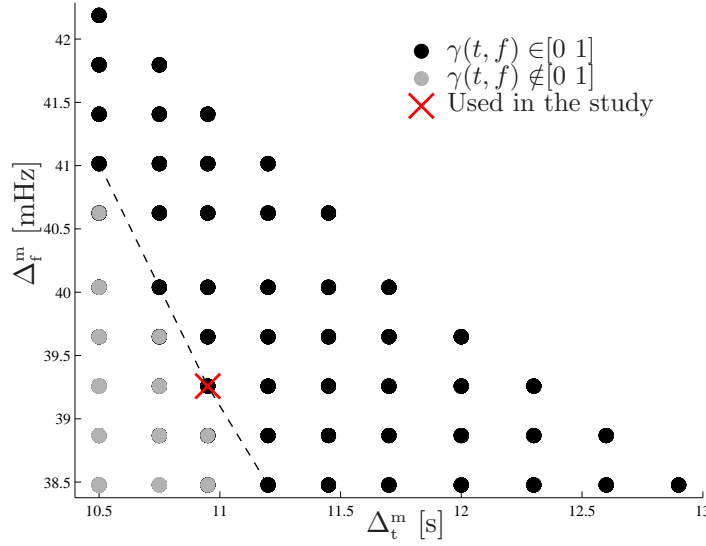
Figure 8.1: Circles represent the time-frequency resolution obtained by tuning the parameters of the kernel (8.12). The kernels that gave $\gamma(t,f) \in [0,1]$ for the entire data-set described in §8.3.2 are indicated in black, and those that gave $\gamma(t,f) \notin [0,1]$ for at least one subject are denoted in gray. The cross represents the resolution of the kernel used in this study.

type (8.12) which, for the whole data-set described in sec. 8.3.2, gave $\gamma(t,f) \in [0,1]$; gray circles represent kernels which gave $\gamma(t,f) \notin [0,1]$ for at least one subject. The closer a point is to the origin of the axes, the finer the TF resolution is. Thus, the most interesting combinations of TF resolutions are those reported on the dashed line. The results shown in the followings were obtained by using a kernel function $\phi_{\text{d-D}}(\tau,\nu)$ which gave $\{\Delta_{\text{t}}^{\text{m}}, \Delta_{\text{f}}^{\text{m}}\} = \{10.95 \text{ s}, 39 \text{ mHz}\}$ (see the cross mark in Fig. 8.1).

8.4.1 Assessment of non-stationarity

In both the data-sets, the hypothesis of stationarity was assessed via the statistical framework described in §8.2.1. Figure 8.2 shows, for a given scale of observation, the relative number of signals that were considered non-stationary by the test. The scale of observation is given as $T_{\text{h}}/T \in [0.05, 0.5]$, where T_{h} is the length of the window of the spectrogram and T is the length of the signals. Depending on the signal, T_{h} goes from 30–40 s to 5–7 min.

All the SAPV signals recorded during the tilt table test were considered non-stationary at every time scale, while one over 14 RRV signals was considered, for each T_{h}/T, stationary.

Interestingly, more than 50% of the signals from Eurobavar data set were considered non-stationary, despite the fact that they were recorded in resting conditions. In panel (a), it is shown that for $x_{\text{RRV}}(t)$, the typical scale of non-stationarity [51], at which it is more likely to reject the null hypothesis of stationarity, corresponds to $T_{\text{h}}/T = 0.1$–0.2 (about 1–2 min). In addition, it is also shown that the number of non-stationary RRV signals was higher in supine than in standing position. In supine position, for
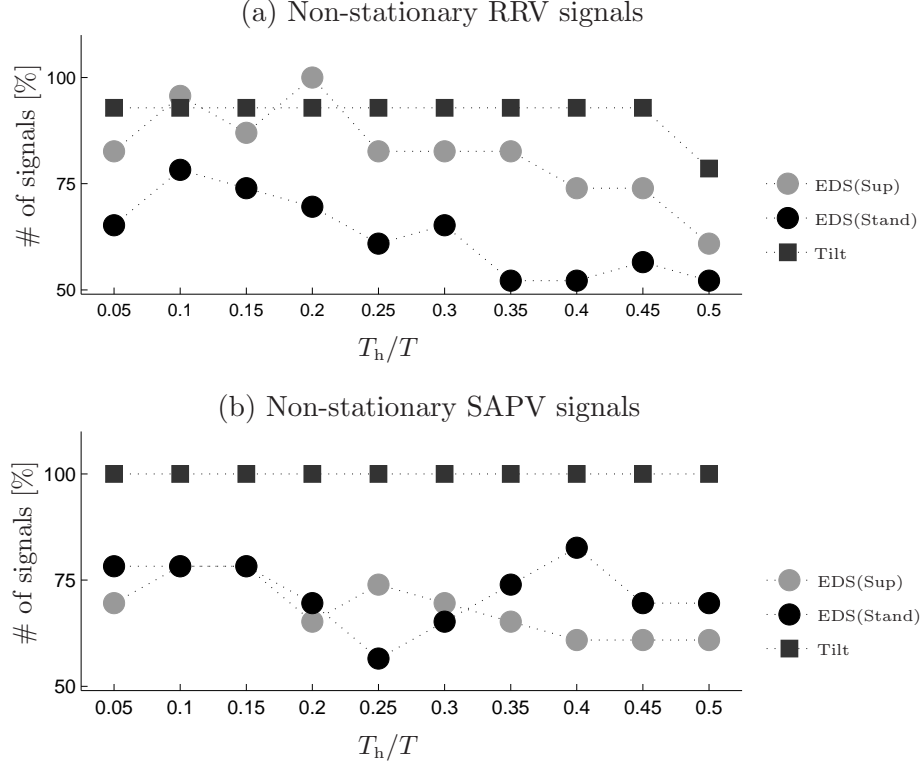
Figure 8.2: Outcomes of the non-stationary test. Results are given as the relative number of signals which were considered non-stationary. Signals recorded during tilt table test are reported by square marks. Signals from Eurobavar data set (EDS) recorded in supine and standing position are represented by gray and black circles, respectively.

$T_{\mathrm{h}}/T < 0.4$, the non-stationary testing was positive for more than 80% of the signals and for $T_{\mathrm{h}}/T = 0.2$, stationarity was rejected in all the signals. In panel (b), it is shown that at about the same scale of observation, about 80% of the SAPV signals were considered non-stationary, regardless of the position of the subjects.

These results suggest that TF analysis may be preferred to traditional methodology requiring the signals to be stationary even when they are recorded in conditions that are supposed to be stationary.

8.4.2 Simulation study

In the simulation study, from each one of the 14 RRV signals, 50 couples of modified signals were generated. For every couple of signals, the general index $\mathcal{I}_{\mathrm{B}}(t) \in \{\gamma_{\mathrm{B}}(t), \theta_{\mathrm{B}}(t), \alpha_{\mathrm{B}}(t)\}$, is estimated in TF regions $\Omega_{\mathrm{B}}^{(\mathcal{I})}$, and the time-course is given as $\mathcal{I}(t) = (\mathcal{I}_{\mathrm{LF}}(t) + \mathcal{I}_{\mathrm{HF}}(t))/2$. Results are shown in Fig. 8.3. Panel (a) depicts the results of coherence analysis. The mean threshold $\overline{\gamma_{\mathrm{TH}}} \approx 0.85$ is reported in dashed line. Epochs of decorrelation and correlation are localized with high temporal resolution. As shown in this illustration, the difference $t_0 - \hat{t}_0$ between the occurrence of an abrupt change of $\gamma_0(t)$ ($\frac{d}{dt}\gamma_0(t_0) = \pm\infty$) and the time instant at which the median time-course of $\gamma(t)$ matches the threshold value ($\gamma^{\mathrm{m}}(\hat{t}_0) = \overline{\gamma_{\mathrm{TH}}}$), is 0, 1.5, and 2.25 s,
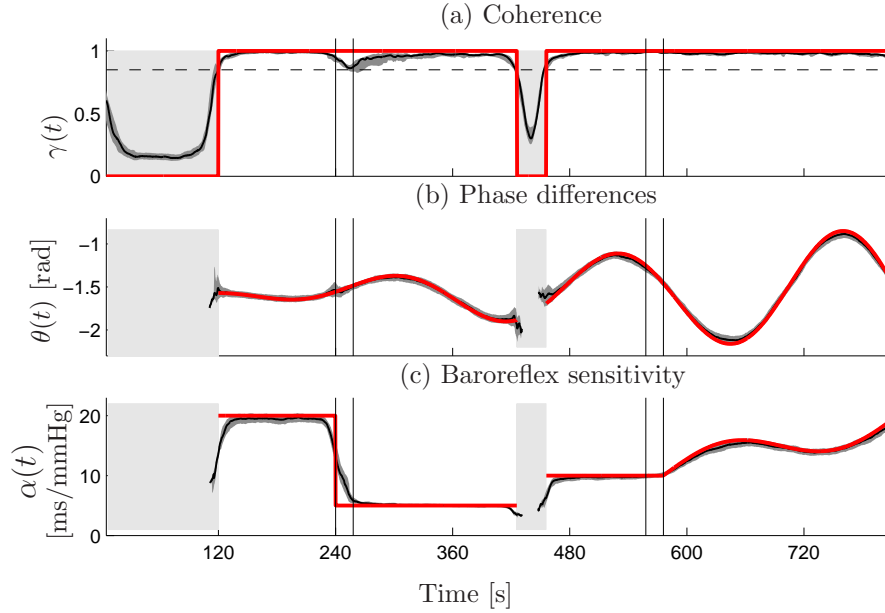
Figure 8.3: Simulation: Time-course of (a) Coherence, (b) Phase differences, (c) Baroreflex sensitivity. Reference values $\gamma_0(t)$, $\theta_0(t)$, $\alpha_0(t)$ are represented in bold red lines. Estimates are represented as median (black line) and interquartile range (gray region). Vertical lines mark supine positions and head-up tilt. Light gray areas represent the intervals during which signals are uncoupled.

respectively. The minimum level of coherence was higher than zero due to the effect of the kernel, while the maximum level of coherence was lower than one due to the time-varying phase difference between the spectral components and due to the noise. The decrease of $\gamma(t)$ observed around $t=240$ s, was due to the step-wise decrease of $\alpha_0(t)$ (see panel (c)). Panel (b) shows that the phase differences estimator (8.20) gives an accurate tracking of the time-course of $\theta_0(t)$. As $\Omega_{\mathrm{B}}^{(\theta)}$ includes only regions where $\gamma(t, f)$ is significant, estimates are given only in TF regions where the signals were locally coupled. In panel (c), it is shown that the time-course of $\alpha(t)$ is estimated with high accuracy. The step-wise decrease in $\alpha(t)$ from 20 to 5 ms/mmHg was approximated by a sigmoid-like pattern. Again, the coherence analysis prevented from including the interval where signals were uncoupled in the analysis.

8.4.3 Tilt table test

The TF representations obtained from the analysis of the RRV and SAPV of one subject (male, 30 years old), are shown in Fig. 8.4. In the auto spectra, shown in Fig. 8.4(a)–(b), the power of the HF modulation was higher than that of the LF one. During head-up tilt, the power of $x_{\mathrm{RRV}}(t)$ and $x_{\mathrm{SAPV}}(t)$ decreased and increased, respectively. The instantaneous frequencies of the HF component of both the signals, as well as those of the cross-spectrum (see $\Omega_{\mathrm{B}}^{(\gamma)}$ in panel (c)), reflect the high variability of the respiratory rate, which fluctuated between 0.15 and 0.25 Hz. Despite the non-stationary structure of the signals, the regions in which the local coupling was statistically significant were localized by TFC analysis (see Fig. 8.4(c)). The head-up

tilt caused the TFPD spectrum $\Theta(t, f)$, shown in Fig 8.4(d), to change quickly, especially in the HF range. In Fig. 8.4(c)–(d), regions $\Omega_{\mathrm{B}}^{(\gamma)}$ and $\Omega_{\mathrm{B}}^{(\theta)}$ are encircled by white contours. By averaging in traditional spectral ranges, instead of using these specific regions, one would have estimated a much lower coherence in the HF range and erroneously detected abrupt changes of phase difference in correspondence of those TF regions in which the signals were not locally coupled (as in LF at $t \approx 240$ s and $t \approx 600$ s).

The time-course of the physiological indices derived from the spectra of Fig. 8.4, as well as the global results, are given in Fig. 8.5. The temporal mean and the standard deviation of the median trends depicted in Fig. 8.5 for each index $\mathcal{I}_{\mathrm{B}}(t)$, epoch, and specific spectral band are given in Table 8.1. In the calculation of these values, the first and last $2\Delta_{\mathrm{t}}^{\mathrm{m}}$ s have been excluded from each of the three epochs. The Wilcoxon rank sum test was applied to statistically compare the temporal mean values of the indices estimated in each of the three conditions, i.e. $\{\overline{\mathcal{I}_{\mathrm{B},1}(t \in T_{\mathrm{k}})}, \ldots, \overline{\mathcal{I}_{\mathrm{B},\mathrm{L}}(t \in T_{\mathrm{k}})}\}$ and $\{\overline{\mathcal{I}_{\mathrm{B},1}(t \in T_{\mathrm{l}})}, \ldots, \overline{\mathcal{I}_{\mathrm{B},\mathrm{L}}(t \in T_{\mathrm{l}})}\}$, where $T_{\mathrm{k}} \neq T_{\mathrm{l}} \in \{T_{\mathrm{es}}, T_{\mathrm{ht}}, T_{\mathrm{ls}}\}$ is the index of the epochs and $L \leq 14$ are the subjects (subjects for which $\mathcal{I}(t)$ was not estimated for more than half the duration of the tilt table test were excluded from the statistical analysis).

In Fig. 8.5(b), it is shown that during the position changes, $T_{\mathrm{es}} \to T_{\mathrm{ht}}$ and $T_{\mathrm{ht}} \to T_{\mathrm{ls}}$, the time-course of $\gamma_{\mathrm{LF}}(t)$ is characterized by two patterns, a first abrupt decrease and a subsequently slower increase. During head-up tilt, restoration of baseline values took about 2 min, and about 1 min later, median $\gamma_{\mathrm{LF}}(t)$ reached values as high as 0.99. After coming back to supine position, $\gamma_{\mathrm{LF}}(t)$ maintained lower values than during the early supine position. In HF, $\gamma_{\mathrm{HF}}(t)$ fluctuated around 0.93±0.02 and did not decrease during the position change from $T_{\mathrm{ht}} \to T_{\mathrm{ls}}$.

The time-course of $\theta_{\mathrm{B}}(t)$ is extracted from $\Theta(t, f)$ by averaging in $\Omega_{\mathrm{B}}^{(\theta)}$, which includes those part of $\Omega_{\mathrm{B}}^{(\gamma)}$ in which the local coupling is significant and whose minimum size is imposed by the opening (8.19). In LF range, the phase differences $\theta_{\mathrm{LF}}(t)$ were about -0.60 ± 0.11 rad ($\mathcal{D}_{\mathrm{LF}}$ about 875±190 ms), thus revealing that a change in the LF oscillation of $x_{\mathrm{SAPV}}(t)$ preceded a correlated change in the LF oscillation of $x_{\mathrm{RRV}}(t)$. In the HF range, head-up tilt provoked a decrease in $\theta_{\mathrm{HF}}(t)$ from positive to negative values, thus showing a change in the prevalent direction of the local coupling between the respiratory-related oscillations of $x_{\mathrm{SAPV}}(t)$ and $x_{\mathrm{RRV}}(t)$.

Index $\alpha_{\mathrm{B}}(t)$ was estimated only in regions centered around $f_{\mathrm{B}}^{(\mathrm{xy})}(t)$ where the local coupling was significant and the phase difference was negative. These conditions determined, for the subject whose TF representations are shown in Fig. 8.4, the patterns observed in Fig. 8.5(m) and 8.5(o). Globally, as shown in Fig. 8.5(n) and 8.5(p), $\alpha_{\mathrm{B}}(t)$ decreased from about 20 ms/mmHg during T_{es} and T_{ls}, to less than 9 ms/mmHg during T_{ht}. Interestingly, the decrease in both $\alpha_{\mathrm{LF}}(t)$ and $\alpha_{\mathrm{HF}}(t)$ due to head-up tilt took few seconds, while the following increase due to the coming back to later supine position was remarkably slower.
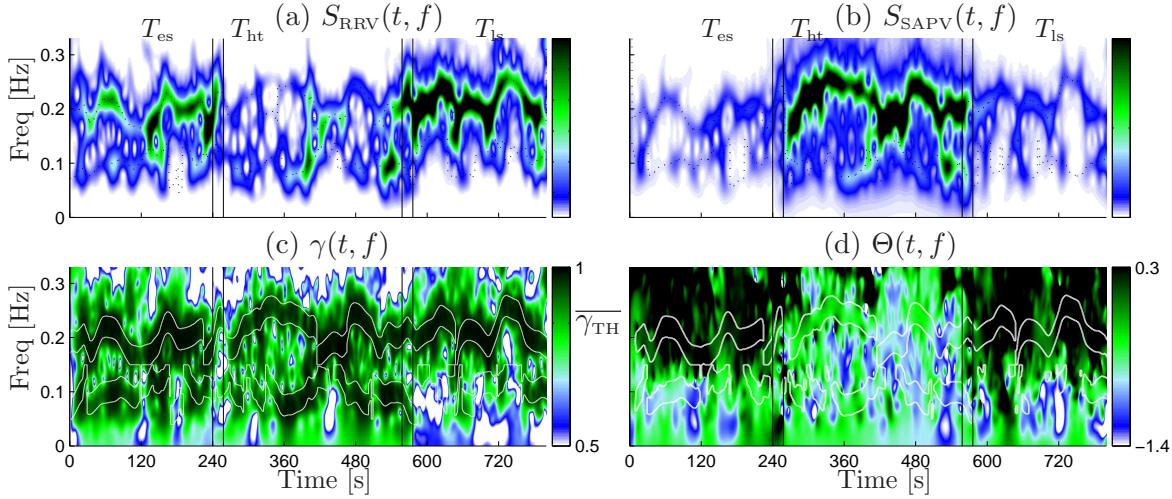
Figure 8.4: Time-frequency representation from one subject. (a)–(b): Smoothed pseudo Wigner-Ville distribution of $x_{\mathrm{RRV}}(t)$ and $x_{\mathrm{SAPV}}(t)$, respectively; Instantaneous frequencies are reported in dotted line; (c) Time-frequency coherence $\gamma(t, f)$; (d) Time-frequency phase difference spectrum $\Theta(t, f)$; In (c)–(d), $\Omega_{\mathrm{B}}^{(\gamma)}$ and $\Omega_{\mathrm{B}}^{(\theta)}$ are encircled by white contour. Vertical lines mark supine positions and head-up tilt.
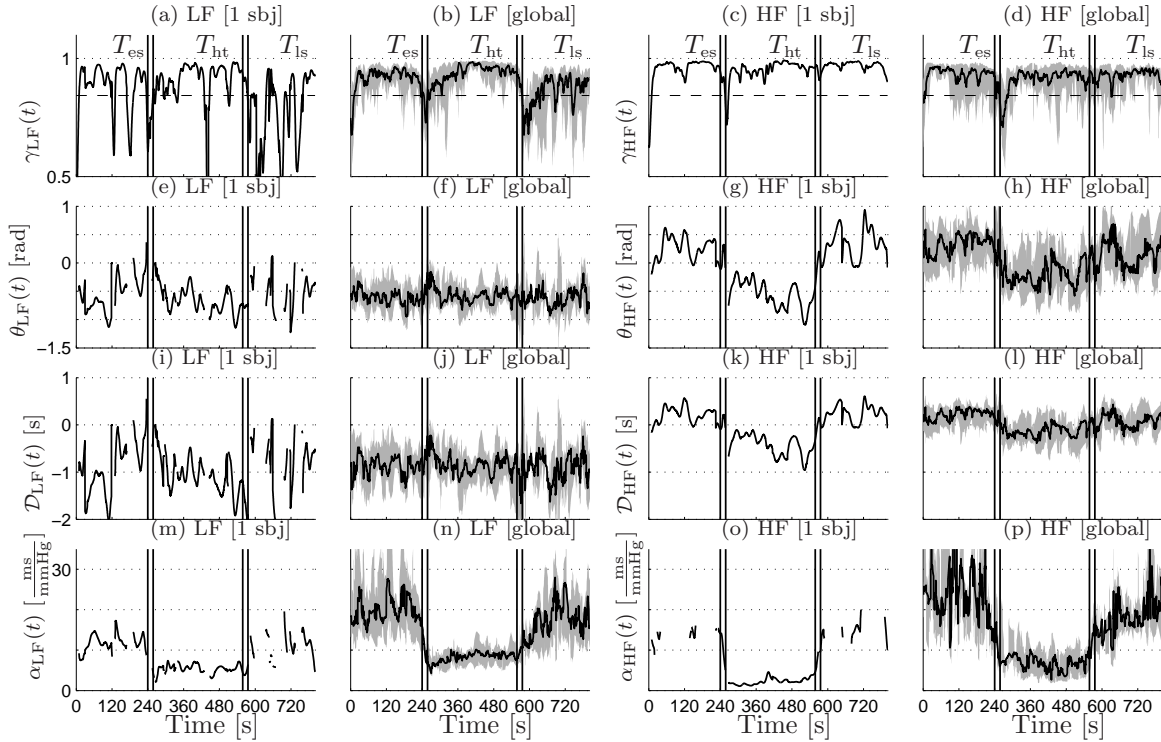
Figure 8.5: Indices during tilt table test: (a)–(d) local coupling $\gamma_{\mathrm{B}}(t)$ as in (8.18); (e)–(h) Phase differences $\theta_{\mathrm{B}}(t)$ as in (8.20); (i)–(l) Time delay $\mathcal{D}_{\mathrm{B}}(t)$ as in (8.21); (m)–(p) Baroreflex sensitivity $\alpha_{\mathrm{B}}(t)$ as in (8.23). First and third columns: results from the subject whose TF representation are shown in Fig. 8.4; Second and fourth columns: global results, median (black lines) and interquartile range (shadowed areas) of the time-courses from all subjects. Vertical lines mark supine positions and head-up tilt.

	Ω_{LF}			Ω_{HF}		
Index	T_{es}	T_{ht}	T_{ls}	T_{es}	T_{ht}	T_{ls}
$\overline{\gamma_{\mathrm{B}}(t)}$	0.93 ± 0.02	0.95 ± 0.04	$0.89\pm0.08^{\dagger}$	0.95 ± 0.02	0.93 ± 0.03	0.94 ± 0.01
$\overline{\theta_{\mathrm{B}}(t)}$	-0.59 ± 0.16	-0.59 ± 0.15	-0.61 ± 0.23	$0.37\pm0.23^{\dagger}$	-0.27 ± 0.22	0.14 ± 0.38
$\overline{\mathcal{D}_{\mathrm{B}}(t)}$	-0.85 ± 0.29	-0.86 ± 0.22	-0.84 ± 0.40	$0.26\pm0.14^{\dagger}$	-0.16 ± 0.16	0.08 ± 0.24
$\overline{\alpha_{\mathrm{B}}(t)}$	$19.77\pm4.51^{\dagger}$	8.62 ± 1.21	$17.87\pm4.44^{\dagger}$	$23.72\pm7.66^{\dagger}$	6.92 ± 2.51	$18.24\pm4.09^{\dagger}$

Table 8.1: Global results of the tilt table test, reported as the average of the median trends shown in Fig. 8.5, evaluated in epochs T_{es}, T_{ht} and T_{ls} (first and last $2\Delta_{\mathrm{t}}^{\mathrm{m}}$ s have been excluded from the analysis). $\dagger$: median values of a given index are statistically significant with respect to those estimated during head-up tilt, T_{ht} ($p < 0.05$)

8.4.4 Eurobavar data set

To assess whether the presented framework can be considered as a generalization of traditional analysis, the Eurobavar data set was processed by both stationary framework (SF) and non-stationary framework (NS), and the results were compared to those presented in [155]. In the SF, indices were obtained by temporal averaging of the TF distributions described in §3, thus representing stationary analysis (marginal spectra were used to obtain power and coherence estimates). In NF, for every subject, the temporal mean of the non-stationary indices described in §8.2.2 were estimated. The results of NF and SF are illustrated in the graphics on the left and right side of Fig. 8.6, respectively. In panels (a)–(d), circles and bars represent the mean and the standard deviation of local coupling and phase differences of the subjects without baroreflex impairment; while in panels (e)–(f), circles and bars represent the mean and the standard error of the BRS for the same subjecs (standard error was estimated for comparison with [155]) . In these graphics, markers $+$ and $\times$ represent the DAN and the HTR patient, respectively. The presented methodology (NF) gave higher coherence estimates than SF. Moreover, coherence estimates obtained by NF were higher in HF than in LF. These differences were due to the use of $\Omega_{\mathrm{B}}^{(\gamma)}$. In $\Omega_{\mathrm{LF}}^{(\gamma)}$, the coupling of the signals from the HTR and DAN patients was not significant for more than 95% of the total length of the recording. Because of the absence of local coupling, in HTR and DAN, phase differences $\theta_{\mathrm{LF}}(t)$ and $\alpha_{\mathrm{LF}}(t)$ were not assessed. Without performing the statistical analysis on the coherence estimates, one could erroneously conclude that in the HTR patient $\overline{\theta_{\mathrm{LF}}(t)} > 0$. For subjects without baroreflex impairment, estimates of the baroreflex sensitivity obtained by both SF and NF frameworks were consistent with those obtained by traditional time-invariant methodologies [155, 251]. In SF framework, for subject without baroreflex impairment (see panel (f)), $\overline{\alpha_{\mathrm{LF}}(t)}$ was 14.07 ± 2.88 ms/mmHg (supine) and 7.58 ± 0.96 (standing) ms/mmHg, while $\overline{\alpha_{\mathrm{HF}}(t)}$ was 18.66 ± 3.23 ms/mmHg (supine) and 8.00 ± 1.36 ms/mmHg (standing). The supine to standing ratio was 1.86 and 2.33 in LF and HF ranges, respectively, which is in line with that obtained in [155]: 1.70 (LF) and 2.63 (HF). By using the presented framework, evidences of baroreflex impairment of DAN and HTR patients were given by high $\theta_{\mathrm{HF}}(t)$, by the persistent absence of coupling between the signals in LF, and highlighted by the fact that no $\alpha(t)$ index could be estimated.
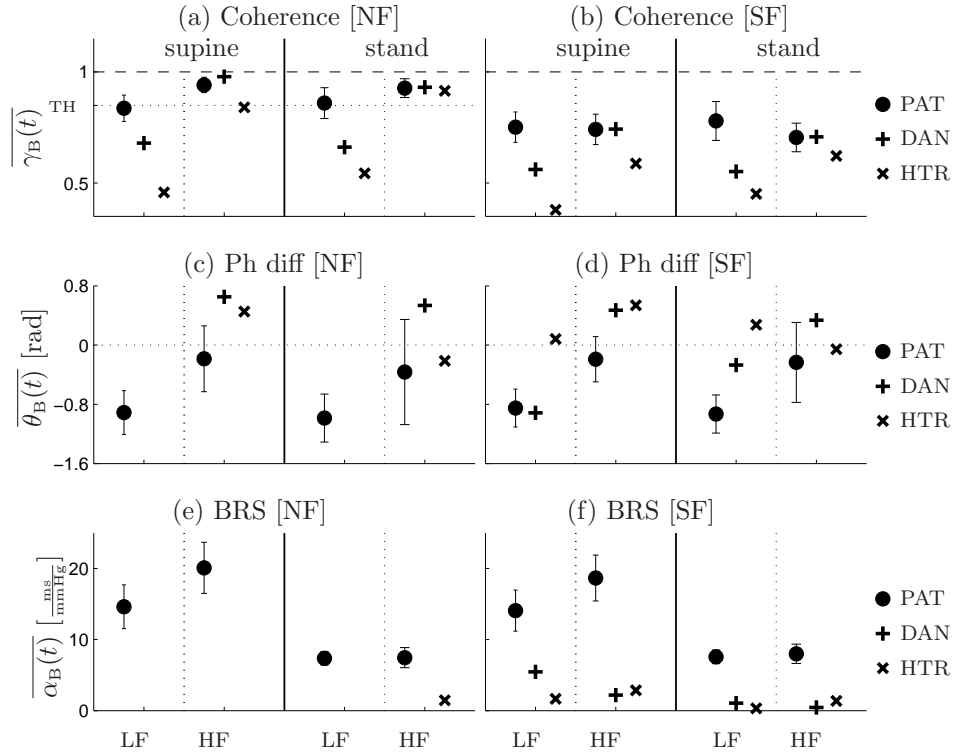
Figure 8.6: Eurobavar data set. On the left, the results obtained by the presented non-stationary framework (NF). On the right, the results obtained by the stationary framework (SF). Markers + and × represent diabetic patient with cardiac autonomic neuropathy (DAN) and heart transplanted patient (HTR), respectively. Circles represent the rest of patients (PAT). (a)–(b) mean ± standard deviation of coherence across subjects; (c)–(d) mean ± standard deviation of phase difference across subjects; (e)–(f) mean± standard error of BRS across subjects.

8.5 Discussion

8.5.1 The cross time-frequency framework

The main purpose of the presented framework is to propose a methodology for the characterization of the dynamic interactions between RRV and SAPV, which accounts for the intrinsic non-stationarity of the cardiovascular system, and which includes the assessment of both the strength and the prevalent direction of the coupling.
The analysis is composed of the following steps:

(i) Choice of the parameters of the kernel of type (8.12) for the estimation of the SPWVD. Among those kernels that can be used in coherence analysis, the one that gives the more appropriate TF resolution should be used (see Fig. 8.1).

(ii) Estimation of the TF power, coherence, and phase difference spectra.

(iii) Localization of specific TF regions from which the indices that describe the cardiovascular interactions are extracted.

(iv) Estimation of indices that quantify the strength of the local coupling, $\gamma_{\mathrm{B}}(t)$, the degree of synchronization, $\theta_{\mathrm{B}}(t)$, the latencies, $\mathcal{D}_{\mathrm{B}}(t)$, and the baroreflex sensitivity, $\alpha_{\mathrm{B}}(t)$.

The advantage of the SPWVD over other TF distributions, such as wavelet and spectrogram, is that it offers the possibility of determining the shape of the smoothing function both in time and frequency, which in turn allows for more accurate localization of cardiovascular dynamics [205]. The quantification of the TF resolution of the SPWVD by $\Delta_{\mathrm{t}}^{\mathrm{m}}$ and $\Delta_{\mathrm{f}}^{\mathrm{m}}$, which is crucial to correctly interpret the results, can also be used to compare the resolution of the SPWVD with that of other types of distributions. However, a comparative analysis goes beyond the scope of this study.
The analysis of the phase differences between $x_{\mathrm{RRV}}(t)$ and $x_{\mathrm{SAPV}}(t)$ is used to infer the prevalent causal direction of the coupling and the time delay, which characterize the system. In turn, the assessment of the prevalent causal direction is necessary to accept the hypothesis of the involvement of the baroreflex in the observed changes. Such a sensitive issue requires robust and accurate estimates. In our framework, robustness and accuracy are ensured by the fact that phase differences are estimated only in TF regions where the local coupling is statistically significant. These regions have a relatively small frequency width, $\Delta_{\mathrm{f}}^{\mathrm{m}}$, and a further control over their size is done by the opening, which discards very small portions of the TF domain from $\Omega_{\mathrm{B}}^{(\theta)}$.
Despite the great number of methodologies proposed for the assessment of the baroreflex, only a few combine non-stationary processing, statistical coherence analysis and assessment of the prevalent causal direction of local coupling. In this methodology, the interactions between the TF structure of the signals are characterized without imposing any assumption or model to the signals. Furthermore, neither coefficient identification nor parameter initialization is needed. Although the linear synchronization indices used in this framework give a rather basic description of the interaction between complex systems [255], they have a clear physical interpretation: $\gamma(t, f)$ quantifies the strength of the local coupling, thus allowing to localize TF regions where signals share approximately the same instantaneous frequency, while $\Theta(t, f)$ quantifies the phase differences, thus allowing to estimate the time delays between changes in the spectral

components of two signals, and determine, in specific TF regions, which signal is leading which.

The SPWVD, whose main property is the independent TF filtering giving high resolution, has never been used to estimate the baroreflex sensitivity as well as the phase differences between cardiovascular signals. Recently, other methods for the estimation of phase differences in the joint TF domain, based on Rihaczek [11], wavelet [66, 153], and reduced interference [235] transforms have been proposed. Contrary to synchronization indices based on the Hilbert transform [198], the presented methodology offers the possibility of separately assessing the degree of synchronization between LF and HF spectral components. Concerning the estimation of TF coherence by SPWVD, the most important issue is the definition of a kernel that completely suppresses the interference terms inherent to the Wigner-Ville distribution. A sufficient smoothing would ensure both positivity of the spectra and boundness of the TF coherence [181]. Kernels of type (8.12) have been shown to provide such a smoothing and have been recently used in cross TF analysis of cardiovascular signals [100, 209, 205].

The results of the simulation study show that this framework is robust and accurate, and are consistent with those obtained in other studies that aimed at assessing the use of the SPWVD in cross TF analysis [205, 206, 207].

To provide a more comprehensive characterization of the cardiovascular interactions, other important physiological parameters, such as respiration, may be included in further studies.

8.5.2   Response to head-up tilt

Mechanisms regulating the cardiovascular response to passive head-up tilt are predominantly studied [168, 71, 167, 194, 250, 219, 198]. Our results show that the local coupling between RRV and SAPV is statistically significant both in LF and HF during most part of the test, even at rest in supine position. During the position changes, the level of coherence abruptly decreased. The time taken by the signals to resynchronize, i.e. to restore significant level of coherence, characterizes the temporal pattern of response of the short-term cardiovascular regulation to an external perturbation.

The results shown that in LF range, SAPV led RRV during the entire test. In HF range, SAPV led RRV only during head-up tilt. These results are in line with those observed in other studies [71, 194, 219].

Owing to the periodicity of the phase differences, it may be possible that instead of occurring that in LF range, $x_{\mathrm{SAPV}}(t)$ was leading $x_{\mathrm{RRV}}(t)$ with $|\theta_{\mathrm{LF}}(t)| \approx 0.6$ rad, $x_{\mathrm{RRV}}(t)$ was actually leading $x_{\mathrm{SAPV}}(t)$ with $|\theta_{\mathrm{LF}}(t)| \approx 5.7$ rad. However, this last possibility, which would imply, for $f_{\mathrm{LF}} = 0.09$ Hz, a time delay of about 10 s, is unlikely, not only because it largely exceeds the range of baroreflex latency ([0.24, 3] s) [71], but also because in this non-stationary framework, such a time delay (close to $\Delta_{\mathrm{t}}^{\mathrm{m}}$) would not be consistent with the level of local coupling as high as $\gamma_{\mathrm{LF}}(t) \approx 0.99$.

The time-course of the baroreflex sensitivity, $\alpha_{\mathrm{B}}(t)$ followed similar patterns both in $\Omega_{\mathrm{LF}}^{(\alpha)}$ and $\Omega_{\mathrm{HF}}^{(\alpha)}$ ranges. In supine position, the high variability of $\alpha_{\mathrm{HF}}(t)$ was due to the fact that it was estimated in few subjects, because in most of them $\theta_{\mathrm{HF}}(t) > 0$. As expected, the baroreflex sensitivity was higher during supine position and lower during

head-up tilt. During the position changes, index $\alpha_{\mathrm{B}}(t)$ was characterized by two different dynamics: When subjects were passively moved from supine to standing position, $\alpha_{\mathrm{B}}(t)$ decreased in few seconds, while when subjects were moved from standing to supine position $\alpha_{\mathrm{B}}(t)$ increased gradually. These different temporal patterns may reflect regulatory mechanisms that act faster in potentially more dangerous situations, such as passive head-up tilt, and slower in less potentially dangerous situations, as coming back to supine position. Similar to what observed in ECG analysis, where the dynamics of the ventricular rate adaptation have been recently shown to have clinical relevance [220], the characterization of these kinds of temporal patterns in a larger study population could allow gaining some insight into cardiovascular dynamics.

8.5.3 Eurobavar data set

The study of the Eurobavar data set showed that:

(i) Non-stationary signal processing should be preferred to study the biomedical signals even when they are acquired in conditions that are usually assumed as stationary;

(ii) The proposed framework can be considered as an improved TF generalization of traditional spectral methods of analysis.

It is widely accepted that biomedical signals are intrinsically non-stationary. The outcomes of the test proposed in [51] confirm that the hypothesis of stationarity is often rejected even for signals during rest. Moreover, it was shown that signals were more likely considered non-stationary for a temporal scale of about 1–2 min. This highlights the importance of methodology characterized by fine temporal resolution.

To compare the results provided by the presented methodology with those obtained by traditional time-invariant ones, we used the results obtained by marginalizing the TF representations given by SPWVD as reference. The results given by this stationary framework are within the variability of those obtained with different techniques of time-invariant analysis [155]. Although the mean results obtained by the presented non-stationary framework are different, they are in line with those obtained by the stationary framework and with those observed in [155]. Our results show that in the diabetic subject with neuropathy and in the short-term transplanted patient, the baroreflex is not active. This implies a lack of coupling in LF range and a causal direction from RRV to SAPV in HF range. These results are in agreement with those observed in [219], and show that the presented methodology correctly detects impairments of the baroreflex.

8.5.4 Further considerations on cross TF analysis of cardiovascular signals

In the cross TF analysis, the processing that leads to the estimation of the RRV and SAPV signals, $x_{\mathrm{RRV}}(t)$ and $x_{\mathrm{SAPV}}(t)$, is of crucial importance because it affects the estimation of the phase differences and latencies between them. For instance, it is

worth noting that the results obtained by analyzing the RRV and SAPV cannot be directly extended to the interactions between the heart rate variability and SAPV signals, because the phase differences between $x(t)$ and $y(t)$ are not equal to those between $x(t)$ and $1/y(t)$ (see §5.2.4).

Furthermore, in the estimation of the RRV signal, two issues should be carefully taken into account:

(i) The choice of the representations of the RRV signal, which can be based on the interpolation of the RR intervals, as done in this study, or on some other model [29, 63, 179, 238].

(ii) The arbitrary assignation of a given heart period interval to a given temporal instant. The physiological phenomena that determine the duration of $t_{n+1}^{QRS} - t_n^{QRS}$ do not occur at time t_n^{QRS} neither at t_{n+1}^{QRS}, but they may be seen as continuous phenomena that are characterized based on information sampled at t_n^{QRS} and t_{n+1}^{QRS}. In this study, we used a non-causal representation of the heart period, i.e. we associated $(t_{n+1}^{QRS} - t_n^{QRS})$ with t_n^{QRS}, to be in line with analogous studies [155]. If we had used a causal representation of the heart period [238], we would have obtained more negative phase differences between the spectral components of the signals, which, in T_{es} and T_{ls} of the tilt table test may have allowed the estimation of $\alpha_{HF}(t)$ for more subjects and longer intervals.

The estimation of the SAPV signal can also affect its degree of synchronization with the RRV signal. The main issue is the place where the arterial pressure is measured and the inclusion of the pulse transit time (PTT) in the estimation of the latencies [100]. Even in the ideal case in which changes in the SAPV and RRV are simultaneous, if the arterial pressure is measured in the finger and RR in correspondence of the heart beat, we would observe a delay related to the PTT.

These technical issues, which neither affect the relative changes of the indices nor the power estimates or the measures derived from them, should be carefully taken into account in the physiological interpretation of the phase differences and latencies.

Part III

Conclusions

Chapter 9

Conclusions

9.1   Methodologies

Synthesis of HRV signals characterized by predetermined time-frequency structure by means of time-varying ARMA models (Chapter §2)

In this chapter, we presented two methodologies to generate real-like HRV signals characterized by controlled time-frequency structure to be used to assess different methods of non-stationary HRV analysis.

In the frameworks, the synthesized signals are stochastic processes whose time-frequency structure is predetermined by choosing either the time-course of the instantaneous frequencies and powers or the shape of the time-frequency model function. The presented methodologies consist of three steps: (a) Choice of the desired time-frequency structure of the signals by choosing a set of design parameters; (b) Automatic identification of the parameters of the corresponding time-varying ARMA models via simple closed-form expressions; (c) Synthesis of the desired stochastic signals.

Two measures to evaluate the goodness of the simulated signals are also given. Using this framework we were able to model the wide range of non-stationarities observed in heart rate modulation during exercise stress testing and experiments of music-induced emotions.

Characterization of HRV signals by time-frequency analysis (Chapter §3)

In this chapter, we first described the Cohen's class, the central role of the Wigner-Ville distribution and the kernel functions. We described three equivalent way to estimate a distribution of the Cohen's class: (i) as the convolution between the Wigner-Ville distribution and a time-frequency kernel; (ii) as the Fourier transform of the non-stationary autocorrelation function weighted by a time-lag kernel function; (iii) as the double Fourier transform of the product between the ambiguity function and a Doppler-lag kernel function.

We described the geometry of the interference terms and we pointed out the importance of the kernel design to eliminate them. Importantly, we introduced two measures to quantify the time-frequency resolution of any time-frequency representation. These measures, i.e. Δ^{m} and $\Delta^{\mathrm{a\%}}$, are necessary to give a correct interpretation of the results of time-frequency analysis and are usefull to compare the performance of different distributions. Therefore, these measures are used trhroughout the entire manuscript.

We introduced the SPWVD and we carried out a simulation study, based on the methodology proposed in §2, to assessed its capability to quantify heart rate variability patterns. We observed that the SPWVD followed the temporal evolution of the spectral components even when sudden and sharp transitions occur.

Then we described a method that performs a parametric decomposition of the smoothed non-stationary autocorrelation function. This methodology can be considered as the combination of parametric and non-parametric analysis and is used in §6 to estimate the time-course of spectral indices.

Characterization of dynamic interactions between cardiovascular signals by time-frequency coherence analysis (Chapter §4)

An assessment of the dynamic interactions between cardiovascular signals can provide valuable information to improve the understanding of cardiovascular control. In this chapter, we described different methodologies for the characterization of time-frequency coherence between cardiovascular signals. These methodologies are based on the SPWVD and multitaper spectrogram (MTSP), and include the automatic assessment of the significance level of coherence estimates.

Two methods were proposed to estimate coherence by SPWVD. In the first one, the straightforward scheme described in §4.3.1, the most appropriate kernel function is empirically chosen among those that provide meaningful coherence estimates over the entire time-frequency domain. In the second one, the geometrical scheme described in §4.3.2, the most appropriate kernel function is estimated based on geometrical relations between the TF structure of the signals and the interference terms. In a simulation study (see §4.3.3), we assessed the estimation error of coherence estimated obtained by geometrical scheme, and we found that the bias was low (< 0.05) for coherence level higher than 0.5, and the standard deviation was always lower than 0.025.

In a comparative study, which includes SPWVD, MTSP and also wavelet transform, we assessed the capability to correctly localize TF regions where signals are locally coupled (see §4.6). In the comparison, both computer-generated data and data from healthy volunteers were used. The SPWVD allows for the localization of these regions with higher accuracy (AC>96.9% for SNR$\geq$5 dB) than the MTSP (AC>84.4% for SNR$\geq$5 dB). For comparison, in fourteen healthy subjects, time-frequecy coherence analysis by SPWVD and MTSP was used to describe the changes that a tilt table test provokes in the cardiovascular control.

By using both computer-generated and recorded physiological data, changes in the local coupling were better localized by SPWVD than MTSP. Moreover, SPWVD used in coherence analysis was shown to be characterized by a better resolution than wavelet

transform previously used in coherence analysis. This is due to the same structural reason which makes the SPWVD more suitable than the spectrogram and wavelet transform for the localization of TF features, namely, the possibility of independently setting the time and frequency filtering. However, in §4.7, some features of the MTSP that could make it useful in coherence analysis were also pointed out.

Characterization of dynamic interactions between cardiovascular signals by time-frequency phase difference analysis (Chapter §5)

In this chapter, cross time-frequency analysis was used to estimate the phase differences, the time delay and the phase locking between cardiovascular signals. Phase differences and time delay give a measure of the changes in the synchronization between two oscillations, while phase locking measures the degree of similarity of these changes across subjects. The presented methodology is based on the SPWVD and includes time-frequency coherence analysis.

Analytical expressions of phase difference and time delay estimates are given for time-varying chirps.

Different simulation studies was carried out to assess the performance of the estimators described in this chapter. In a first simulation study involving highly non-stationary synthetic signals, this methodology provided accurate estimates of the temporal changes of the phase differences, with an error characterized by interquartile ranges lower than 2% and 9% for SNR equal to 20 dB and 0 dB, respectively. A comparative study showed that the proposed estimator outperformed an estimator based on the integration of the difference between the instantaneous frequency of each spectral component. In another simulation study, based on recorded physiological data, similar estimation errors were estimated, while the comparison with the estimator based on the integration of the difference between the instantaneous frequency of each spectral component showed that the latter did not give reliable estimates, thus pointing out the usefulness of our time-frequency framework to analyze physiological data.

In the last simulation study, it was shown that in highly non-stationary signals the presented methodology reliably followed abrupt time delay changes, with a time of adaptation lower than 10 s.

9.2 Physiological studies

Dynamic assessment of the autonomic response to music-induced emotions characterized by same valence (Chapter §6)

In this study we proposed a comprehensive methodology for the assessment of the time-course of physiological indices related to musical stimuli. The method, which includes the parametric decomposition of the Wigner-Ville distribution presented in §3.3, is shown to provide a reliable characterization of the autonomic response, by

identifying common trends and by assessing the different dynamics induced by listening to music. The experimental results revealed the transient nature of music-related patterns and they highlighted the importance of an approach based on time-frequency analysis.

All kinds of stimuli provoked significant changes compared to the resting (silent) condition, while during listening to pleasant music the heart and respiratory rates were higher (for more than 80% of stimulus duration, $p < 10^{-5}$) and the power of HF modulation was lower (for more than 70% of stimulus duration, $p < 0.05$) than during listening to unpleasant stimuli. The identification of common trends which depend on specific stimuli suggests the need for further studies on the dynamic relationship between musical and autonomic features to improve the potential use of music in therapeutic applications.

In a subgroup of 58 subjects, cross time-frequency analysis described throughout §4–§5, was used to assess the influence of music on the cardio-respiratory coupling. It was shown that the coherence between respiration and heart rate variability increased during every condition and decreased during the interval in between two conditions. This could be due to a sympathetic activation during the auto-evaluation task or due to the waiting of the next musical excerpt. The analysis of phase difference and time delay showed that respiration drove the respiratory sinus arrhythmia with a latency of about 100 ms. The median time course of the time delay was slightly lower during the listening of pleasant music than during the other conditions, probably due to higher respiratory rate.

Time-frequency comparison between HRV and PRV from the PPG signal (Chapter §7)

In this chapter, we used the methodology presented in §3–4 to compare the time-frequency structure of heart rate variability and pulse rate variability (PRV) derived from the photoplethysmographic signal. The aim of the study was to assess whether PRV could be used as a surrogate for HRV.

Classical indices of time-invariant analysis derived from PRV presented similar values to the indices derived from HRV, with no statistically significant differences between them, and strong linear correlation ($\rho_{\mathcal{I}} > 0.97$). These results were in agreement with previous works that suggested that PRV could be used as an alternative measurement of HRV during stationary conditions.

A comparison of time-varying analysis based on the SPWVD was carried out in order to evaluate the usefulness of PRV as a surrogate measurement of HRV during non-stationary conditions. We observed that: (i) Instantaneous power content estimated from HRV and PRV were highly correlated (0.98 ± 0.04 and 0.95 ± 0.06 for LF and HF bands respectively); (ii) Differences between the power content estimated from HRV and PRV were small ($\overline{\delta_{\mathrm{B}}(k,t)} < 10^{-3} \ s^{-2}$); (iii) The time-frequency spectra of both signals were highly correlated (0.99 ± 0.01); (iv) Time-frequency coherence in LF and HF bands was high (0.97 ± 0.04 and 0.89 ± 0.08, respectively); (v) The physiological analysis to evaluate the autonomic modulation changes of heart rate during tilt table test showed that the same conclusions could be inferred from HRV and PRV analysis.

Our results indicated that there were some small differences in the time-varying spectral indices extracted from HRV and PRV, mainly in the respiratory band. Nevertheless, these differences were sufficiently small to suggest the use of the PRV signal as an alternative measurement of HRV signal during non-stationary conditions, at least during tilt table test. Finally, we pointed out that these differences are related to the PTT variability.

Characterization of the dynamic interactions between heart rate and arterial pressure by cross time-frequency analysis (Chapter §8)

In this chapter, we adjust the methodologies presented in §4–§5 to the analysis of the dynamic interactions between the R–R variability (RRV) and the systolic arterial pressure variability (SAPV). The methodology accounts for the intrinsic non-stationarity of the cardiovascular system and includes the assessment of both strength and prevalent direction of the local coupling. The SPWVD distribution was used to estimate the time-frequency power, coherence and phase difference spectra with fine time-frequency resolution. The interactions between the low and high frequency (LF and HF) spectral components of the signals are quantified by time-varying indices, including the local coupling, phase differences, time delay and baroreflex sensitivity (BRS). Every index is extracted from a specific time-frequency region, localized by combining information from the different spectra.

In 14 healthy subjects, head up tilt provoked an abrupt decrease in the cardiovascular coupling; a rapid change in the phase difference (from 0.37 ± 0.23 to -0.27 ± 0.22 rad) and time delay (from 0.26 ± 0.14 to -0.16 ± 0.16 s) in the high frequency (HF) band; and a decrease in the BRS (from 23.72 ± 7.66 to 6.92 ± 2.51 ms/mmHg). In the LF range, during head up tilt, restoration of baseline level of cardiovascular coupling took about 2 min, and SAPV preceded RRV of about 0.85 s during all the test.

The analysis of the Eurobavar data set showed that the presented methodology represents an improved TF generalization of traditional time-invariant methodologies and can reveal baroreflex impairment.

Additionally, we applied a framework to statistically quantify the degree of non-stationarity of the signals studied in this chapter, and the results suggested the use of non-stationary signal processing techniques also to analyze signals recorded in conditions that are usually supposed to be stationary.

Chapter 10

Future extensions

In this manuscript, a relative large number of topics which may be used as starting point for further analysis has been described. In the following, for each one of the main topics of the thesis, a short list of possible future extensions is given.

10.1 Methodological studies

Time-frequency synthesis of real-like cardiovascular signals

In §2 we propose a procedure to generate non-stationary random processes with predetermined spectral features, such as instantaneous central frequencies, amplitudes and powers. It would be interesting to extend this procedure to multivariate analysis. In a bivariate model, pairs of non-stationary random processes with predetermined cross-spectral features can be generated. This may allow one to test algorithms for TF coherence and TF phase difference estimation in a controlled stochastic framework. To this end, one can write the analytical expressions of cross transfer functions and coherence in terms of poles and zeros, determine the relationship between pole location and coherence level and modify the pole configuration of the system to generate signals related by predetermined interactions. Another useful application of such a procedure, is the validation of algorithms for causal analysis [87, 194, 14], which have been often tested using very simple models.

Cross time-frequency analysis of cardiovascular signals

- Signal-dependent optimal kernel for coherence analysis: Time-frequency analysis based on Cohen's class offers the possibility of improving the methodology described in §3–§5 in many different ways. For instance, the kernel used for TF coherence estimation (4.11) is a simplified version of a more flexible one [72], whose shape in the ambiguity function is not limited to ellipses. It would be interesting to determine for any particular signal the kernel shape that better represents its TF structure. In the Nineties, some interesting algorithms for signal-dependent optimal kernel design were proposed [25, 26]. This algorithms aim at adjusting the shape of a kernel by minimizing a cost function that represents the trade off between smoothing and given spectral properties of the

signals. Following this idea, in §4.3.2 we proposed a signal-dependent scheme to automatically determine the minimal degree of filtering which allows to obtain coherence estimates bounded between zero and one [206]. The main limitation of our algorithm was that the filtering in frequency direction was determined through a time-consuming iteration process. The determination of a procedure that, without need of an iteration process, automatically adjusts the degree of smoothing to the TF structure of the signals and that provides reliable coherence estimates, would represent a great improvement. Indeed, it would allow overcoming the main disadvantage of SPWVD coherence with respect to wavelet or MTSP, namely, that while wavelet and MTSP always provide reliable coherence estimates, SPWVD does not. As pointed out in §4.3.2, the key of the problem is the determination of geometrical relationships between the TF structure of the signals and the geometry of the kernel, especially in the ambiguity domain.

- Comparison with TVAR models: In §4 we perform a comparative study between TF coherence based on SPWVD, MTSP and continuous wavelet transform. Although many substantial differences exist between these distributions, they can all be seen as particular members of Cohen's class. A comparison with other non stationary methodologies widely used in cardiovascular analysis, such as recursive least squares AR models [165], can help to better asses the performance of the methodologies presented in this work.

- Reassignment of TF coherence: Another improvement in cross TF analysis may be made by extending TF reassignment to TF coherence. Reassignment is a technique that provides excellent localization of spectral components, by performing an a-posteriori compensation for the smoothing [9, 254]. The main issue is that reassignment is based on the assignment of the value of a TF function to another point, localized as the center of gravity of a specific function. Therefore, the extension of reassignment to cross spectra, which are complex functions, is not straightforward since it is not clear how to define the center of gravity of a complex function. Another problem is that reassignment yields noisy representations [254], that may reduce the reliability of coherence estimates.

- Multitaper SPWVD for coherence analysis: In §4.6, we showed that SPWVD coherence estimates were more accurate than MTSP estimates. Nevertheless, we also mentioned some interesting properties of MTSP. The application of a multitaper scheme on the SPWVD may results in a new TF coherence representation characterized by good TF resolution, as the SPWVD, and robustness, as MTSP. A possible way to design multitaper SPWVD would be to estimate the kernels associated to Hermite spectrogram, which are Laguerre functions (4.30), and to modify their shape in order to reduce their low-pass properties.

- Bivariate empirical mode decomposition: Bivariate empirical mode decomposition [224] is a recent technique that allows jointly decomposing a pair of signals in their intrinsic modes. A procedure which combines EMD and time-frequency analysis may offers the possibility of estimating TF representations which better localize the spectral features of the signals. Main steps of this procedure should comprise: estimation of intrinsic modes, TF analysis of the intrinsic modes of interest, recomposition of the entire TF spectrum of the signal. The advantage

194

of such a scheme is that intrinsic modes are monocomonent oscillations, and as such they are expected to be free from outer interference terms. This scheme could be also used in coherence analysis, where the issue of reducing interference terms is crucial.

- TF partial coherence: In this work, cross TF analysis was limited to non-stationary estimation of coherence and phase difference. In a multivariate analysis based on at least three signals, partial coherence can be used to estimate the coupling of two signals after having removed the influence that a third signal exerts over them [38]. To the extent of our knowledge, partial coherence has never been used in a TF framework. The definition of a TF partial coherence can be used to simultaneously studying the dynamic interactions between arterial pressure, heart rate and respiration, whose relationships are still largely unclear.

Finally, it is worth mentioning that the main limitation of multivariate analysis based on cross-spectral identification is the assumption of an implicit open loop model for the system. This implies that, although causal information may be inferred, to a certain degree, by phase difference estimation, cross TF analysis is not able to describe feedback and feedforward pathways of closed loops separately, neither to discriminate between direct and indirect interactions. The definition of a methodology to identify TF transfer functions to perform non-parametric multivariate analysis would pave the road to new methodology for assessing causality and directionality.

10.2 Physiological applications

- Further study RSA during music-induced emotions: In §6 we showed that musical stimuli characterized by different emotional valence provoked different patterns of response in HRV and respiration. In particular, respiratory frequency and RSA amplitude were the most sensitive physiological parameters to music. Although we did not observe differences in coherence and phase difference between the experimental conditions, it would be interesting to further study cardio-respiratory interactions. Pattern analysis [236, 246] is a recent methodology used to explore the changes of RSA during the different phases of the respiratory cycle. Main advantage of this technique is that it allows capturing non-linear patterns contained in the morphology of RSA. The limitation is that it requires stationarity and controlled breathing. Time-frequency analysis may be used to extend this methodology to non-stationary conditions, thus allowing the tracking of RSA changes in spontaneous breathing under music influence. Additionally, it would be interesting to use cross TF analysis to characterize changes also in other cardiovascular variables, such as blood pressure or skin conductance, as well as to find dynamic correlations between the TF structure of the musical excerpts and physiological rhythms [39, 40].
- Photoplethysmographic signal: In §7 we showed that a strict correlation exists between HRV and pulse rate variability estimated from the photoplethysmo-

graphic (PPG) signal. Given that HRV is known to contain an oscillation synchronous with respiration, TF analysis could be used to estimate the respiratory frequency from the PPG signal. Furthermore, it is known that respiration also modulates the amplitude of the PPG signal. Thus, one can design an algorithm that combines respiratory influences on pulse rate and pulse amplitude variability to improve the estimation of the respiratory rate. In particular, coherence analysis can be used to localize TF regions where both modulations are simultaneously present. From this regions, robust estimates of respiratory frequency could be extracted.

- Pulse transit time: In §7, we introduced the pulse transit time (PTT) signal, which measures the time it takes the pulse wave to travel from the heart to the periphery. PTT was shown to provide valuable information about cardiovascular control. The possibility of extracting from PTT variability indices correlated to blood pressure variability is actually matter of debate. A characterization of the dynamic interactions between PTT and the other principal cardiovascular signals, such as HRV, systolic and diastolic blood pressure, and respiration can help to determine how much PTT correlates with any of these important parameters. In particular, if strong correlations were observed, PTT variability may be used as indirect measurement of its correlated signals. On the other hand, if no correlations were found, then it can be speculated that PTT variability carries new valuable information about cardiovascular dynamics.

- In §8, we described an example of application of cross TF analysis to the study of cardiovascular regulation during tilt table test. Cross TF analysis was used to characterize dynamic interactions between RRV and SAPV. Owing to the primary influence that respiration has on cardiovascular variability, it should be included in the analysis.

As a final consideration, it is important to note that the applications shown in this study mostly aim at characterizing dynamic interactions. A characterization is necessary since, as already said at the very beginning of this manuscript, it helps us to elucidate how the system works, when it works, and what may go wrong when it does not. As a next step, we should focus on the identification of those situations in which the system does not work. In other words, indices extracted from TF analysis should be applied to detect dysfunctions of the system. In the most part of the cases, time-frequency and time-varying analysis is finally used as if it was stationary: the time-course of given physiological indices is averaged and mean values from different populations are compared. This is equivalent to discard much of the non-stationary information, which is coded in the "morphology" of the time-course, and that may have clinical relevance. To fully exploit the potential of non-stationary analysis, further studies should focus on the extraction of indices from the time course of physiological indices, which should capture the information carried by transients, shapes, irregularities, etc., of the time-courses. This kind of analysis of the time course of the indices estimated by (cross) time-frequency representations may help one to move from the characterization of the functioning of the system to the detection of its dysfunctions.

Part IV

Appendix

Appendix A

The ANS-UZ data base

In different parts of this dissertation, we used physiological recorded data from a tilt table test. In this Annex, we briefly describe the data base. Data were collected by Dr. Ana Mincholé in 2009 at the Centro Politecnico Sueprior, in Zaragoza, Spain.
The data base consists of 17 healthy subjects aged 28.5 ± 2.8 years. Among the participants, 11 were male and 6 female.
The tilt table protocol consisted in:

- Early supine position (T_{es}): 4 min.

- Head up tilt position (T_{ht}): 5 min.

- Later supine position (T_{ls}): 4 min.

The automatic table took about 18 s to move from the early supine position to head up tilt and to move back from head up tilt to later supine position. This protocol is also illustrated in the graphic of Fig. 7.1.
The recorded signals include:

- 12-lead ECG (sampling frequency 1000 Hz), acquired by means of Biopac MP150 system.

- Blood pressure measured in the finger (sampling frequency 250 Hz), acquired by means of Finometer system. During the procedure, the Finometer® was recalibrated at the beginning of T_{ht} and T_{ls}. The recalibration took few seconds and introduced artefacts which were detected and corrected by interpolation. Arterial pressure from the finger was not corrected for the hydrostatic gradient change during tilt.

- Respiratory signal (sampling frequency 125 Hz), acquared by TSD201 transducer that measure thoracic expansion and contraction while breathing.

- Pulse photoplethysmography signal (sampling frequency 250 Hz), recorded from the index finger using the Biopacs OXI100C amplifier with the TSD123 transducer.

In the following, we briefly describe the instruments used in the recording of the data base.
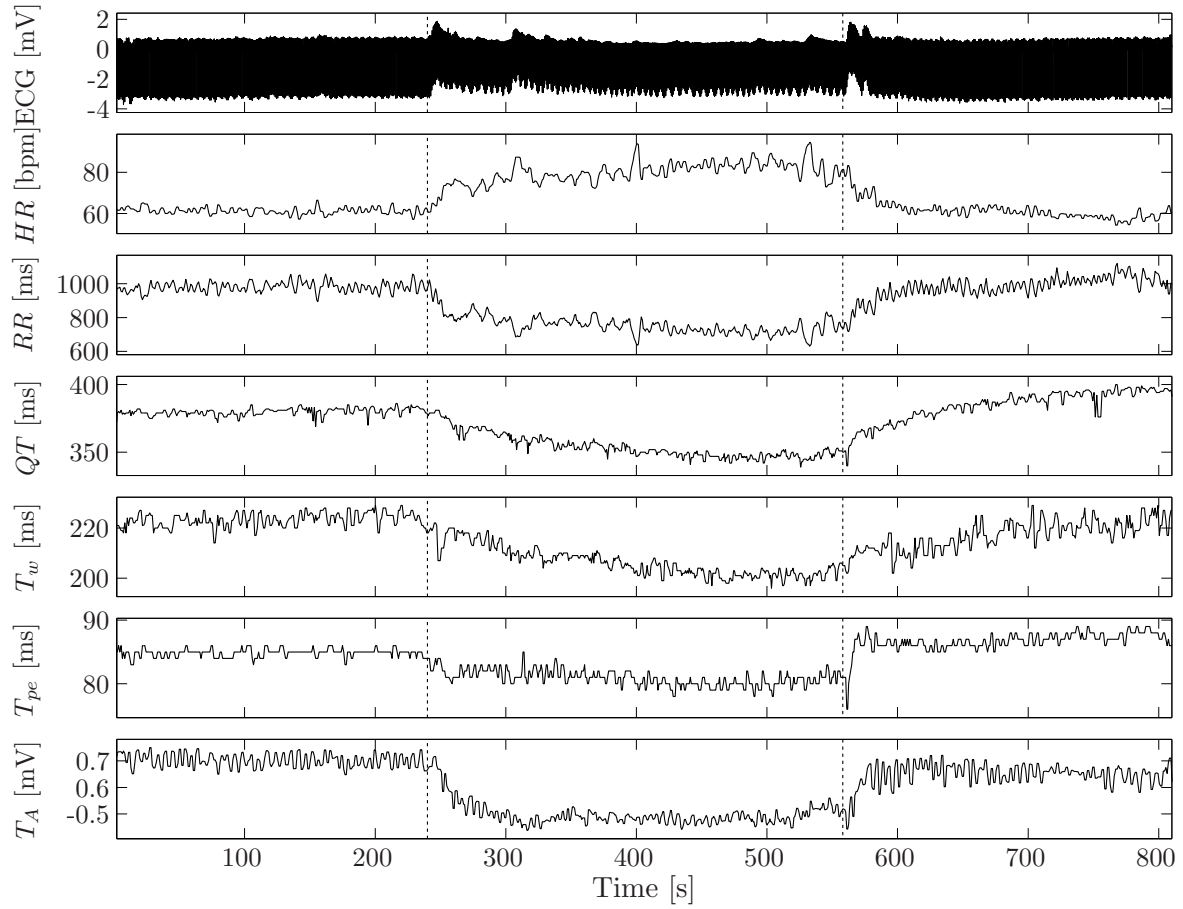
Figure A.1: Example of different repolarization intervals and an ECG lead during the tilt test.

Biopac MP150

In order to record and acquire several biomedical signals, we have used the Biopac MP150 data acquisition and analysis system which consists of the following units:

- MP150 acquisition system: It connects up to sixteen analog input channels plus two analog output channels, sixteen digital leads and a synchronization input. It consists of a dual analog-digital converter (ADC) of 16 bits and maximum sampling frequency of 400 kHz for each channel.

- Universal Interface module UIM100C: It is used to connect 100-series amplifier modules and signal cables to the acquisition module MP150. The UIM100C also provides a direct link to the analog and digital I/O lines of the MP device when collecting or sending data to external equipment.

- Amplifiers: The amplifiers can be of general purpose as the DA100C to amplify different type of signals or specific for an specific type of signal. In our case we have use the specific amplifiers ECG100C (ECG signals), RSP100C (respiratory signal) and OXI100C (photoplethysmographic (PPG) signal). Also, we have used the transducer TSD160A to monitor differential pressure that is connected to the amplifier DA100C.

- Sensors and transducers: we have used different sensors or transducers that monitor biomedical signals, such as disposable Ag-AgCl to measure potential over the body surface, TSD201 transducer to measure abdominal or thoracic expansion and contraction while breathing, TSD160A to monitor differential pressure, and photoelectric pulse transducer TSD123 to measure changes in infrared reflectance resulting from varying blood flow.

Biopac MP150 allows us to acquire standard 12-lead ECG using the Biopacs ECG100C amplifier and disposable Ag-AgCl electrodes with a hardware amplification of 1000. Besides, allows to synchronize external analog signals such as the blood pressure signal acquired from the Finometer device.

Finometer

This device measures the blood pressure in a continuous way and non invasively by the volume-clamp method, first introduced by Czech physiologist Peñaz in 1967. With this method, finger arterial pressure is measured using a finger cuff and an inflatable bladder in combination with an infrared plethysmograph, which consists of an infrared light source and detector. The infrared light is absorbed by the blood, and the pulsation of arterial diameter during a heart beat causes a pulsation in the light detector signal.

The first step in this method is determining the proper unloaded diameter of the finger arteries, the point at which finger cuff pressure and intra-arterial pressure are equal and at which the transmural pressure across the finger arterial walls is zero. Then the arteries are clamped (kept at this unloaded diameter) by varying the pressure of the finger cuff inflatable bladder using the fast cuff pressure control system.

A servo-controller system usually defines a target value or setpoint and a measured value that is compared with this setpoint. In the servo-controller the setpoint is the signal of the plethysmograph (unloaded diameter of the arteries) that must be clamped. The measured value comes from the light detector. The amplified difference between the setpoint and measured value, the error signal, is used to control a fast pneumatic proportional valve in the frontend unit. This proportional valve modulates the air pressure generated by the air compressor, thus causing changes in the finger cuff pressure in parallel with intra-arterial pressure in the finger so as to dynamically unload the arterial walls in the finger. The cuff pressure thus provides an indirect measure of intra-arterial pressure. The device has also a height sensor to account for the difference in pressure between the heart and the finger due to the different altitudes. From these measurements, the device is able to reconstruct the arterial blood pressure. The device is connected to a PC by a parallel port, or by four analog inputs and four analog outputs to record the different signals in a synchronized way.

Finometer works with a sampling frequency of 200 Hz, quantification of 12 bits and resolution of 0.25 mmHg/LSB. Digitalized signal is converted into an analog in the device and gets into an analog input to the interface UIM100C to be resampled and digitalized by the MP150 (with a sampling frequency of 250 Hz and 16 bits of quantification). As a consequence, this blood pressure signal is delayed 5 seconds (introduced by the DAC of the Finometer) with respect of the other signals acquired directly in the Biopac MP150.

Appendix B

Scientific contributions

The methodologies and results presented in this dissertation and elaborated during my PhD studies have been partially published in the following works:

International Journals

(i) <u>M. Orini</u>, R. Bailón, R. Enk, S. Koelsch, L.T. Mainardi, P. Laguna: A method for continuously assessing the autonomic response to music-induced emotions through hrv analysis. Med Biol Eng Comput **48**(5), 423–433 (2010)

(ii) <u>M. Orini</u>, R. Bailón, E. Gil, L.T. Minardi, P. Laguna: Framework for continuous quantification of spectral coherence using quadratic time-frequency distributions: exploring cardiovascular coupling. International Journal of Bioelectromagnetism[1] **12**, 177–182 (2010)

(iii) <u>M. Orini</u>, R. Bailón, L.T. Mainardi, P. Laguna and P. Flandrin: Characterization of the dynamic interactions between cardiovascular signals by time–frequency coherence. IEEE Trans Biomed Eng. (In Press)

(iv) <u>M. Orini</u>, P. Laguna, L.T. Mainardi and R. Bailón: Assessment of the dynamic interactions between heart rate and arterial pressure by cross time-frequency analysis Physiol. Meas. (In Press)

(v) <u>M. Orini</u>, R. Bailon, L.T. Mainardi, P. Laguna: Synthesis of non stationary HRV signals following predetermined spectral patterns by means of time–varying ARMA models. Biomedical Signal Processing & Control (In Press)

(vi) E. Gil, <u>M. Orini</u>, R. Bailón, J.M. Vergara, L.T. Mainardi, P. Laguna: Photoplethysmography pulse rate variability as a surrogate measurement of heart rate variability during non-stationary conditions. Physiological Measurement **31**(9), 1271 (2010).

(vii) R. Bailón, L.T. Mainardi, <u>M. Orini</u>, L. Srnmo, P. Laguna: Analysis of heart rate variability during exercise stress testing using respiratory information. Biomedical Signal Processing & Control **5**(4), 299 – 310(2010)

---

[1] International Journal of Bioelectromagnetism is not in journal citation reports (JCR)

(viii) R. Bailón, G. Laouini, C. Grao, <u>M. Orini</u>, P. Laguna, O. Meste: The integral pulse frequency modulation model with time-varying threshold: Application to heart rate variability analysis during exercise stress testing. IEEE Trans Biomed Eng. **58**(3), 642 – 652 (2011).

International conferences

(i) <u>M. Orini</u>, R. Bailón, P. Laguna, L.T. Mainardi: Modeling and estimation of time-varying heart rate variability during stress test by parametric and non parametric analysis. Computers in Cardiology, pp. 29–32 (2007)

(ii) <u>M. Orini</u>, B.F. Giraldo, R. Bailón, M. Vallverdu, L.T. Mainardi, S. Benito, I. Diaz, P. Caminal: Time-frequency analysis of cardiac and respiratory parameters for the prediction of ventilator weaning. 30nd Annual International Conference of the IEEE EMBS. pp. 2793–2796 (2008)

(iii) <u>M. Orini</u>, R. Bailón, L.T. Mainardi, A. Mincholé, P. Laguna: Continuous quantification of spectral coherence using quadratic time-frequency distributions: error analysis and application. Computers in Cardiology (2009)

(iv) <u>M. Orini</u>, R. Bailón, E. Gil, L.T. Mainardi, P. Laguna: Framework for continuous quantification of spectral coherence using quadratic time-frequency distributions: exploring cardiovascular coupling. Internat Conf Biosignal Interpretation (2009)

(v) <u>M. Orini</u>, L.T. Mainardi, E. Gil, P. Laguna, R. Bailón Luesma: Dynamic assessment of spontaneous baroreflex sensitivity by means of time-frequency analysis using either RR or pulse interval variability. 32nd Annual International Conference of the IEEE EMBS. pp. 1630–1633. (2010)

(vi) E. Gil, <u>M. Orini</u>, R. Bailón, J.M. Vergara, L.T. Mainardi, P. Laguna: Time-varying spectral analysis for comparison of hrv and ppg variability during tilt table test. 32nd Annual International Conference of the IEEE EMBS. pp. 3579–3582 (2010)

(vii) E. Gil, <u>M. Orini</u>, R. Bailón, P. Laguna, J.M. Vergara: Comparative analysis between ppg variability and hrv during non-stationary tilt table test. 6th Conference of the European Study Group on Cardiovascular Oscillations (2010)

(viii) E. Cirugeda, <u>M. Orini</u>, R. Bailón, P. Laguna: Respiratory frequency estimation from heart rate variability signals in non-stationary conditions based on the wigner–ville distribution. Computing in Cardiology (2010)

(ix) <u>M. Orini</u>, R. Bailón, L.T. Mainardi, P. Laguna: Time-frequency phase differences and phase locking to characterize dynamic interactions between cardiovascular signals 33nd Annual International Conference of the IEEE EMBS. pp. – (2011)

(x) <u>M. Orini</u>, M.D. Pelaez, R. Bailón, E. Gil: Estimation of the respiratory rate from photoplethysmography by cross time-frequency analysis Computing in Cardiology (2011)

(xi) <u>M. Orini</u>, R. Bailón, L.T. Mainardi, P. Laguna: Characterization of the dynamic interactions between cardiovascular signals by cross time–frequency analysis: phase differences, time delay and phase locking Congress of numerical methods in engineering (2011)

National conferences

(i) <u>M. Orini</u>, E. Gil, R. Bailón, L.T. Mainardi, P. Laguna: Comparison of the TF structure of PPGV and HRV by means of bivariate TF analysis. II congresso del gruppo nazionale di bioingegneria (GNB) (2010).

(ii) E. Cirugeda, <u>M. Orini</u>, R. Bailón, P. Laguna: Estimación de la Frecuencia Respiratoria Mediante Análisis Tiempo-Frecuencia de la Senal de Variabilidad del Ritmo Cardíaco XXVII Congreso Anual de la Sociedad espanola de Ingeniera Biomédica, pp. 613-616 (2009)

(iii) <u>M. Orini</u>, R. Bailón, A. Minchole, L.T. Mainardi, P. Laguna: Metodologa para el seguimiento de las dinámicas cardiovasculares a través de la coherencia tiempo-frecuencia. XXVII Congreso Anual de la Sociedad espanola de Ingeniera Biomédica, pp. 629-632 (2009)

(iv) <u>M. Orini</u>, R. Bailón, P. Laguna, L.T. Mainardi: Assessing the influence of the music on the heart rate variability by means of time-frequency analysis. I congresso del gruppo nazionale di bioingegneria (GNB) (2008)

(v) <u>M. Orini</u>, B. Giraldo, R. Bailón, V. Vallverdu, L.T. Mainardi, S. Benito, I. Diaz, P. Caminal: Seguimiento de parámetros cardio-respiratorios para la prediccíon de éxito en la prueba de desconexión de la ventilación mecánica XXVI Congreso Sociedad Espanola de Ingeniera Biomédica. pp. 375–378 (2008)

Bibliography

[1] Heart rate variability: standards of measurement, physiological interpretation and clinical use. task force of the european society of cardiology and the north american society of pacing and electrophysiology. Circulation **93**(5), 1043–1065 (1996)

[2] Akselrod, S., Gordon, D., Ubel, F.A., Shannon, D.C., Barger, A.C., Cohen, R.J.: Power spectrum analysis of heart rate fluctuations: a quantitative probe of beat-to-beat cardiovascular control. Science **213**, 220–222 (1981)

[3] Akselrod, S., Oz, O., Greenberg, M., Keselbrener, L.: Autonomic response to change of posture among normal and mild-hypertensive adults: investigation by time-dependent spectral analysis. J Autonom. Nerv. Syst. **64**, 33–43 (1997)

[4] Aletti, F., Bassani, T., Lucini, D., Pagani, M., Baselli, G.: Multivariate decomposition of arterial blood pressure variability for the assessment of arterial control of circulation. IEEE Trans. Biomed. Eng. **56**(7), 1781–1790 (2009)

[5] Allen, J.: Photoplethysmography and its application in clinical physiological measurement. Physiol Meas **28**(3), R1–39 (2007)

[6] Allen, J., Murray, A.: Age-related changes in peripheral pulse timing characteristics at the ears, thumbs and toes. Journal of Human Hypertension **16**, 711–717 (2002)

[7] Arce, G.R., Hasan, S.R.: Elimination of interference terms of the discrete Wigner distribution using nonlinear filtering. IEEE Trans. Signal Process. **48**(8), 2321–2331 (2000)

[8] Auger, F., Chassande-Mottin, E.: Time-Frequency Analysis, chap. Quadratic Time-Frequency Analysis I: Cohen's Class, pp. 131–163. ISTE (2010)

[9] Auger, F., Flandrin, P.: Improving the readability of time-frequency and time-scale representations by the reassignment method. IEEE Trans. Signal Process. **43**(5), 1068–1089 (1995)

[10] Auger, F., Flandrin, P., P., G., Olivier, L.: Time-frequency toolbox. Tech. rep., http://www.nongnu.org/tftb/

[11] Aviyente, S., Bernat, E.M., Evans, W.S., Sponheim, S.R.: A phase synchrony measure for quantifying dynamic functional integration in the brain. Hum Brain Mapp pp. 80–93 (2010)

[12] Aviyente, S., Evans, W.S., Bernat, E.M., Sponheim, S.: A time-varying phase coherence measure for quantifying functional integration in the brain. In: Proc. IEEE

International Conference on Acoustics, Speech and Signal Processing ICASSP 2007, vol. 4, pp. IV–1169–IV–1172 (2007)

[13] Aviyente, S., Williams, W.J.: Multitaper marginal time-frequency distributions. Signal Process. **86**(2), 279–295 (2006)

[14] Baccala, L.A., Sameshima, K.: Partial directed coherence: a new concept in neural structure determination. Biological Cybernetics **84**, 463–474 (2001)

[15] Badra, L.J., Cooke, W.H., Hoag, J.B., Crossman, A.A., Kuusela, T.A., Tahvanainen, K.U.O., Eckberg, D.L.: Respiratory modulation of human autonomic rhythms. Am. J. Physiol. Heart Circ. Physiol. **280**(6), H2674–H2688 (2001)

[16] Bailón, R., Laguna, P., Mainardi, L., Sörnmo, L.: Analysis of heart rate variability using time-varying frequency bands based on respiratory frequency. In: Proc. 29th Annual Int Conf IEEE–EMBS 2007, pp. 6674–6677 (2007)

[17] Bailón, R., Laguna, P., Mainardi, L., Sörnmo, L.: Analysis of heart rate variability using time-varying frequency bands based on respiratory frequency. In: Proc. of the 29th Int. Conf. of the IEEE Eng. in Med. and Biol. Soc., pp. 6674–6677. IEEE-EMBS Society, Lyon (2007)

[18] Bailón, R., Laouini, G., Grao, C., Orini, M., Laguna, P., Meste, O.: The integral pulse frequency modulation model with time-varying threshold: Application to heart rate variability analysis during exercise stress testing

[19] Bailón, R., Mainardi, L., Orini, M., Sörnmo L.and Laguna, P.: Analysis of heart rate variability during exercise stress testing using respiratory information. Biomedical Signal Processing and Control **5**, 299–310 (2010)

[20] Bailón, R., Mainardi, L.T., Laguna, P.: Time-frequency analysis of heart rate variability during stress testing using a priori information of respiratory frequency. In: Proc. Conf. Computers in Cardiology, pp. 169–172 (2006)

[21] Bailón, R., Mateo, J., Olmos, S., Serrano, P., Garcia, J., del Rio, A., Ferreira, I.J., Laguna, P.: Coronary artery disease diagnosis based on exercise electrocardiogram indexes from repolarisation, depolarisation and heart rate variability. Med. Biol. Eng. Comput **41**(5), 561–571 (2003)

[22] Bailón, R., Serrano, P., Laguna, P.: Influence of time-varying mean heart rate in coronary artery disease diagnostic performance of heart rate variability indices from exercise stress testing. J Electrocardiol (2011)

[23] Bailón, R., Sörnmo, L., Laguna, P.: ECG-derived respiratory frequency estimation. In: G. Clifford, F. Azuaje, P. McSharry (eds.) Advanced methods and tools for ECG data analysis, pp. 215–244. Artech House Inc. (2006)

[24] Bailón, R., Sörnmo, L., Laguna, P.: A robust method for ECG-based estimation of the respiratory frequency during stress testing. IEEE Trans. Biomed. Eng. **53**(7), 1273–1285 (2006)

[25] Baraniuk, R.G., Jones, D.L.: A signal-dependent time-frequency representation: optimal kernel design. IEEE Trans. Signal Process. **41**(4), 1589–1602 (1993)

[26] Baraniuk, R.G., Jones, D.L.: A signal-dependent time-frequency representation: fast algorithm for optimal kernel design. IEEE Trans. Signal Process. **42**(1), 134–146 (1994)

[27] Barbieri, R., Bianchi, A., Triedman, J., Mainardi, L., Cerutti, S., Saul, J.: Model dependency of multivariate autoregressive spectral analysis. IEEE Eng. Med. Biol. Mag. **16**(5), 74–85 (1997)

[28] Barbieri, R., Brown, E.: Analysis of heartbeat dynamics by point process adaptive filtering. IEEE Trans. Signal Process. **53**(1), 4–12 (2006)

[29] Barbieri, R., Matten, E.C., Alabi, A.A., Brown, E.N.: A point-process model of human heartbeat intervals: new definitions of heart rate and heart rate variability. American Journal of Physiology - Heart and Circulatory Physiology **288**(1), H424–H435 (2005)

[30] Barbieri, R., Parati, G., Saul, J.: Closed- versus open-loop assessment of heart rate baroreflex. Engineering in Medicine and Biology Magazine, IEEE **20**(2), 33–42 (2001)

[31] Baselli, G., Caiani, E., Porta, A., Montano, N., Signorini, M.G., Cerutti, S.: Biomedical signal processing and modeling in cardiovascular systems. Critical Reviews in Biomedical Engineering **30**(1-3), 55–84 (2002)

[32] Baselli, G., Porta, A., Ferrari, G.: Heart rate variability, chap. Models for the analysis of cardiovascular variability signals, pp. 135–145. M. Malik and A.J. Camm (1995)

[33] Baselli, G., Porta, A., Rimoldi, O., Pagani, M., Cerutti, S.: Spectral decomposition in multichannel recordings based on multivariate parametric identification. IEEE Trans. Biomed. Eng. **44**(11), 1092–1101 (1997)

[34] Baskerville, A.L., Eckberg, D.L., Thompson, M.A.: Arterial pressure and pulse interval responses to repetitive carotid baroreceptor stimuli in man. The Journal of Physiology **297**(1), 61–71 (1979)

[35] Bassani, T., Magagnin, V., Guzzetti, S., Baselli, G., Citerio, G., Porta, A.: Testing the involvement of baroreflex during general anesthesia through granger causality approach. Computers in Biology and Medicine **In Press, Corrected Proof**, – (2011)

[36] Bayram, M., Baraniuk, R.: Multiple window time-frequency analysis. In: Time-Frequency and Time-Scale Analysis, 1996., Proceedings of the IEEE-SP International Symposium, pp. 173–176 (1996)

[37] Bayram, M., Baraniuk, R.: Nonlinear and Nonstationary Signal Processing, chap. Multiple Window Time-Varying Spectrum Estimation, pp. 292–316. Univ. Press (1996)

[38] Bendat, J., Piersol, A.: Random Data: Analysis and Measurement Procedures. Wiley Series in Probability and Statistics. John Wiley & Sons (2010)

[39] Bernardi, L., Porta, C., Casucci, G., Balsamo, R., Bernardi, N.F., Fogari, R., Sleight, P.: Dynamic interactions between musical, cardiovascular, and cerebral rhythms in humans. Circulation **119**(25), 3171–3180 (2009)

[40] Bernardi, L., Porta, C., Sleight, P.: Cardiovascular, cerebrovascular, and respiratory changes induced by different types of music in musicians and non-musicians: the importance of silence. Heart (British Cardiac Society) **92**(4), 445–452 (2006)

[41] Bernardi, L., Solda, A.R., Coats, A.J.S., Reeder, M., Calciati, A., Garrard, C.S., Sleight, P.: Autonomic control of skin microvessels: Assessment by power spectrum of photoplethysmographic waves. Clinical Science **90**, 345–355 (1996)

[42] Bianchi, A.M., Mainardi, L.T., Petrucci, E., Signorini, M.G., Mainardi, M., Cerutti, S.: Time-variant power spectrum analysis for the detection of transient episodes in HRV signal. IEEE Trans. Biom. Eng. **40**(2), 136–144 (1993)

[43] Bigot, J., Longcamp, M., Maso, F.D., Amarantini, D.: A new statistical test based on the wavelet cross-spectrum to detect time-frequency dependence between non-stationary signals: Application to the analysis of cortico-muscular interactions. Neuroimage (2011)

[44] Blain, G., Meste, O., Bermon, S.: Influences of breathing patterns on respiratory sinus arrhythmia in humans during exercise. Am. J. Physiol. Heart Circ. Physiol. **288**(2), H887–95 (2005)

[45] Blasi, A., Jo, J., Valladares, E., Juarez, R., Baydur, A., Khoo, M.: Autonomic cardiovascular control following transient arousal from sleep: A time-varying closed-loop model. IEEE Trans. Biomed. Eng. **53**(1), 74–82 (2006)

[46] Blinowska, K.: Review of the methods of determination of directed connectivity from multichannel data. Med. Biol. Eng. Comput **49**, 521–529 (2011)

[47] de Boer, R., Karemaker, J., Strackee, J.: Relationships between short-term blood-pressure fluctuations and heart-rate variability in resting subjects i: a spectral analysis approach. Med. Biol. Eng. Comput **23**, 352–358 (1985)

[48] de Boer, R., Karemaker, J., Strackee, J.: Relationships between short-term blood-pressure fluctuations and heart-rate variability in resting subjects ii: a simple model. Med. Biol. Eng. Comput **23**, 359–364 (1985)

[49] Bolanos, M., H. Nazeran, Haltiwanger, E.: Comparison of Heart Rate Variability Signal Features Derived from Electrocardiography and Photoplethysmography in Healthy Individuals. Engineering in Medicine and Biology Society. Proceedings of the 28th Annual International Conference of the IEEE pp. 4289–4294 (2006)

[50] Borgnat, P., Flandrin, P.: Stationarization via surrogates. Journal of Statistical Mechanics: Theory and Experiment **2009**(01), P01,001 (2009)

[51] Borgnat, P., Flandrin, P., Honeine, P., Richard, C., Xiao, J.: Testing stationarity with surrogates: A time-frequency approach. IEEE Trans. Signal Process. **58**(7), 3459–3470 (2010)

[52] Boudreaux-Bartels, G., Parks, T.: Time-varying filtering and signal estimation using Wigner distribution synthesis techniques. IEEE Trans. Acoust., Speech and Signal Process. **34**(3) (1986)

[53] Bradley, M.M., Lang, P.J.: Affective reactions to acoustic stimuli. Psychophysiology **37**(2), 204–215 (2000)

[54] Brittain, J.S., Halliday, D.M., Conway, B.A., Nielsen, J.B.: Single-trial multiwavelet coherence in application to neurophysiological time series. IEEE Trans. Biomed. Eng. **54**(5), 854–862 (2007)

210

[55] Brown, E.N., Barbieri, R., Ventura, V., Kass, R.E., Frank, L.M.: The time-rescaling theorem and its application to neural spike train data analysis. Neural Comput **14**(2), 325–346 (2002)

[56] Bruns, A.: Fourier-, hilbert- and wavelet-based signal analysis: are they really different approaches? J Neurosci Methods **137**(2), 321–332 (2004)

[57] Carter, G.C.: Coherence and time delay estimation. Proc. IEEE **75**(2), 236–255 (1987)

[58] Chan, H.L., Huang, H.H., Lin, J.L.: Time-frequency analysis of heart rate variability during transient segments. Ann Biomed Eng **29**(11), 983–996 (2001)

[59] Charkoudian, N., Rabbitts, J.A.: Sympathetic neural mechanisms in human cardiovascular health and disease. Mayo Clinic Proceedings **84**(9), 822–830 (2009)

[60] Charlot, K., Cornolo, J., Brugniaux, J.V., Richalet, J.P., Pichon, A.: Interchangeability between heart rate and photoplethysmography variabilities during sympathetic stimulations. Physiol Meas **30**(12), 1357–1369 (2009)

[61] Chen, W., Kobayashi, T., Ichikawa, S., Takeuchi, Y., Togawa, T.: Continuous estimation of systolic blood pressure using the pulse arrival time and intermittent calibration. Med. Biol. Eng. Comput. **38**, 569–574 (2000)

[62] Chen, Z., Brown, E.N., Barbieri, R.: Assessment of autonomic control and respiratory sinus arrhythmia using point process models of human heart beat dynamics. IEEE Trans. Biomed. Eng. **56**(7), 1791–1802 (2009)

[63] Chen, Z., Purdon, P.L., Harrell, G., Pierce, E.T., Walsh, J., Brown, E.N., Barbieri, R.: Dynamic assessment of baroreflex control of heart rate during induction of propofol anesthesia using a point process method. Ann Biomed Eng (2010)

[64] Chon, K.H., Dash, S., Ju, K.: Estimation of respiratory rate from photoplethysmogram data using time-frequency spectral estimation. IEEE Trans Biomed Eng **56**(8), 2054–2063 (2009)

[65] Cirillo, L., Zoubir, A., Amin, M.: Parameter estimation for locally linear fm signals using a time-frequency hough transform. IEEE Trans. Signal Process. **56**(9), 4162–4175 (2008)

[66] Cnockaert, L., Migeotte, P.F., Daubigny, L., Prisk, G.K., Grenez, F., Sá, R.C.: A method for the analysis of respiratory sinus arrhythmia using continuous wavelet transforms. IEEE Trans. Biomed. Eng. **55**(5), 1640–1642 (2008)

[67] Cohen, L.: Time-frequency distributions-a review. Proceedings of the IEEE **77**(7), 941–981 (1989)

[68] Cohen, L., Posch, T.: Generalized ambiguity functions. In: Proc. IEEE Int Acoustics, Speech, and Signal Processing Conf. ICASSP '85, vol. 10, pp. 1033–1036 (1985)

[69] Conci, F., Di Rienzo, M., Castiglioni, P.: Blood pressure and heart rate variability and baroreflex sensitivity before and after brain death. Journal of Neurology, Neurosurgery & Psychiatry **71**(5), 621–631 (2001)

[70] Constant, I., Laude, D., Murat, I., Elghozi, J.L.: Pulse rate variability is not a surrogate for heart rate variability. Clinical Science **97**, 391–397 (1999)

[71] Cooke, W.H., Hoag, J.B., Crossman, A.A., Kuusela, T.A., Tahvanainen, K.U.O., Eckberg, D.L.: Human responses to upright tilt: a window on central autonomic integration. The Journal of Physiology **517**(2), 617–628 (1999)

[72] Costa, A., Boudreau-Bartels, G.: Design of time-frequency representations using a multiform, tiltable exponential kernel. IEEE Trans. Signal Process. **43**(10), 2283–2301 (1995)

[73] Cunningham, G.S., Williams, W.J.: Kernel decomposition of time-frequency distributions. IEEE Trans. Signal Process. **42**(6), 1425–1442 (1994)

[74] Daubechies, I.: Time-frequency localization operators: a geometric phase space approach **34**(4), 605–612 (1988)

[75] deBoer, R.W., Karemaker, J.M., Strackee, J.: Hemodynamic fluctuations and baroreflex sensitivity in humans: a beat-to-beat model. Am J Physiol **253**(3 Pt 2), H680–H689 (1987)

[76] Di Rienzo, M., Parati, G., Radaelli, A., Castiglioni, P.: Baroreflex contribution to blood pressure and heart rate oscillations: time scales, time-variant characteristics and nonlinearities. Phil Trans R Soc A **367**(1892), 1301–1318 (2009)

[77] Dutoit, A.P., Hart, E.C., Charkoudian, N., Wallin, B.G., Curry, T.B., Joyner, M.J.: Cardiac baroreflex sensitivity is not correlated to sympathetic baroreflex sensitivity within healthy, young humans. Hypertension **56**(6), 1118–1123 (2010)

[78] Eckberg, D.L.: Temporal response patterns of the human sinus node to brief carotid baroreceptor stimuli. The Journal of Physiology **258**(3), 769–782 (1976)

[79] Eckberg, D.L.: Sympathovagal balance : A critical appraisal. Circulation **96**(9), 3224–3232 (1997)

[80] Eckberg, D.L.: The human respiratory gate. The Journal of Physiology **548**(2), 339–352 (2003)

[81] Eckberg, D.L.: Point:counterpoint: respiratory sinus arrhythmia is due to a central mechanism vs. respiratory sinus arrhythmia is due to the baroreflex mechanism. J Appl Physiol **106**(5), 1740–2; discussion 1744 (2009)

[82] Eckberg, D.L., Drabinsky, M., Braunwald, E.: Defective cardiac parasympathetic control in patients with heart disease. New England Journal of Medicine **285**(16), 877–883 (1971)

[83] Faes, L., Nollo, G.: Biomedical Engineering, Trends in Electronics, Communications and Software, chap. Multivariate Frequency Domain Analysis of Causal Interactions in Physiological Time Series (2011)

[84] Faes, L., Nollo, G., Chon, K.H.: Assessment of granger causality by nonlinear model identification: application to short-term cardiovascular variability. Ann Biomed Eng **36**(3), 381–395 (2008)

[85] Faes, L., Nollo, G., Porta, A.: Information domain approach to the investigation of cardio-vascular, cardio-pulmonary and vasculo-pulmonary causal couplings. Frontiers in Physiology **2**(0) (2011)

[86] Faes, L., Pinna, G.D., Porta, A., Maestri, R., Nollo, G.: Surrogate data analysis for assessing the significance of the coherence function. IEEE Trans. Biomed. Eng. **51**(7), 1156–1166 (2004)

[87] Faes, L., Porta, A., Nollo, G.: Testing frequency-domain causality in multivariate time series. IEEE Trans. Signal Process. **57**(8), 1897–1906 (2010)

[88] Faes, L., Widesott, L., Del Greco, M., Antolini, R., Nollo, G.: Causal cross-spectral analysis of heart rate and blood pressure variability for describing the impairment of the cardiovascular control in neurally mediated syncope. IEEE Trans. Biomed. Eng. **53**(1), 65–73 (2006)

[89] Faes, L., Zhao, H., Chon, K.H., Nollo, G.: Time-varying surrogate data to assess nonlinearity in nonstationary time series: Application to heart rate variability. IEEE Trans. Biomed. Eng. **56**(3), 685–695 (2009)

[90] Flandrin, P.: Some features of time-frequency representations of multicomponent signals (1984)

[91] Flandrin, P.: Maximum signal energy concentration in a time-frequency domain. In: Proc. Int Acoustics, Speech, and Signal Processing ICASSP-88. Conf, pp. 2176–2179 (1988)

[92] Flandrin, P.: Time-Frequency/Time-Scale Analysis. Academic Press, New York (1999)

[93] Flandrin, P.: Time-Frequency Signal Analysis and Processing, chap. Ambiguity Function, pp. 160–167. Elsevier (2003)

[94] Folland, G.: Harmonic Analysis in Phase Space. Princeton, NJ: Princeton University Press (1989)

[95] Foo, J.Y.A., Lim, C.S.: Pulse transit time as an indirect marker for variations in cardiovascular related reactivity. Technol Health Care **14**(2), 97–108 (2006)

[96] Frattola, A., Parati, G., Gamba, P., Paleari, F., Mauri, G., Di Rienzo, M., Castiglioni, P., Mancia, G.: Time and frequency domain estimates of spontaneous baroreflex sensitivity provide early detection of autonomic dysfunction in diabetes mellitus. Diabetologia **40**, 1470–1475 (1997)

[97] Gallet, C., Chapuis, B., Barrs, C., Julien, C.: Time-frequency analysis of the baroreflex control of renal sympathetic nerve activity in the rat. Journal of Neuroscience Methods **In Press, Uncorrected Proof**, –

[98] Gil, E., Bailón, R., Vergara, J., Laguna, P.: Ptt variability for discrimination of sleep apnea related decreases in the amplitude fluctuations of ppg signal in children. IEEE Trans. Biomed. Eng. (2010)

[99] Gil, E., Mendez, M., Vergara, J.M., Cerutti, S., Bianchi, A.M., Laguna, P.: Discrimination of sleep-apnea-related decreases in the amplitude fluctuations of ppg signal in children by HRV analysis. IEEE Trans. Biomed. Eng. **56**(4), 1005–1014 (2009)

[100] Gil, E., Orini, M., Bailón, R., Vergara, J.M., Mainardi, L., Laguna, P.: Photoplethysmography pulse rate variability as a surrogate measurement of heart rate variability during non-stationary conditions. Physiol Meas **31**(9), 1271 (2010)

[101] Gil, E., Orini, M., Bailón, R., Vergara, J.M., Mainardi, L., Laguna, P.: Time-varying spectral analysis for comparison of HRV and PPG variability during tilt table test. Conf Proc IEEE Eng Med Biol Soc **2010**, 3579–3582 (2010)

[102] Gil, E., Vergara, J.M., Laguna, P.: Detection of decreases in the amplitude fluctuation of pulse photoplethysmography signal as indication of obstructive sleep apnea syndrome in children. Biomed. Signal Process. Control **3**, 267–277 (2008)

[103] Gladkova, I., Chebanov, D.: On the synthesis problem for a waveform having a nearly ideal ambiguity surface. RADAR 2004 - International Conference on Radar Systems (2004)

[104] Glass, L.: Synchronization and rhythmic processes in physiology. Nature **410**(6825), 277–284 (2001)

[105] Goldberger, J.J., Challapalli, S., Tung, R., Parker, M.A., Kadish, A.H.: Relationship of heart rate variability to parasympathetic effect. Circulation **103**(15), 1977–1983 (2001)

[106] Gomez, P., Danuser, B.: Affective and physiological responses to environmental noises and music. International Journal of Psychophysiology **53**(2), 91–103 (2004)

[107] Gomez, P., Danuser, B.: Relationships between musical structure and psychophysiological measures of emotion. Emotion (Washington, D.C.) **7**(2), 377–387 (2007)

[108] Goren, Y., Davrath, L.R., Pinhas, I., Toledo, E., Akselrod, S.: Individual time-dependent spectral boundaries for improved accuracy in time-frequency analysis of heart rate variability. IEEE Trans. Biomed. Eng. **53**(1), 35–42 (2006)

[109] Gouveia, S., Rocha, A.P., Laguna, P., Lago, P.: Time domain baroreflex sensitivity assessment by joint analysis of spontaneous sbp and rr series. Biomedical Signal Processing and Control **4**(3), 254 – 261 (2009)

[110] Grinsted, A., Moore, J.C., Jevrejeva, S.: Application of the cross wavelet transform and wavelet coherence to geophysical time series. Nonlinear Processes in Geophysics **11**, 561–566 (2004)

[111] Groothuis, J.T., Thijssen, D.H.J., Lenders, J.W.M., Deinum, J., Hopman, M.T.E.: Leg vasoconstriction during head-up tilt in patients with autonomic failure is not abolished. Journal of Applied Physiology **110**(2), 416–422 (2011)

[112] Grossman, P., Taylor, E.W.: Toward understanding respiratory sinus arrhythmia: Relations to cardiac vagal tone, evolution and biobehavioral functions. Biological Psychology **74**(2), 263–285 (2007)

[113] Grossman, P., Wilhelm, F.H., Spoerle, M.: Respiratory sinus arrhythmia, cardiac vagal control, and daily activity. Am. J. Physiol. Heart Circ. Physiol. **287**(2), H728–H734 (2004)

[114] Guyton, A., Hall, J.: Textbook on medical physiology (2005)

[115] Guyton, A., Hall, J.: Textbook of Medical Physiology, chap. The Autonomic Nervous System and the Adrenal Medulla, pp. 748–760. Guyton, A.C. and Hall, J.E. (2006)

[116] Hayano, J., Barros, A.K., Kamiya, A., Ohte, N., Yasuma, F.: Assessment of pulse rate variability by the method of pulse frequency demodulation. Biomed Eng Online **4**, 62 (2005)

[117] Hayano, J., Yasuma, F.: Hypothesis: respiratory sinus arrhythmia is an intrinsic resting function of cardiopulmonary system. Cardiovascular Research **58**(1), 1–9 (2003)

[118] Hayano, J., Yasuma, F., Okada, A., Mukai, S., Fujinami, T.: Respiratory sinus arrhythmia: A phenomenon improving pulmonary gas exchange and circulatory efficiency. Circulation **94**(4), 842–847 (1996)

[119] Hayes, M.J., Smith, P.R.: A new method for pulse oximetry possessing inherent insensitivity to artifact. IEEE Trans. Biomed. Eng. **48**, 452–461 (2001)

[120] Heesch, C.M.: Reflexes that control cardiovascular function. Advances in Physiology Education **277**(6), S234–S243 (1999)

[121] Hertzman, A.B.: The blood supply of various skin areas as estimated by the photoelectric plethysmograph. Am. J. Physiol **124**, 328–340 (1938)

[122] Hlawatsch, F.: Digital signal processing. pp. 363–267 (1984)

[123] Hlawatsch, F.: Duality and classification of bilinear time-frequency signal representations. IEEE Trans. Signal Process. **39**(7), 1564–1574 (1991)

[124] Hlawatsch, F., Boudreaux-Bartels, G.F.: Linear and quadratic time-frequency signal representations. Signal Processing Magazine, IEEE **9**(2), 21–67 (1992)

[125] Hlawatsch, F., Flandrin, P.: The Wigner Distribution - theory and applications in signal processing, chap. The interference structure of the Wigner distribution and related time-frequency signal representations, pp. 59–113. Elsevier (1997)

[126] Hlawatsch, F., Kozek, W.: Second-order time-frequency synthesis of nonstationary random processes. IEEE Trans. Inform. Theory **41**(1), 255–267 (1995)

[127] Huang, N.E., Shen, Z., Long, S.R., Wu, M.C., Shih, H.H., Zheng, Q., Yen, N.C., Tung, C.C., Liu, H.H.: The empirical mode decomposition and the hilbert spectrum for nonlinear and non-stationary time series analysis. Proceedings of the Royal Society of London. Series A: Mathematical, Physical and Engineering Sciences **454**(1971), 903–995 (1998)

[128] Iwanaga, M., Kobayashi, A., Kawasaki, C.: Heart rate variability with repetitive exposure to music. Biological psychology **70**(1), 61–66 (2005)

[129] Jachan, M., Matz, G., Hlawatsch, F.: Time-frequency arma models and parameter estimators for underspread nonstationary random processes

[130] Jasson, S., Médigue, C., Maison-Blanche, P., Montano, N., Meyer, L., Vermeiren, C., Mansier, P., Coumel, P., Malliani, A., Swynghedauw, B.: Instant power spectrum analysis of heart rate variability during orthostatic tilt using a time-frequency-domain method. Circulation **96**(10), 3521–3526 (1997)

[131] Jasson, S., Médigue, C., Maison-Blanche, P., Montano, N., Meyer, L., Vermeiren, C., Mansier, P., Coumel, P., Malliani, A., Swynghedauw, B.: Instant power spectrum analysis of heart rate variability during orthostatic tilt using a time-/frequency-domain method. Circulation **96**(10), 3521–3526 (1997)

[132] Javorka, M., Lazarova, Z., Tonhajzerova, I., Turianikova, Z., Honzikova, N., Fiser, B., Javorka, K., Baumert, M.: Baroreflex analysis in diabetes mellitus: linear and nonlinear approaches. Med. Biol. Eng. Comput. **49**(3), 279–288 (2011)

[133] Jeong, J., Williams, W.J.: Kernel design for reduced interference distributions. IEEE Trans. Signal Process. **40**(2), 402–412 (1992)

[134] Johnsen, S.J., Andersen, N.: On power estimation in maximum entropy spectral analysis. Geophysics **43**(4), 681–690 (1978)

[135] Julien, C.: The enigma of mayer waves: Facts and models. Cardiovasc Res **70**(1), 12–21 (2006)

[136] Julien, C., Parkes, M.J., Tzeng, S.Y.C., Sin, P.Y.W., Ainslie, P.N., van de Borne, P., Fortrat, J.O., Custaud, M.A., Gharib, C., Porta, A., Vallais, F., Baselli, G., Pagani, M., Lucini, D., Hughson, R.L., Taylor, J.A., Tan, C.O., Baekey, D.M., Dick, T.E., Paton, J.F.R., Taha, B.: Comments on point:counterpoint: respiratory sinus arrhythmia is due to a central mechanism vs. respiratory sinus arrhythmia is due to the baroreflex mechanism. J Appl Physiol **106**(5), 1745–1749 (2009)

[137] Julu, P.O.O., Cooper, V.L., Hansen, S., Hainsworth, R.: Cardiovascular regulation in the period preceding vasovagal syncope in conscious humans. J Physiol **549**(1), 299–311 (2003)

[138] Karemaker, J.: The riddles of heart rate variability. Clinical Autonomic Research **11**, 65–66 (2001). 10.1007/BF02322048

[139] Karemaker, J., Wesseling, K.: Variability in cardiovascular control: The baroreflex reconsidered. Cardiovascular Engineering **8**, 23–29 (2008)

[140] Karemaker, J.M.: Why do we measure baroreflex sensitivity the way we do? Clin Auton Res **12**(6), 427–428 (2002)

[141] Karemaker, J.M.: Counterpoint: respiratory sinus arrhythmia is due to the baroreflex mechanism. J Appl Physiol **106**(5), 1742–3; discussion 1744 (2009)

[142] Karemaker, J.M.: Last word on point:counterpoint: respiratory sinus arrhythmia is due to a central mechanism vs. respiratory sinus arrhythmia is due to the baroreflex mechanism. J Appl Physiol **106**(5), 1750 (2009)

[143] Kashihara, K., Kawada, T., Sugimachi, M., Sunagawa, K.: Wavelet-based system identification of short-term dynamic characteristics of arterial baroreflex. Ann Biomed Eng **37**(1), 112–128 (2009)

[144] Keissar, K., Davrath, L.R., Akselrod, S.: Coherence analysis between respiration and heart rate variability using continuous wavelet transform. Phil. Trans. R. Soc. A **367**(1892), 1393–1406 (2009)

[145] Keissar, K., Maestri, R., Pinna, G.D., Rovere, M.T.L., Gilad, O.: Non-invasive baroreflex sensitivity assessment using wavelet transfer function-based time-frequency analysis. Physiol Meas **31**(7), 1021–1036 (2010)

[146] Keselbrener, L., Akselrod, S.: Selective discrete fourier transform algorithm for time-frequency analysis: method and application on simulated and cardiovascular signals. IEEE Trans. Biom. Eng. **43**(8), 789–802 (1996)

[147] Khanokh, B., Slovik, Y., Landau, D., Nitzan, M.: Sympathetically induced spontaneous fluctuations of the photoplethysmographic signal. Med. Biol. Eng. Comput. **42**(1), 80–85 (2004)

[148] Kumaresan, R., Tufts, D.: Estimating the parameters of exponentially damped sinusoids and pole-zero modeling in noise. IEEE Trans. ASSP **30**, 833–840 (1982)

[149] La Rovere, M.T., Bigger, J.T., Marcus, F.I., Mortara, A., Schwartz, P.J.: Baroreflex sensitivity and heart-rate variability in prediction of total cardiac mortality after myocardial infarction. The Lancet **351**(9101), 478 – 484 (1998)

[150] La Rovere, M.T., Pinna, G.D., Maestri, R., Mortara, A., Capomolla, S., Febo, O., Ferrari, R., Franchini, M., Gnemmi, M., Opasich, C., Riccardi, P.G., Traversi, E., Cobelli, F.: Short-term heart rate variability strongly predicts sudden cardiac death in chronic heart failure patients. Circulation **107**(4), 565–570 (2003)

[151] La Rovere, M.T., Pinna, G.D., Raczak, G.: Baroreflex sensitivity: measurement and clinical implications. Ann Noninvasive Electrocardiol **13**(2), 191–207 (2008)

[152] Lachaux, J., Rodriguez, E., Martinerie, M.L.V.Q.A.L.J., Varela, F.: Studying single-trials of phase-synchronous activity in the brain. Int J Bifurcat Chaos **10**, 2439–39 (2000)

[153] Lachaux, J.P., Lutz, A., Rudrauf, D., Cosmelli, D., Quyen, M.L.V., Martinerie, J., Varela, F.: Estimating the time-course of coherence between single-trial brain signals: an introduction to wavelet coherence. Neurophysiol Clin **32**(3), 157–174 (2002)

[154] Lachaux, J.P., Rodriguez, E., Martinerie, J., Varela, F.J.: Measuring phase synchrony in brain signals. Hum Brain Mapp **8**(4), 194–208 (1999)

[155] Laude, D., Elghozi, J.L., Girard, A., Bellard, E., Bouhaddi, M., Castiglioni, P., Cerutti, C., Cividjian, A., Rienzo, M.D., Fortrat, J.O., Janssen, B., Karemaker, J.M., Lefthériotis, G., Parati, G., Persson, P.B., Porta, A., Quintin, L., Regnard, J., Rdiger, H., Stauss, H.M.: Comparison of various techniques used to estimate spontaneous baroreflex sensitivity (the eurobavar study). Am J Physiol Regul Integr Comp Physiol **286**(1), R226–R231 (2004)

[156] Li, D., Jung, R.: Quantifying coevolution of nonstationary biomedical signals using time-varying phase spectra. Ann Biomed Eng **28**(9), 1101–1115 (2000)

[157] Lombardi, F.: Clinical implications of present physiological understanding of HRV components. Cardiac Electrophysiology Review **6**, 245–249 (2002)

[158] Lovett, E.G., Ropella, K.M.: Time-frequency coherence analysis of atrial fibrillation termination during procainamide administration. Ann Biomed Eng **25**(6), 975–984 (1997)

[159] Lu, G., Yang, F.: Limitations of oximetry to measure heart rate variability measures. Cardiovasc Eng **9**(3), 119–125 (2009)

[160] Lu, G., Yang, F., Taylor, J.A., Stein, J.F.: A comparison of photoplethysmography and ECG recording to analyse heart rate variability in healthy subjects. J Med Eng Technol **33**(8), 634–641 (2009)

[161] Lu, S., Zhao, H., Ju, K., Shin, K., Lee, M., Shelley, K., Chon, K.: Can photoplethysmography variability serve as an alternative approach to obtain heart rate variability information? Journal of Clinical Monitoring and Computing **22**(1), 23–29 (2008)

[162] Ma, T., Zhang, Y.T.: Spectral Analysis of Pulse Transit Time Variability and Its Coherence with Other Cardiovascular Variabilities. In: Proceedings of the 28th Annual International Conference of the IEEE EMBS, pp. 996–999 (2006)

[163] Magagnin, V., Bassani, T., Lucini, D., Pagani, M., Caiani, E.G., Cerutti, S., Porta, A.: Empirical mode decomposition to assess baroreflex gain from spontaneous variability during exercise in humans. Conf Proc IEEE Eng Med Biol Soc **1**, 2236–2239 (2009)

[164] Mainardi, L., Montano, N., Cerutti, S.: Automatic decomposition of Wigner distribution and its application to heart rate variability. Methods Inf. Med. **43**, 17–21 (2004)

[165] Mainardi, L.T.: On the quantification of heart rate variability spectral parameters using time-frequency and time-varying methods. Phil Trans R Soc A **367**(1887), 255–275 (2009)

[166] Mainardi, L.T., Bianchi, A., Cerutti, S.: Time-frequency and time-varying analysis for assessing the dynamic responses of cardiovascular control. Critical Reviews in Biomed. Eng. **30 (1-2)**, 181–223 (2002)

[167] Mainardi, L.T., Bianchi, A.M., Cerutti, S.: Time-frequency and time-varying analysis for assessing the dynamic responses of cardiovascular control. Critical Reviews in Biomedical Engineering **30**(1-3), 175–217 (2002)

[168] Mainardi, L.T., Bianchi, A.M., Furlan, R., Piazza, S., Barbieri, R., di Virgilio, V., Malliani, A., Cerutti, S.: Multivariate time-variant identification of cardiovascular variability signals: a beat-to-beat spectral parameter estimation in vasovagal syncope. IEEE Trans. Biom. Eng. **44**(10), 978–989 (1997)

[169] Malik, M., Eckberg, D.L.: Sympathovagal balance: A critical appraisal response. Circulation **98**(23), 2643–2644 (1998)

[170] Malliani, A., Julien, C., Billman, G.E., Cerutti, S., Piepoli, M.F., Bernardi, L., Sleight, P., Cohen, M.A., Tan, C.O., Laude, D., Elstad, M., Toska, K., Evans, J.M., Eckberg, D.L.: Cardiovascular variability is/is not an index of autonomic control of circulation. Journal of Applied Physiology **101**(2), 684–688 (2006)

218

[171] Malliani, A., Pagani, M., Lombardi, F., Cerutti, S.: Cardiovascular neural regulation explored in the frequency domain. Circulation **84**, 482–492 (1991)

[172] Malliani, A., Pagani, M., Montano, N., Mela, G.S.: Sympathovagal balance: A reappraisal. Circulation **98**(23), 2640–2643 (1998)

[173] Malpas, S.C.: Sympathetic nervous system overactivity and its role in the development of cardiovascular disease. Physiological Reviews **90**(2), 513–557 (2010)

[174] Marple, S.L.: Digital spectral analysis: with applications. Prentice-Hall, Inc. Upper Saddle River, NJ, USA (1986)

[175] Martin, W., Flandrin, P.: Wigner-Ville spectral analysis of nonstationary processes. IEEE Trans. Acoust., Speech and Signal Processing **33**(6), 1461–1470 (1985)

[176] Martin, W.A., Camenzind, E., Burkhard, P.R.: ECG artifact due to deep brain stimulation. Lancet **361**(9367), 1431 (2003)

[177] Martinez, J.P., Almeida, R., Olmos, S., Rocha, A.P., Laguna, P.: A wavelet-based ECG delineator: Evaluation on standard databases. IEEE Trans. Biomed. Eng. **51**(4), 570–581 (2004)

[178] Mateo, J., Laguna, P.: Improved heart rate variability signal analysis from the beat occurrence times according to the ipfm model. IEEE Trans. Biomed. Eng. **47**(8), 985–996 (2000)

[179] Mateo, J., Laguna, P.: Analysis of heart rate variability in the presence of ectopic beats using the heart timing signal. IEEE Trans. Biomed. Eng. **50**(3), 334–343 (2003)

[180] Mateo, J., Laguna, P.: Analysis of heart rate variability in the presence of ectopic beats using the heart timing signal. IEEE Trans. Biomed. Eng. **50**, 334–343 (2003)

[181] Matz, G., Hlawatsch, F.: Time-frequency coherence analysis of nonstationary random processes. In: Proc. Tenth IEEE Workshop Statistical Signal and Array Processing, pp. 554–558 (2000)

[182] Matz, G., Hlawatsch, F.: Nonstationary spectral analysis based on time-frequency operator symbols and underspread approximations. IEEE Trans. Inf. Theory **52**(3), 1067–1086 (2006)

[183] Mendelson, Y.: Pulse Oximetry: Theory and Applications for Noninvasive Monitoring. Clinical chemistry **38**(9), 1601–1607 (1992)

[184] Mendez, M.O., Bianchi, A.M., Montano, N., Patruno, V., Gil, E., Mantaras, C., Aiolfi, S., Cerutti, S.: On arousal from sleep: time-frequency analysis. Med. Biol. Eng. Comput. **46**, 341–351 (2008)

[185] Merri, M., Farden, D.C., Mottley, J.G., Titlebaum, E.L.: Sampling frequency of the electrocardiogram for spectral analysis of the heart rate variability. IEEE Trans. Biomed. Eng. **37**(1), 99–106 (1990)

[186] Meste, O., Khaddoumi, B., Blain, G., Bermon, S.: Time-varying analysis methods and models for the respiratory and cardiac system coupling in graded exercise. IEEE Trans. Biomed. Eng. **52**(11), 1921–1930 (2005)

[187] Meste, O., Khaddoumi, B., Blain, G., Bermon, S.: Time-varying analysis methods and models for the respiratory and cardiac system coupling in graded exercise. IEEE Trans. Biomed. Eng. **52**(11), 1921–1930 (2005)

[188] Montano, N., Ruscone, T.G., Porta, A., Lombardi, F., Pagani, M., Malliani, A.: Power spectrum analysis of heart rate variability to assess the changes in sympathovagal balance during graded orthostatic tilt. Circulation **90**, 1826–1831 (1994)

[189] Muma, M., Iskander, D.R., Collins, M.J.: The role of cardiopulmonary signals in the dynamics of the eye's wavefront aberrations. IEEE Trans. Biomed. Eng. **57**(2), 373–383 (2010)

[190] Naschitz, J.E., Bezobchuk, S., Mussafia-Priselac, R., Sundick, S., Dreyfuss, D., Khorshidi, I., Karidis, A., Manor, H., Nagar, M., Peck, E.R., Peck, S., Storch, S., Rosner, I., Gaitini, L.: Pulse transit time by r-wave-gated infrared photoplethysmography: review of the literature and personal experience. J Clin Monit Comput **18**(5-6), 333–342 (2004)

[191] Neto, E.P.S., Custaud, M.A., Cejka, J.C., Abry, P., Frutoso, J., Gharib, C., Flandrin, P.: Assessment of cardiovascular autonomic control by the empirical mode decomposition. Methods Inf Med **43**(1), 60–65 (2004)

[192] Nitzan, M., Babchenko, A., Khanokh, B., Landau, D.: The variability of the photoplethysmographic signal–a potential method for the evaluation of the autonomic nervous system. Physiol Meas **19**(1), 93–102 (1998)

[193] Nollo, G., Faes, L., Antolini, R., Porta, A.: Assessing causality in normal and impaired short-term cardiovascular regulation via nonlinear prediction methods. Phil Trans R Soc A **367**(1892), 1423–1440 (2009)

[194] Nollo, G., Faes, L., Porta, A., Antolini, R., Ravelli, F.: Exploring directionality in spontaneous heart period and systolic pressure variability interactions in humans: implications in the evaluation of baroreflex gain. Am J Physiol Heart Circ Physiol **288**(4), H1777–H1785 (2005)

[195] Novak, P., Novak, V.: Time/frequency mapping of the heart rate, blood pressure and respiratory signals. Med. Biol. Eng. Comput. **31**(2), 103–110 (1993)

[196] Nowak, J.A., Ocon, A., Taneja, I., Medow, M.S., Stewart, J.M.: Multiresolution wavelet analysis of time-dependent physiological responses in syncopal youths. Am J Physiol Heart Circ Physiol **296**(1), H171–H179 (2009)

[197] Nyklícek, I., Thayer, J., Van Doornen, L.: Cardiorespiratory differentiation of musically-induced emotions. Journal of Psychophysiology **11**(4), 304–321 (1997)

[198] Ocon, A.J., Medow, M.S., Taneja, I., Stewart, J.M.: Respiration drives phase synchronization between blood pressure and rr interval following loss of cardiovagal baroreflex during vasovagal syncope. Am J Physiol Heart Circ Physiol **300**(2), H527–H540 (2011)

[199] Oldfield, R.C.: The assessment and analysis of handedness: The edinburgh inventory. Neuropsychologia **9**(1), 97 – 113 (1971)

[200] Olshansky, B., Sabbah, H.N., Hauptman, P.J., Colucci, W.S.: Parasympathetic nervous system and heart failure. Circulation **118**(8), 863–871 (2008)

[201] Orini, M., Bailón, R., Enk, R., Koelsch, S., Mainardi, L.T., Laguna, P.: A method for continuously assessing the autonomic response to music-induced emotions through HRV analysis. Med. Biol. Eng. Comput. **48**(5), 423–433 (2010)

[202] Orini, M., Bailón, R., Gil, E., Minardi, L., Laguna, P.: Framework for continuous quantification of spectral coherence using quadratic time-frequency distributions: exploring cardiovascular coupling. International Journal of Bioelectromagnetism **12**, 177–182 (2010)

[203] Orini, M., Bailón, R., Laguna, P., Mainardi, L.T.: Modeling and estimation of time-varying heart rate variability during stress test by parametric and non parametric analysis. In: Proc. Conf. Computers in Cardiology, pp. 29–32 (2007)

[204] Orini, M., Bailón, R., Mainardi, L., Laguna, P.: Synthesis of HRV signals characterized by predetermined time-frequency structure by means of time-varying arma models. Biomedical Signal Processing and Control **In Press, Corrected Proof**, – (2011)

[205] Orini, M., Bailón, R., Mainardi, L., Laguna, P., Flandrin, P.: Characterization of the dynamic interactions between cardiovascular signals by time–frequency coherence. IEEE Trans. Biomed. Eng. **in press** (2011)

[206] Orini, M., Bailón, R., Mainardi, L., Mincholé, A., Laguna, P.: Continuous quantification of spectral coherence using quadratic time-frequency distributions: error analysis and application. Proc. Conf. Computers in Cardiology (2009)

[207] Orini, M., Bailón, R., Mainardi, L.T., Laguna, P.: Time-frequency phase differences and phase locking to characterize dynamic interactions between cardiovascular signals. Conf Proc IEEE Eng Med Biol Soc **1**

[208] Orini, M., Laguna, P., Mainardi, L., Bailón, R.: Characterization of the dynamic interactions between cardiovascular signals by cross time-frequency analysis: phase differences, time delay and phase locking. Proc. Conf. on numerical method in engineering pp. – (2011)

[209] Orini, M., Mainardi, L.T., Gil, E., Laguna, P., Bailón, R.: Dynamic assessment of spontaneous baroreflex sensitivity by means of time-frequency analysis using either rr or pulse interval variability. Conf Proc IEEE Eng Med Biol Soc **1**, 1630–1633 (2010)

[210] Pagani, M., Lombardi, F., Guzzetti, S., Rimoldi, O., Furlan, R., Pizzinelli, P., Sandrone, G., Malfatto, G., Dell'Orto, S., Piccaluga, E.: Power spectral analysis of heart rate and arterial pressure variabilities as a marker of sympatho-vagal interaction in man and conscious dog. Circulation Research **59**(2), 178–193 (1986)

[211] Pagani, M., Lombardi, F., Guzzetti, S., Rimoldi, O., Furlan, R., Pizzinelli, P., Sandrone, G., Malfatto, G., Dell'Orto, S., Piccaluga, F., Turiel, M., Baselli, G., Cerutti, S., Malliani, A.: Power spectral analysis of heart rate and arterial pressure variabilities as a marker of sympatho-vagal interaction in man and conscious dogs. Circulation Research **59**, 178–193 (1986)

[212] Pagani, M., Somers, V., Furlan, R., Dell'Orto, S., Conway, J., Baselli, G., Cerutti, S., Sleight, P., Malliani, A.: Changes in autonomic regulation induced by physical training in mild hypertension. Hypertension **12**(6), 600–610 (1988)

[213] Parati, G.: Arterial baroreflex control of heart rate: determining factors and methods to assess its spontaneous modulation. The Journal of Physiology **565**(3), 706–707 (2005)

[214] Parati, G., Di Rienzo, M., Bertinieri, G., Pomidossi, G., Casadei, R., Groppelli, A., Pedotti, A., Zanchetti, A., Mancia, G.: Evaluation of the baroreceptor-heart rate reflex by 24-hour intra- arterial blood pressure monitoring in humans. Hypertension **12**(2), 214–222 (1988)

[215] Parati, G., Mancia, G., Rienzo, M.D., Castiglioni, P., Taylor, J.A., Studinger, P.: Point:counterpoint: Cardiovascular variability is/is not an index of autonomic control of circulation. Journal of Applied Physiology **101**(2), 676–682 (2006)

[216] Pola, S., Macerata, A., Emdin, M., Marchesi, C.: Estimation of the power spectral density in nonstationary cardiovascular time series: assessing the role of the time-frequency representations (TFR). IEEE Trans. Biomed. Eng. **43**(1), 46–59 (1996)

[217] Porta, A., Aletti, F., Vallais, F., Baselli, G.: Multimodal signal processing for the analysis of cardiovascular variability. Phil Trans R Soc A **367**(1887), 391–409 (2009)

[218] Porta, A., Baselli, G., Rimoldi, O., Malliani, A., Pagani, M.: Assessing baroreflex gain from spontaneous variability in conscious dogs: role of causality and respiration. Am J Physiol Heart Circ Physiol **279**(5), H2558–H2567 (2000)

[219] Porta, A., Catai, A.M., Takahashi, A.C.M., Magagnin, V., Bassani, T., Tobaldini, E., van de Borne, P., Montano, N.: Causal relationships between heart period and systolic arterial pressure during graded head-up tilt. Am. J. Physiol. Regul. Integr. Comp. Physiol. **300**(2), R378–R386 (2011)

[220] Pueyo, E., Husti, Z., Hornyik, T., Baczkó, I., Laguna, P., Varró, A., Rodríguez, B.: Mechanisms of ventricular rate adaptation as a predictor of arrhythmic risk. Am J Physiol Heart Circ Physiol **298**(5), H1577–H1587 (2010)

[221] Pyetan, E., Akselrod, S.: Do the high-frequency indexes of hrv provide a faithful assessment of cardiac vagal tone? a critical theoretical evaluation

[222] Quyen, M.L.V., Foucher, J., Lachaux, J., Rodriguez, E., Lutz, A., Martinerie, J., Varela, F.J.: Comparison of hilbert transform and wavelet methods for the analysis of neuronal synchrony. J Neurosci Methods **111**(2), 83–98 (2001)

[223] Rajendra Acharya, U., Paul Joseph, K., Kannathal, N., Lim, C., Suri, J.: Heart rate variability: a review. Med. Biol. Eng. Comput **44**(12), 1031–1051 (2006)

[224] Rilling, G., Flandrin, P., Gonalves, P., Lilly, J.M.: Bivariate empirical mode decomposition. IEEE Signal Processing Letters **14**(12), 936–939 (2007)

[225] Robbe, H.W., Mulder, L.J., Rddel, H., Langewitz, W.A., Veldman, J.B., Mulder, G.: Assessment of baroreceptor reflex sensitivity by means of spectral analysis. Hypertension **10**(5), 538–543 (1987)

[226] Robinson, T.G., Dawson, S.L., Eames, P.J., Panerai, R.B., Potter, J.F.: Cardiac baroreceptor sensitivity predicts long-term outcome after acute ischemic stroke. Stroke **34**(3), 705–712 (2003)

[227] Rudrauf, D., Douiri, A., Kovach, C., Lachaux, J.P., Cosmelli, D., Chavez, M., Adam, C., Renault, B., Martinerie, J., Quyen, M.L.V.: Frequency flows and the time-frequency dynamics of multivariate phase synchronization in brain signals. Neuroimage **31**(1), 209–227 (2006)

[228] Sammler, D., Grigutsch, M., Fritz, T., Koelsch, S.: Music and emotion: electrophysiological correlates of the processing of pleasant and unpleasant music. Psychophysiology **44**(2), 293–304 (2007)

[229] Saul, J.P., Berger, R.D., Albrecht, P., Stein, S.P., Chen, M.H., Cohen, R.J.: Transfer function analysis of the circulation: unique insights into cardiovascular regulation. Am. J. Physiol. Heart Circ. Physiol. **261**(4), H1231–H1245 (1991)

[230] Schreiber, T., Schmitz, A.: Surrogate time series. Physica D: Nonlinear Phenomena **142**(3-4), 346 – 382 (2000)

[231] Seidel, H., Herzel, H., Eckberg, D.L.: Phase dependencies of the human baroreceptor reflex. Am. J. Physiol. Heart Circ. Physiol. **272**(4), H2040–H2053 (1997)

[232] Sejdic, E., Djurovic, I., Jiang, J.: Time-frequency feature representation using energy concentration: An overview of recent advances. Digital Signal Processing **19**(1), 153 – 183 (2009)

[233] Selvaraj, N., Jaryal, A., Santhosh, J., Deepak, K.K., Anand, S.: Assessment of heart rate variability derived from finger-tip photoplethysmography as compared to electrocardiography. J Med Eng Technol **32**(6), 479–484 (2008)

[234] Shepard, R.N.: Circularity in judgments of relative pitch. The Journal of the Acoustical Society of America **36**(12), 2346–2353 (1964)

[235] Shin, Y.J., Gobert, D., Sung, S.H., Powers, E.J., Park, J.B.: Application of cross time-frequency analysis to postural sway behavior: the effects of aging and visual systems. IEEE Trans. Biomed. Eng. **52**(5), 859–868 (2005)

[236] Sin, P.Y.W., Galletly, D.C., Tzeng, Y.C.: Influence of breathing frequency on the pattern of respiratory sinus arrhythmia and blood pressure: old questions revisited. Am. J. Physiol. Heart Circ. Physiol. **298**(5), H1588–H1599 (2010)

[237] Sleight, P., Bernardi, L.: Sympathovagal balance. Circulation **98**(23), 2640 (1998)

[238] Sörnmo, L., Laguna, P.: ECG signal processing: Heart rate variability. In: Bioelectrical Signal Processing in Cardiac and Neurological Applications, pp. 567 – 631. Academic Press (2005)

[239] de Souza Neto, E.P., Abry, P., Loiseau, P., Cejka, J.C., Custaud, M.A., Frutoso, J., Gharib, C., Flandrin, P.: Empirical mode decomposition to assess cardiovascular autonomic control in rats. Fundam Clin Pharmacol **21**(5), 481–496 (2007)

[240] Taylor, J.A., Eckberg, D.L.: Fundamental relations between short-term rr interval and arterial pressure oscillations in humans. Circulation **93**(8), 1527–1532 (1996)

[241] Thomas, G.D.: Neural control of the circulation. Advances in Physiology Education **35**(1), 28–32 (2011)

[242] Thomson, D.J.: Spectrum estimation and harmonic analysis. Proc. IEEE **70**(9), 1055–1096 (1982)

[243] Thomson, D.J.: Multiple-window spectrum estimates for non-stationary data. In: Proc. Ninth IEEE SP Workshop Statistical Signal and Array Processing, pp. 344–347 (1998)

[244] Thomson, D.J.: Jackknifing multitaper spectrum estimates. IEEE Signal Processing Magazine **24**(4), 20–30 (2007)

[245] Toledo, E., Gurevitz, O., Hod, H., Eldar, M., Akselrod, S.: Wavelet analysis of instantaneous heart rate: a study of autonomic control during thrombolysis. Am. J. Physiol. Regul. Integr. Comp. Physiol. **284**, R1079–R1091 (2003)

[246] Tzeng, Y.C., Sin, P.Y.W., Galletly, D.C.: Human sinus arrhythmia: inconsistencies of a teleological hypothesis. Am. J. Physiol. Heart Circ. Physiol. **296**(1), H65–H70 (January 2009)

[247] Vallais, F., Baselli, G., Lucini, D., Pagani, M., Porta, A.: Spontaneous baroreflex sensitivity estimates during graded bicycle exercise: a comparative study. Physiol Meas **30**(2), 201–213 (2009)

[248] Virtanen, M., Khnen, M., Nieminen, T., Karjalainen, P., Tarvainen, M., Lehtimki, T., Lehtinen, R., Nikus, K., Kbi, T., Niemi, M., Niemel, K., Turjanmaa, V., Malmivuo, J., Viik, J.: Heart rate variability derived from exercise ECG in the detection of coronary artery disease. Physiol Meas **28**(10), 1189–1200 (2007)

[249] Wahlberg, P., Hansson, M.: Kernels and multiple windows for estimation of the Wigner-Ville spectrumof gaussian locally stationary processes. IEEE Trans. Signal Process. **55**(1), 73–84 (2007)

[250] Westerhof, B.E., Gisolf, J., Karemaker, J.M., Wesseling, K.H., Secher, N.H., van Lieshout, J.J.: Time course analysis of baroreflex sensitivity during postural stress. Am. J. Physiol. Heart Circ. Physiol. **291**(6), H2864–H2874 (2006)

[251] Westerhof, B.E., Gisolf, J., Stok, W.J., Wesseling, K.H., Karemaker, J.M.: Time-domain cross-correlation baroreflex sensitivity: performance on the eurobavar data set. J Hypertens **22**(7), 1371–1380 (2004)

[252] White, L.B., Boashash, B.: Cross spectral analysis of nonstationary processes. IEEE Trans. Inf. Theory **36**(4), 830–835 (1990)

[253] Wiklund, U., Akay, M., Morrison, S., Niklasson, U.: Wavelet decomposition of cardiovascular signals for baroreceptor function tests in pigs. IEEE Trans. Biomed. Eng. **49**(7), 651–661 (2002)

[254] Xiao, J., Flandrin, P.: Multitaper time-frequency reassignment for nonstationary spectrum estimation and chirp enhancement. IEEE Trans. Signal Process. **55**(6), 2851–2860 (2007)

[255] Xiao, X., Mullen, T.J., Mukkamala, R.: System identification: a multi-signal approach for probing neural cardiovascular regulation. Physiol Meas **26**(3), R41–71 (2005)

[256] Xu, Y., Haykin, S., Racine, R.J.: Multiple window time-frequency distribution and coherence of eeg using slepian sequences and hermite functions. IEEE Trans. Biomed. Eng. **46**(7), 861–866 (1999)

[257] Yan, Y., Poon, C., Zhang, Y.: Reduction of motion artifact in pulse oximetry by smoothed pseudo Wigner-Ville distribution. Journal of NeuroEngineering and Rehabilitation **2** (2005)

[258] Yasuma, F., Hayano, J.i.: Respiratory sinus arrhythmia*: Why does the heartbeat synchronize with respiratory rhythm? Chest **125**(2), 683–690 (2004)

[259] Yoshiya, I., Shimada, Y., Tanaka, K.: Spectrophotometric monitoring of arterial oxygen saturation in the fingertip. Med. Biol. Eng. Comput. **18**(1), 27–32 (1980)

[260] Zhan, Y., Halliday, D., Jiang, P., Liu, X., Feng, J.: Detecting time-dependent coherence between non-stationary electrophysiological signals–a combined statistical and time-frequency approach. J Neurosci Methods **156**(1-2), 322–332 (2006)

[261] Zhao, H., Cupples, W.A., Ju, K.H., Chon, K.H.: Time-varying causal coherence function and its application to renal blood pressure and blood flow data. IEEE Trans. Biomed. Eng. **54**(12), 2142–2150 (2007)

[262] Zhao, H., Lu, S., Zou, R., Ju, K., Chon, K.H.: Estimation of time-varying coherence function using time-varying transfer functions. Ann Biomed Eng **33**(11), 1582–1594 (2005)